ABSTRACT

Title of Dissertation: INVESTIGATION OF VAPOR INJECTION HEAT PUMP SYSTEM WITH A FLASH TANK UTILIZING R410A AND LOW-GWP REFRIGERANT R32

Xing Xu, Doctor of Philosophy, 2012

Dissertation Directed by: Professor Reinhard Radermacher
Department of Mechanical Engineering

Vapor injection technique has proven to be effective in improving heat pump system performance, especially for cooling application at high ambient and heating application at low ambient temperature conditions. Recent research on vapor injection technique has been mostly focused on the internal heat exchanger cycle and flash tank cycle. The flash tank cycle typically shows better performance than the internal heat exchanger cycle. However, the flash tank cycle control strategy is not yet clearly defined. Improper system control strategy would result in undesirable amount of liquid refrigerant injected to the compressor or poor system performance.

In this research work, a novel cycle control strategy for a residential R-410A vapor injection flash tank heat pump system was developed and experimentally investigated. The proposed cycle control strategy utilizes an electronic expansion valve

(EEV) coupled with a proportional-integral-derivative (PID) controller for the upper-stage expansion and a thermostatic expansion valve (TXV) for the lower-stage expansion, and applies a small electric heater in the vapor injection line to introduce superheat to the injected vapor thus providing a control signal to the upper-stage EEV. The proposed control strategy functions effectively for both transient and steady-state operating conditions.

As global warming has raised more critical concerns in recent years, refrigerants with high global warming potentials (GWP) are facing the challenges of being phased out. R410A, with a GWP of 2,088, has been widely used in residential air-conditioners and heat pump systems. A potential substitute for R410A is R32, which has a GWP of 675. This research work also investigates the performance difference using R410A and R32 in a vapor-injected heat pump system. A drop-in test was performed using R32 in a heat pump system that is designed to utilize R410A, for both cooling and heating conditions. Through experimentation, it was found that there was improvement for capacity and coefficient of performance (COP) using R32, as compared to an identical cycle using R410A. The compressor, heat exchangers and two-stage vapor injection cycle have been modeled and validated against experimental data to facilitate an optimization study. Heat exchangers were optimized using 5 mm copper tubes and result in significant cost reduction while maintaining the same capacity. Compressor cooling was investigated to decrease the high compressor discharge temperature for R32.

INVESTIGATION OF VAPOR INJECTION HEAT PUMP SYSTEM WITH A FLASH TANK UTILIZING R410A AND LOW-GWP REFRIGERANT R32

By

Xing Xu

Dissertation submitted to the Faculty of the Graduate School of the
University of Maryland, College Park, in partial fulfillment
of the requirements for the degree of
Doctor of Philosophy
2012

Advisory Committee:
Professor Reinhard Radermacher, Chair/Advisor
Research Associate Professor Yunho Hwang
Professor Gregory Jackson
Associate Professor Bao Yang
Associate Professor Peter Sunderland (Dean's Representative)

Dedication

To my wife
and my parents for their love and support

Acknowledgements

I would like to thank my advisor, Dr. Reinhard Radermacher, for his kindness of offering me this opportunity to work at University of Maryland College Park. His dedications to scientific research and visions in leading CEEE have inspired me, and his insights and guidance have always been very helpful and encouraging.

I also would like to thank my immediate research advisor, Dr. Yunho Hwang, for his kindness in helping me on my research in CEEE. Dr. Hwang is very knowledgeable, and the suggestions he gives always motivate me to explore further.

I would like to thank the CEEE lab manager, Jan Muehlbauer, for all the lab work he taught me. Hongtao Qiao and Long Huang gave me valuable suggestions on the simulation using CEEE software packages and modeling work. The discussions with Hoseong Lee, Daniel Leighton and Magnus Eisele have always been very helpful. I also would like to thank other colleagues that I have worked with, and I have learned a lot from all of them. In addition, the support from the sponsors of the Alternative Cooling Technologies and Applications Consortium at the University of Maryland, and Emerson Climate Technologies are greatly appreciated.

Finally, I would like to thank my wife, who has helped me a lot during my PhD study. The love she gives me and the sacrifices she has made always give me the courage to overcome the difficulties in the journey of pursuing a PhD. I also would like to thank my parents in China for their love and support. I am deeply grateful to all of them.

Table of Contents

List of Tables

List of Figures

Nomenclature

Acronyms and Abbreviations:

ASHRAE	American Society of Heating, Refrigeration and Air-Conditioning Engineers
AHRI	Air-Conditioning, Heating, and Refrigeration Institute
CEEE	Center for Environmental Energy Engineering
CFC	Chlorofluorocarbons
COP	Coefficient of Performance
EES	Engineering Equation Solver
EEV	Electronic Expansion Valve
FPI	Fins per inch
FTC	Flash Tank Cycle
GA	Genetic Algorithm
HCFC	Hydrochlorofluorocarbons
HFC	Hydrofluorocarbons
HFO	Hydrofluoroolefins
HP	Heat Pump
HX	Heat Exchanger
HVAC	Heating, Ventilation and Air-Conditioning
IHXC	Internal Heat Exchanger Cycle
MFR	Mass Flow Rate
MOGA	Multi-Objective Genetic Algorithm
OD	Outer Diameter
OEM	Original Equipment Manufacturer
P-h	Pressure Enthalpy
PID	Proportional Integral Derivative
RPM	Revolution per minute
TEWI	Total Equivalent Warming Impact
TXV	Thermostatic Expansion Valve
VI	Vapor Injection

Symbols:

A	Area of the nozzle exit plane, m^2
A_i	Heat transfer area inside of the compressor shell, m^2
A_o	Heat transfer area outside of the compressor shell, m^2
A_{plate}	Compressor middle plate area, m^2
C_d	Air nozzle discharge coefficient

C_p	Air specific heat capacity, $J/kg \cdot K$
C_1 to C_{10}	Coefficients for compressor model
h	Refrigerant enthalpy, J/kg
h_{fg}	Latent heat, J/kg
h_{liq}	Flash tank liquid height, m
Δh_{air}	Outlet and inlet air enthalpy difference, J/kg
Δh_{ref}	Outlet and inlet refrigerant enthalpy difference, J/kg
$\dot{m}$	Mass flow rate, kg/s
$\dot{m}_{air}$	Air mass flow rate, kg/s
$\dot{m}_{inj,vap}$	Injected vapor mass flow rate, kg/s
$\dot{m}_{inj,liq}$	Injected liquid mass flow rate, kg/s
$\dot{m}_{liq}$	Liquid mass flow rate, kg/s
$\dot{m}_{ref}$	Refrigerant mass flow rate, kg/s
$\dot{m}_{suc}$	Suction mass flow rate, kg/s
$\dot{m}_{total}$	Total refrigerant mass flow rate, kg/s
$\dot{m}_{vap}$	Vapor mass flow rate, kg/s
P	Pressure, Pa
ΔP	Pressure drop, Pa
$P_{A,low}$	Percentage of the compressor surface area for the low-pressure cylinder
$\dot{P}_{comp}$	Compressor power consumption, W
$\dot{P}_{motor}$	Total motor power, W
$\dot{P}_{motor,high}$	Power consumption of the high-stage compression, W
$\dot{P}_{motor,low}$	Power consumption of the low-stage compression, W
$\dot{P}_{total}$	Total power consumption, W
$\dot{Q}$	Cooling and heating capacity, W
$\dot{Q}_{air}$	Air-side capacity, W
$\dot{Q}_{loss}$	Total heat loss of the compressor, W
$\dot{Q}_{loss,high}$	Heat loss of the high-pressure cylinder to the ambient, W
$\dot{Q}_{loss,low}$	Heat loss of the low-pressure cylinder to the ambient, W
$\dot{Q}_{motor}$	Compressor motor heat, W
$\dot{Q}_{net}$	Net capacity, W

$\dot{Q}_{plate}$	Heat transfer through the middle plate of compressor, W
$\dot{Q}_{ref}$	Refrigerant-side capacity, W
$\dot{Q}_{shell}$	Total heat transfer between refrigerant and compressor shell, W
$\dot{Q}_{shell,high}$	Heat transfer between refrigerant and high-pressure cylinder of compressor, W
$\dot{Q}_{shell,low}$	Heat transfer between refrigerant and low-pressure cylinder of compressor, W
r	Portion of refrigerant that flows directly into the scroll compression chamber
$S_{\tan k}$	Flash tank intersectional area, m^2
Δt_{air}	Outlet and inlet air temperature difference, ºC
T_{amb}	Ambient temperature, ºC
T_{cond}	Condensing temperature, ºC
T_{int}	Refrigerant temperature in low-pressure cylinder of compressor, ºC
T_{plate}	Compressor high-low pressure separating plate temperature, ºC
$T_{sat,inj}$	Saturation injection temperature, ºC
$T_{shell,high}$	Compressor shell temperature of the high-pressure cylinder, ºC
$T_{shell,low}$	Compressor shell temperature of the low-pressure cylinder, ºC
T_{sup}	Superheat, K
T_{evap}	Evaporating temperature, ºC
T_1	Compressor shell suction port temperature, ºC
T_{1a}	Compressor scroll suction temperature, ºC
T_2	Compressor shell discharge port temperature, ºC
T_{2a}	Compressor scroll discharge temperature, ºC
$U_{i,high}$	Heat transfer coefficient on high-pressure cylinder inside of the compressor shell, $W/kg \cdot K$
$U_{i,low}$	Heat transfer coefficient on low-pressure cylinder inside of the compressor shell, $W/kg \cdot K$
U_o	Heat transfer coefficient of the outer shell of the compressor, $W/kg \cdot K$
U_{plate}	Heat transfer coefficient of compressor middle plate, $W/kg \cdot K$
V_1	Low-stage compressor volume, m^3
V_2	High-stage compressor volume, m^3
V_{liq}	Liquid volume, m^3

$V_{\tan k}$	Flash tank volume, m^3
V_{vap}	Vapor volume, m^3
$\dot{W}_{blower}$	Indoor blower power consumption, W
W_{in}	Humidity ratio of air at heat exchanger inlet, kg/kg
$\dot{W}_{total}$	Total power consumption, W
x_n	"n"th variable

Greek Letters:

α	Vapor injection ratio
β	Liquid injection ratio
ε	Performance difference of R32 vs. R410A
ρ	Density, kg/m^3
ρ_{air}	Density of the air through the nozzle, kg/m^3
ρ_{1a}	Low-stage refrigerant suction density, kg/m^3
$\eta_{ise,high}$	High-stage isentropic efficiency
$\eta_{ise,high,s}$	High-stage isentropic efficiency based on scroll parameters
$\eta_{ise,low}$	Low-stage isentropic efficiency
$\eta_{ise,low,s}$	Low-stage isentropic efficiency based on scroll parameters
η_{motor}	Motor efficiency
$\eta_{vol,high}$	High-stage volumetric efficiency
$\eta_{vol,high,s}$	High-stage volumetric efficiency based on scroll parameters
$\eta_{vol,low}$	Low-stage volumetric efficiency
$\eta_{vol,low,s}$	Low-stage volumetric efficiency based on scroll parameters
γ	Performance variation of a vapor-injected system vs. a non-vapor-injected system
ω_f	Systematic uncertainty of parameter f
ω_P	Systematic uncertainty of pressure
ω_{rand}	Random uncertainty
ω_{sys}	Systematic uncertainty
ω_T	Systematic uncertainty of temperature
ω_{total}	Total uncertainty
$\omega_{T_{sup}}$	Systematic uncertainty of superheat

ω_{x_n}	Systematic uncertainty of parameter x_n

Subscripts:

air	Air
in	Inlet condition
inj	Injection
out	Outlet condition
P	Pressure
ref	Refrigerant
suc	Suction
T	Temperature

1. Introduction and literature review

1.1 Background

Vapor compression cycle has been widely used in the residential houses for both cooling and heating applications. A typical vapor compression cycle is comprised of a compressor, a condenser, an expansion valve and an evaporator. The schematic and Pressure-enthalpy (P-h) diagram are shown in Figure 1-1. Vapor refrigerant is compressed in the compressor, and turns into high-pressure and high-temperature state. Then the refrigerant flows through the condenser for condensing. Vapor refrigerant is changed into liquid refrigerant after dissipating heat in the condenser. The liquid refrigerant flows through the expansion valve, and its pressure and temperature are decreased dramatically. The liquid refrigerant turns into two-phase refrigerant. Then the two-phase refrigerant flows through the evaporator, absorbs heat from the evaporator, and turns into vapor refrigerant. The compressor draws the vapor refrigerant from the outlet of the evaporator for compression to form a closed-loop vapor compression cycle.

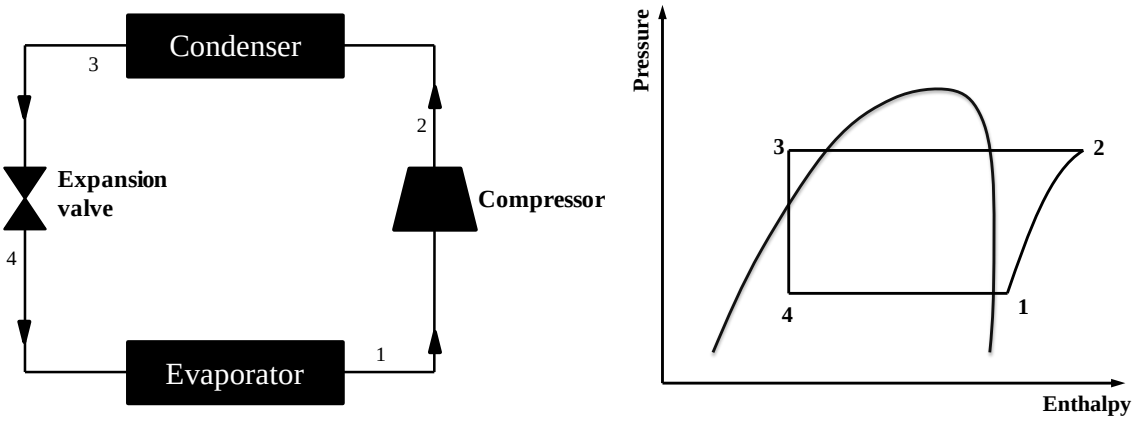

Figure 1-1: The schematic and P-h diagram of a typical vapor compression cycle

This cycle works quite well in moderate ambient temperature conditions. However, the system performance degradation becomes quite significant when the ambient temperature decreases to be much lower than -8℃ for the heating application, or much higher than 35℃ for the cooling application. For the low ambient temperature heating condition, the evaporating temperature in the evaporator should be lower than that of the ambient environment in order to absorb heat from the ambient, which results in low refrigerant density in the compressor suction port. As a result, the refrigerant mass flow rate is quite low. Moreover, the isentropic efficiency of the compressor at low temperature is not high either, thus the power consumption of the compressor becomes excessively high. The overall effect is that the heating capacity and the heating coefficient of performance (COP) are reduced compared to the operation at moderate ambient temperature conditions. For the high ambient temperature cooling application, the condensing temperature in the condenser needs to be higher than the ambient in order to dissipate heat to the ambient environment, and therefore the compressor has to compress the refrigerant to a higher pressure and temperature in order to dump the heat from the condenser. This also elevates the compressor power consumption, and thus reduces the cooling COP. Moreover, the compressor discharge temperature is excessively high at high ambient temperature conditions, which might degrade the lubricating oil in the compressor, and harm the reliability of the system operation.

With the above mentioned issues, the refrigerant injection technique was introduced. A simple schematic of the refrigerant injection cycle is shown in Figure 1-2. Partial of the refrigerant after the upper-stage expansion is extracted and injected to the

compressor. It has proven to be effective in ensuring the reliable cycle operation and improving the performance of a vapor compression cycle.

Refrigerant injection can be classified into two types: liquid refrigerant injection and vapor refrigerant injection. “Liquid” injection and “vapor” injection refers to the state in which the refrigerant is injected to the compressor. The former is commonly used for decreasing the extremely high discharge temperature of the compressor, and ensuring the reliable system operation. The latter is used for so-called “economizer cycle” to improve the cooling/heating capacity at the same stroke volume of the compressor (Dutta et al., 2001).

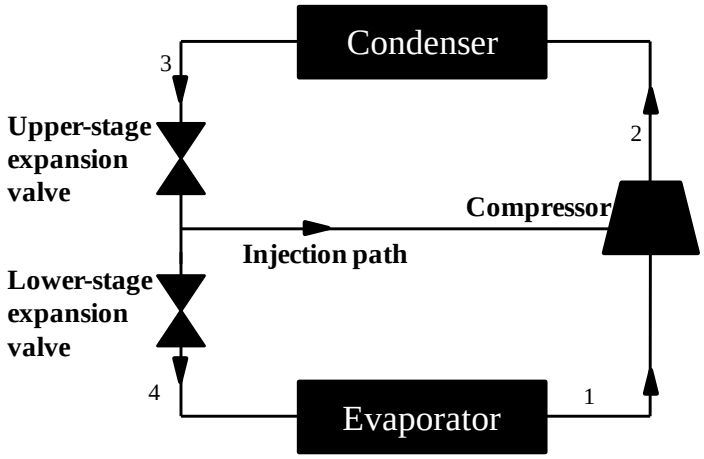

Figure 1-2: A simple schematic of a typical refrigerant injection cycle

1.2 Introduction to refrigerant injection

1.2.1 Liquid refrigerant injection

Liquid refrigerant injection refers injecting liquid-state refrigerant into the compressor. The injection location can either be the compressor suction port or the intermediate location of the compressor. The principle of liquid injection into the

compressor is not a new concept. United States patents existed since 1946 for reciprocating compressors and later for rolling piston compressors (Holtzapple, 1989). Haselden (1976) patented liquid refrigerant injection applied to a screw compressor. The liquid refrigerant was injected to seal the compressor rotor clearance. A number of designs (Kamimura et al., 1999; Cho and Bai, 2003; Fujita and Amo, 2003; Bush et al., 2004; Ignatiev and Caillat, 2008) were also patented with respect to the liquid refrigerant injection technique.

Operating compressors at high compression ratios can result in excessively high discharge temperatures, which can chemically degrade refrigerant oil and lead to mechanical failure. Therefore, employing liquid injection is a good option when high pressure ratios are reached. Dutta et al. (2001) investigated the influence of liquid refrigerant injection on the performance of a scroll compressor both experimentally and theoretically. The oil temperature was maintained to be constant in the first experiments. It was found that the injection increased the compressor power and decreased the compressor efficiency. Later the system was operated without controlling the compressor oil temperature. Slight improvement was observed for the system performance. This was due to the fact that the liquid injection tended to decrease the oil temperature, which led to improvement in the system performance. Sami et al. (2001; 2002; 2003a; 2003b) did a series of liquid injection testing with different refrigerant mixtures such as R404A, R410A, R407C and R507C, and concluded that the liquid injection was effective in reducing the compressor discharge temperature. Cho et al. (2003) studied an inverter-driven scroll compressor with liquid injection at different compressor frequencies. The

liquid injection under high frequency was very effective in attaining prominent performance and reliability of the compressor. Some disadvantages were found with injection at low frequency with respect to the compressor power, capacity and adiabatic efficiency due to high leakage through the gap in the scroll wrap. Kang et al. (2008) studied the effects of liquid refrigerant injection on the performance of a refrigerant system with an accumulator heat exchanger. It was found that the liquid injection coupled with an accumulator exchanger was effective for controlling adequate subcooling and the compressor discharge temperature of the compressor at high ambient temperatures. Liu et al. (2008) studied the liquid injection using a rotary compressor for a heat pump water heating system. It was found that the compressor discharge temperature decreased significantly due to the liquid injection. The liquid refrigerant injection mass flow rate was quite small compared to the mass flow rate of the main circuit; therefore the capacity remained almost the same when compared to the case without the injection.

1.2.2 Vapor refrigerant injection

Vapor refrigerant injection typically refers to injecting vapor refrigerant to an intermediate location of the compressor. Compared to liquid refrigerant injection, more benefits were found for the vapor injection technique, and are listed as follows:

(1) Capacity improvement in severe climate (heat pumping at lower than -8℃ and air conditioning of higher than 35℃ of ambient temperature) was significant, which provides alternative heating/cooling method in cold/hot ambient climates. Figure 1-3 shows the design comparison of a conventional heat pump system and a vapor injection heat pump system. It can be seen that the heating demand increases with decreasing

ambient temperature, and the cooling demand increases with increasing ambient temperature. The intersections of the demand and system capacity show the design points of a heat pump system. It can be seen that the design points of a vapor injection system can be extended compared to a conventional heat pump system.

(2) System capacity can be varied by controlling the injected refrigerant mass flow rate, which permits some energy savings by avoiding intermittent operation of the compressor.

(3) The compressor discharge temperature of a vapor injection cycle is lower than that of a conventional single stage cycle. Therefore, the working envelop of the compressor is improved.

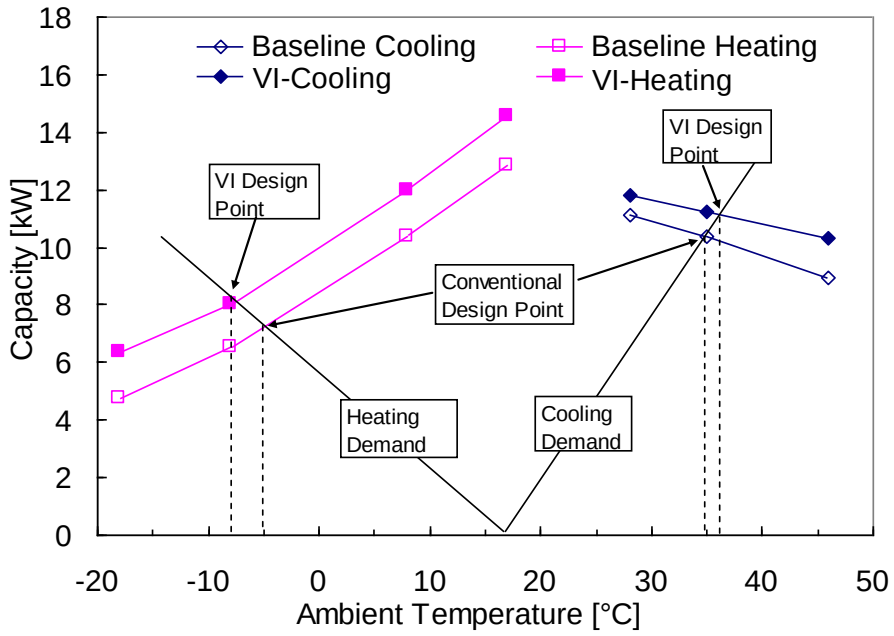

Figure 1-3: Comparison of system design points of a conventional system and a vapor injection system (Wang, 2009c)

Vapor injection has been marketed since 1979 for room air conditioners (Umezu and Suma, 1984). Ueno and Fukuhara (1982) presented a vapor refrigerant injection system with a rotary compressor. A flash tank was used as the liquid and vapor separator. An injection control valve was employed to control the injection process, in order to control the system capacity. Atsumi et al. (1985) also presented a vapor injection system employing the flash tank as the two-phase separator. Abel et al. (2007) presented a vapor injection system employing a scroll compressor. Baek et al. (2008) experimentally studied a CO_2 heat pump system coupled with vapor injection. The heating capacity and COP of the system with vapor injection were improved by 45% and 24%, respectively, over the non-injection system at the outdoor temperature of -8℃. Ma and Zhao (2008) studied the vapor injection heat pump cycle employing a flash tank coupled with a scroll compressor. The system demonstrated sufficient heating capacity of 8.15 kW at a condensing temperature of 45℃ and an evaporating temperature of -25℃, which they concluded was sufficient for heating in severely cold regions. Cao et al. (2009a) studied a heat pump water heater using a vapor injection system with a mixture of R22/R600a. It was found that compared with using R22 as the refrigerant, the heating capacity and COP of the system with the mixing refrigerant of R22/R600a were higher when the vapor injection was used. Moreover, the compressor discharge temperature could be controlled below 100℃. Cho et al. (2009) investigated the performance and operating characteristics of a two-stage CO_2 cycle with vapor injection. The maximum COP improvement of cooling mode was 16.5% compared to the two-stage non-injection cycle.

1.2.3 Internal heat exchanger cycle

Two typical refrigerant injection cycles can be found in the literature: vapor injection cycle with a flash tank and vapor injection cycle with an internal heat exchanger. The schematics and P-h diagrams of the internal heat exchanger cycle are shown in Figure 1-4. The cycle operates as follows: the refrigerant exiting the compressor circulates through the condenser first, and is then separated into two paths. One path flows through the upper-stage expansion valve and enters the internal heat exchanger, where it provides subcooling to the refrigerant coming from the other path. The two-phase refrigerant absorbs heat in the internal heat exchanger and turns into vapor state, which is then injected to the compressor. The subcooled liquid enters the lower-stage expansion valve, through the evaporator, and flows to the compressor suction. The essential reason that the internal exchanger cycle can improve both the capacity and COP compared to the single stage cycle is as follows: The liquid refrigerant entering the internal heat exchanger is subcooled by the two-phase refrigerant entering the internal heat exchanger from the other path. From Figure 1-4 it can be seen that state 3 is extended to state 5. Therefore, after the lower-stage expansion, the enthalpy difference across the evaporator is larger than the single stage cycle. Although the vapor injection reduces the refrigerant mass flow rate through the evaporator, the increased enthalpy difference increases the two-phase heat transfer area in the evaporator. Therefore, the overall effect is that the system capacity is increased. In addition, vapor injection reduces the compressor discharge temperature because the injected vapor temperature is less than that of the vapor in the compressor. Therefore, the compression process is closer to

isentropic process compared to the single stage cycle. Thus the compression power can be reduced, leading to the increase of system COP. A number of studies have shown the potential capacity and COP improvement by employing the internal heat exchanger cycle (Ma et al., 2003; Ma and Chai, 2004; Hwang et al., 2004; Tian et al., 2006; Tian and Liang, 2006; Bertsch and Groll, 2008; Cao et al., 2009a; 2009b).

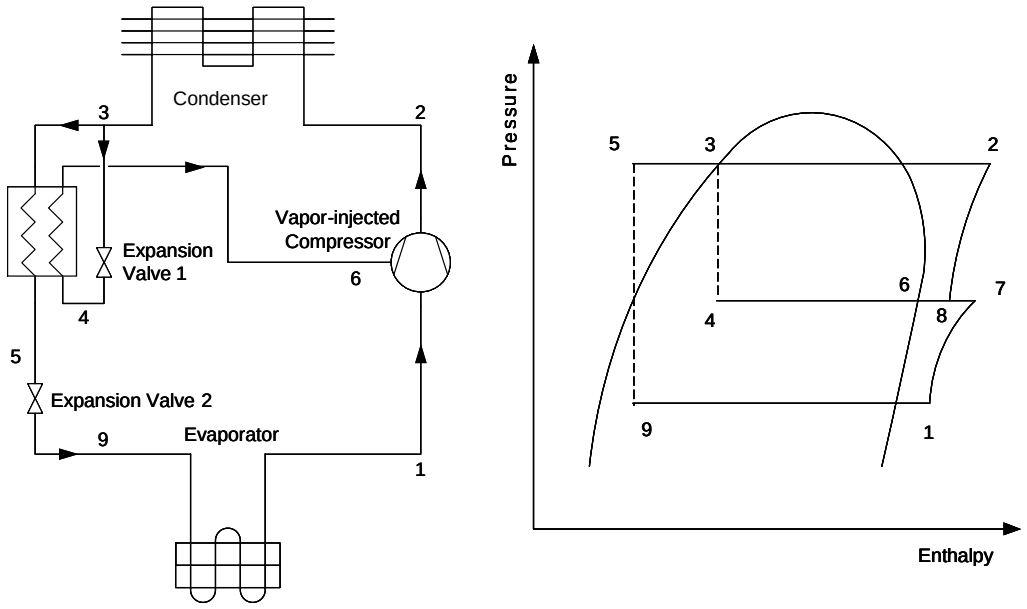

Figure 1-4: Schematic and P-h diagram of an internal heat exchanger vapor injection cycle (Wang, 2008)

1.2.4 Flash tank cycle

Figure 1-5 shows the schematic and the P-h diagram of the flash tank cycle. The working principle is as follows: the refrigerant discharged from the compressor flows through the condenser and then through the upper-stage expansion valve; then it is separated into liquid phase and vapor phase in the flash tank. The liquid refrigerant enters the lower-stage expansion valve, circulates through the evaporator, and enters the

compressor suction port. The vapor refrigerant is injected to the intermediate pressure port of the compressor. From Figure 1-5 it can be seen that due to the two-phase separation in the flash tank, the liquid entering the evaporator has lower enthalpy compared to that of a single stage cycle. Thus the enthalpy difference across the evaporator is greater than that of a single stage cycle. Similar to the internal heat exchanger cycle, the vapor injection reduces the refrigerant mass flow rate through the evaporator. However, the increased enthalpy difference increases the two-phase heat transfer area in the evaporator. Therefore, the overall effect is that the system capacity is increased. The increased system capacity also leads to an increase in the system COP. The saturated vapor from the flash tank also has lower temperature than that of the vapor in the compressor, which helps to reduce the compressor discharge temperature. A number of patents have detailed the refrigerant injection cycle coupled with a flash tank (Ueno and Fukuhara, 1982; Atsumi et al., 1985; Abel et al., 2007; Moriwaki et al., 2008). Numerous research articles (Baek et al., 2008; Ma and Zhao, 2008; Wang, 2008; Wang et al., 2009c; Fan et al., 2008; Xu et al., 2010a, 2010b, 2011a, 2011b, 2011c, 2012; Qiao et al., 2012) also discussed in detail on the flash tank cycle.

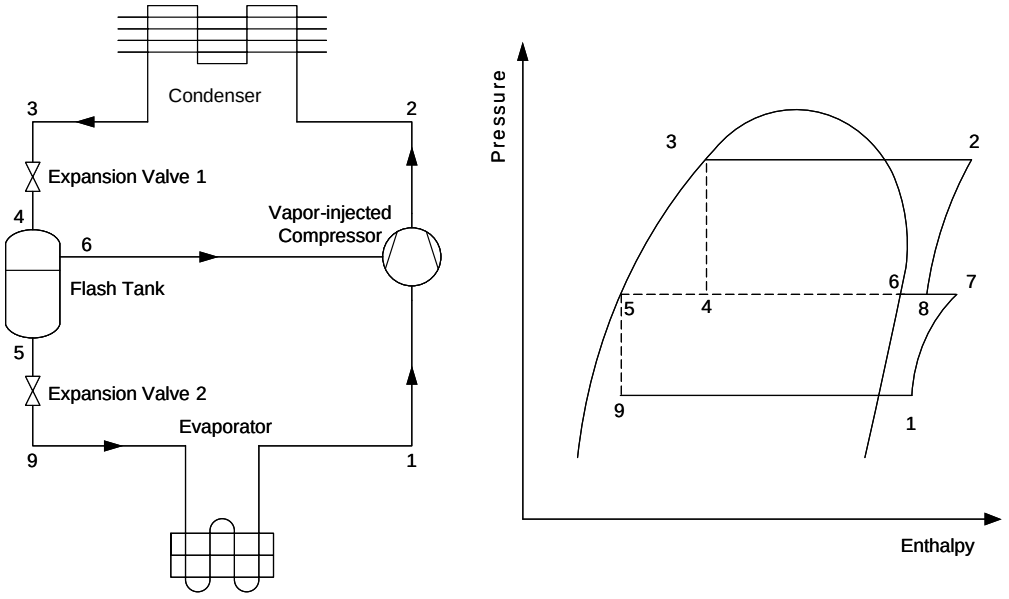

Figure 1-5: Schematic and P-h diagram of a flash tank vapor injection cycle (Wang, 2008)

1.3 Literature review on refrigerant injection

1.3.1 System level research

A number of research projects on refrigerant injection techniques have been conducted on the system level. These research projects have been categorized into low ambient temperature heating, heat pump water heating, high ambient temperature cooling, cycle comparison and cycle control strategy, and are summarized in detail in the following sections.

1.3.1.1 Low ambient temperature heating

Conventional air source heat pump undergoes significant performance degradation at extremely cold climates. This is due to reduced volumetric efficiency of compressors and decreased refrigerant mass flow rate. In such climates, the refrigerant

injection techniques present prominent features. The improvement of capacity and COP are significant compared to conventional systems. A number of research projects have been conducted for the low temperature heating application. Hirano et al. (1993) tested a heat pump using a scroll compressor coupled with liquid refrigerant injection, which was proven to work smoothly at a low ambient temperature of -20 ℃. Ma et al. (2003) studied an air source heat pump employing vapor injection coupled with an internal heat exchanger. The system was tested for a whole winter in Beijing, China. The system was operated reliably at the ambient temperature as low as -15 ℃. It was also found that the heating capacity and COP improved remarkably compared to the conventional heat pump cycle. He et al. (2006) conducted a field-testing of a R22 vapor injection heat pump. The results showed that the heating capacity and COP of the vapor injection system improved by 34% and 6%, respectively at an outdoor ambient temperature of -20 ℃ and an indoor temperature of 20 ℃, when compared to the conventional system. Tian et al. (2006a) studied an air source heat pump employing vapor injection coupled with an internal heat exchanger. Through the experiments it was found that the heating COP was over 2.0 when the condensing temperature was 50 ℃ and the evaporating temperature was -25 ℃. The system ran safely and steadily. Huang et al. (2007) conducted a field-testing of a R407C vapor injection heat pump. The field unit was installed in a 105 m^2 semi-detached three bedroom family house in the United Kingdom, and had been operated since February 2006. It was found that such a unit was capable of economically heating a typical family home in the United Kingdom. Baek et al. (2008) tested a CO_2 heat pump cycle with vapor injection. The heating capacity and COP were improved by 45% and

24%, respectively, compared to a non-injection system at the outdoor temperature of -8℃. Bertsch and Groll (2008) tested a two-stage heat pump system at low ambient temperature. The heating COP was found to be 2.1 at the ambient temperature of -30℃. Wang (2008) conducted a series of testing using the vapor injection technique, and reported a maximum capacity and COP improvement of 33% and 23%, respectively, when the ambient temperature was -18℃. Joppolo et al. (2010) studied a 20 kW air-to-water heat pump equipped with vapor injection scroll compressor using R407C as the refrigerant. Their work showed that the heating capacity remained almost the same for the vapor injection operation when the water outflow temperature increased. While for the non-injection operation, the system capacity decreased with the increasing outflow water temperature. The compressor discharge temperature was also reduced significantly due to vapor injection. As summarized, the refrigerant injection techniques indeed improve the heat pump performance significantly at extremely low ambient temperatures.

1.3.1.2 Heat pump water heating

As the trend of energy saving becomes pronounced, more and more substitutes for a conventional electric water heater appeared in the market. Heat pump water heater is a good substitute for electric water heater for residential hot water use. A heat pump water heater utilizes the heat rejected from the condenser of a vapor compression cycle. By applying the refrigerant injection techniques, the capacity of the heat pump water heater can be improved. This is due to the increase of refrigerant mass flow rate through the condenser, which leads to greater heat transfer through the condenser. Ma and Chai (2004) tested a heat pump cycle with hot water supply. The prototype demonstrated high

temperature and capacity water supply even at the ambient temperature of -10 ℃ to -15 ℃. Liu et al. (2008) tested a heat pump water heater employing the liquid injection technique. It was found that the water heating capacity increased significantly, together with a lower rate of power consumption increase, which led to an increase of the overall COP. The hot water also greatly reduced the defrosting time. Fan et al. (2008) tested a heat pump water heater using R22 as the refrigerant at ambient temperatures of -30 ℃ to 12 ℃. The hot water temperature was between 55 ℃ to 60 ℃. With vapor injection, the hot water heating capacity increased from 2.0 kW to 2.8 kW, together with a COP increase from 1.5 to 1.8. Cao et al. (2009a) studied a heat pump water heater using mixture of R22/R600a. By using the vapor injection technique, the water heater exhibited better performance at low ambient temperature with 85/15% composition. Cao et al. (2009b) also tested a heat pump water heater using suction stream liquid injection. They found that the heating capacity decreased with the injection ratio. The discharge temperature, however, was effectively decreased by the liquid injection. They also presented a theoretical model to predict the performance of the heat pump water heater. The modeling results matched well with the experimental ones with accuracy of 10%.

1.3.1.3 High ambient temperature cooling

In addition to the remarkable improvement in heating mode, refrigerant injection also poses prominent features when applied to the air conditioning systems. The cooling capacity can be greatly enhanced by applying refrigerant injection. Bertsch and Groll (2008) tested a vapor injection cycle at the ambient temperature of 50 ℃. The system demonstrated sufficient capacity for cooling application. Due to the vapor injection effect,

the compressor discharge temperature remained below 105 ℃ and worked reliably. Cho et al. (2009) tested a two-stage CO_2 cycle with vapor injection for the cooling mode operation. The cooling COP of the two-stage cycle was enhanced by 16.5% over that of the two-stage non-injection cycle. The compressor discharge temperature was also decreased by 5 ℃ to 7 ℃, due to the inter-cooling effect from the vapor injection. Wang et al. (2009c) tested both the internal heat exchanger cycle and the flash tank cycle at severe climates. The two cycles showed comparable performance improvement compared to the baseline without injection. It was found that the cooling COP and capacity improvements at ambient temperature of 46 ℃ were 2% and 15%, respectively.

1.3.1.4 Cycle comparison

From a thermodynamics point of view, the performance of the internal heat exchanger cycle and the flash tank cycle should have similar performance. From the P-h diagrams in Figure 1-4 and Figure 1-5 it can be seen that the working principle is to decrease the evaporator inlet enthalpy by two-stage expansion. The only difference is to achieve it by sub-cooling through the additional heat exchanger or by two-phase separation in the flash tank. However, the actual performance of the flash tank cycle is superior to that of the internal heat exchanger cycle. Wang (2008) has experimentally shown that the flash tank cycle has 2%~5% higher heating capacity and COP than those of the internal heat exchanger cycle. Ma and Zhao (2008) concluded that the heating capacity and COP of the flash tank cycle were 10.5% and 4.3% higher than those of the internal heat exchanger cycle, respectively. The essential reason is that the internal heat exchanger introduces additional pressure drop to the injected vapor, and therefore lowers

the benefits of vapor injection. On the contrary, the liquid and vapor separation in the flash tank leads to a saturated state of refrigerant, and therefore there is no additional pressure drop introduced for the vapor injection process. Additionally, the cost of a flash tank is expected to be less than that of a heat exchanger, therefore the flash tank cycle becomes more attractive to academic researchers and industrial manufacturers. However, there is also advantage of the internal heat exchanger cycle. Comparing the operating range of the injection pressure, the internal heat exchanger cycle has a much wider operating range than that of the flash tank cycle, as shown in Figure 1-6. Nguyen et al. (2007) conducted a series of tests to investigate the performance of a vapor-injected compressor in an air-source R407C heat pump, and applied both an internal heat exchanger and a flash tank cycle. They also concluded that the internal heat exchanger cycle with thermostatic expansion valves (TXVs) had a wider injection operating range compared to the flash tank cycle. In all, flash tank cycle is more favorable in terms of the system performance improvement and the relatively low cost, and the internal heat exchanger cycle is more favorable to achieve a wider injection operating range.

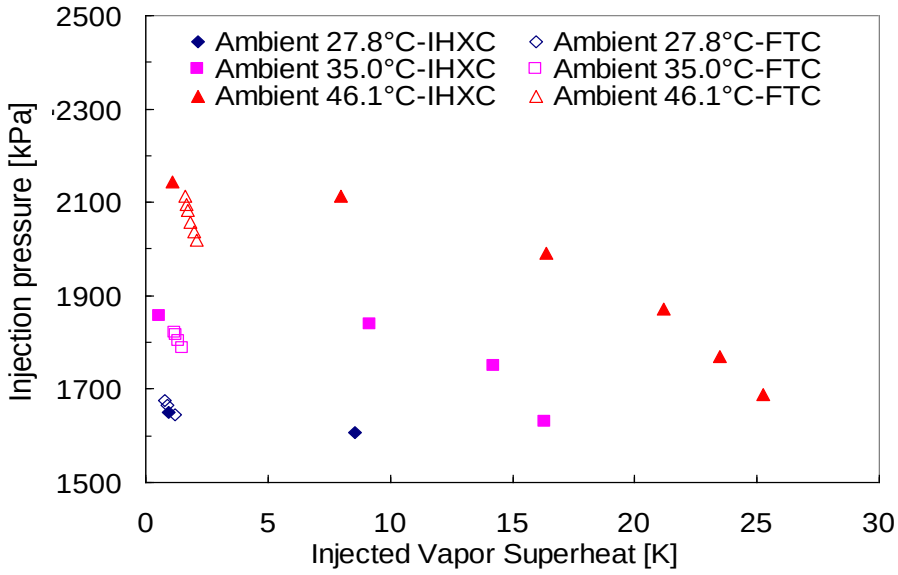

Figure 1-6: Injection pressure comparison of internal heat exchanger cycle and flash tank cycle (Wang, 2008)

1.3.1.5 Cycle control strategy

In spite of all the advantages of refrigerant injection discussed in this research work, proper controls of the vapor injection cycles are still quite challenging. The first issue is the appropriate control of the refrigerant injection control valve. Leimbach and Heffner (1992) proposed a refrigerant injection valve based on temperature responsive sensor. It controls the opening of injection port by measuring the compressor discharge temperature. Lifson and Taras (2008) developed a time dependent vapor injection scheme to reduce losses and to enhance the performance. In their work, a fast-acting control valve was placed on the vapor injection line in the vicinity of the vapor injection port to control the timing during which vapor injection would occur.

Conventional air conditioning/heat pump systems are typically equipped with a single expansion valve, and therefore the system control is much simpler. In the refrigerant injection system, two expansion valves are presented. The appropriate control of the two expansion valves is critical to the reliable operation of the system. Moreover, the performance improvement is closely related to the expansion valves' control. It should also be noted that the control strategies vary for the internal heat exchanger cycle and the flash tank cycle.

Conventional TXV control employs the evaporator outlet superheating as the control parameter to regulate the expansion valve opening. A sensing bulb and a pressure balancing line are attached to the evaporator outlet, which measure the degree of superheat at the evaporator outlet to control the expansion valve opening. The two expansion valves in the internal heat exchanger cycle can both adopt this method for each of the controls; therefore the control strategy of the internal heat exchanger cycle is relatively easier. The upper-stage expansion valve can use the internal heat exchanger outlet superheating to control its opening, and the lower stage expansion valve can use the evaporator outlet superheating to control its opening. This method has been used by Wang (2008) in the experimental studies of the internal heat exchanger cycle and proven to work effectively.

Compared to the internal heat exchanger cycle, the flash tank cycle is more difficult to control. The vapor refrigerant separated in the flash tank is in a saturated state, and therefore a conventional TXV does not function properly in this case because it causes TXV hunting (Beeton and Pham, 2003). As a result, an electronic expansion valve

(EEV) is more suitable for the flash tank cycle (Nguyen et al., 2006). However, an additional liquid level sensor is needed to measure the liquid refrigerant level in the flash tank, which can work as the control parameter of the EEV. This increases the overall system cost significantly. Jang et al. (2010) presented the method of using the flash tank inlet and outlet mass balance in order to estimate the liquid level in the flash tank. However, it's not clear whether additional sensors, such as mass flow meters, are needed to accurately measure the refrigerant mass flow rate. Consequently, the development of an effective flash tank cycle control strategy is essential to the industrial application of the flash tank cycle.

1.3.2 Component level research

1.3.2.1 Compressor research

There are four main types of refrigerant compressors for residential and industrial applications: screw compressor, rotary compressor, scroll compressor and reciprocating compressor. A number of papers and patents presented the technique of applying refrigerant injection employing different types of compressors.

In the early research on screw compressors, design issues were found to be the high discharge temperature and the clearance spaces between the rotors, and between each rotor and the casing. One solution was to inject oil into the machine. However, this posed the disadvantage that a large quantity of oil was required and large oil separators were needed, and additional power was needed in pumping the oil. Alternatively, liquid refrigerant injection was proposed (Moody and Hamilton, 1975; Haselden, 1976) from the condenser to the compressor, at or near the delivery port so that the centrifugal force

imparted by the peripheries of rotors tended to keep the liquid near the outer peripheries of the rotors.

Hickman and Neal (1984) studied the refrigerant injection techniques for rotary compressors. It was found that the performance of the compressor improved due to the power input reduction associated with the injection. Shcherba et al. (1987) and Berezin (1987) simulated the effects of the injection pressure and the injection location on the performance of a rotary compressor. Liu et al. (2008) studied the liquid injection using a rotary compressor. As the interest in using CO_2 as the refrigerant increased, there was also study using rotary compressor for a CO_2 cycle (Baek et al., 2008).

As is known, one major risk of the refrigerant injection is the slugging problem. Slugging is detrimental to the reliability of compressors. A reciprocating compressor has the highest volume compression gradient among different types of compressors; hence the damage is the greatest. Therefore, it is more reliable not to inject the refrigerant directly to the compressor. Cavallini et al. (2005) studied a two-stage transcritical carbon dioxide cycle experimentally and theoretically. They used two reciprocating compressors in series, and the refrigerant was injected into a chamber that was mixed with the refrigerant discharged from the lower-stage compressor. This worked in a manner similar to that of a single compressor with an injection port.

As the research on scroll compressors went deeper, it was found that the scroll compressor has the smallest volume compression gradient. Therefore, it can handle the slugging problem to a certain extent (Liu and Soedel, 1994; 1995). Moreover, the scroll compressor has several independent compression chambers, the injection is relatively

easy to be equipped and the injection pressure is controllable with changing the port position. Therefore, more research on refrigerant injection techniques have been focused on its application to the scroll compressor (Ishii et al., 1998; Chen et al., 2002; Cho et al., 2000, 2003; Dutta et al., 2001; Schein and Radermacher, 2001; Winandy and Lebrun, 2002; Cavallini et al., 2005; Wang, 2005; He et al., 2006; Wang et al., 2007; Skinner, 2008; Wang, 2008; Wang et al., 2008a; 2009a; 2009b; 2009c). However, it is still difficult and expensive to redesign the scroll compressor with injection port that is matched with a heat pump system. If the performance of an injection heat pump with a twin rotary compressor is equivalent to that with a scroll compressor, then the application of the injection technique into the twin rotary compressor can be very attractive. Thus, it is also worthwhile to investigate the feasibility on the application of the injection technique into the twin rotary compressor. Therefore, there are researchers studying for the application of the twin rotary type compressor to the injection heat pump system (Tian et al., 2006; Tian and Liang, 2006; Heo et al., 2007).

Park et al. (2002) developed a thermodynamic model for a variable speed scroll compressor with refrigerant injection using continuity, energy conservation and real gas equation. Their model was able to predict the performance within 10% for approximately 90% of the experimental data. Figure 1-7 shows the variation of compressor discharge temperature with different injection frequencies. It can be seen that the compressor discharge temperature decreases and then increases with increasing frequency. High temperatures at low frequencies are resulted from reduced refrigerant mass by leakages. As the frequency increases from 60 to 90 Hz, the discharge temperature gradually

increases due to a rise of power input, reduction of efficiency and suction gas heating (Park, 2002). Similar results can be seen from Figure 1-8 by Cho et al. (2003). From Figure 1-9 it can be seen that as the frequency increases, the capacity increases, and then the slope gradually decreases. Similar results were also obtained by Cho et al. (2000). Tian et al. (2006a) conducted experimental study on a variable frequency two-stage air source heat pump. It was found that the heating capacity increases rapidly with increasing power frequency, and then the slope gradually decreases, as shown in Figure 1-10.

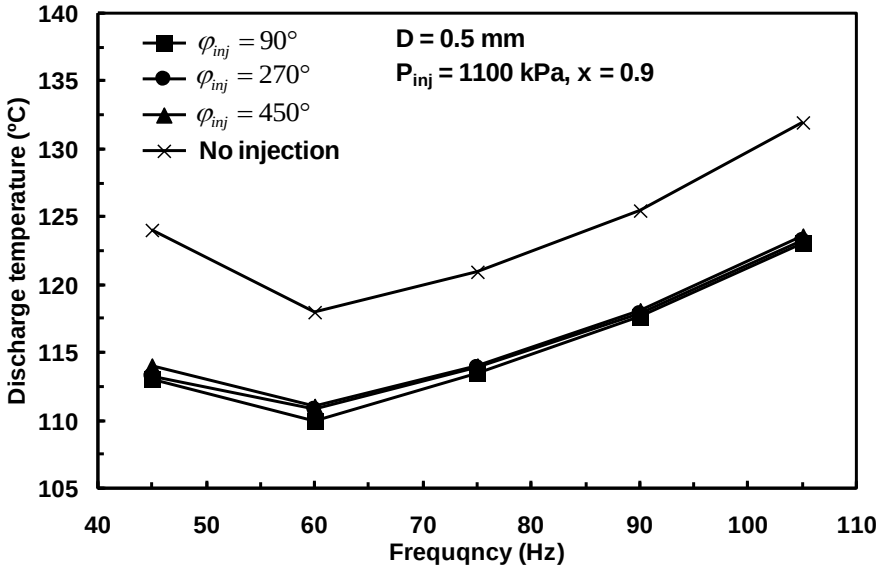

Figure 1-7: Variation of discharge temperature with different injection frequencies (Park et al., 2002)

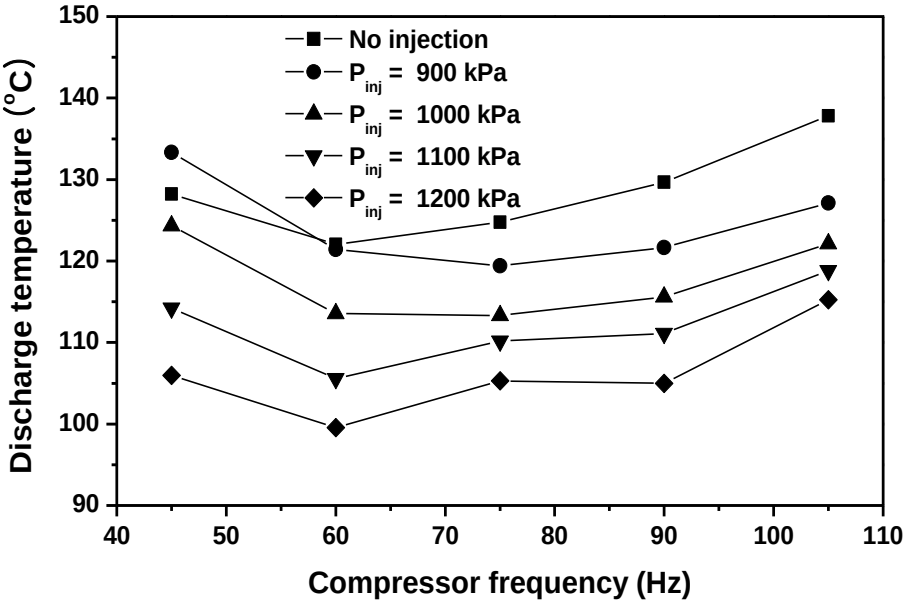

Figure 1-8: Variation of discharge temperature with different frequencies

(Cho et al., 2003)

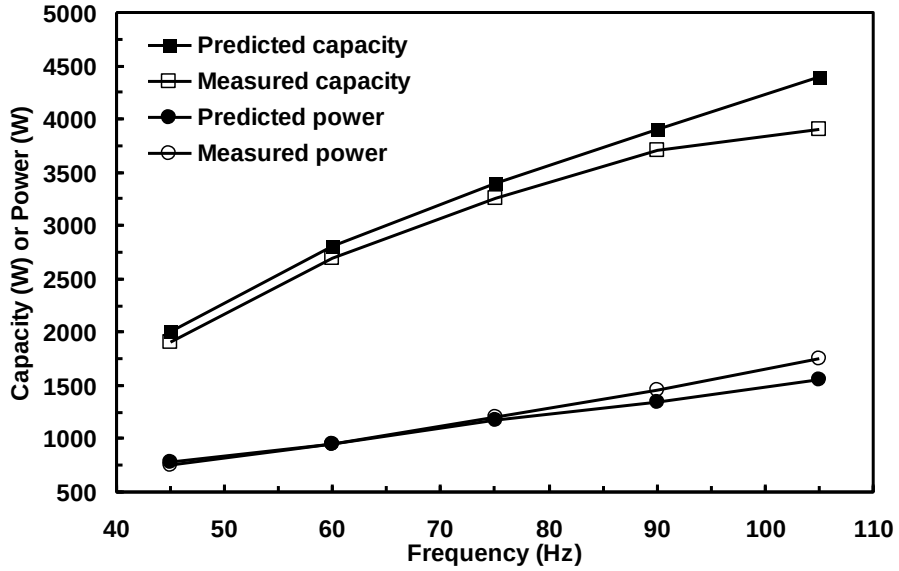

Figure 1-9: Capacity and power variations with different frequencies

(Park et al., 2002)

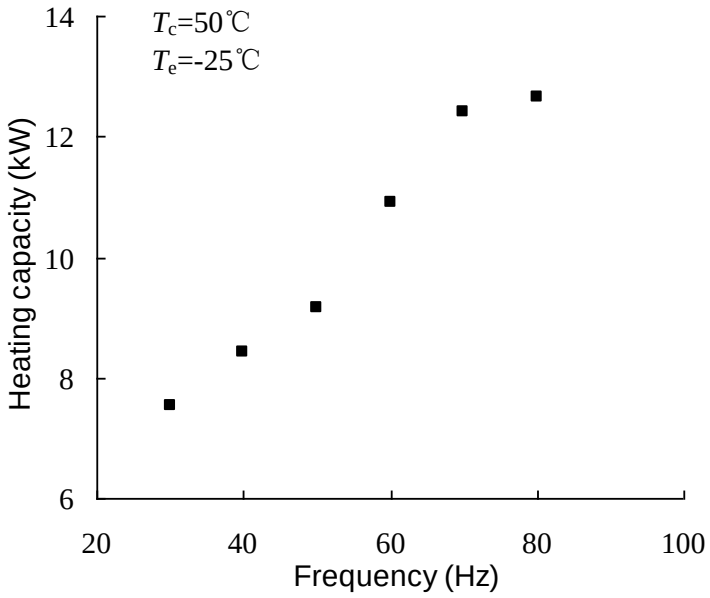

Figure 1-10: Variation of heating capacity with different frequencies at -25 ℃ evaporating temperature and 50 ℃ condensing temperature (Tian et al., 2006a)

1.3.2.2 Injection research

Injection research incorporates the injection port location, injection pressure, injection ratio, etc. Wang et al. (2009a) have conducted a comprehensive numerical investigation on the parameters that affect the performance of scroll compressor, as shown in Table 1-1. Symbols " ↑ " and " ↓ " indicate the trend of increase and decrease, respectively. "→" indicates that the parameter remains unchanged as the corresponding parameter varies.

Table 1-1: Effects of injection parameters on the main performance of scroll compressor (Wang, 2009a)

	Injection mass flow rate ratio	Compressor work	Discharge temperature	Volumetric efficiency
Injection enthalpy: ↑	↓	↑	↑	↓
Injection pressure: ↑	↑	↑	↓	↓
Injection area: ↑	↑ →	↑ →	↓ →	↓
Injection position: ↑	↓	↓	→	↑
One-way valve: Yes	↑	↑	↓	↓
Frequency: ↑	↓	↑	↓	↑

Early research on the refrigerant injection location was focused on the system level, namely the compressor suction, the intermediate location of the compressor, and the compressor discharge port (Ayub et al., 1992; Hirano et al., 1993). Later it was found that the injection to the intermediate location of the compressor was most effective in enhancing the system performance, while the scroll compressor was widely recognized as the most suitable for refrigerant injection. Therefore, more in-depth research was carried out on the optimum injection port location in the scroll compressor. The injection location determines the start time of the injection. The closer to the suction pocket the

injection port is, the earlier the injection starts. For an ideal two-stage vapor compression heat pump system, optimum system performance could be achieved by setting the same compression ratio between the high and low pressure sides. However, the optimum ratio for a real system is different from that of an ideal system (Baek et al., 2008), since the compression process is not isentropic. Therefore, the injection port location is critical since it is directly associated with the low and high side pressures of the compressor. Wang et al. (2009a) analyzed how the change of low side and high side compression ratios affected the indicated compressor efficiency, as shown in Figure 1-11. The relative indicated efficiency is defined as the ideal power consumption of compressor when the refrigerant coming from suction and injection ports is compressed to the discharge pressure in isentropic process divided by real compressor work. It was found that the compressor indicated efficiency reached maximum values when the low side and high side compression ratios were between 0.78 and 0.83. For a two-stage scroll compressor, the injection process can be considered as a one-dimensional compressible flow in a nozzle with an isentropic compression assumption (Park et al., 2002). Wang et al. (2009a) improved this model and concluded that the optimum injection position was different depending on the optimum targets, such as energy efficiency ratio, COP, cooling capacity and heating capacity.

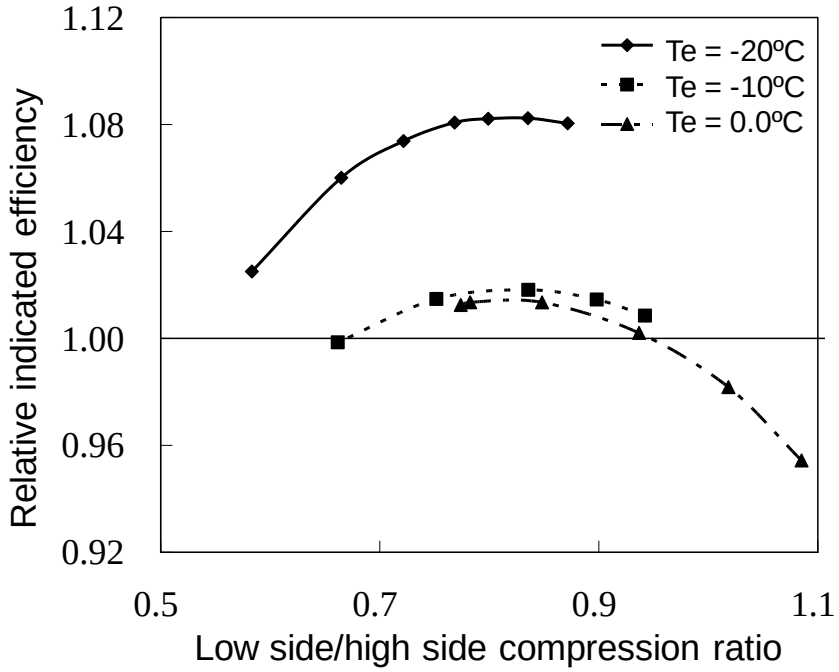

Figure 1-11: Compressor indicated efficiency versus the compression ratio (Wang et al., 2009a)

The injection pressure refers to the pressure at which the refrigerant is injected to the compressor. The injection pressure is a critical factor for the injection process. The basic condition for the injection to occur is that the injected refrigerant pressure should be higher than that of the compressor injection port. The injection pressure has an impact on the evaporator inlet enthalpy, as well as the injected mass flow rate and the compressor suction mass flow rate. Therefore, it influences the compressor power and system capacity significantly. In addition, its effect on the system performance varies for the internal heat exchanger cycle and the flash tank cycle.

For the internal heat exchanger cycle, the increase of injection pressure results in the increase of mass flow in the injection line. This is because the mass flow rate is

driven by the pressure difference at the internal heat exchanger outlet and the injection port of the compressor. With the increasing mass flow rate, the heat transfer through the internal heat exchanger could be enhanced, which further reduces the inlet enthalpy through the evaporator. This is favorable for increasing the system cooling capacity. However, enhancing the heat transfer could raise the degree of superheat of the injected vapor. If the superheating of the injected vapor becomes excessively high, the two-phase heat transfer area would be greatly reduced, resulting in the reduction of the inlet enthalpy of the refrigerant entering the evaporator. Therefore, the injection pressure should be within a certain range to achieve the maximum cooling capacity. Wang et al. (2009a) numerically analyzed the effect of injection pressure in the internal heat exchanger cycle, and showed that the optimum cooling capacity occurred at an appropriate injection pressure. Wang et al. (2009c) investigated the effect of injection pressure experimentally for both the internal heat exchanger cycle and the flash tank cycle. The results indicated that the cooling capacity increased first with increasing injection pressure and then began to decrease after reaching the maximum point.

For the flash tank cycle, increasing the injection pressure typically leads to higher injected refrigerant mass flow rate. However, as the injection pressure increases, the enthalpy of refrigerant entering the evaporator also increases, which can be seen from the P-h diagram in Figure 1-5. Moreover, the compressor power consumption increases dramatically with the increasing injected mass flow rate. Therefore, increasing injection pressure does not necessarily improve the cooling performance. For the heating mode, as the injected mass flow rate becomes higher, the benefits of vapor injection become more

pronounced. As a result, vapor injection is more beneficial for the heating mode than the cooling mode. Moreover, given a certain condensing and evaporating pressures, the injection pressure also determines the vapor quality after the upper-stage expansion. Typically higher injection pressure would lead to a smaller vapor quality, which indicates that the available vapor that can be injected to the compressor becomes less. Therefore, within a certain injection pressure, the injected mass flow rate increases with injection pressure. After it reaches a maximum value, the increase of injection pressure would result in more liquid refrigerant flowing to the flash tank. The liquid level in the flash tank then increases, and brings a limit to the maximum injection pressure as well as the injection ratio.

Refrigerant injection ratio is typically defined as the ratio of injected refrigerant mass flow rate to the compressor suction mass flow rate. The variation of refrigerant injection ratio poses a significant impact on the system performance. Winandy and Lebrun (2002) investigated the effect of refrigerant injection ratio on a CO_2 air conditioning system. A maximum of 30% capacity improvement was reported at the injection ratio of 37%. The power consumption increased almost proportional to the capacity gain, which resulted in a fairly constant COP. The discharge temperature slightly increased at an injection ratio less than 30%. This shows that the optimum injection ratio might be different depending on the target parameter.

In addition, the injection ratio is closely related to the injection pressure. High injection pressure tends to increase the injected mass flow rate. Therefore, the effect of injection ratio is similar to that of the injection pressure. The effect of injection ratio on

the performance of the internal heat exchanger cycle and the flash tank cycle can be obtained in the same manner.

1.3.2.3 Flash tank design

The design of the flash tank is critical to the reliable system operation. Ideally, the liquid and vapor separated in the flash tank can remain in single phase when exiting the flash tank. However, the liquid and vapor separation cannot be ideal in practice. If the vapor refrigerant exiting the flash tank is mixed with a large volume of liquid, then the vapor injected to the compressor is actually in two-phase state. This is detrimental to the reliability of the compressor. Therefore, it's crucial to design a flash tank to achieve high separation efficiency.

The design of the flash tank can be traced back to the 1950s. Reynolds (1950) presented the study of designing a flash tank. The flash tank was used to flash high-pressure steam into low-pressure steam, in order to create hot water supply. The design concepts were originated from the designing of a boiler, although the conditions in a boiler are different and more severe. The tank volume and the disengagement area of flashing were considered in designing the flash tank. Reynolds (1955) presented another article about the flash tank design. The separation efficiency was discussed regarding the pressure and the velocity of the vapor.

As the interest of using the flash tank increased for a refrigerant injection cycle, a number of designs have been patented for the flash tank (Lord et al., 1997; Hill et al., 2005; Lifson et al., 2006; Pham et al., 2007; 2008; 2009). Figure 1-12 shows the schematic of the flash tank designed by Pham et al. (2009). The refrigerant inlet is

located at the middle part of the flash tank. The refrigerant flows in the tangential direction of the wall so that it can follow the curve of the wall, which aids the process of separation. Moreover, two baffle plates are installed inside of the flash tank. The purpose is to aid the separation so that liquid refrigerant can be maintained in the lower part of the flash tank while vapor can flow to the upper part of the tank. Wang et al. (2009b) proposed a hybrid flash tank that utilizes a floating ball as the device to control the expansion valve opening, as shown in Figure 1-13. In this design, the saturated vapor leaving the tank can be super-heated; therefore it can provide the possibility of using TXV as the expansion valve. However, this approach is yet to be experimentally tested to prove its validity.

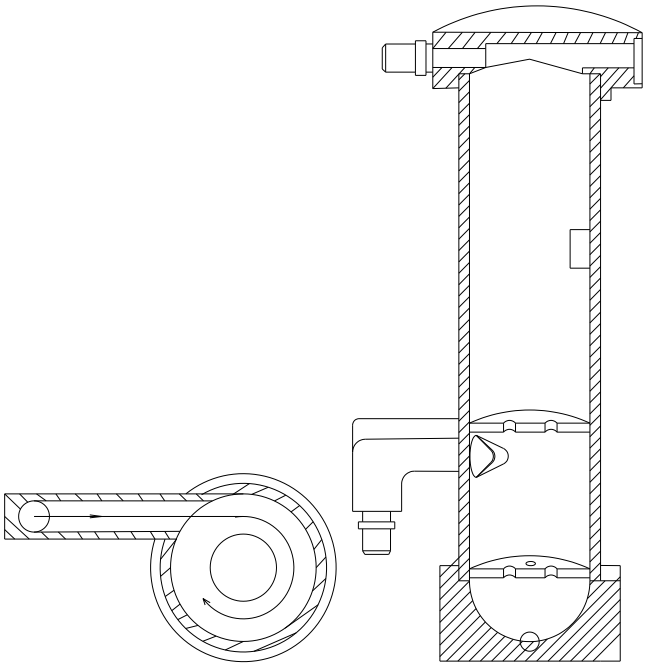

Figure 1-12: Flash tank design (Pham et al., 2009)

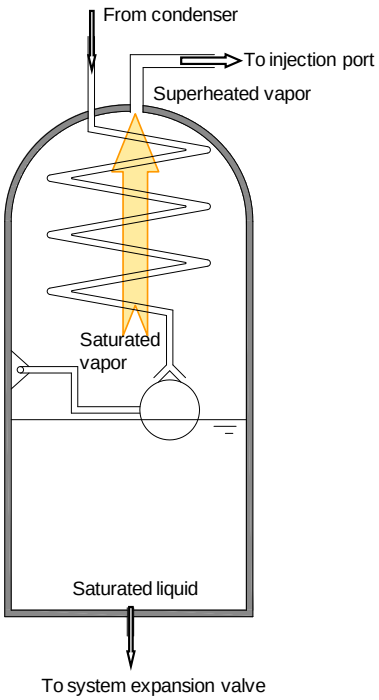

Figure 1-13: Hybrid flash tank (Wang, 2009b)

1.4 Literature review on refrigerant substitutes for R410A

Chlorofluorocarbons (CFCs) and hydrochlorofluorocarbons (HCFCs) have been widely used in air-conditioning and refrigerant industry since the 1920s. However, it was pointed out that CFCs could cause the depletion of stratospheric ozone layer (Monica and Roland, 1974), and there was a rising attention of controlling CFCs and HCFCs for environmental concerns. Although R22 has been widely used in residential air conditioners and commercial chillers, it has faced the challenges of being phased out. In 1987, Montreal Protocol designated the phase out of ozone depleting refrigerants CFCs and HCFCs. Followed by its amendments, the phase-out deadlines have been specified on R22 in different countries and regions. Industrially developed countries will thoroughly ban the use of R22 by 2020. EU and Japan have banned the import of R22 air

conditioners since January 1st, 2004. USA prohibited the use of R22 as a refrigerant in new equipment starting from January 1st, 2010. China will freeze R22 consumption in 2015, and ban the use of R22 in the air conditioning industry starting from 2040 (Chen, 2008). As a result, hydrofluorocarbons (HFCs) such as R134a and R410A were developed as alternative refrigerants in the 1990s. In 1997, Kyoto Conference announced that the production and use of HFCs should also be regulated due to their high global warming potentials (GWPs).

In Europe, refrigerants with GWPs over 150 from 2011 are banned for use in new mobile air conditioners. As a result, R134a with a GWP of 1,430, which is currently widely used in the automobiles, will be phased out in the automobile industry. In the residential application, R410A with a GWP of 2,088 (IPCC, 2007), may also face the same challenge. Research efforts have been performed to search for substitutes for R410A. Pande et al. (1996) tested three refrigerants in a residential heat pump system: R32, R410A (R32/R125, 50/50 wt.%) and R410B (R32/R125, 45/55 wt.%), and compared with R22. It was found out that R32 yielded the best performance. R32 showed cooling seasonal performance 5% better than R22 and heating seasonal performance 3% to 4% better than R22. R410A and R410B showed 2% to 3% better cooling seasonal performance, and equivalent heat seasonable performance as that of R22. Yajima et al. (2000) investigated the performance and total equipment warming impact (TEWI) of a 16 kW prototype with a variable speed compressor. Test results showed that the COP of R32 was higher than that of R410A not only under the rated capacity, but also even under the capacity reduced by compressor speed control. In Tokyo area, its TEWI dropped by 18%

in comparison with that of R410A, and the direct impact portion of R32 decreased to 7% of the total impact. Taira et al. (2011) proposed a notion of diversity of refrigerant choice, and suggested that R32 is a refrigerant enabling quick action again global warming. Tu et al. (2011) compared the performance of R410A and R32 in a thermodynamic model and conducted experiments at different operating conditions in a 3.2 kW residential heat pump unit. The thermodynamic cycle showed that R32 had 15% higher in cooling capacity and 6% higher in cooling COP. Volumetric cooling and heating capacities increased 7% to 9%, respectively, and the heating COP was comparable to that of R410A. Experiments showed 8% and 3% higher in cooling and heating capacities, respectively, and 3% and 2% higher in cooling and heating COPs, respectively. Huang et al. (2011) tested an air-to-water heat pump with tube-bundle-double-pipe heat exchanger. Test results showed that the charge of R32 was 66% of R410A. Cooling performance of R32 was close to that of R410A, and heating COP was 14% higher than that of R410A. The displacement of an R32 compressor should be reduced by 7% as compared to a compressor for R410A. Bella and Kaemmer (2011) performed the analysis of R32 versus R410A in air conditioning and heat pump applications with a scroll compressor. They concluded that R32 is ready and could be implemented soon. They also reported that the application envelope for a heat pump system will be decreased when switching from R410A to R32.

Due to the property difference between R410A and R32, the volumetric capacity of R32 is higher than that of R410A. Therefore, there are also research efforts on mixing R32 with other refrigerants as the substitute for R410A. Cawley (2003) filed a patent

proposing adding a small portion of R134a to R32 as a drop-in replacement for R410A in terms of volumetric capacity at typical air conditioning system operating conditions. Koyama et al. (2010) performed drop-in experiments of R410A, R1234ze and the mixture of 50/50 wt.% R1234ze/R32 in the heating mode, using a vapor compression heat pump system developed for R410A. The COP was found to be 7.5% lower than that of R410A at the same heating load of 2.8 kW. Mixture of R1234ze/R32 is considered to be applicable as low-GWP alternatives for R410A by adjusting the composition of the mixture and by reconsidering the design parameter of components of room air-conditioning system. It was concluded that mixture of R1234ze and R32 can be a candidate to replace R410A. Koyama et al. (2011) performed experimental testing of R410A, R1234ze and R32 in the heating mode. The COP of 20/80 wt.% R1234ze/R32 showed almost the same heating load as R410A. However, refrigerant mixtures of R32 with some other refrigerants such as R134a and R1234yf may result in a zeotropic mixture. The resulting temperature glide is not favorable for heat pump systems. Moreover, there were also other issues reported by using refrigerant mixtures. Gebbie et al. (2007) tested a heat pump unit with a refrigerant mixture of 30/70 wt.% R32/R134a. They examined transient performance trends using refrigerant mixture and compared that with pure refrigerant R32. It was observed that R32/R134a tests exhibited capacity oscillations early in each transient test that were not present during R32 tests. They concluded that circulating refrigerant mass and composition are the primary controlling factors with regard to transient capacity oscillations.

As can be seen in research efforts in the literature, although R32 has been studied experimentally and theoretically, all works have been conducted on a conventional single stage vapor compression cycle. Employing refrigerant R32 in a vapor injection two-stage system would be worth for investigation since there was no open publication on such research effort. This research work will investigate the vapor injection system performance using R410A, and then perform drop-in tests using R32 to explore the benefits and challenges of replacing R410A with R32.

1.5 Summary of literature review

Table 1-2 shows a selection of research groups and their research focuses on refrigerant injection. It can be seen that both the system level and the component level have been studied extensively. Among all the categories, the flash tank cycle, vapor injection and application using scroll compressors show the greatest interest from different research groups.

From the literature review it can be seen that the current research on refrigerant injection techniques falls into two categories: system level research and component level research. The system research is focused on low ambient temperature heating, heat pump water heating, high ambient temperature cooling, cycle comparison, and control strategy development. The internal heat exchanger cycle and flash tank cycle are the two typical cycles for refrigerant injection. The flash tank cycle is more favorable than the internal heat exchanger cycle due to its superior performance and the fact that the cost of a flash tank is lower than that of an internal heat exchanger. The component level research is focused on the compressor, the injection process and the flash tank design. Different

types of compressor employing the refrigerant injection are presented. The scroll compressor is the most attractive option employing the refrigerant injection among all the compressor alternatives. However, there are not many open publications on the control strategy of the flash tank cycle. Improper system control may result in an undesirable amount of liquid refrigerant flooding the compressor, which is detrimental to a compressor. Moreover, the injection pressure is affected by the control of expansion valves, and inappropriate control may lead to poor system performance due to improper injection pressures. Therefore, the control strategy of the flash tank cycle is a critical issue that needs to be addressed in order to implement such a cycle in commercial products in a large scale.

Table 1-2: Selection of research groups and their focuses on refrigerant injection techniques

Research group	System level							Component level													
	Application			Cycle configuration		Injection type		Compressor type				Compressor speed	Refrigerant type			Injection research			Flash tank design	Expansion valve	
	Low ambient temperature heating	Heat pump water heating	High ambient temperature cooling	Internal heat exchanger cycle	Flash tank cycle	Vapor injection	Liquid injection	Screw compressor	Rotary compressor	Reciprocating compressor	Scroll compressor	Variable speed	R22	R410A	CO_2	Injection port lcoation	Injection pressure	Injection ratio		TXV	EXV
Abel et al., 2007					√	√					√										
Atsumi et al., 1985					√	√															
Baek et al., 2008	√				√	√			√						√						√
Bertsch and Groll, 2008	√	√	√	√		√					√			√							√
Bush et al., 2004							√	√													
Cao et al., 2009a		√		√		√					√		√				√				
Cao et al., 2009b		√		√			√				√		√				√				
Cavallini et al., 2005				√						√					√		√				
Cho et al., 2003a							√				√	√	√			√	√	√			
Cho et al., 2009			√		√	√									√						√
Dutta et al., 2001				√			√				√							√			
Fan et al., 2008		√			√	√					√		√								
Haselden, 1976							√	√													
Ignatiev and Caillat, 2008					√		√				√										
Ishii et al., 1998					√	√					√					√					
Kang et al., 2008			√	√			√											√			√
Lifson et al., 2006						√	√	√													
Lifson et al., 2008				√		√					√						√				
Liu et al., 2008		√		√			√		√												√
Ma et al., 2003	√			√		√					√		√								
Ma and Chai, 2004	√			√		√					√		√				√				
Ma and Zhao, 2008	√				√	√					√		√								
Moriwaki et al., 2008					√	√	√														
Park et al., 2002											√	√						√			
Pham et al., 2007; 2008; 2009																			√		
Reynolds, 1950; 1955																			√		
Tian et al., 2006a	√			√													√				
Ueno and Fukuhara, 1982					√	√			√												
Wang, 2008; Wang et al., 2009c	√		√	√	√	√					√			√			√	√		√	
Wang et al., 2008; 2009a											√					√	√	√			
Winandy and Lebrun, 2002				√		√	√				√						√	√			

Note: "√" means that the research is related to the specified category.

Moreover, as the global warming has become a more critical issue in recent years, there has been continuing research effort in looking for candidates to replace refrigerants with high GWPs. R32 has been the highly ranked candidate to replace R410A in residential applications. The past work done on R32 was mostly focused on a single stage cycle without vapor injection, and therefore, it is worthwhile to investigate the performance in a two-stage vapor injection cycle using R32, and to explore the benefits and challenges by using R32 as a strong candidate to replace R410A. In addition, a system designed for R410A may not be optimized for R32. Consequently, it is also worthwhile to perform an optimization study to design the components to be best suited for the replacement candidate R32.

1.6 Research objectives

The objective of this study is to investigate a residential heat pump system with a vapor-injected scroll compressor comprehensively. The system used to perform the experimental test is originally designed for R410A. The system control strategy is firstly analyzed and a novel control strategy is experimentally investigated. The system performance is evaluated utilizing R410A, and then drop-in tests are performed using a low-GWP refrigerant R32 without any system modifications. Component and system simulations are performed and validated with experimental data, and an optimization study is also conducted.

1.6.1 Experimental work

The experiment work consists of:

1. Construction of the experimental test facility of the flash tank vapor injection heat pump system
2. Installation of a flow visualization window to the flash tank in order to monitor the refrigerant liquid levels during the experimental tests
3. Development of a proper control strategy of the flash tank cycle for both steady-state and transient operation conditions
4. Investigation of the flash tank cycle performance for both cooling and heating modes at different operation conditions utilizing R410A
5. Drop-in tests of R32, and exploration of the potential benefits and challenges using R32 in a heat pump system for both with vapor injection and without vapor injection modes

1.6.2 Simulation and optimization

The simulation and optimization work consists of:

1. Simulation of the condenser and evaporator, and model validation using experimental results
2. Two-stage vapor injected compressor modeling, and compressor model validation using experimental results
3. Investigation of compressor cooling by utilizing proper liquid injection to lower the compressor discharge temperature

4. Design optimization of heat exchangers for R32 using 5 mm copper tubes by including design parameters of tube length, tube horizontal and vertical spacing, fin pitch, tubes per bank, number of tube banks, and heat exchanger circuitry
5. Thermodynamic cycle modeling for R410A and R32, and two-stage vapor injection cycle modeling using CEEE software packages, and model validation with experimental results

2. Experimental setup

2.1 Test facility

The system used to perform the experimental test is a 3-ton residential heat pump system equipped with a scroll compressor utilizing R410A as its working fluid. The original system from the manufacturer includes an indoor unit and an outdoor unit. The indoor unit was installed in a closed air psychrometric loop, in which the temperature, relative humidity and air volume flow rate could be controlled. The closed air loop mimics the indoor conditions. The outdoor unit was installed in an environmental chamber, where the temperature and the relative humidity could be controlled. The environmental chamber mimics the outdoor ambient weather conditions. The indoor and outdoor units were connected with copper tubes that have a total length of 50 feet (15 m). The liquid line of the system utilizes the copper tube with an outer diameter of 3/8 inches (9.53 mm), and the vapor line of the system utilizes the copper tube with an outer diameter of 7/8 inches (22.23 mm).

2.1.1 Indoor unit

The indoor unit is shown in Figure 2-1. The upper part of the indoor unit is a blower that drives the air in the practical application. The lower part is an "A" shape heat exchanger, as shown in Figure 2-2. The blower of the indoor unit was removed and only the heat exchanger was used in the experiment. This is because the closed air psychrometric loop has a blower that can accurately control the air volume flow rate. The air flows vertically upward from the bottom to the top of the indoor heat exchanger. In the cooling mode, the indoor heat exchanger serves as the evaporator; in the heating

mode, the indoor heat exchanger functions as the condenser. The indoor heat exchanger was equipped with a TXV. The specifications of the indoor heat exchanger are shown in Table 2-1.

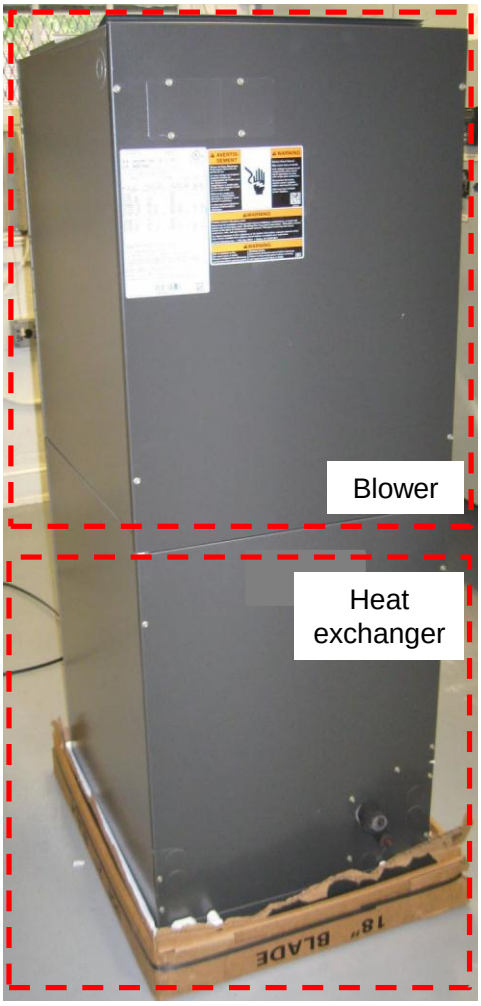

Figure 2-1: The complete indoor unit with the heat exchanger and the blower

Figure 2-2: The indoor heat exchanger

Table 2-1: Indoor and outdoor heat exchangers specifications

Parameter	Unit	Indoor Heat Exchanger	Outdoor Heat Exchanger
Tube length	mm	483	2,565
Tube outer diameter	mm	9.5	7.9
Tube wall thickness	mm	0.8	0.8
Tubes per bank	ea	26	32
Number of tube banks	ea	3	2
Coil in parallel	-	2	1
Tube horizontal spacing	mm	25.4	15.7
Tube vertical spacing	mm	25.4	24.1
Fins per inch	-	12	22
Fin thickness	mm	0.1	0.1
Fin types	-	Wavy fin	Wavy fin

2.1.2 Outdoor unit

The outdoor unit is shown in Figure 2-3. The compressor used in the system is a scroll compressor. The compressor originally installed in the system was a non-injected

scroll compressor. The specification of the compressor is shown in Table 2-2. To test the vapor injection performance of the system, the compressor was replaced with a vapor-injected scroll compressor that has the same specification as the original non-injected compressor shown in Table 2-2. Figure 2-4 shows the physical comparison between the non-injected and vapor-injected compressors. The expansion valve used in the outdoor unit is a TXV. A four-way valve was installed in the outdoor unit in order to reverse the refrigerant flow direction from cooling to heating mode. It should be noted that there is no accumulator in the outdoor unit. In the cooling mode, the outdoor unit works as the condenser; while in the heating mode, the outdoor unit functions as the evaporator.

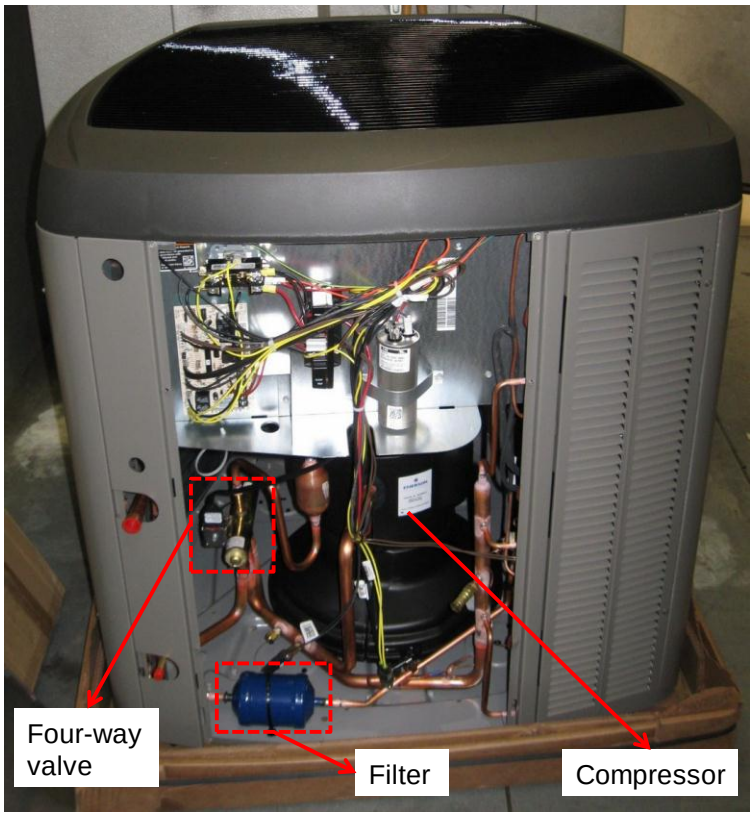

Figure 2-3: The outdoor heat exchanger

Table 2-2: Specification of the compressor

Compressor	Unit	Specification
Manufacturer	-	Copeland
Model number	-	ZP31K5E-PFV-130
Refrigerant type	-	R410A
Displacement	cm^3	29.5
Operation speed	rpm	3,500
Length/Width	cm	24.3
Height	cm	38.8
Net weight	kg	22.5

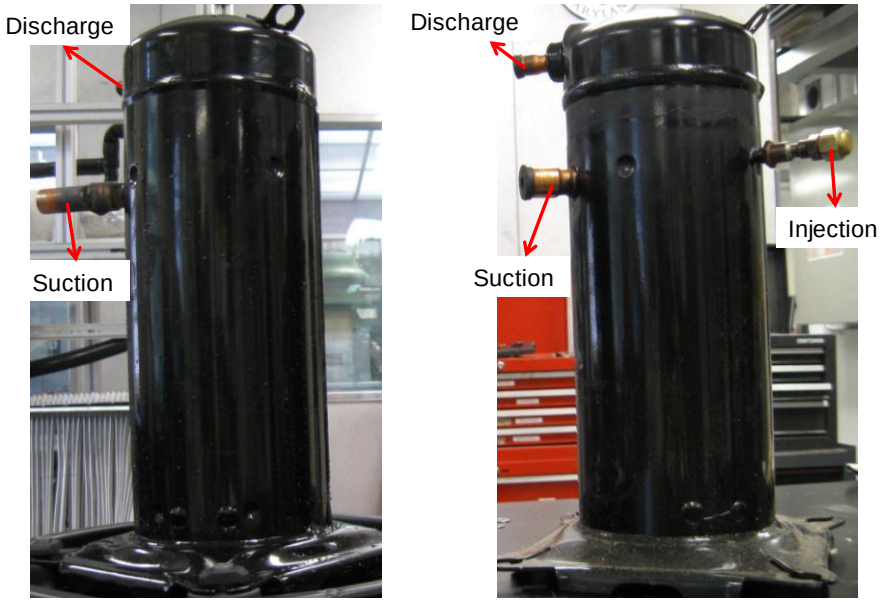

Figure 2-4: Comparison between non-injected compressor (left) and vapor-injected compressor (right)

2.1.3 Flash tank with a flow visualization window

The flash tank used in the experimental study is shown in Figure 2-5. It is a cylindrical shape vessel with one inlet and two outlets. The two-phase flow enters the tank from the port located in the middle of the tank. The inlet is in the tangential direction of the interior wall to facilitate the liquid and vapor separation. The liquid exits the tank from the bottom port, and the vapor leaves the tank from the top port. The flash tank in different view angles can be seen in Figure 2-6. A visualization window with a sight glass was welded into the wall of the flash tank in order to visualize the liquid-vapor separation and to monitor the liquid level variations. The material of the sight glass is a tempered borosilicate, and a schematic of the visualization window is shown in Figure 2-7. The specifications of the flash tank are shown in Table 2-3.

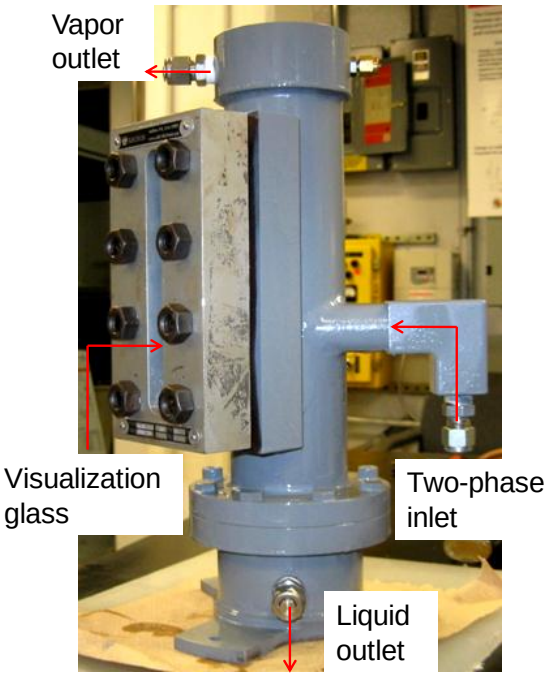

Figure 2-5: Flash tank used in the experimental study

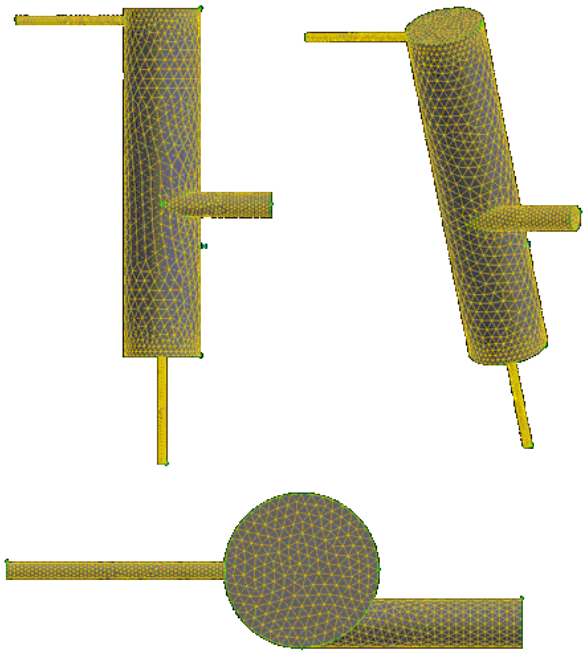

Figure 2-6: Flash tank from different view angles

Table 2-3: Specifications of the flash tank

Parameter	Unit	Dimension
Flash tank height	m	0.32
Diameter	m	0.07
Flash tank volume	m^3	0.001
Sight glass height	m	0.15

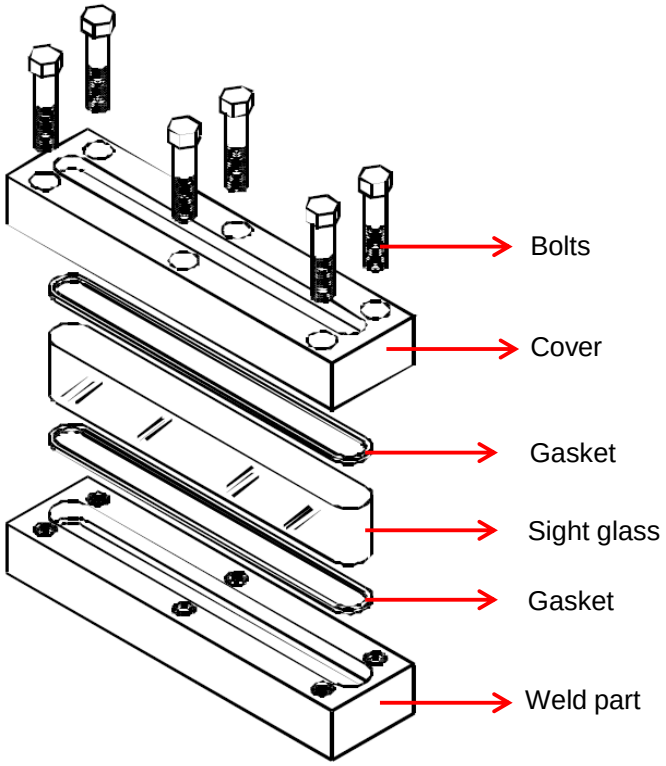

Figure 2-7: Schematic of the visualization window and welding parts

(Archon Industries, Inc.)

2.1.4 Schematic of test facility

Figure 2-8 shows the schematic of the test facility of a vapor injection cycle, with a flash tank using R410A as the refrigerant. It is comprised of a closed air loop and units located in the environmental chamber. In the cooling mode, the refrigerant leaves the compressor, entering the outdoor unit for condensing. After the upper-stage expansion valve (2), the refrigerant enters the flash tank; the vapor refrigerant is injected to the compressor, while the liquid refrigerant enters the lower-stage expansion valve (4), and circulates through the indoor unit. After evaporating at the indoor unit, the refrigerant then enters the suction port of the compressor to complete the closed-loop cycle. In the

heating mode, the four way valve is reversed, and therefore it reverses the refrigerant flow direction. The refrigerant leaving the compressor circulates through the indoor unit for condensing. Then it is expanded through the upper-stage expansion valve (2), and enters the flash tank. The vapor refrigerant is injected to the compressor; meanwhile the liquid refrigerant circulates through the lower-stage expansion valve (3), evaporates in the outdoor coil, and then enters the compressor to complete the cycle.

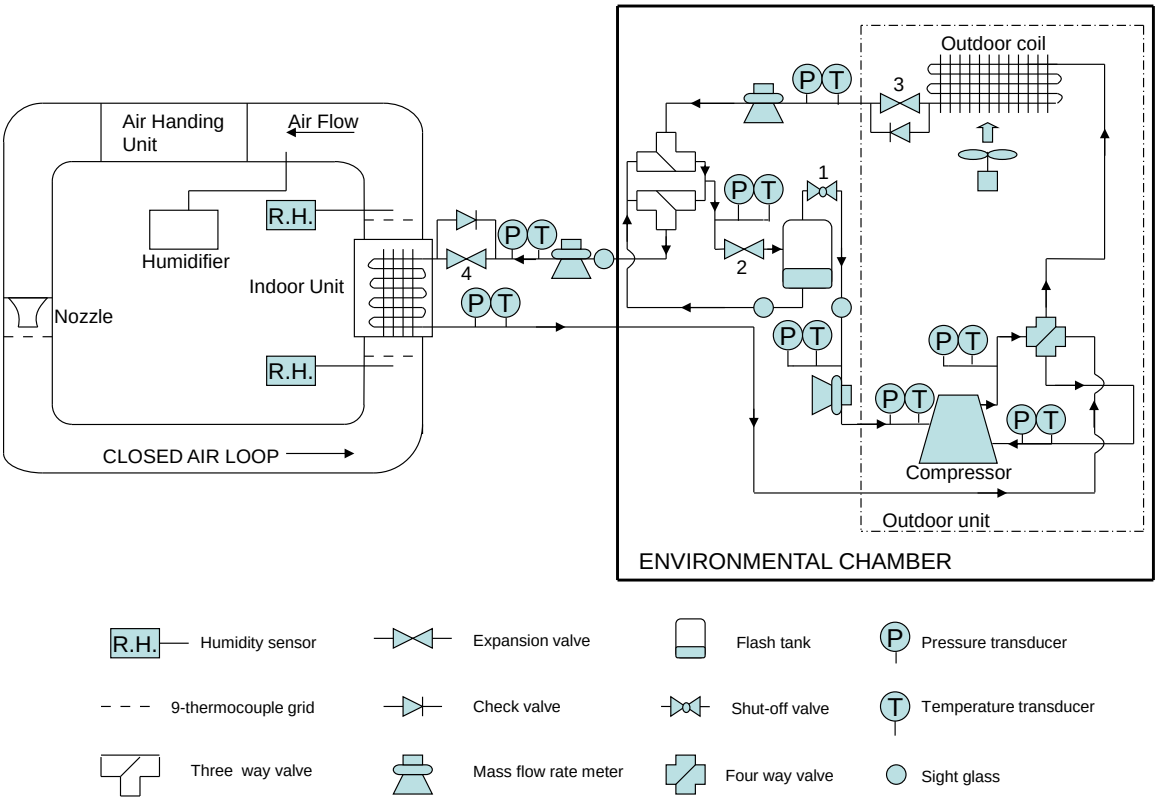

Figure 2-8: Schematic of the flash tank vapor injection heat pump system for cooling mode operation

2.2 Instrumentation and measurement

2.2.1 Temperature measurement

The refrigerant temperatures at different locations were measured by T-type in-stream thermocouples. The locations of those thermocouples are illustrated in Figure 2-8. The thermocouples were inserted into the center of refrigerant tube lines, and contact the refrigerant flow directly to measure the refrigerant bulk temperature accurately. In the case of the air-side temperature measurements, two thermocouple grids were installed at the upstream and the downstream of the indoor unit, which is shown in Figure 2-8. Each thermocouple grid consists of 9 T-type thermocouples. The thermocouples were distributed evenly in a particular cross-section area, and connected in a parallel manner to measure the average temperature of the air flowing through the cross-section area (ASHRAE Handbook, 2001). Mesh sheets were installed in front of the thermocouple grids to ensure a uniform air flow profile. Two thermocouple grids were also installed at the inlet and the outlet of the outdoor unit to measure the air temperatures entering and leaving the outdoor unit, respectively. The specifications of the thermocouples were shown in Table 2-4.

Table 2-4: Specifications of thermocouples

Manufacturer	Omega Engineering, Inc.
Model No.	T Type Thermocouple
Temperature range	-270 ℃ to 400 ℃
Accuracy	0.5 ℃

2.2.2 Pressure measurement

Pressure transducers were installed in the refrigerant tube lines to measure the pressures of the refrigerant. The locations of the pressure transducers are illustrated in Figure 2-8. A differential pressure transducer was installed to measure the pressure drop across the nozzle in the closed air loop. The specifications of the pressure transducers and the differential pressure transducer are listed in Table 2-5.

Table 2-5: Specifications of pressure transducers

Item	Pressure Transducers	Pressure Transducers	Differential Pressure Transducers
Manufacturer	Setra Systems, Inc	WIKA, Inc	Setra System, Inc
Model No.	280E	S-10	264
Range	0 ~ 3,447 kPa	0 ~ 6,894 kPa	0 ~ 1.245 kPa
Accuracy	±0.11% Full Scale	±0.125% Full Scale	±1% Full Scale

2.2.3 Relative humidity measurement

The relative humidity of the air in the closed loop was measured by two relative humidity sensors, located at the upstream and the downstream of the indoor unit. The relative humidity together with the temperature of the air was used to calculate the air properties in the closed loop. The specifications of the humidity sensors are shown in Table 2-6.

Table 2-6: Specifications of relative humidity sensors

Manufacturer	Vaisala
Model No.	HMP233
Range	-40 ℃ to 80 ℃; 0 to 100%
RH accuracy	±1%
Temperature accuracy	±0.2 ℃
Stability	±0.5% Annual

2.2.4 Dew point measurement

Two dew point sensors were used to measure the dew points of the outdoor unit inlet and outlet of air stream. Specifications of the dew point sensors are shown in Table 2-7.

Table 2-7: Specifications of dew point sensors

Manufacturer	General Eastern
Model No.	Hygro-M2
Range	-80 ℃ to 95 ℃
Dew point accuracy	±0.2 ℃

2.2.5 Power consumption and line voltage measurements

The power consumption and line voltage of the heat pump system were measured by an AC watt transducer and a voltage transducer, respectively. The specification of the watt transducer and line voltage transducer are shown in Table 2-8.

Table 2-8: Specifications of AC watt transducer and voltage meter

Manufacturer	Ohio Semitronics	
Model No.	PC5	VT-240A
Range	0 to 5 kW	0 to 300 V
Accuracy	±0.5% Full Scale	±0.25% Full Scale

2.2.6 Refrigerant mass flow rate and air volume flow rate measurements

The refrigerant mass flow rates were measured by Coriolis mass flow meters. The location of the mass flow rate meters is shown in Figure 2-8. The mass flow meters installed in the liquid lines were used to measure the refrigerant mass flow rate through the condenser, and the mass flow meter installed in the vapor injection line was used to measure the injected vapor refrigerant mass flow rate. The specifications of the mass flow meters are shown in Table 2-9.

The air volume flow rate in the closed loop was measured by a standard 6-inch (15.2 cm) nozzle. The nozzle was installed in the closed loop, which is shown in Figure 2-8. The air volume flow rate was calculated by Equation 2-1 (ASHRAE Standard 41.2, 1987).

Table 2-9: Specifications of mass flow meters

Parameter	Mass flow meters in liquid line	Mass flow meter in vapor injection line
Manufacturer	Micro Motion, Inc.	Micro Motion, Inc.
Model No.	DS 025	CMF 025
Range	0 ~ 100 g/s	0 ~ 30 g/s
Zero stability	0.038g/s	0.038g/s
Accuracy	$\pm 0.15\% \pm [(\frac{ZeroStability}{Flowrate}) \times 100\%]\%$ of flow rate	$\pm 0.50\% \pm [(\frac{ZeroStability}{Flowrate}) \times 100\%]\%$ of flow rate

$$V = C_d A \sqrt{\frac{2\Delta P}{\rho_{air}}} \qquad \textbf{Equation 2-1}$$

Where C_d is the nozzle discharge coefficient, and A is the area measured at the plane of nozzle exit. The discharge coefficient C_d has been determined as 0.986 according to the nozzle calibration results.

2.2.7 Liquid level measurement in the flash tank

To better measure the liquid level inside of the flash tank, a capacitance liquid level sensor was utilized, as shown in Figure 2-9. The liquid level sensor was inserted into the flash tank, connected by an NPT fitting at the top of the tank, which is shown in Figure 2-10. The working principle of the sensor was as follows: the capacitances detected by the probe are different for the section which is submerged in the liquid and

the section exposed to the vapor. The capacitance is then converted to a current signal and recorded in the computer through the data acquisition system. The purpose of measuring the liquid level is to better analyze the behavior of liquid level variations at different operating conditions. The specification of the capacitance liquid level sensor is shown in Table 2-10. The liquid level sensor has a length of 25.4 cm that is equivalent to 80% of the flash tank height. Therefore, it should be noted that the sensor cannot measure the liquid level that is lower than 20% of the flash tank height, since the sensor was installed through the top of the flash tank.

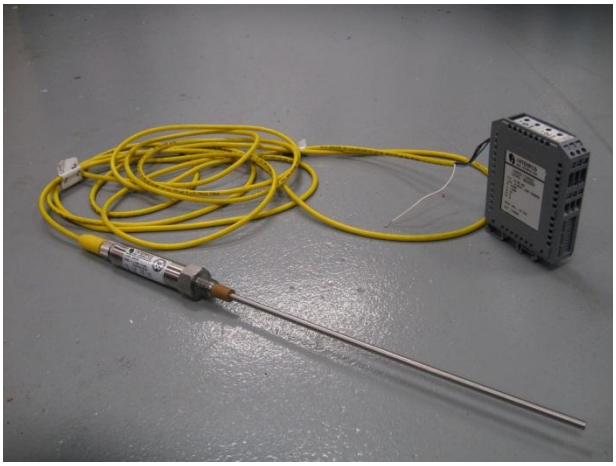

Figure 2-9: Capacitance liquid level sensor and transmitter

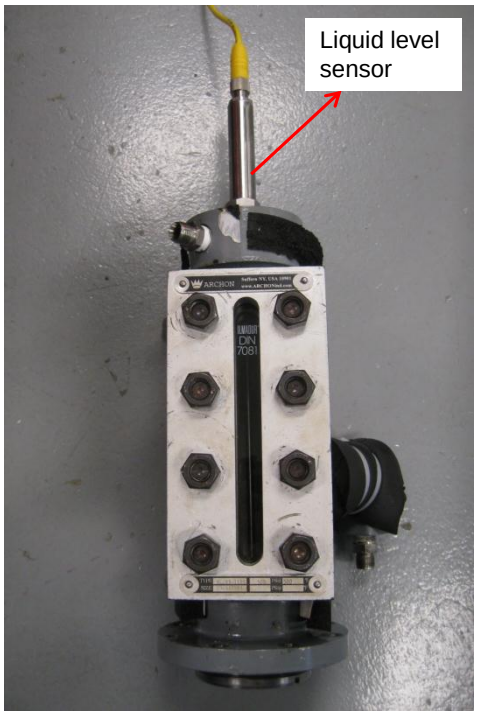

Figure 2-10: Flash tank with the liquid level sensor installed

Table 2-10: Specification of the capacitance liquid level sensor

Manufacturer	Intempco Inc.
Model No.	LTX50
Range	0 cm ~ 25.4 cm
Accuracy	±0.25 cm

2.3 Equipment calibrations

The calibration of the instrumentation was conducted before the experimental study. Thermocouples have been tested in ice/water bath. Pressure transducers have been calibrated by using a digital pressure calibrator having a resolution of 0.1 kPa. Different pressure transducer was calibrated by measuring the pressure difference between water columns. Relative humidity sensors were calibrated by comparing the relative humidity of standard solutions. Dew point sensors were calibrated by instrumentation manufacturer. The refrigerant mass flow meters were calibrated by weighing the water in a specific time period. The air nozzle was calibrated by installing an electric heater in the closed air loop and calculating the discharge coefficient through energy balance. The capacitance liquid level sensor was calibrated in the system with directly measuring the liquid level in the flash tank.

2.4 Data acquisition system

Instruments in the air side and the refrigerant side were connected to FieldPoint data acquisition modules from National Instruments. The modules were connected to a data acquisition computer, and communicated with a data acquisition program. The data

acquisition program was developed by using the LabView software package (National Instruments). The instruments output voltage or current signals, and the signals were transmitted to the data acquisition program. Calibration equations were manually provided to the data acquisition program to convert the original voltage and current signals to target parameters such as pressure, mass flow rate, etc. The measured parameters (pressure, temperature, relative humidity, dew point, mass flow rate, liquid level, and power consumption) can be directly displayed in the data acquisition program during the experimental tests. The system performance indices (capacity and COP) can also be calculated in the data acquisition program. The data was measured with a two-second interval, and recorded through the data acquisition program into an Excel spreadsheet. The data in steady state condition was recorded for 30 minutes, and averaged for the system performance analysis. (ASHRAE Standard 116, 2010)

2.5 System performance evaluation

2.5.1 Air-side capacity

Air-side capacity is an important parameter to evaluate the system performance. When there is no condensation of water occurring on the indoor heat exchanger, the air-side capacity is calculated by Equation 2-2.

$$\dot{Q}_{air} = \frac{\dot{m}_{air} C_p (t_{air,in} - t_{air,out})}{1 + W_{out}} \qquad \textbf{Equation 2-2}$$

where $\dot{m}_{air}$ is the air mass flow rate in the closed air psychrometric loop, and C_p is the specific heat capacity of air. $t_{air,in}$ and $t_{air,out}$ are the inlet and outlet air temperatures of

the indoor heat exchanger, respectively. W_{out} is the air humidity ratio at the outlet of the heat exchanger. When there is water condensing on the indoor heat exchanger, the air-side capacity is calculated by Equation 2-3 to include both the sensible and latent heats.

$$\dot{Q}_{air} = \frac{\dot{m}_{air}(h_{air,in} - h_{air,out})}{1 + W_{out}} \qquad \textbf{Equation 2-3}$$

where $h_{air,in}$ and $h_{air,out}$ are the inlet and outlet air enthalpies of the indoor heat exchanger, respectively.

2.5.2 Refrigerant-side capacity

The refrigerant-side capacity was defined multiplying the refrigerant mass flow rate by the outlet and inlet enthalpy difference, which is shown in Equation 2-4:

$$\dot{Q}_{ref} = \dot{m}_{ref}(h_{ref,out} - h_{ref,in}) \qquad \textbf{Equation 2-4}$$

where $\dot{m}_{ref}$ is the refrigerant mass flow rate, and $h_{ref,out}$ and $h_{ref,in}$ are the outlet and inlet refrigerant enthalpies of the indoor heat exchanger, respectively.

2.5.3 Energy balance

Energy balance was defined as the capacity difference between the refrigerant side and air side divided by the refrigerant side capacity as described by Equation 2-5:

$$Energy\ Balance = \frac{\dot{Q}_{ref} - \dot{Q}_{air}}{\dot{Q}_{ref}} \qquad \textbf{Equation 2-5}$$

Basically energy balances during different tests should be within 6% to ensure the validity of test results according to ASHRAE Standard 116 (2010).

2.5.4 Power consumption

Power consumption by the outdoor unit was measured directly by a watt meter, which includes the compressor and outdoor fan power consumptions. The original blower matching the indoor unit was disassembled and the indoor air was driven by the blower of the air handling unit in the closed air psychrometric loop. Therefore, the realistic power consumption by the Original Equipment Manufacturer (OEM) blower could not be measured directly. To consider the effect of indoor blower on the system performance, power consumption data from the OEM was used. The average power consumption of the original blower matching the indoor coil was 152 W.

2.5.5 COP

The COP of the heat pump system was defined as the net capacity divided by total power consumption, described by Equation 2-6:

$$COP = \frac{\dot{Q}_{net}}{\dot{W}_{total}} \qquad \textbf{Equation 2-6}$$

where $\dot{W}_{total}$ is the total power consumption, including the compressor power consumption, the outdoor fan power consumption as well as the indoor blower power consumption. $\dot{Q}_{net}$ is the net capacity, considering the indoor blower's thermal effect on the capacity. For the cooling mode, the indoor blower works as a heat source which is unfavorable for the cooling capacity, therefore, the net capacity is described by Equation 2-7:

$$\dot{Q}_{net} = \dot{Q}_{air} - \dot{W}_{blower} \qquad \textbf{Equation 2-7}$$

where $\dot{W}_{blower}$ is the power consumption by the indoor blower. For the heating mode, the indoor blower works as a heat source which is favorable for the heating capacity, therefore, the net capacity is described by Equation 2-8:

$$\dot{Q}_{net} = \dot{Q}_{air} + \dot{W}_{blower} \qquad \textbf{Equation 2-8}$$

Vapor injection ratio α is defined as the injected vapor refrigerant mass flow rate divided by the suction mass flow rate, as shown in Equation 2-9:

$$\alpha = \frac{\dot{m}_{inj,vap}}{\dot{m}_{suc}} \times 100\% \qquad \textbf{Equation 2-9}$$

where $\dot{m}_{inj,vap}$ is the injected vapor refrigerant mass flow rate, and $\dot{m}_{suc}$ is the compressor suction mass flow rate.

To compare the difference between R32 and R410A, the performance of R410A is used as the baseline. The variation (ε) is defined in Equation 2-10:

$$\varepsilon = \frac{y_{R32} - y_{R410A}}{y_{R410A}} \times 100\% \qquad \textbf{Equation 2-10}$$

where y_{R32} represents the parameters of R32, and y_{R410A} represents the parameters of R410A. The parameters include capacity, COP, system power consumption and refrigerant mass flow rate.

To evaluate the performance comparison between with and without vapor injection, the performance without vapor injection is used as the baseline. The performance variation is defined in Equation 2-11:

$$\gamma = \frac{z_{vi} - z}{z} \times 100\% \qquad \textbf{Equation 2-11}$$

where z_{vi} represents the parameters of the cycle performance with vapor injection, and z represents the parameters of the cycle without vapor injection. The parameters include capacity, COP and system power consumption.

2.6 Test conditions

The test conditions followed ASHRAE Standard 116 (2010), and extended conditions of 46 ℃ for cooling and -18 ℃ for heating were added to investigate the system behaviors at severe weather conditions, as shown in Table 2-11. The volume flow rate of the air circulating the indoor heat exchanger was set to be 0.58 m^3/s according to the manufacturer's installation manual. The refrigerant charge amount was determined from charge optimization tests. The voltage supply to the heat pump system during the experimental study was measured to be 212 V (±1 V). Moreover, the degree of superheat at the compressor suction port was maintained at 8 K for the system performance evaluation.

Table 2-11: Test conditions

Test	Indoor			Outdoor				Operation
	DB	WB	RH	DB	WB	RH	DP	
Extended condition	26.7°C	19.4°C	50.66%	46.1°C	NA	NA	NA	Steady State Cooling
A				35.0°C				Steady State Cooling
B				27.8°C				Steady State Cooling
D		⩽13.9°C	⩽21.41%					Cyclic Cooling
High Temp Cyclic	21.1°C	⩽15.6°C	⩽56.42%	8.3°C	6.1°C	72.9%	3.7°C	Cyclic Heating
High Temp2				8.3°C	6.1°C	72.9%	3.7°C	Steady State Heating
Low Temp				-8.3°C	-9.4°C	69.8%	-12.3°C	Steady State Heating
Extended condition				-17.8°C	NA	NA	NA	Steady State Heating

2.7 Uncertainty analysis

Total uncertainty is comprised of systematic uncertainty and random uncertainty, as shown in Equation 2-12:

$$\omega_{total} = \omega_{sys} + \omega_{rand}$$ **Equation 2-12**

Random uncertainty refers to the standard deviation for each test, and systematic uncertainty is defined by Equation 2-13:

$$\omega_f = \sqrt{\left(\frac{\partial f}{\partial x_1}\omega_{x_1}\right)^2 + \left(\frac{\partial f}{\partial x_2}\omega_{x_2}\right)^2 + \cdots + \left(\frac{\partial f}{\partial x_n}\omega_{x_n}\right)^2}$$ **Equation 2-13**

Where f is the target parameter, and x_n is the variable which the target parameter is dependent upon. For example, superheating is a function of the suction temperature T and saturated temperature at the suction pressure P, as shown in Equation 2-14:

$$T_{\text{sup}} = f(T, P)$$ **Equation 2-14**

Therefore, the systematic uncertainty can be calculated by Equation 2-15:

$$\omega_{T_{\text{sup}}} = \sqrt{\left(\frac{\partial T_{\text{sup}}}{\partial T}\omega_T\right)^2 + \left(\frac{\partial T_{\text{sup}}}{\partial P}\omega_P\right)^2}$$ **Equation 2-15**

Uncertainties of all other parameters were calculated likewise. The average uncertainties of all parameters were calculated and listed in Table 2-12.

Table 2-12: Uncertainty of the experimental tests

Parameter	Systematic	Random	Total
Thermocouple (range: -200 ~ 350 ℃)	0.5 ℃	0.11 ℃	0.61 ℃
Pressure transducer (range: 0 ~ 3,447 kPa)	3.79 kPa	2.25 kPa	6.04 kPa
Pressure transducer (range: 0 ~ 6,895 kPa)	8.62 kPa	5.70 kPa	14.32 kPa
Relative humidity sensor (range: 0% ~ 100%)	1.0%	0.19%	1.19%
Dew point sensor (range: -80 ~ 95 ℃)	0.2 ℃	0.06 ℃	0.26 ℃
Mass flow meter liquid line (range: 0 ~ 100 g/s)	0.13 g/s	0.16 g/s	0.29 g/s
Mass flow meter vapor line (range: 0 ~ 30 g/s)	0.09 g/s	0.08 g/s	0.17 g/s
Watt meter (range: 0 ~ 5 kW)	25 W	6.4 W	31.4 W
Refrigerant-side capacity	0.6%	0.5%	1.1%
Refrigerant-side COP	1.1%	0.5%	1.6%
Air-side capacity	6.5%	1.0%	7.5%
Air-side COP	6.6%	1.2%	7.8%

3. Control strategy analysis

3.1 Control strategy analysis for a single stage cycle

A typical single stage vapor compression cycle has a high-pressure side and a low-pressure side in the system, and the pressure drop between the high pressure and low pressure sides is controlled by the opening of the expansion valve. Figure 3-1 shows the schematic and P-h diagram of a conventional single stage vapor compression cycle. In such a cycle, the evaporator outlet superheat is typically utilized as the control signal for the expansion valve. The purpose of maintaining a certain degree of superheat at the evaporator outlet is to ensure the refrigerant to be in vapor state at the compressor suction port in order to protect the compressor. If the actual superheat at the evaporator outlet is higher than the target value, then the expansion valve's opening is increased in order to allow more refrigerant to flow into the evaporator for evaporation, and then reduces the actual superheating to the target value; if the actual superheat at the evaporator outlet is lower than the target value, then the expansion valve's opening is decreased in order to allow less refrigerant to flow into the evaporator, and increase the actual superheating to reach the target value. The control of such system is relatively simple, and a TXV is typically implemented for this application. Figure 3-2 shows the schematic of a TXV. It is comprised of a valve body and a sensing bulb. The working principle of a TXV can be seen in Figure 3-3. The sensing bulb, which provides a downward force, is attached to the tube surface of the evaporator outlet. The pressure inside of the evaporator provides an upward force, and there is also a force from the spring. The three forces balance the opening of the valve by controlling the needle position inside of the valve. When the

degree of superheat increases, the bulb temperature increases, and then downward force becomes greater, causing the valve opening to increase. If the degree of superheat decreases, the bulb pressure decreases, and then the downward force becomes smaller, causing the valve opening to decrease. The advantage of a TXV is that it's relatively cheap, and it has simple mechanical control. The disadvantage of a TXV is that the control is not quite accurate, and the response is not fast.

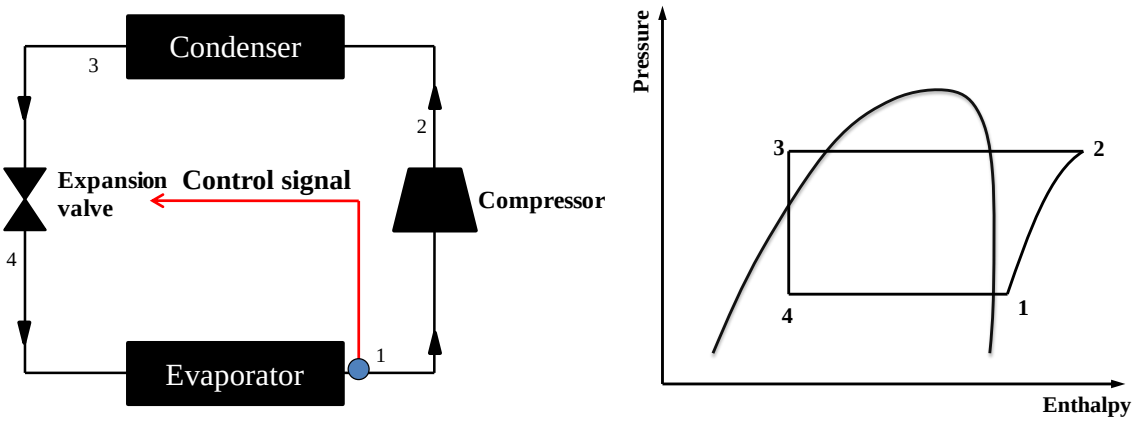

Figure 3-1: Conventional single stage vapor compression cycle

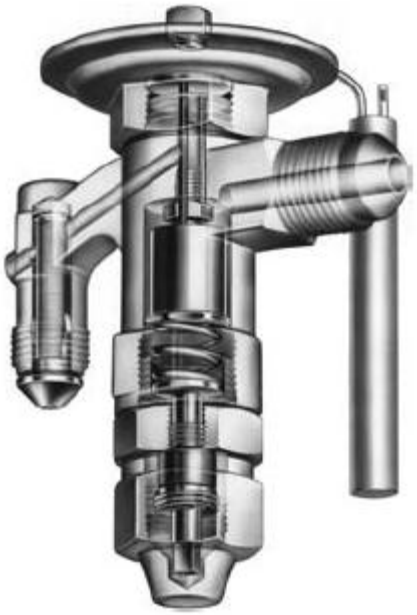

Figure 3-2: A typical TXV (Sporlan Bulletin, 2005)

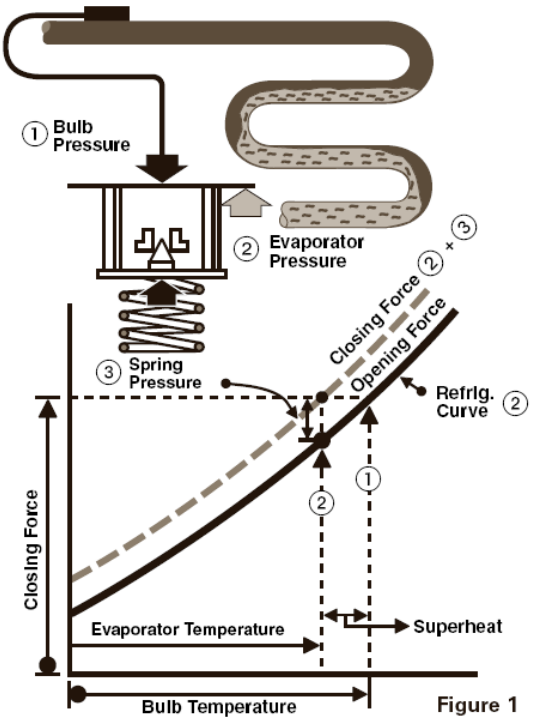

Figure 3-3: Working principle of a TXV (Sporlan Bulletin, 2005)

Another valve that can be used for the control of a vapor compression system is an EEV. Figure 3-4 shows a typical EEV and the control wiring diagram. The working principle of an EEV is similar to that of a TXV. It also utilizes the evaporator outlet superheat as the control signal. The difference is that it requires a direct measurement of the pressure and temperature at the evaporator outlet to calculate the degree of superheat. The superheat is then fed back as an input to the control board, and it outputs a control signal that determines the valve position by regulating a motor attached to the valve.

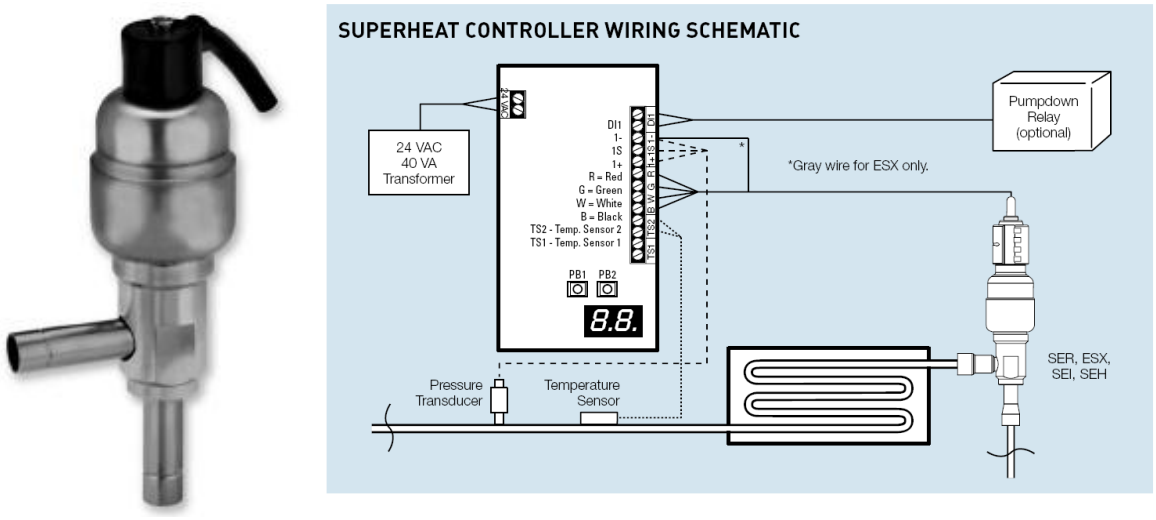

Figure 3-4: A typical EEV and the control wiring diagram (Sporlan Bulletin, 2008)

3.2 Control strategy analysis for a two-stage flash tank cycle

Figure 3-5 shows the schematic and P-h diagram of a two-stage vapor compression cycle with a flash tank. Compared to a single stage cycle that only has one expansion valve, this system has two-stage expansions controlled by an upper-stage expansion valve and a lower-stage expansion valve. Moreover, a vapor injection control valve is typically employed to control the on/off of the vapor injection. Therefore, these three valves are critical to achieve automatic control of the flash tank cycle.

The upper-stage expansion valve is critical to the system operation because it is closely related to the system performance. If the opening of the upper-stage expansion valve increases, the refrigerant through the valve is less expanded, decreasing the vapor quality of the refrigerant entering the flash tank. The liquid level in the flash tank would then tend to increase. On the other hand, if the opening of the upper-stage expansion decreases, the refrigerant through the expansion valve is further expanded, increasing the

vapor quality of the refrigerant entering the flash tank. The liquid level in the flash tank would then tend to decrease. Moreover, increasing the opening of the upper-stage expansion valve decreases the pressure drop across the valve, therefore raising the injection pressure in the flash tank, and vice versa. When the upper-stage expansion valve is controlled properly, the injection pressure in the flash tank should reach a certain level to enable sufficient refrigerant injected to the compressor, while maintaining the liquid refrigerant in the flash tank at an appropriate level to ensure the safety of the compressor.

The lower-stage expansion valve influences the evaporating pressure, which is also related to the system performance. It affects the evaporator outlet superheat, which needs to be maintained at a certain level in order to maintain vapor-state refrigerant entering the compressor suction port.

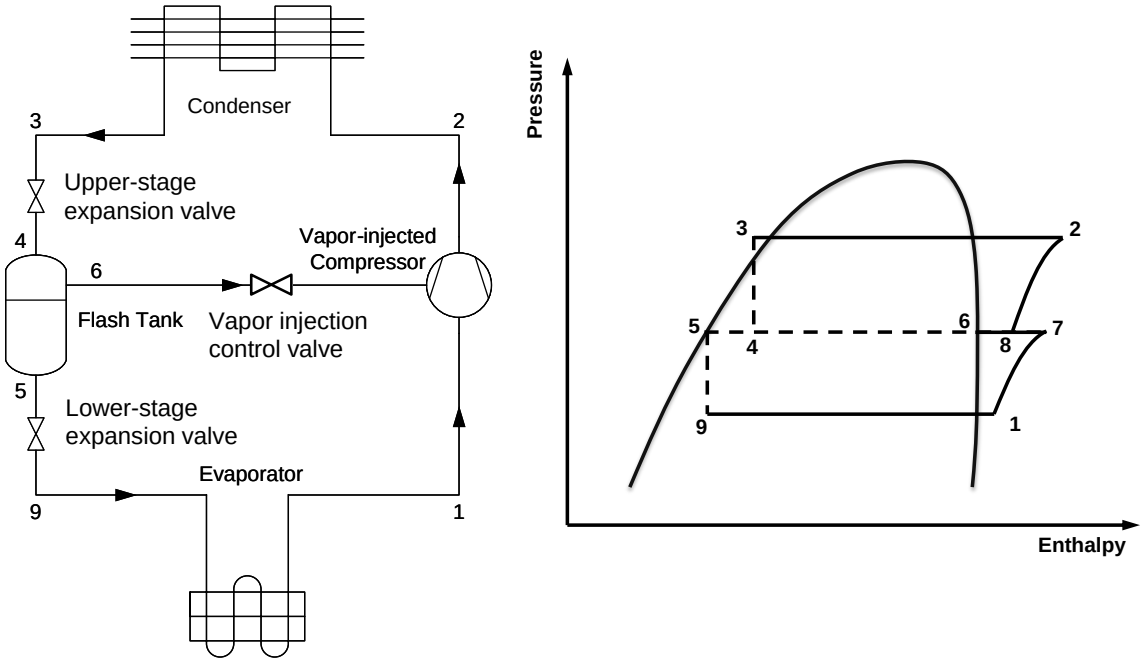

Figure 3-5: Schematic of a two-stage vapor injection cycle with a flash tank

The vapor injection control valve is relatively easy to control. When the vapor injection cycle needs to be initiated, the valve can be turned on. If only a conventional single stage cycle is needed, then this valve can be turned off so that the system can be operated as a conventional cycle. Moreover, if the liquid level increases unexpectedly, and liquid refrigerant is fed through the injection line to the compressor, then the injection control valve can be turned off to ensure the safety of the compressor. A properly functioning shut-off valve would satisfy these requirements.

The control of the lower-stage expansion valve is not difficult either. The valve is closely related to the evaporating pressure, and further related to the evaporator outlet superheat. Therefore, the superheat of the evaporator outlet can be utilized to control the opening of the lower-stage expansion valve. Wang (2008) has experimentally shown that a TXV can function properly for the lower-stage expansion. Compared to the control of the two valves described above, the upper-stage expansion valve is the most difficult to control. A conventional TXV would not function properly due to the saturated state of the injected vapor, and zero degree of superheat would cause TXV hunting (Beeton and Pham, 2003). Some studies have shown that EEV can be used for the upper-stage expansion control (Nakamura, 2007; Saito, 2007). However, no detailed information regarding the control strategy was disclosed. It's known that the response of an EEV is faster than a TXV, therefore, it's more effective to implement an EEV for the upper-stage expansion control.

3.3 Upper-stage expansion valve control options and comparisons

As discussed above, the upper-stage expansion valve control is the key for a two-stage vapor injection cycle with a flash tank. The main difficulty of the upper-stage expansion valve is that the injected vapor is in a saturated state; therefore, both a TXV and an EEV don't function properly with 0 K superheat. Moreover, different ambient temperatures result in different refrigerant mass flow rates, and therefore, lead to various expansion requirements. In addition, the flash tank liquid levels might be different due to different expansion requirements; and transient operation conditions make control even more difficult. It's known that improper control of expansion valves may result in uncontrollable amount of liquid injection, and this is detrimental to the compressor. Therefore, a proper control for the liquid level is a key issue.

3.3.1 Control option 1

Figure 3-6 shows the schematic of a control strategy employing a liquid level sensor. The liquid level sensor is inserted to the flash tank in order to measure the liquid level inside of the flash tank. The working principle of this control strategy can be explained by the flow diagram in Figure 3-7. As the liquid level increases to exceed a target level, the EEV opening is decreased, increasing the vapor quality of the refrigerant entering the flash tank. As a result, the liquid level inside of the flash tank is decreased. Similarly, as the liquid level decreases lower than a target level, the EEV opening increases, reducing the vapor quality of the refrigerant entering the flash tank. Therefore, the liquid level is increased. This control strategy can effectively maintain the liquid level to a property level inside of the flash tank.

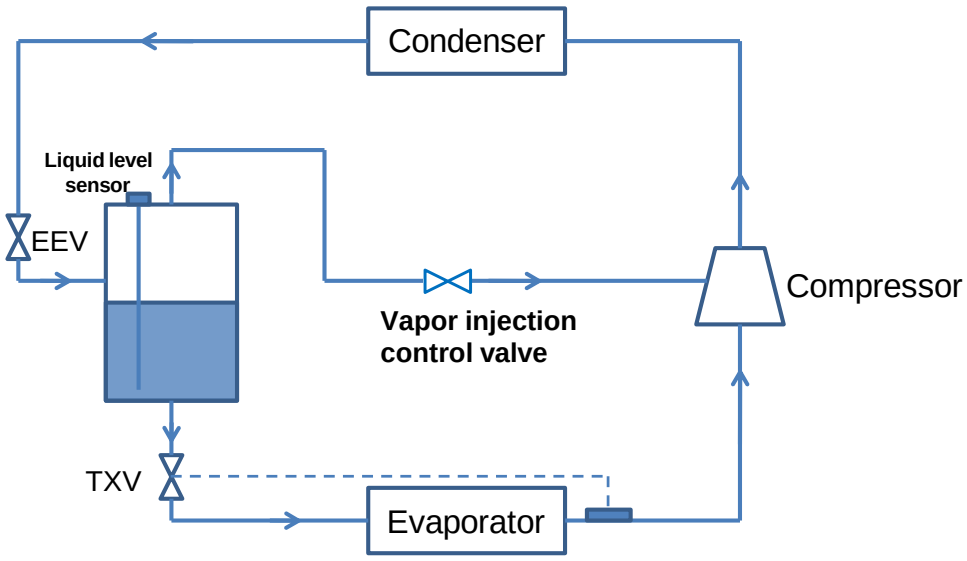

Figure 3-6: Control strategy employing a liquid level sensor

The major advantage of this control strategy is that the direct measurement of the liquid level gives a critical parameter to control the EEV. This method would work effectively in different temperature conditions, and in both steady-state and transient operating conditions. However, the biggest challenge of this method is the requirement of an accurate liquid level sensor. This can be feasible for experimental tests in a laboratory. However, an accurate liquid level sensor plus the corresponding transmitters could increase the overall system cost significantly, and therefore, reduce the feasibility to implement this method in actual commercial products.

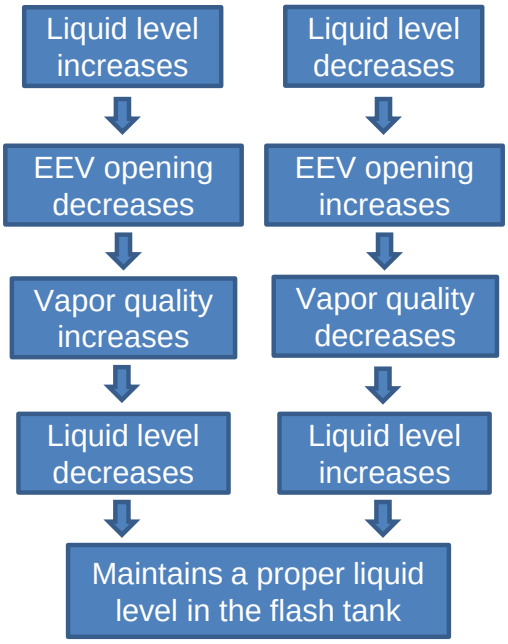

Figure 3-7: Working principle of employing a liquid level sensor

3.3.2 Control option 2

Figure 3-10 shows a control method employing mass balance in a control volume to calculate the liquid level height inside of the flash tank in order to control the upper-stage expansion valve. Taking the flash tank as the control volume, Equation 3-1 can be derived. The total refrigerant mass flow rate at a certain time interval is equivalent to the liquid and vapor mass flow rates exiting the flash tank, plus the liquid and vapor refrigerants remain in the flash tank.

$$\int \dot{m}_{total} dt = \int \dot{m}_{vap} dt + \int \dot{m}_{liq} dt + \rho_{vap} V_{vap} + \rho_{liq} V_{liq} \qquad \textbf{Equation 3-1}$$

It's also known that:

$$V_{vap} + V_{liq} = V_{\tan k} \qquad \textbf{Equation 3-2}$$

$$V_{liq} = S_{\tan k} \cdot h_{liq} \qquad \textbf{Equation 3-3}$$

where V_{vap} and V_{liq} stand for the volume occupied by vapor and liquid in the flash tank, respectively. $S_{\tan k}$ is the cross-sectional area of the flash tank, and h_{liq} is the liquid height inside of the flash tank. The liquid and vapor densities can be obtained by measuring the pressure and temperature of the fluid inside of the flash tank. The volume of the flash tank and the cross-sectional area of the flash tank can be measured. Therefore, the liquid height can be easily calculated once the refrigerant mass flow rates can be obtained. In experimental tests in a laboratory, mass flow meters can be installed to measure the refrigerant mass flow rates in different paths. However, this is still not quite feasible for an actual product which would require accurate measurement of refrigerant mass flow rate in the system.

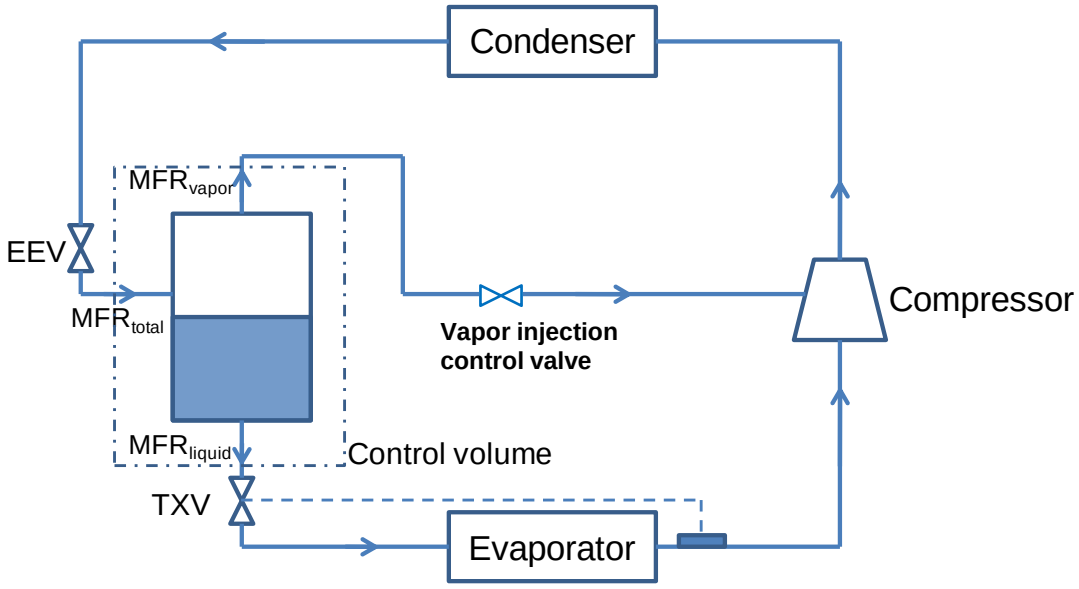

Figure 3-8: Control strategy employing mass balance in the flash tank

3.3.3 Control option 3

Figure 3-9 shows the control option employing a floating device. The floating device is installed inside of the flash tank and its position changes simultaneously with the liquid level. This floating device is attached to a sensor that records the position of the floating device. The position of the floating device provides a measurement of the liquid level inside of the flash, and therefore, can be used to regulate the upper-stage EEV opening. However, there is a major challenge of this method due to installation difficulty. The flash tank used in this experimental study only has a diameter of 7 cm, and it is quite difficult to install such a floating device plus the additional location sensor in such limited space.

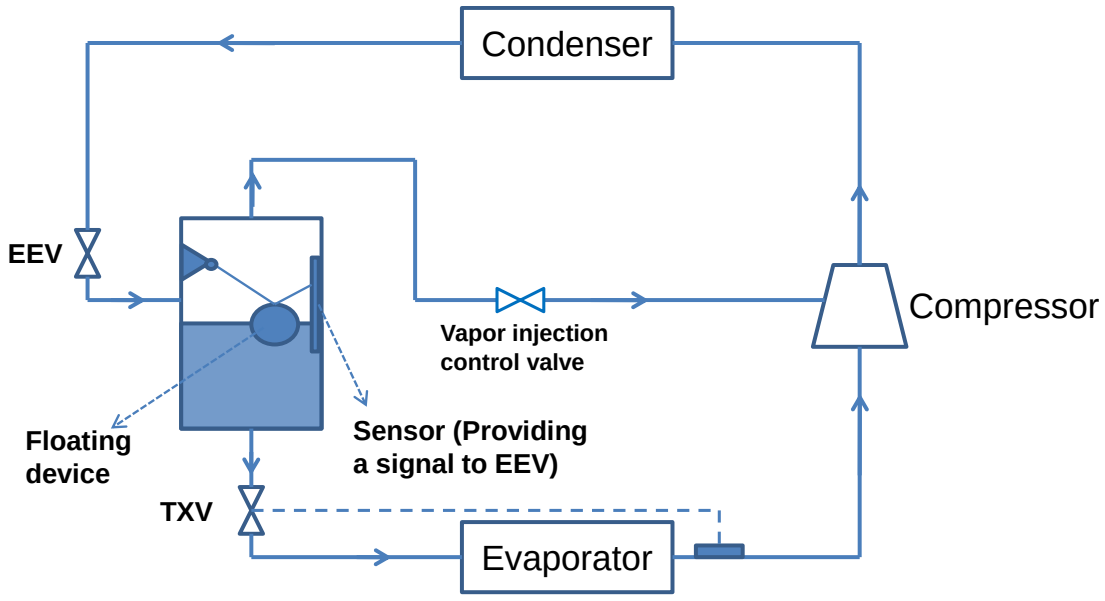

Figure 3-9: Control option employing a floating device

3.3.4 Control option 4

Since an expansion valve requires a certain degree of superheat in order to function properly, it's possible to introduce superheat to the injected vapor to achieve the control purpose. The heat can be coming from the condenser, or more easily, from the compressor discharge line. Therefore, it's possible to implement a simple tube-in-tube heat exchanger to conduct heat from the compressor discharge line to the vapor injection line to superheat the injected vapor. In the experimental study, a small electric heater can be implemented to introduce superheating to the injected vapor just to examine the feasibility of this approach.

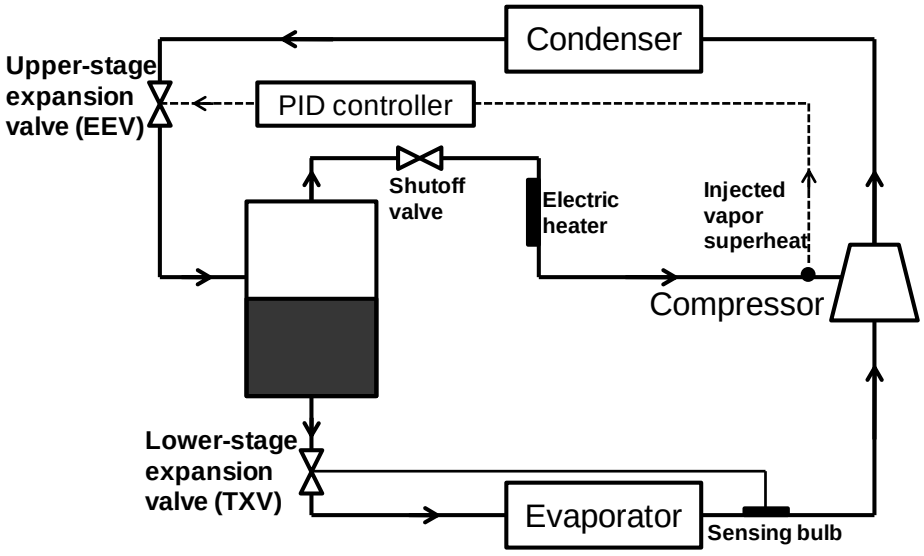

Figure 3-10: Schematic of the control strategy for the flash tank cycle by introducing superheating to the injected vapor

Figure 3-10 shows a control method for the flash tank cycle by introducing superheating to the injected vapor. A small belt-shape electric heater was wrapped onto the tube surface of the vapor injection line in order to introduce a certain degree of

superheat to the injected vapor. The electric heater is shown in Figure 3-11. The power input of the electric heater is controlled by a transformer, and therefore, the output of the heater can be varied continuously from 0 W to 400 W.

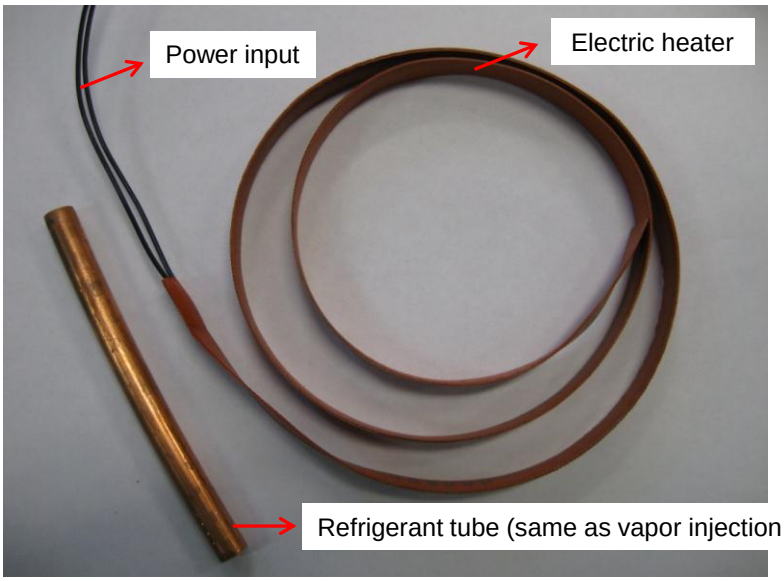

Figure 3-11: Belt-shape electric heater used in the experiment

The superheat of the injected vapor is used as an input to a proportional-integral-derivative (PID) controller, which controls the opening of an EEV for the upper-stage expansion. The PID controller integrated with EEV was programmed in LabView data acquisition program. The flow chart of the control strategy and the system operation procedure can be seen in Figure 3-12. Once the vapor compressor cycle is turned on and the vapor injected is initiated, the electric heater can be powered up. By setting the target superheat, the PID controller regulates the EEV opening to reach the target superheating. The user interface of the EEV-PID controller is shown in Figure 3-13. This interface provides the convenience to control the system either by automatic or manual control. In the automatic control mode, the PID controller automatically controls the injected vapor

superheat to reach the set point value by regulating the upper-stage EEV opening. In the manual mode, the EEV opening can be controlled by the manual input value of the valve opening. In the experimental study, the automatic control mode was used to reach the automatic control of the system.

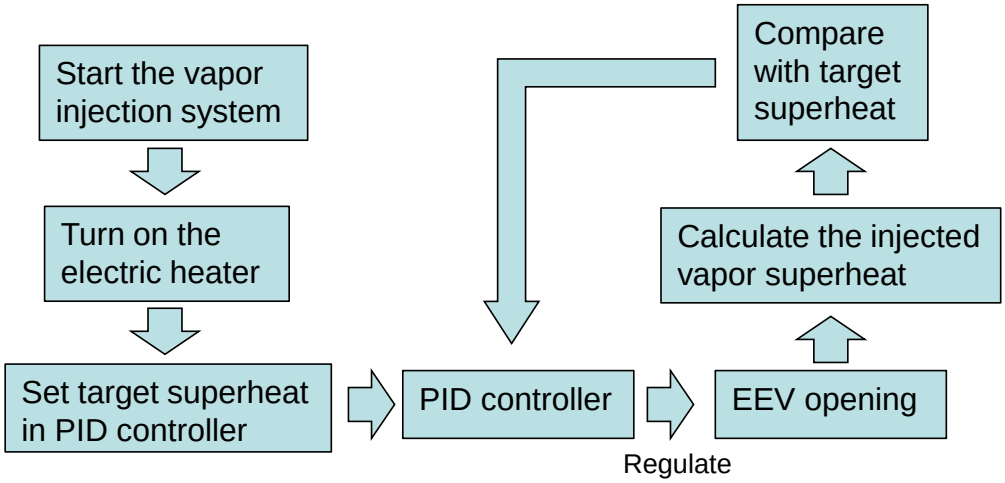

Figure 3-12: Flow chart of the control strategy and system operation procedure

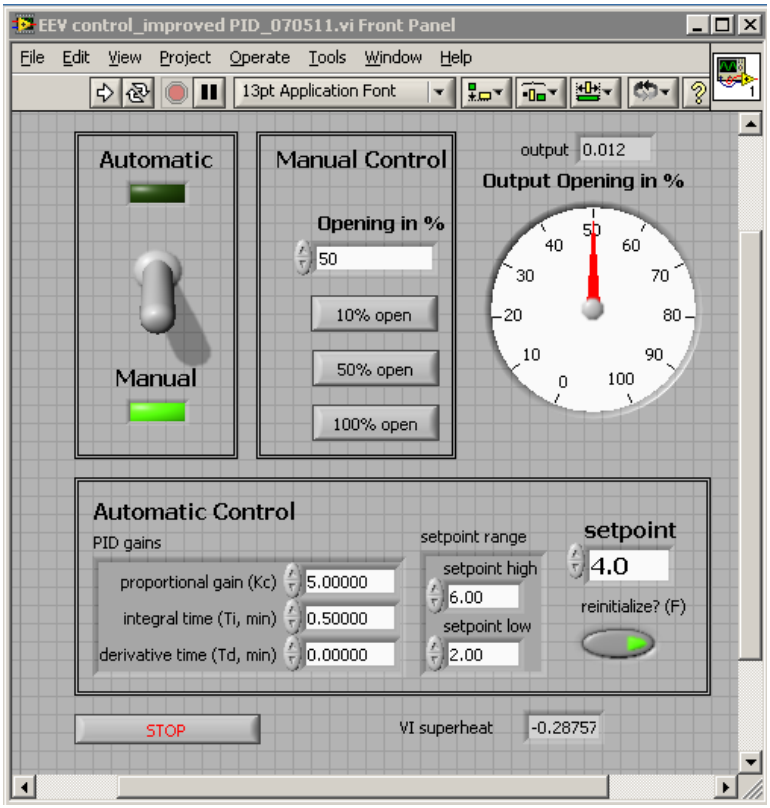

Figure 3-13: The user interface of the EEV-PID controller

Essentially the control goal is to avoid liquid level reaching too high and causing uncontrollable amount of liquid injection to the compressor. The control algorithm works as follows: A target degree of superheat is assigned to the PID controller to control the EEV opening. If the liquid refrigerant is to be injected with vapor refrigerant to the compressor by the liquid flooding in the flash tank, the superheat of the injected vapor would decrease rapidly. In this event, the upper-stage EEV would reduce its opening to maintain the target degree of superheat. This reduces the amount of liquid flowing from the condenser to the flash tank, which reduces the flash tank liquid level and effectively avoids liquid injection to the compressor. By installing an electric heater coupled with a

PID controller, it avoids the additional cost of installing a liquid level sensor in potential industrial application. Therefore, it's a more cost-effective method than the other options.

The lower-stage expansion valve employs a TXV, which utilizes the evaporator outlet superheat for the expansion control. The original OEM TXV installed in the system was found out to be not functioning properly; therefore, it was replaced with a Sporlan TXV that has a nominal capacity of 14-21 kW. It was oversized than a regular TXV used in a 3-ton system to function better in cases when there is occasional bubbling flowing in the flash tank liquid outlet. The upper-stage EEV (Sporlan) has 500 steps, and is shown in Figure 3-14. The vapor injection control valve installed in the vapor injection line is a manually operated shut-off valve. In the vapor injection test, this valve is fully opened to allow vapor refrigerant to be injected to the compressor.

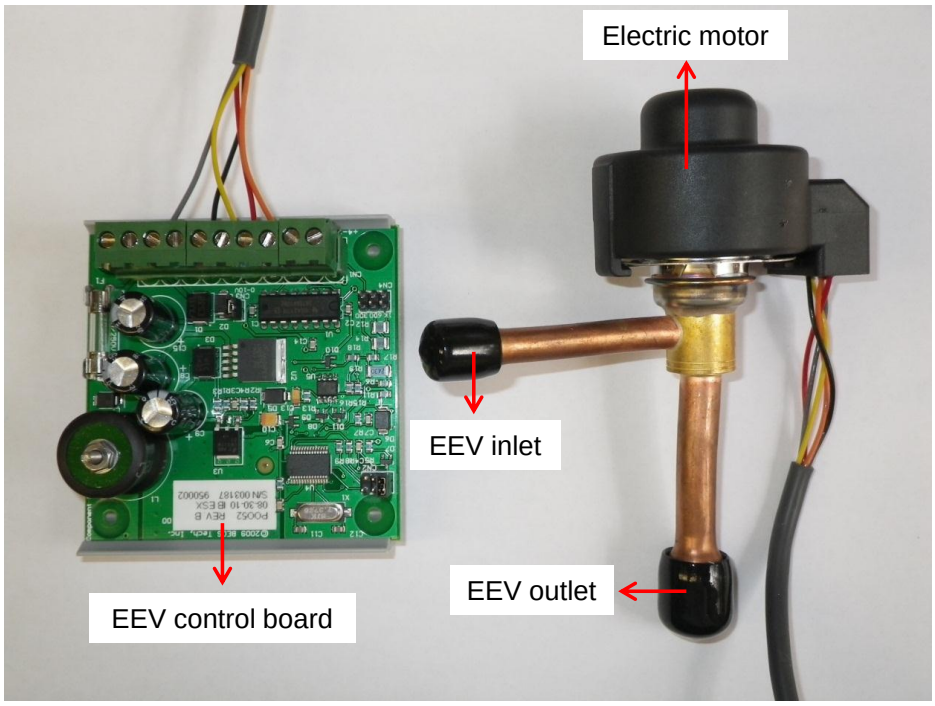

Figure 3-14: EEV used in the experiment

3.4 Experimental results

To validate the effectiveness of this control strategy, the system was operated in different temperature conditions, as specified in Table 2-11. Moreover, both steady-state and transient tests were performed to investigate the system response in different operation modes.

3.4.1 Steady-state tests of different injection superheats and heater power inputs

The injected vapor superheat is affected by two factors: the electric heater power input and EEV opening. The EEV opening affects the injected vapor superheat because it controls the injection pressure in the flash tank. The system performance varies depending on the heater power input as well as the selected superheat setting. Both cooling and heating tests were conducted.

3.4.1.1 Steady state cooling test

Figure 3-15 shows the injection pressure variations at different ambient temperature conditions, heater power input and degrees of superheat. It can be seen that the injection pressure increases as the injected vapor superheat decreases. The injection pressure also increases with the increasing heater power input. The main reason is that decreasing the injected vapor target superheat and increasing the heater power input causes the upper-stage EEV to increase its opening, and therefore, leads to higher injection pressure in the flash tank. The variations of the EEV opening are shown in Figure 3-16. The trend corresponds to the injection pressure variations in Figure 3-15.

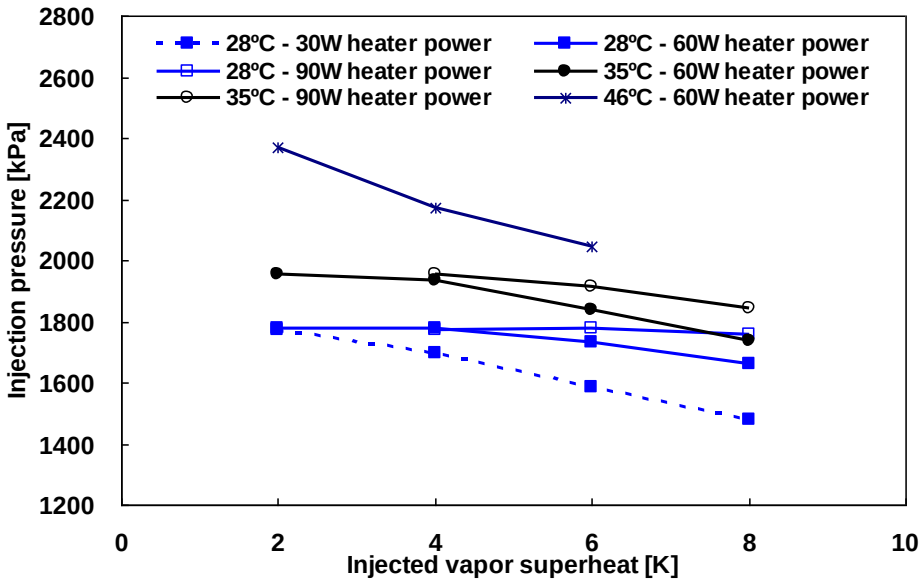

Figure 3-15: Steady-state test of injection pressure variations at different ambient conditions, heater power input and degrees of superheat

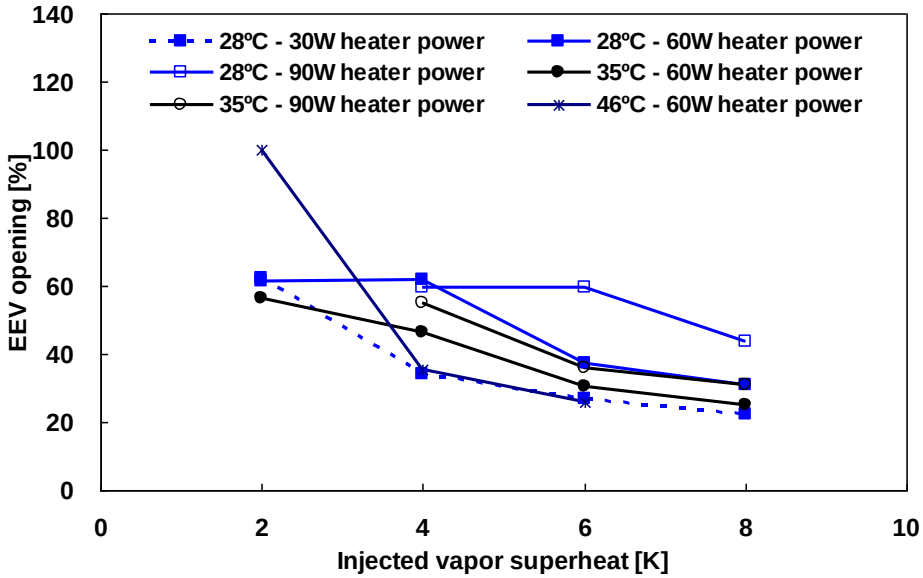

Figure 3-16: Steady-state test of EEV opening variations at different ambient conditions, heater power input and degrees of superheat

Liquid level variations in the flash tank at different conditions are shown in Figure 3-17. The liquid levels at different operating conditions are not exceeding 80% of the flash tank, which effectively avoids unexpected liquid injection and ensures the safety of the compressor. It should be noted that the liquid level sensor installed in the flash tank cannot measure liquid level lower than 20% of the flash tank height due to geometry limitation; therefore, the lowest liquid level results shown in the figure is 20%. The general trend is that as the target superheat decreases, the liquid level increases due to the increasing opening of the upper-stage EEV.

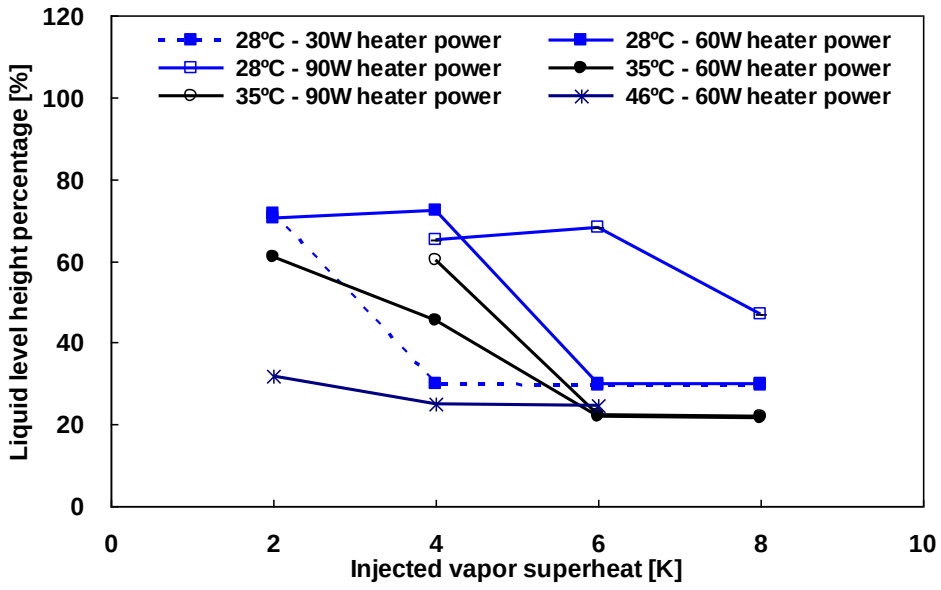

Figure 3-17: Flash tank liquid level variations at different steady-state cooling ambient conditions, heater power input and degrees of superheat

Figure 3-18 illustrates the steady-state test results of cooling COP variations with different ambient conditions, heater power input and degrees of superheat. For 28℃ condition, the COP variations with 60 W and 90 W heater power input are small, yet the

COP tends to decrease with 30 W heater power input. This means that the system performance is not that sensitive when the heater power input is higher than 60 W. At 30 W heater power input, the performance is more sensitive to the heater power input. As the target superheat increases, the injection pressure needs to be lowered in order to reach the target superheat. Lower injection results in lower cooling COP in such case.

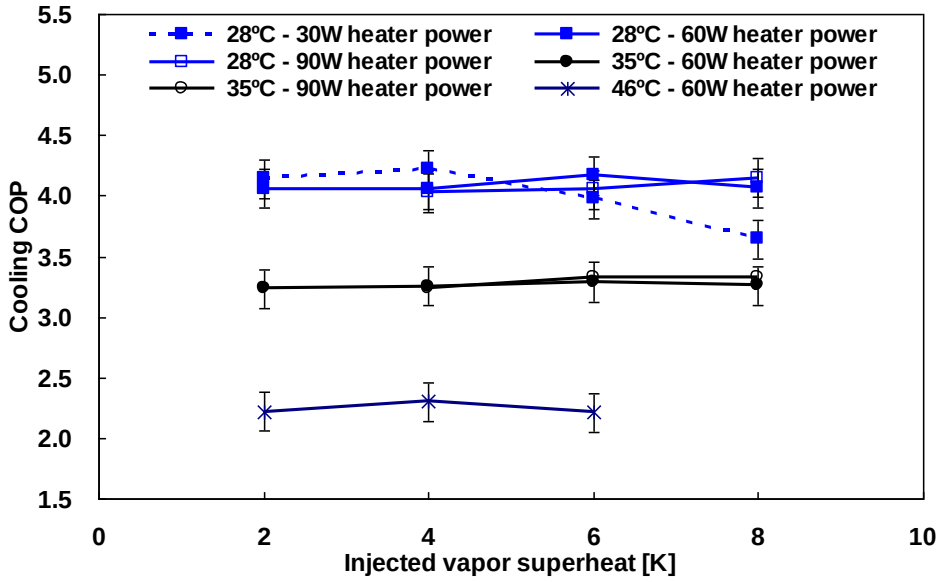

Figure 3-18: Steady-state test of cooling COP variations at different ambient conditions, heater power input and degrees of superheat

The cooling capacity variations show similar trend as the cooling COP variations, which is shown in Figure 3-19. It can be seen that the cooling capacity variations are relatively small when the heater power input is higher than 60 W, yet degradation was observed when 30 W heater power input was applied. This can also be explained by the injection pressure variations, which is similar to the COP variations.

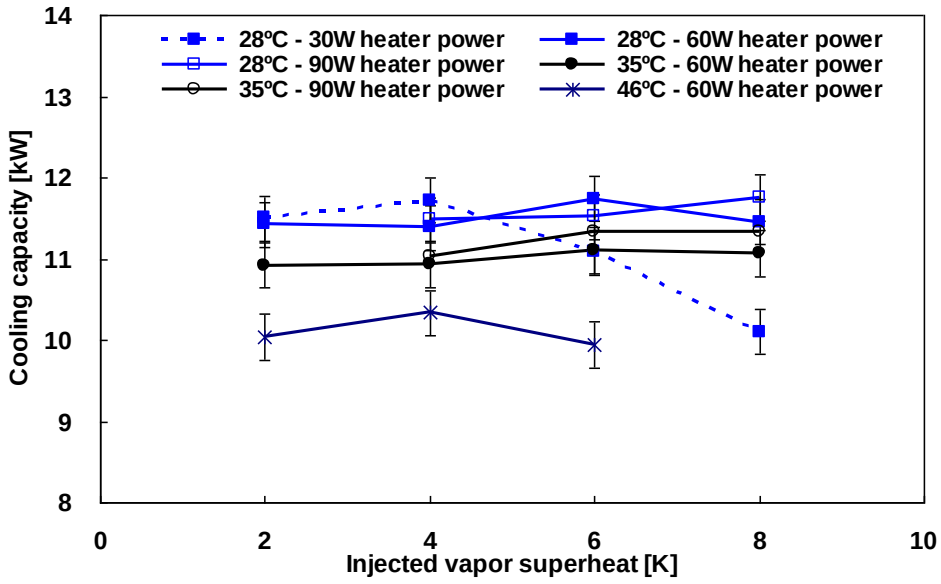

Figure 3-19: Steady-state test of cooling capacity variations at different ambient conditions, heater power input and degrees of superheat

3.4.1.2 Steady state heating test

Figure 3-20 shows the injection pressure variations at different ambient conditions, heater power input and degrees of superheat. Test at -8 ℃ was not included because frost accumulation at this test conditions was severe, and therefore it's very hard to obtain accurate data at this condition. At the extreme heating condition of -18 ℃, the humidity ratio of the ambient air is low. Therefore, the frost accumulation phenomenon was not as bad as the condition of -8 ℃. From the results it can be seen that the injection pressure increases as the degree of superheat decreases, and also increases with the increasing heater power input. This is due to the fact that the upper-stage EEV opening increases as the target injection superheat decreases, and also increases as the heater power input increases. The EEV variations can be seen in Figure 3-21.

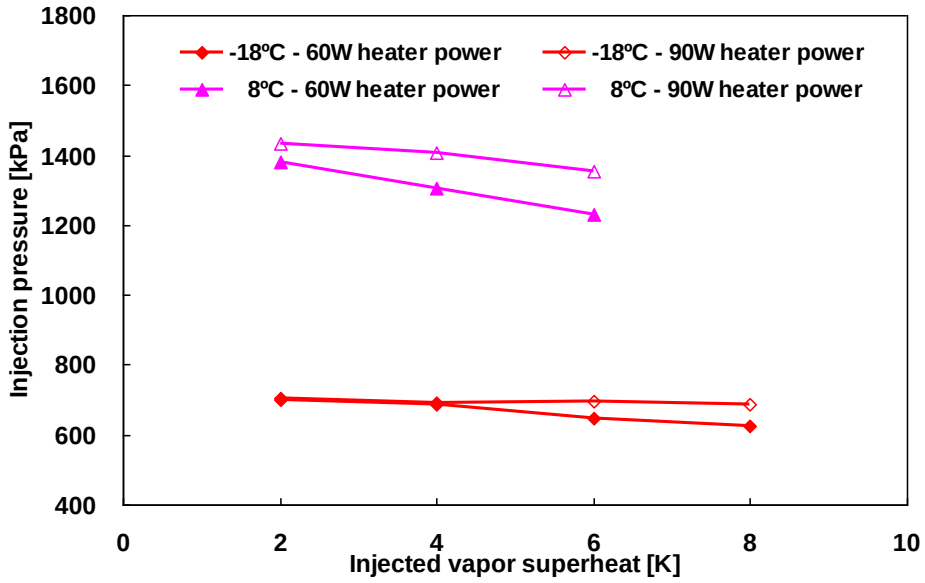

Figure 3-20: Steady-state tests of injection pressure variations at different ambient conditions, heater power input and degrees of superheat

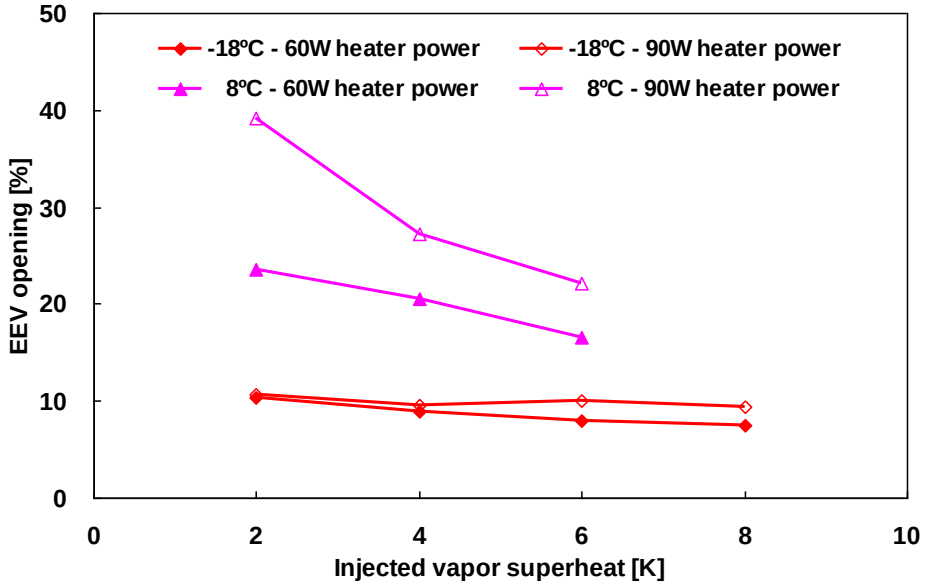

Figure 3-21: Steady-state tests of EEV opening variations at different ambient conditions, heater power input and degrees of superheat

Figure 3-22 shows the flash tank liquid level variations at different operating conditions. It can be seen that the liquid level at -18℃ with 90 W heater power input is significantly higher than other conditions. This is due to the fact that at -18℃, the refrigerant mass flow rate in the system is much lower than that at other conditions as a result of the low refrigerant density at the compressor suction. The injection pressure is also much lower than that at other conditions. Therefore, 90 W heater power input can actually generate a very high superheat to the injected vapor. The upper-stage EEV tends to always increase its opening in order to decrease the injected vapor superheat, and causes the liquid in the flash tank always maintain a very high level. As a consequence, the heater power input of 90 W is slightly over-supplied. In this scenario the system stability is also compromised since the liquid level is very high. When the power input decreases to 60 W, the liquid level in the flash tank drops rapidly.

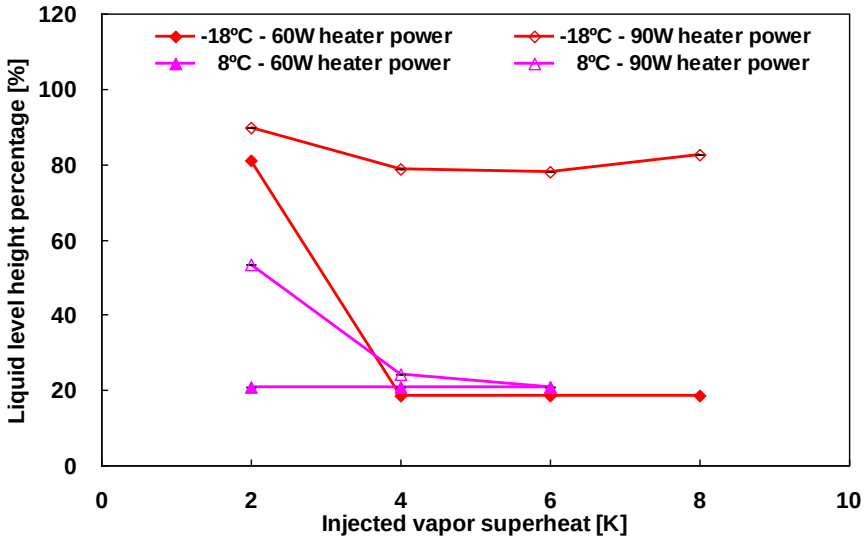

Figure 3-22: Steady-state tests of flash tank liquid level variations at different ambient conditions, heater power input and degrees of superheat

Figure 3-23 shows the steady-state heating COP variations at different ambient conditions, heater power input and degrees of superheat. At 8℃ condition, the general trend is that higher heater power input yields higher heating COP, and lowering the target superheat also results in higher COP. An explanation for this is that when the target superheat is set to be a constant value, increasing the heater power input induces the EEV to enlarge its opening in order to increase the injection pressure in the flash tank, thus maintaining the same degree of superheat. This results in higher injection ratio and improves heating COP. Likewise, if the heater power input is kept constant, decreasing the target superheat value also results in increased injection pressure in order to match the decreasing superheat. For -18℃ condition with 60 W heater power input, the trend is similar to that of 8℃ condition. However, as the heater power input increases to 90 W, the heating COP remains almost constant. This is because at this condition, the system injection pressure already reaches its maximum, and therefore, lowering the superheat cannot increase the injection pressure any more. This corresponds to the variations of the liquid level in the flash tank, as shown in Figure 3-22. The heating capacity variation shows the same trend as the heating COP, as shown in Figure 3-24.

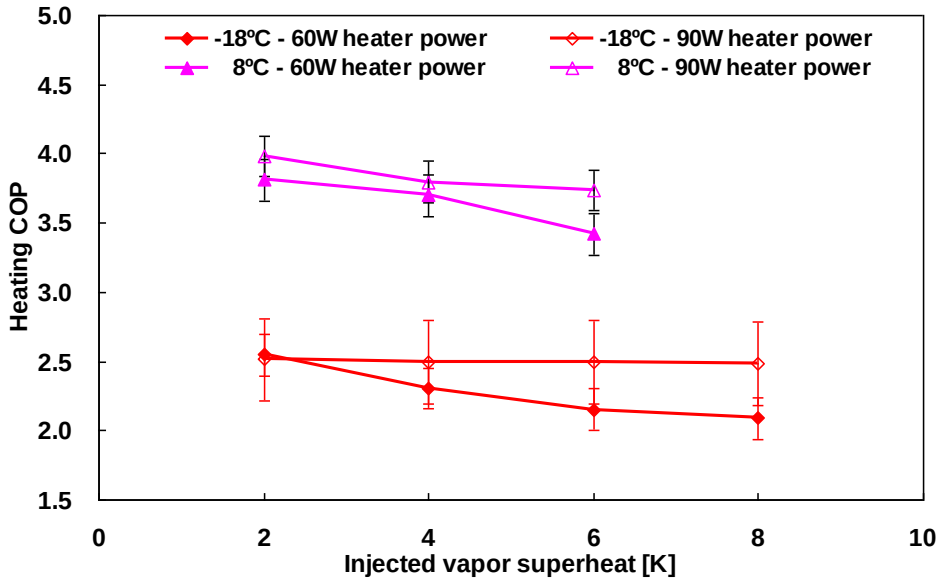

Figure 3-23: Steady-state tests of heating COP variations at different ambient conditions, heater power input and degrees of superheat

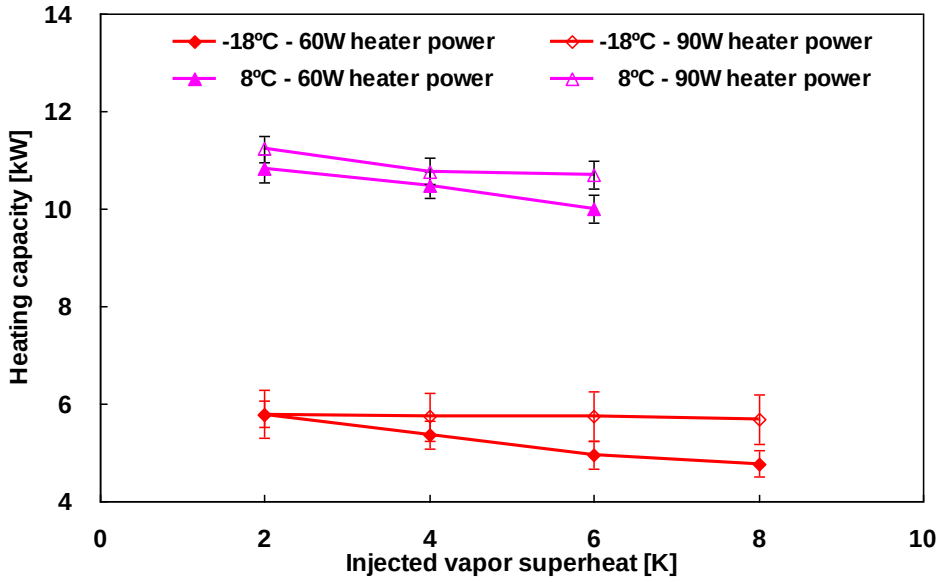

Figure 3-24: Steady-state tests of heating capacity variations at different ambient conditions, heater power input and degrees of superheat

3.4.1.3 Steady-state results and discussions

Through steady-state tests at different ambient temperature conditions, it's observed that the PID-EEV controller function property in controlling the liquid level in the flash tank. The general trend seen in the experiment is that the EEV opening increases as the target superheat decreases, and increases with increasing heater power input. The EEV opening is directly associated with the injection pressure and the liquid level inside of the flash tank. For the cooling mode, there is no big difference with 60 W and 90 W heater power input, yet 30 W heater power input seems to be insufficient in reaching optimum performance. The optimum performance was observed with 4 K to 6 K degrees of superheat. For the heating mode, 90W heater power input shows better performance than 60 W heater power input at 8℃ condition. At -18℃ condition, 90 W heater power input seems to be over-supplied, and therefore 60 W heater power input is more appropriate.

In overall, when both the system performance and reliability are both considered, 4 K to 6 K degrees of superheat is preferred. For the heating mode, 60 W heater power input is preferred to 90 W; for the cooling mode, heater power input between 60 W to 90 W seems to be more appropriate.

3.4.2 Cooling cyclic test

In the real application, the air conditioning/heat pump systems are turned on and off frequently. Therefore, it's worthwhile to investigate the system's cyclic performance. According to ASHRAE Standard 116 (2010), cooling and heating cyclic tests are comprised of 6 minutes compressor "on" time, followed by 24 minutes compressor "off"

time. Cooling and heating cyclic tests were conducted at ambient temperatures of 28℃ and 8℃, respectively.

3.4.2.1 PID tuning of cooling cyclic test

PID gains are critical factors that affect the transient behavior of the PID controller, and therefore, it's necessary to find out the appropriate PID gains in order to reach the optimum performance for the system control. The output of the PID controller in this study was normalized to be -100 to 100 to obtain more general results for PID gains. The proportional gain makes a change to the output that is proportional to the current error value. The integral gain is the sum of the instantaneous error over time and gives the accumulated offset that should have been corrected previously. The derivative of the process error is calculated by determining the slope of the error over time and multiplying this rate of change by the derivative gain. Different combinations of PID gains were tried, and from the experiment it was found out that the EEV experienced large oscillations when the derivative gain was used, and therefore the derivative gain was set to be zero.

Figure 3-25 shows the injected vapor superheat variations of PID tuning results of the cooling cyclic test. From the results it can be seen that small P and I gains tend to yield a large variation, and with larger P and I gains the control curve looks better. P = 5.0, I = 0.5, D = 0, and P = 10, I= 0.5, D = 0, together with P = 15, I = 1.0, D = 0 outperformed other three different combinations of PID gains. Figure 3-26 shows the EEV opening variations during the PID tuning of cooling cyclic test. The combination of P = 2.0, I = 0.2, D = 0 and P = 5.0, I = 0.5, D = 0 yield the least variations, and other PID

gains result in relative large variation of the EEV opening. Figure 3-27 shows the variations of indoor heat exchanger outlet air temperature variations. It can be observed that with P = 2.0, I = 0.2, D = 0 and P = 5.0, I = 0.5, D = 0, the temperature variation is more smooth, and this corresponds to the variations of EEV opening, as shown in Figure 3-26. From the performance point of view, P = 5.0, I = 0.5, D = 0 outperformed P = 2.0, I = 0.2, D = 0. As a consequence, considering the time for the injected vapor superheat to reach steady state, the variation of the EEV opening, and the air side performance, P = 5.0, I = 0.5, D = 0 was found to be the most appropriate PID gains for the cooling cyclic control.

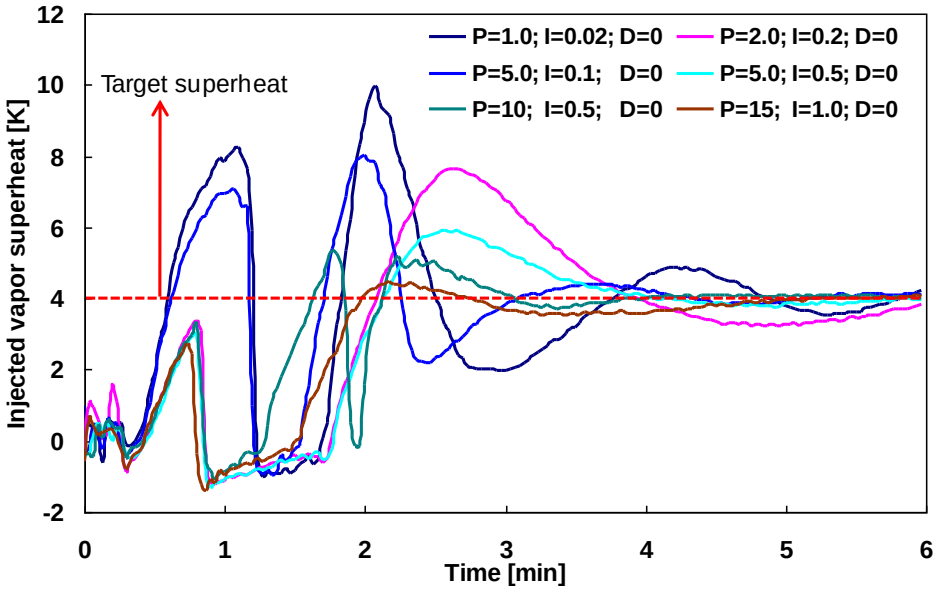

Figure 3-25: PID tuning of cooling cyclic test: injected vapor superheat variations

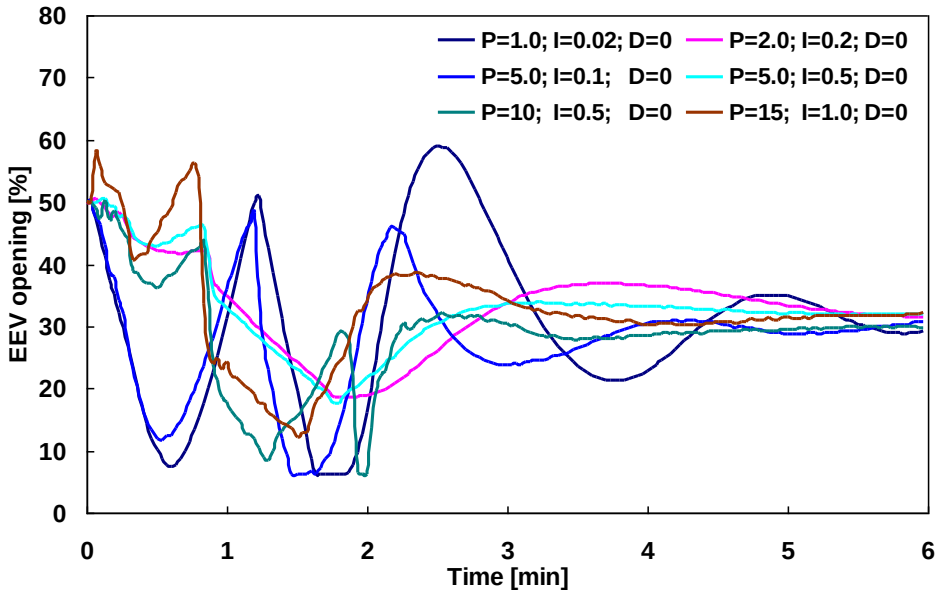

Figure 3-26: PID tuning of cooling cyclic test: EEV opening variations

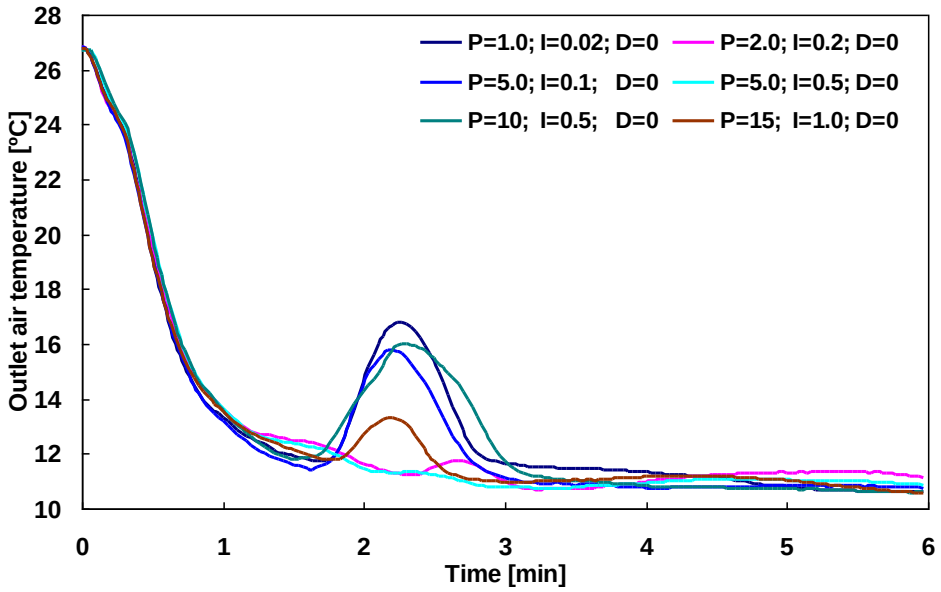

Figure 3-27: PID tuning of cooling cyclic test: indoor heat exchanger outlet air temperature

3.4.2.2 Time delay to initiate the PID controller

After selecting the optimum PID gains, it's also interesting to study whether there is any difference if the PID controller is initiated with different time delays after the system is started. Since the cyclic test requires the system to be turned "on" for 6 minutes, and then turned "off", therefore, the delay time was selected to be between 1 minute and 5 minutes. Figure 3-28 shows the indoor heat exchanger air outlet temperature variations with different delay time to initiate the PID controller. It can be seen that only with 1 minute delay time, the transition of air side temperature is not smooth, and there is no difference between other delay time and the case without delay initiating the PID controller. Therefore, it's recommended to turn on the PID controller when the system is started, and no delay for the PID controller is needed.

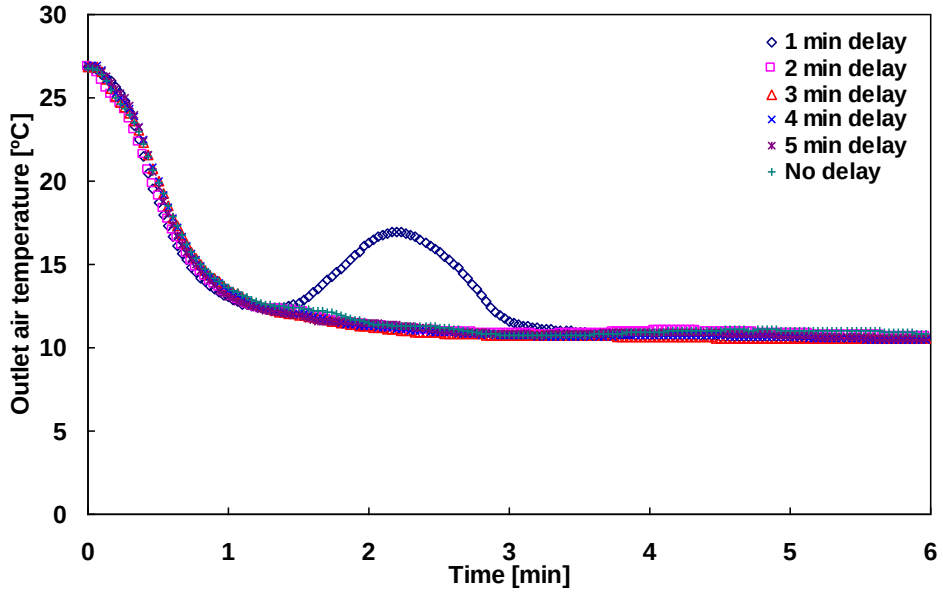

Figure 3-28: Cooling cyclic test: performance variations with different time delays for PID controller

3.4.2.3 Cooling cyclic test results

Figure 3-29 shows the cooling cyclic test results with vapor injection "on" and "off". It can be seen that the indoor heat exchanger outlet air temperature with vapor injection "on" is lower than with vapor injection "off", which means that the cooling capacity delivered by vapor injection "on" is higher than with vapor injection "off". Calculation shows the capacity improvement is 10.1%. However, the power consumption also becomes higher as vapor injection is initiated, which also can be seen from Figure 3-29. This results in a degradation of cooling COP of 2.4%, which is within measurement uncertainty. Therefore, the vapor injection can still be beneficial when larger cooling capacity is needed in moderate temperature conditions, although some compromise in COP is observed. This again shows that vapor injection is less beneficial for the cooling application compared to low temperature heating application.

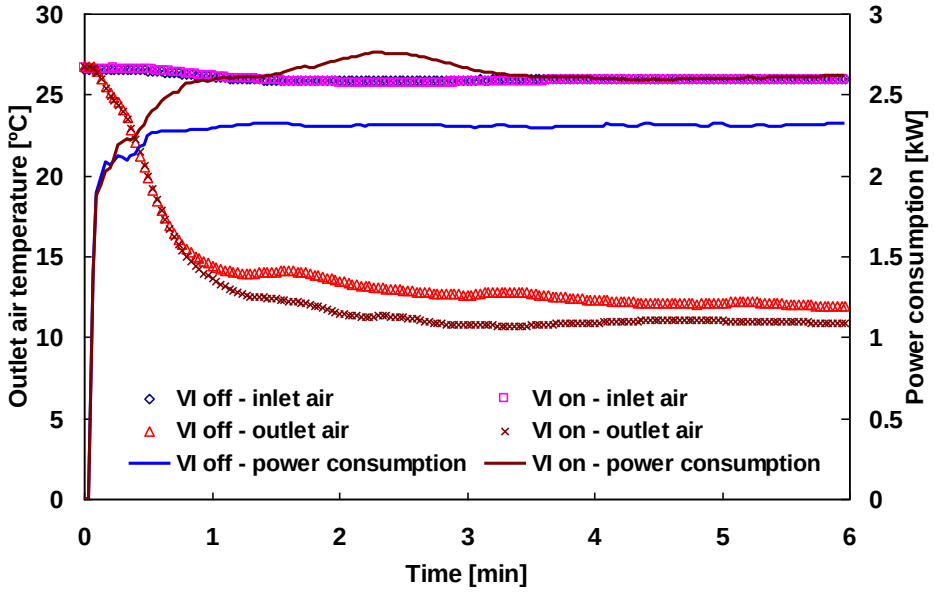

Figure 3-29: Cooling cyclic test: comparison between VI "on" and VI "off"

3.4.3 Heating cyclic test

3.4.3.1 PID tuning of heating cyclic test

PID tuning was also conducted for heating cyclic test in a similar manner as the cooling cyclic test. Figure 3-30 shows the injected vapor superheat variations using different combinations of PID gains. Similar trend could be seen as in the cooling cyclic test. Small P and I gains tend to yield a large variation of the control variable, and P = 10, I = 0.5, D = 0 and P = 15, I = 1.0, D = 0 result in the least variations of the injected vapor superheat. Figure 3-31 shows the EEV opening variations with different PID gains. P = 1.0, I = 0.02, D = 0 and P = 5.0, I = 0.1, D = 1 result in large variations of the EEV opening, and other PID gains lead to less variations of the EEV opening. Figure 3-32 illustrates the indoor heat exchanger outlet temperature variations with different PID gains. The optimum performance was reached when P = 10, I = 0.5, D = 0. Therefore, P = 10, I = 0.5 and D = 0 was selected for the PID gains for heating cyclic test.

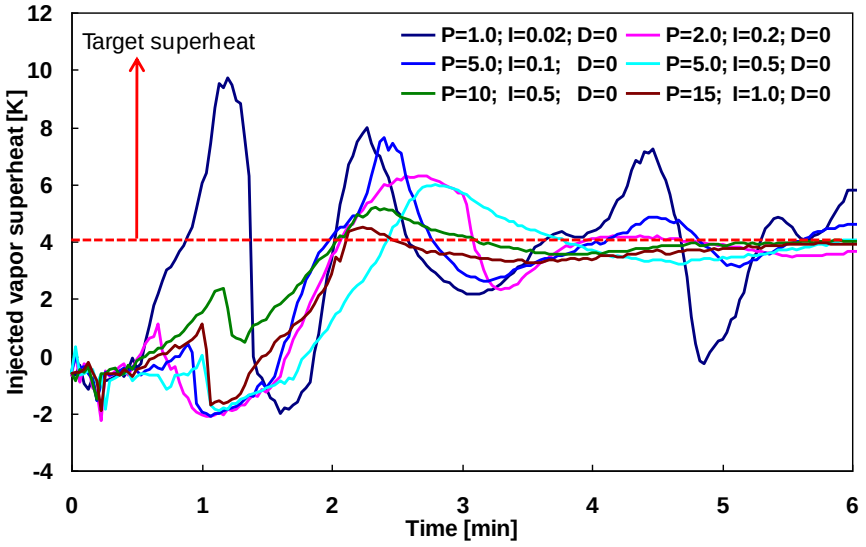

Figure 3-30: PID tuning of heating cyclic test: injected vapor superheat variations

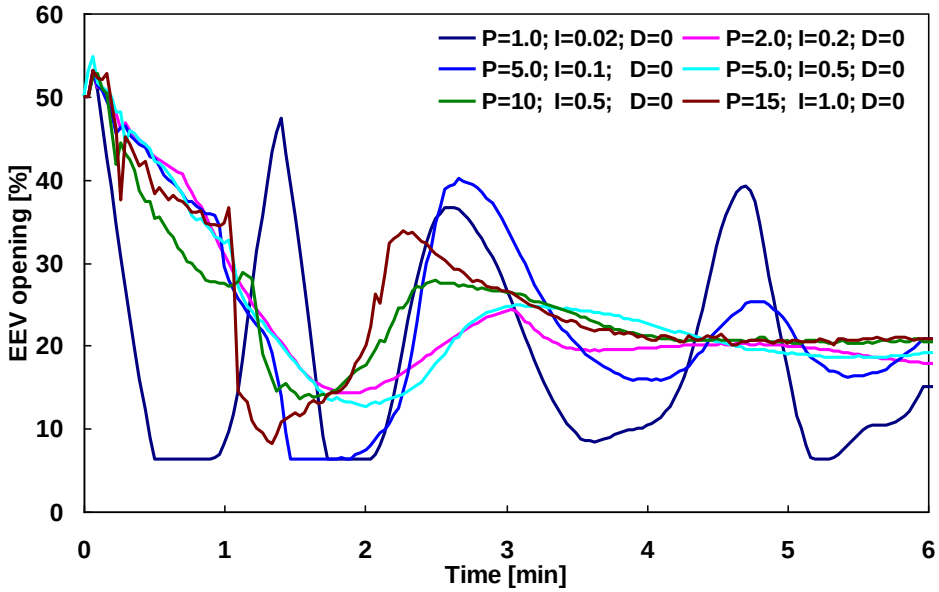

Figure 3-31: PID tuning of heating cyclic test: EEV opening variations

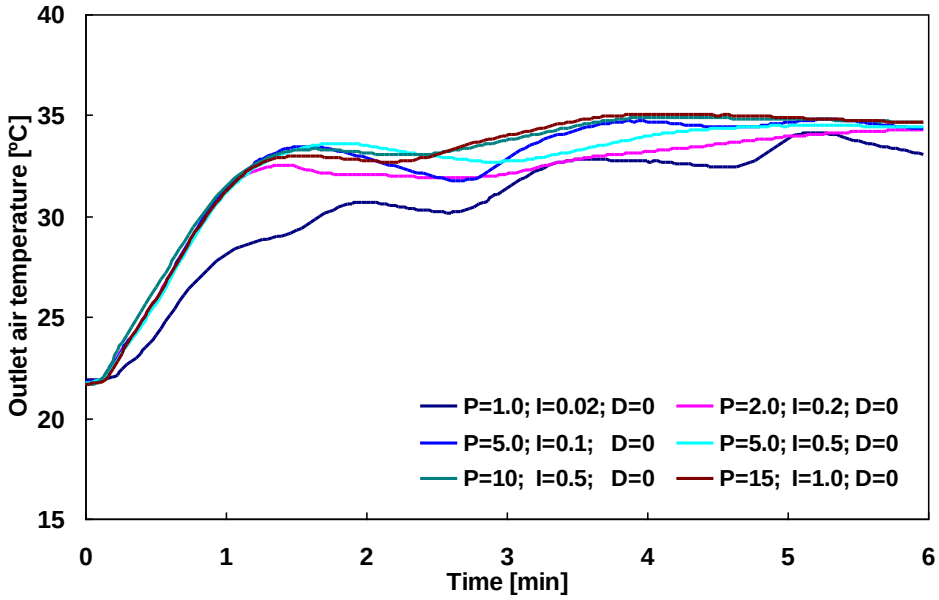

Figure 3-32: PID tuning of heating cyclic test: indoor heat exchanger outlet air temperature

3.4.3.2 Time delay to initiate the PID controller

Different time delays for the heating cyclic test were also performed. Figure 3-33 shows the air outlet temperature variations with different time delays to initiate the PID controller. It was also found that the maximum performance can be achieved when there is no delay in turning on the PID controller, which means that the PID controller was turned on as soon as the system is turned on. Therefore, there is no need for time delay in initiating the PID controller.

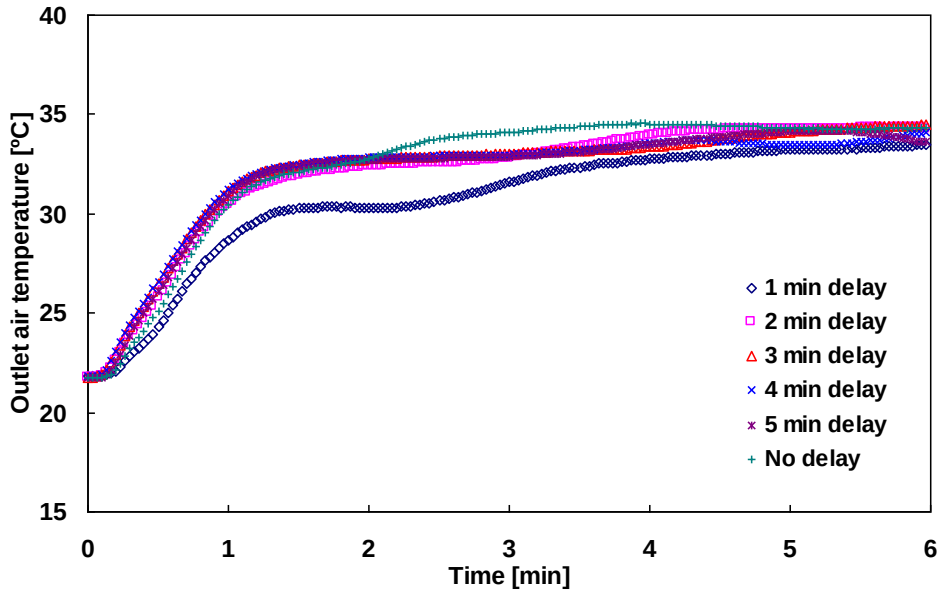

Figure 3-33: Heating cyclic test: performance variations with different time delays for PID controller

3.4.3.3 Heating cyclic test results

Figure 3-34 shows the heating cyclic test results with vapor injection "on" and "off". It can be seen that there is no visible difference in the air outlet temperature for vapor injection "on" and "off" modes, which indicates that the heating capacity with

vapor injection “on” and “off” is almost the same. Calculation shows that the improvement is only 0.6%, which is within the measurement uncertainty. However, the power consumption with vapor injection “on” is significantly higher than that with vapor injection “off”, and this yields a degradation of heating COP of 13.4%.

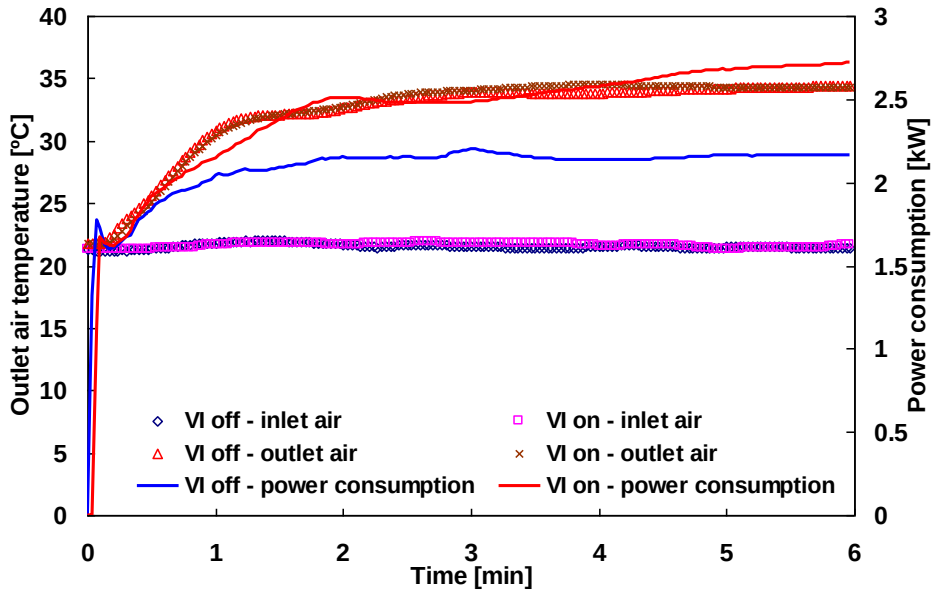

Figure 3-34: Heating cyclic test: comparison between VI “on” and VI “off”

3.4.4 Cyclic test results and discussions

From the cooling and heating cyclic tests it can be seen that PID gains are important parameters that significantly affect the system performance. P = 5.0, I = 0.5, D = 0 was found to be the most appropriate PID gains for the cooling cyclic control, and P = 10, I = 0.5 and D = 0 were most suitable PID gains for heating cyclic test. The difference in P gain value in cooling and heating tests may be due to different performance behavior of lower-stage expansion valve. Although lower-stage expansion valve for cooling and heating tests has the same nominal capacity, the manufacture

imperfection may introduce difference in its response, which further affects the PID gains for the upper-stage expansion valve. Different time delays were tried for cooling and heat cyclic tests, and it was found that the initiating the PID controller following the start of system yields the best performance. For cooling cyclic mode, a capacity improvement of 10.1% was observed, and a COP degradation of 2.4% was noticed. For heating cyclic mode, a capacity improvement of 0.6% was observed, yet a COP degradation of 13.4% was seen. However, it should be noted that the cooling and heating COPs at the cyclic conditions with vapor injection "on" are not as good as the scenarios with vapor injection "off". This is not due to the PID controller but rather due to the fact that the vapor injection technique only shows COP improvement at low ambient temperatures. At moderate ambient temperature conditions, the vapor injection can be beneficial for capacity improvement; however, the system COP is typically compromised. More detailed data on the system performance comparison between with and without vapor injection is discussed in Chapter 4.

3.5 Chapter summary and conclusions

This chapter investigates the control strategy of a flash tank vapor injection heat pump cycle experimentally. The general control strategy for a single stage cycle and two-stage cycles has been discussed. For a single stage cycle, the control strategy is relatively simple by implementing a TXV or an EEV. However, the control for a two-stage cycle flash tank cycle is much more difficult due to the complexity associated with the flash tank. Unexpected amount of liquid injection would occur if the system is controlled inappropriately, which may be detrimental to the compressor.

Several control options on a two-stage flash tank cycle have been discussed. The most cost-effective control strategy is to implement a small electric heater to the injected vapor line to introduce superheat to the injected vapor. In an actual commercialized product, this can also be achieved by exchanging heat from the compressor discharge line to the vapor injection line by utilizing a small tube-in-tube heat exchanger since the heat requirement is less than 100 W. An EEV coupled with a PID controller in data acquisition software was employed to provide accurate control of the injected vapor superheat. Through steady-state and transient cooling and heating tests, it was found that the injected vapor superheat can be effectively used as the control signal of the upper-stage expansion valve. In the steady-state test, the effect of different settings of superheat and heater power input on the system performance was also investigated. It was observed that the injection pressure and liquid level increases as the target superheat decreases, and as the electric heater power input increases. Considering the system performance and reliability of controlling the flash tank liquid level, 4 K to 6 K degrees of superheat is a recommended value. For the heating mode, 60 W heater power input is preferred to 90 W; for the cooling mode, heater power input between 60 W and 90 W is recommended.

In the transient study, different PID gains were investigated regarding their effects on the system performance, and most suitable PID gains were obtained for cooling and heating cyclic tests. Different time delays were tried for initiating the PID controller, and it was found that initiating the PID controller following the startup of the system yields the best performance, and no time delay is needed. It was also found out that the PID controller was able to provide accurate control of the EEV to reach the target superheat.

4. Performance comparison between R32 and R410A

4.1 Property comparison between R32 and R410A

Table 4-1 shows basic properties comparison of R32 and R410A. R410A is a refrigerant mixture of R32 and R125 with 50/50 wt.%. The molecular weight of R32 is 28% lower than that of R410A. Critical pressure and temperature of R32 are 850 kPa and 6.0 K higher than those of R410A, respectively. Both R410A and R32 have very similar boiling point. As discussed before, the main environmental benefit of R32 over R410A is due to the fact that R32 has a much lower GWP of 675, compared to R410A with a GWP of 2,088.

Table 4-1: Basic property comparison (EES, 2011; IPCC, 2007)

Property	Unit	R410A	R32
Composition	-	R32/R125 (50/50 wt.%)	Pure fluid
Molecular weight	g/mol	72.6	52.0
Critical pressure	MPa	4.93	5.78
Critical temperature	℃	72.1	78.1
Critical density	kg/m^3	489.0	424.1
Normal boiling point	℃	-51.5	-51.7
GWP	-	2,088	675

Table 4-2: Properties of R410A and R32 in typical condensing and evaporating conditions (EES, 2011)

Parameter	Unit	R410A		R32	
Temperature	℃	44	10	44	10
Saturated vapor pressure	kPa	2,653	1,081	2,729	1,107
Liquid density	kg/m^3	953.2	1,133	872.6	1,020
Vapor density	kg/m^3	115.6	41.9	82.4	30.2
Latent heat	kJ/kg	151.7	209.9	226.7	298.9
Liquid specific heat	kJ/(kg K)	1.89	1.57	2.25	1.80
Vapor specific heat	kJ/(kg K)	1.94	1.23	2.07	1.34
Liquid thermal conductivity	mW/(m K)	75.1	98.1	105.1	136.4
Vapor thermal conductivity	mW/(m K)	18.7	13.6	21.4	15.3
Liquid viscosity	μPa s	92.0	147.3	92.6	139.5
Vapor viscosity	μPa s	15.7	12.7	14.0	12.0
Suction specific volume @ 10 ℃	m^3/kg	-	0.0238	-	0.00331
Volumetric cooling capacity	kJ/m^3	-	8,804	-	9,039

Table 4-2 shows properties of R410A and R32 in typical condensing and evaporating conditions for air conditioning application (Tu et al., 2011). With a condensing temperature of 44 ℃ and an evaporating temperature of 10 ℃, the latent heat of R32 is 40% to 50% respectively higher than that of R410A. Moreover, the liquid thermal conductivity

of R32 is 40% higher than that of R410A at both condensing and evaporating conditions, and this would greatly enhance the heat transfer rate when using R32. However, the suction vapor density of R32 is 28% lower than that of R410A, and this leads to a decrease of the refrigerant mass flow rate. The overall effect with differences in the refrigerant density and latent heat result in an increase of 3% in the volumetric capacity comparing R32 to R410A. At the same condensing and evaporating conditions, the viscosity of R32 is typically lower than that of R410A, and together with the smaller refrigerant mass flow rate for R32, this would decrease the pressure drop across heat exchangers for R32 as well.

Figure 4-1 shows the volumetric capacity comparison of R32 and R410A at different evaporating conditions. It can be seen that both the volumetric capacities of R410A and R32 increase as the evaporating temperature increases. The rate of increase for R32 is slightly higher than that of R410A. This leads to the trend that the volumetric capacity difference between R32 and R410A becomes larger as the evaporating temperature increases. In the cooling mode, the system evaporating temperature is relatively high, and therefore, the compressor is more beneficial for R32 than for R410A. For the heating mode, the evaporating temperature decreases as the ambient temperature decreases, and as a result, there is less benefit for R32 compared to R410A.

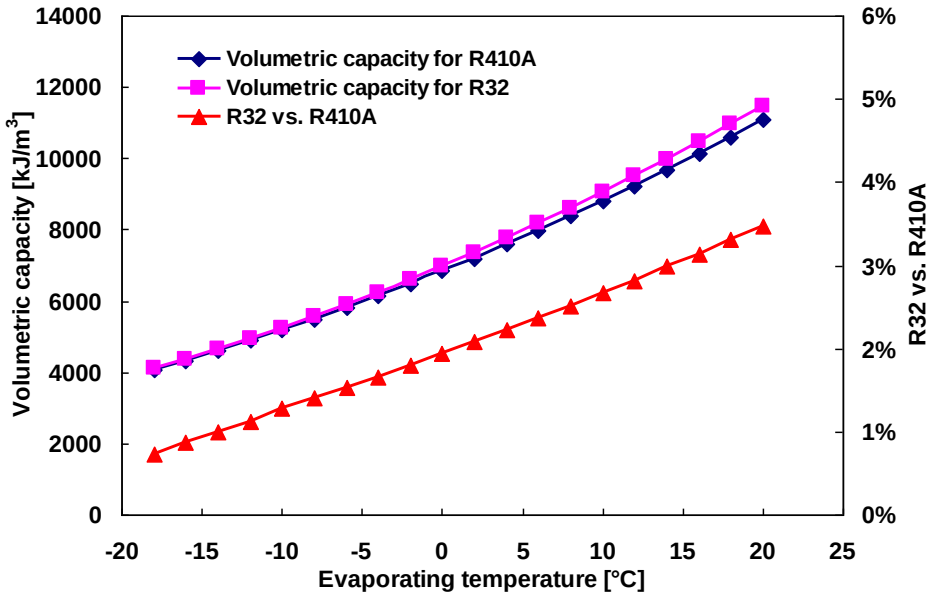

Figure 4-1: Volumetric capacity comparison of R32 and R410A at different evaporating temperatures

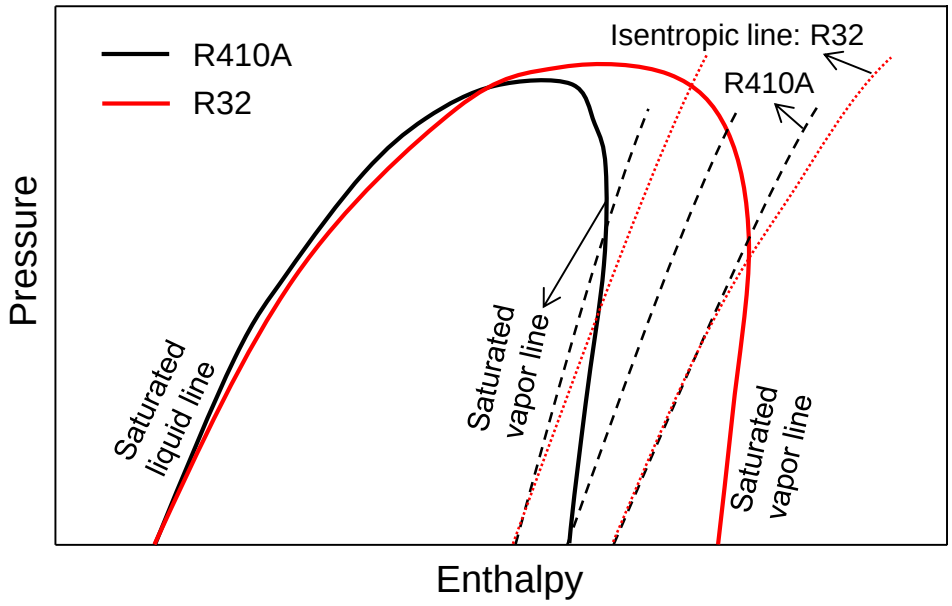

Figure 4-2: Property comparison of R32 and R410A in a P-h diagram

Figure 4-2 shows the P-h diagrams of R32 and R410A in comparison. It can be easily seen that the enthalpy difference between the saturation vapor and liquid lines of R32 is always larger than that of R410A, and therefore, the latent heat of R32 is higher than that of R410A. The slope of isentropic lines of R32 is also lower than that of R410A, and therefore, the compressor power consumption per unit mass flow rate of R32 is typically higher than that of R410A in an identical pressure lift condition.

4.2 Refrigerant charge optimization tests

4.2.1 Charge optimization test for R410A

The main purpose of charge optimization test is to identify the optimum charge amount so that the system can achieve optimum performance. ASHRAE High Temp 2 condition with an ambient temperature of 8 ℃ was selected as the charge optimization test condition (ASHRAE Standard 116, 2010). The vapor injection control valve was closed during the refrigerant charge optimization test, and the upper-stage expansion valve was also fully open to keep the system as a conventional single stage cycle. Indoor air volume flow rate was maintained at a constant value of 0.58 m^3/s according to the manufacturer's specifications.

Figure 4-3 shows the compressor suction superheat variations during the charge optimization test. It can be seen that constant degree of superheat of 8 K is maintained. Figure 4-4 shows the COP variation of the refrigeration charge optimization for heating mode. It can be seen that maximum COP is observed with 6.9 kg of refrigerant charge. Figure 4-5 shows the condenser outlet subcooling. The trend shows that the degree of subcooling increases constantly with the increasing refrigerant charge. With 6.9 kg of

refrigerant charge, the subcooling is less than 1 K. Therefore, to ensure sufficient subcooling at the condenser outlet, 7.0 kg was selected as the optimum charge for the heating mode for R410A. For the cooling mode tests performed following the heating mode tests, it was found that 7.0 kg was not sufficient. This is due to the fact that the outdoor heat exchanger is larger than the indoor heat exchanger. In the cooling mode, the outdoor heat exchanger functions as the condenser, and thus requires more refrigerant charge. Therefore, the refrigerant charge was slightly adjusted to 7.5 kg for the cooling mode for R410A.

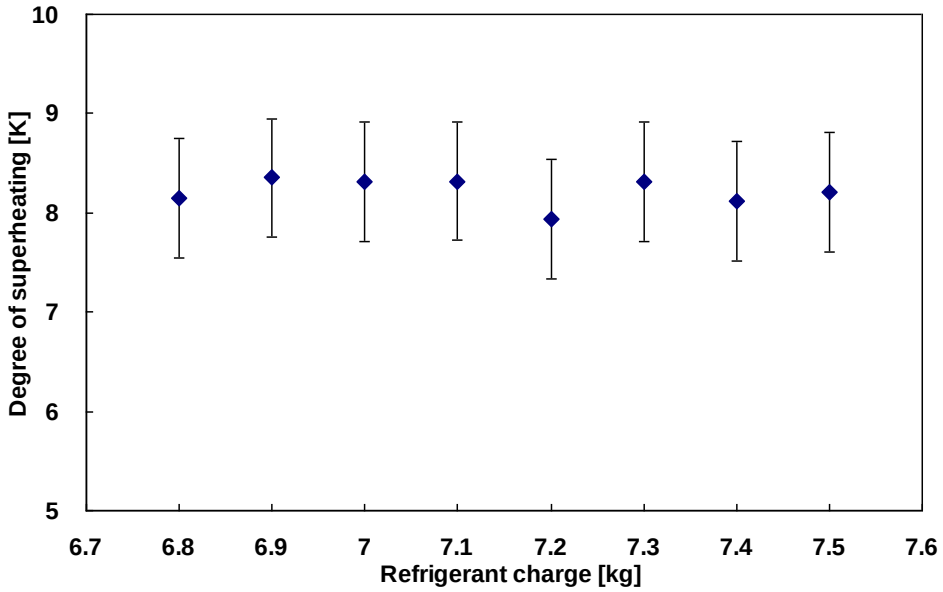

Figure 4-3: Compressor suction superheating variations during the charge optimization test for R410A

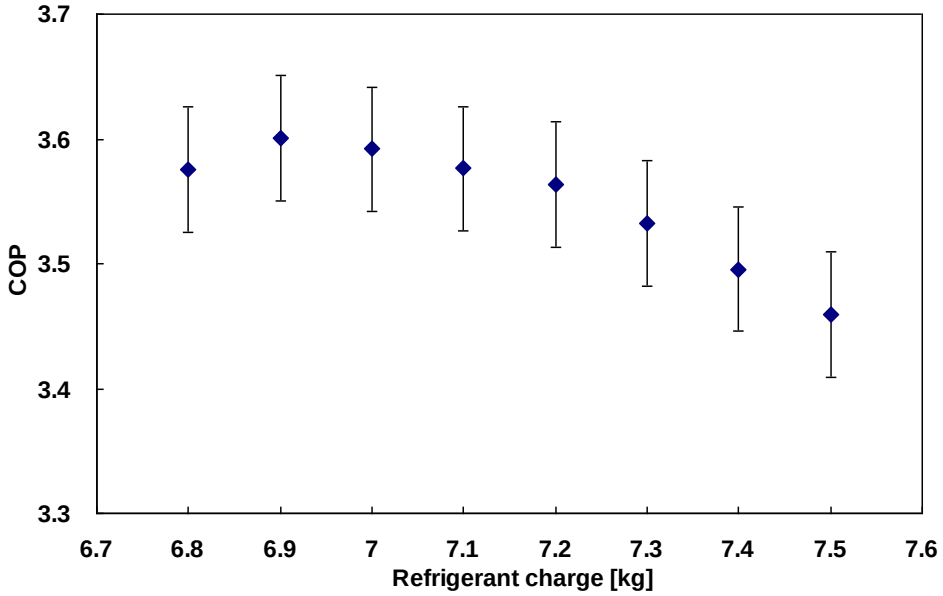

Figure 4-4: System COP variations during the charge optimization test for R410A

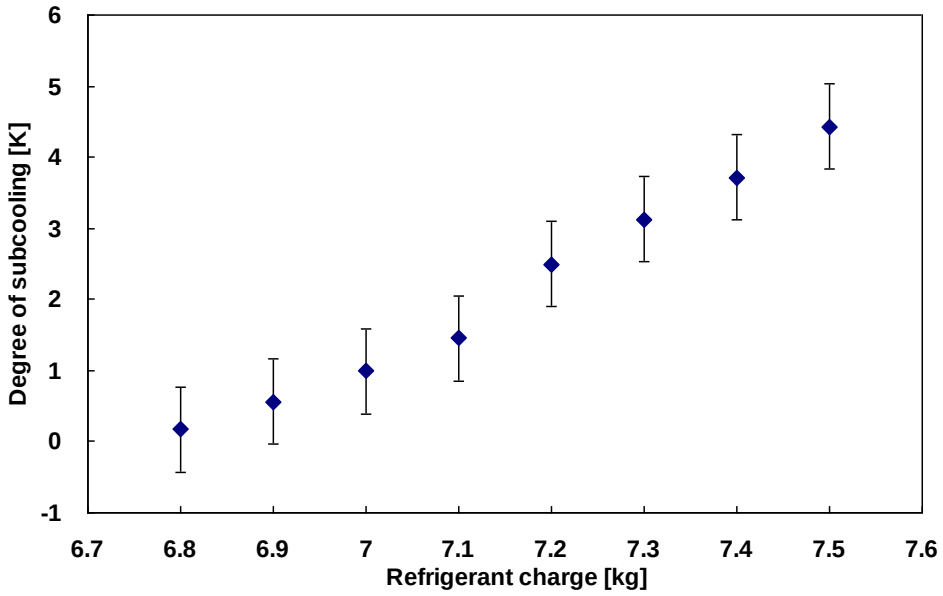

Figure 4-5: Degree of subcooling variations during the charge optimization test for R410A

4.2.2 Charge optimization test for R32

Heating charge optimization test was conducted for R32 at ASHRAE Standard High Temperature 2 condition (ASHRAE Standard 116, 2010), which has an ambient temperature of 8ºC. Moreover, a cooling charge optimization test was also conducted for R32. The cooling charge optimization test was conducted at ASHRAE Standard A condition, which has an ambient temperature of 35ºC. The vapor injection valve was turned off during the charge optimization test. Figure 4-6 shows the COP variations with different refrigerant charge amount for both cooling and heating modes. It can be seen that the optimum COP is observed when the charge amount is 5.0 kg. It's also interesting to see that the system COP is nearly the same as the refrigerant charge is between 4.5 kg and 6.5 kg. The main reason is that the flash tank in the system works as a liquid receiver when the vapor injection is turned off, and the refrigerant is just filling up the flash tank as charge increases from 4.5 kg to 6.5 kg. Figure 4-7 shows the capacity variations with different refrigerant charges. It can be seen that with 5.0 kg, capacity is also close to an optimum value.

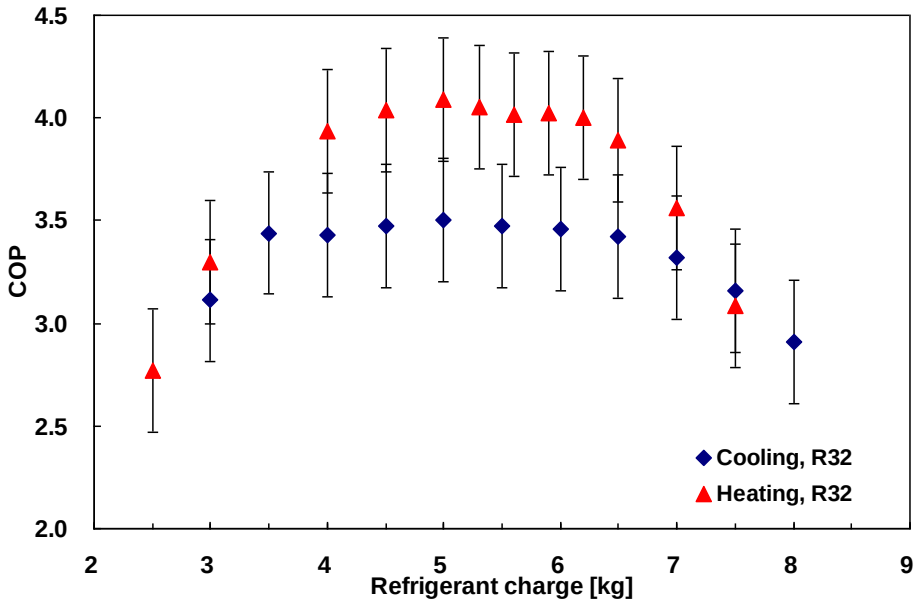

Figure 4-6: COP variations with different refrigerant charge for R32

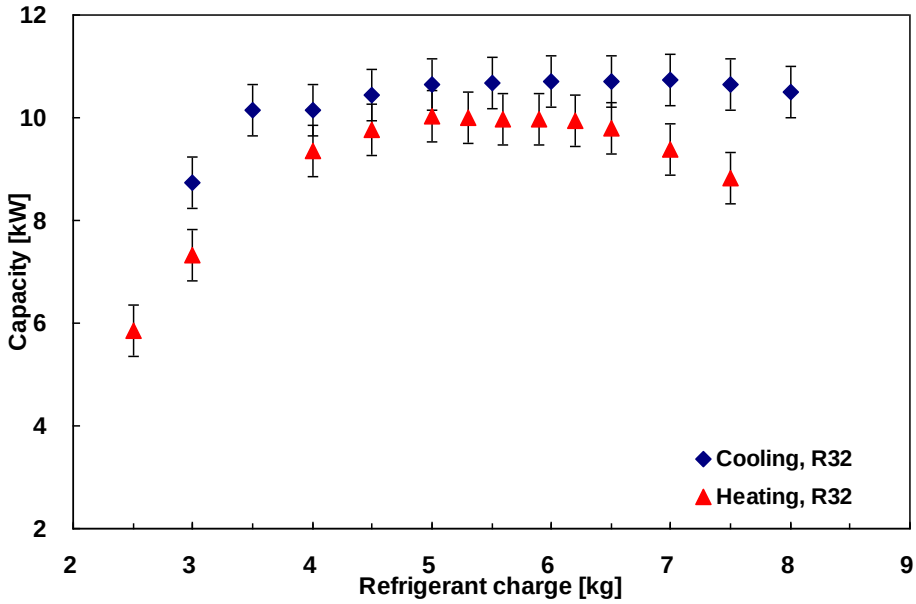

Figure 4-7: Capacity variations with different refrigerant charge for R32

Figure 4-8 shows the compressor suction superheating variations with different refrigerant charge amounts. When the refrigerant charge is below 4.0 kg, the superheating

couldn’t be maintained to be a constant value between 7 K and 8 K. This indicates that the system is significantly undercharged with less than 4.0g kg refrigerant charge. As the refrigerant charge increases, the superheating can be always maintained to be a constant value between 7 K and 8 K. Figure 4-9 shows the condenser outlet subcooling variations with different refrigerant charge. The degree of subcooling is observed to be close to 0 K when refrigerant charge is less than 4.0 kg. With 5.0 kg charge, the subcooling is observed to be 1 K or so. There is a rapid increase of subcooling as the refrigerant charge amount is over 6.5 kg.

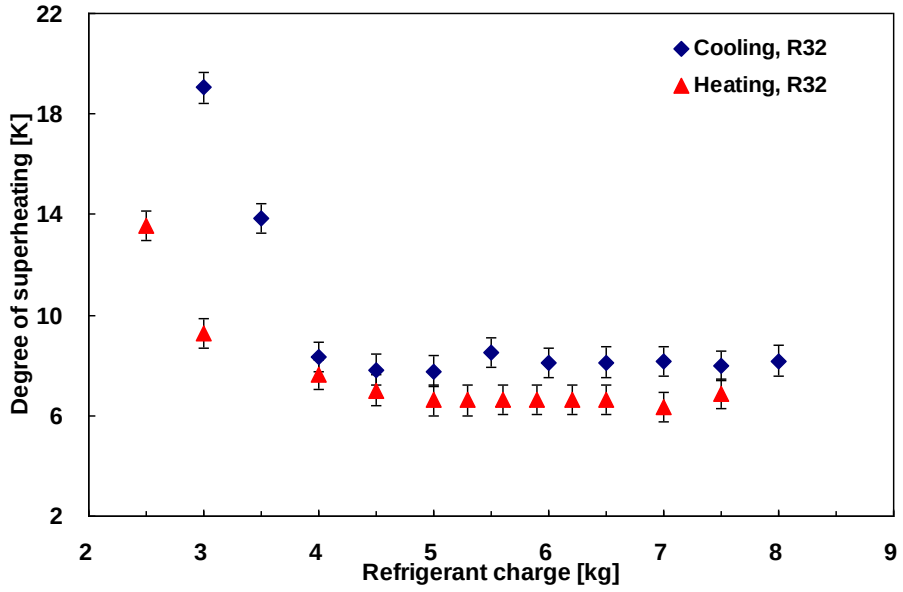

Figure 4-8: Superheating variations with different refrigerant charge for R32

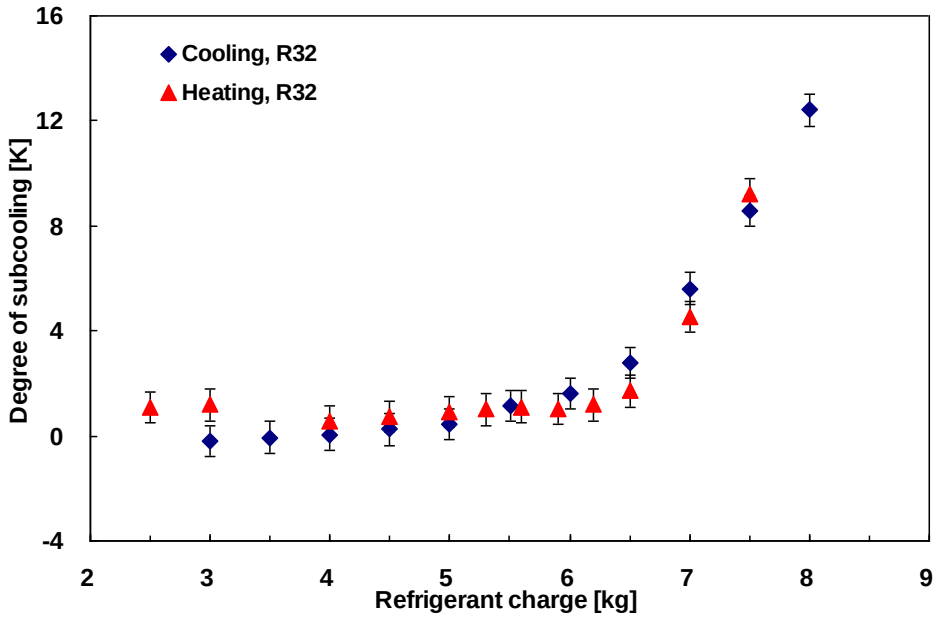

Figure 4-9: Subcooling variations with different refrigerant charge for R32

It should be noted that the refrigerant charge effect for a two-stage vapor injection cycle is differently from a conventional single stage cycle. Figure 4-10 shows a single stage and a two-stage cycle in P-h diagrams. For a single stage cycle, the condenser outlet subcooling increases as the refrigerant charge increases. As can be seen from the P-h diagram, the condenser outlet state is shifted from "1" to "1'" as the refrigerant charge increases. This leads to larger enthalpy difference across the evaporator, and therefore, increases the system cooling capacity. However, the effect of refrigerant charge is different for a two-stage vapor injection cycle. As seen from the P-h diagram for the two-stage cycle, the condenser outlet state is shifted from "1" to "1'" as the refrigerant charge increases. The upper-stage expansion process is, therefore, shifted from "1–2" to "1'–2'". This indicates that the vapor quality after the upper-stage expansion is decreased, and the vapor refrigerant available to be injected to the compressor also becomes less. Thus,

more liquid is present after the upper-stage expansion, and this also poses the issue to increasing liquid level inside of the flash tank. Consequently, a two-stage vapor injection flash tank cycle prefers the charge that minimizes the subcooling at the condenser outlet.

In summary, the optimum refrigerant charge amount for R32 was determined to be 5.0 kg. For R410A, 7.0 kg was selected for the optimum charge amount for the heating mode, and 7.5 kg was selected for the cooling mode.

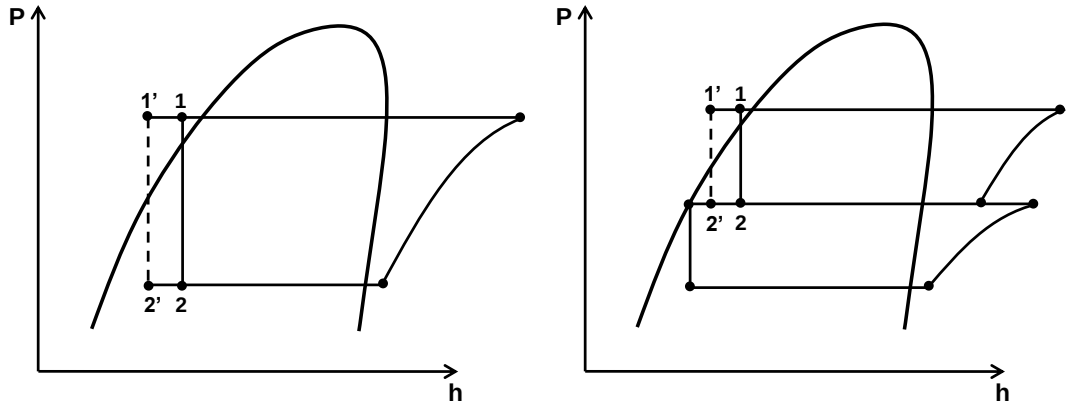

Figure 4-10: Refrigerant charge analysis for a single stage cycle and a two-stage cycle

4.3 Performance comparison between R32 and R410A without vapor injection

The purpose of this experimental study is to investigate the performance difference between R32 and R410A in both with and without vapor injection. The heat pump system used to perform the experiments is originally designed for R410A. Drop-in test was performed with R32 without any system modifications.

First, experimental tests were conducted without vapor injection. In such a case the heat pump system works as a conventional single stage vapor compression cycle.

Figure 4-11 to Figure 4-13 show the comparison between R32 and R410A at different operating conditions without vapor injection. As seen from Figure 4-11, the dotted line divides the ambient temperatures into heating mode and cooling mode results on the left and right, respectively. Comparing R32 to R410A without vapor injection, the capacity and COP improvements are observed to be 3% to 10% and 2% to 9%, respectively. The maximum improvement is observed at the cooling condition of 46 ℃. However, it is noticed that there is no improvement at the ambient temperature condition of -18 ℃. The power consumption using R32 is observed to be 1% to 5% higher than that of R410A. Figure 4-12 shows the refrigerant mass flow rate comparison between R32 and R410A at different ambient temperatures. R32 shows a lower mass flow rate compared to R410A, and this is due to the density difference at the compressor suction port. The mass flow rate difference is observed to be -31% to -28%, and the biggest difference is noticed at the ambient temperature of -18 ℃. Figure 4-13 shows the compressor discharge temperature comparison between R32 and R410A. The discharge temperatures using R32 are significantly higher than those of R410A. The difference is quite remarkable at the ambient temperature of -18 ℃, at which an increase of 34 K is observed. This also brings up a challenge regarding the compressor design when switching from R410A to R32. In this case compressor cooling can be an effective approach. Detailed analysis for the compressor cooling is shown in Chapter 7.

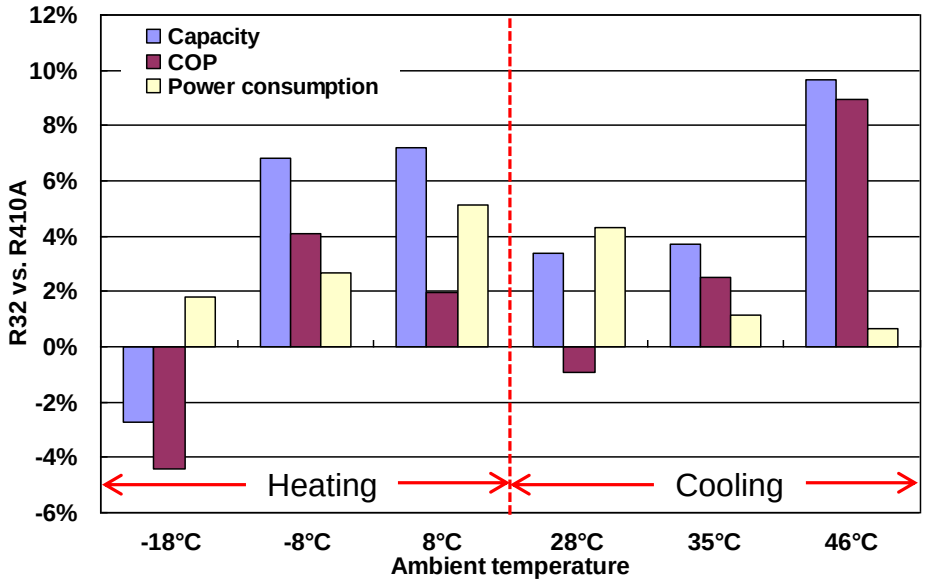

Figure 4-11: Comparison of capacity, COP and power consumption between R32 and R410A in a non-injection system, using R410A as the baseline

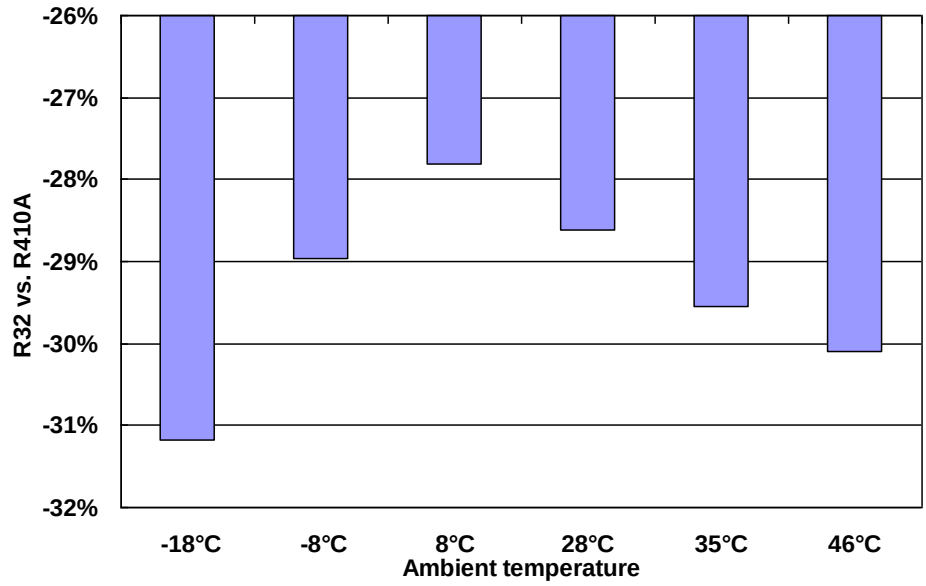

Figure 4-12: Comparison of refrigerant mass flow rate between R32 and R410A in a non-injection system, using R410A as the baseline

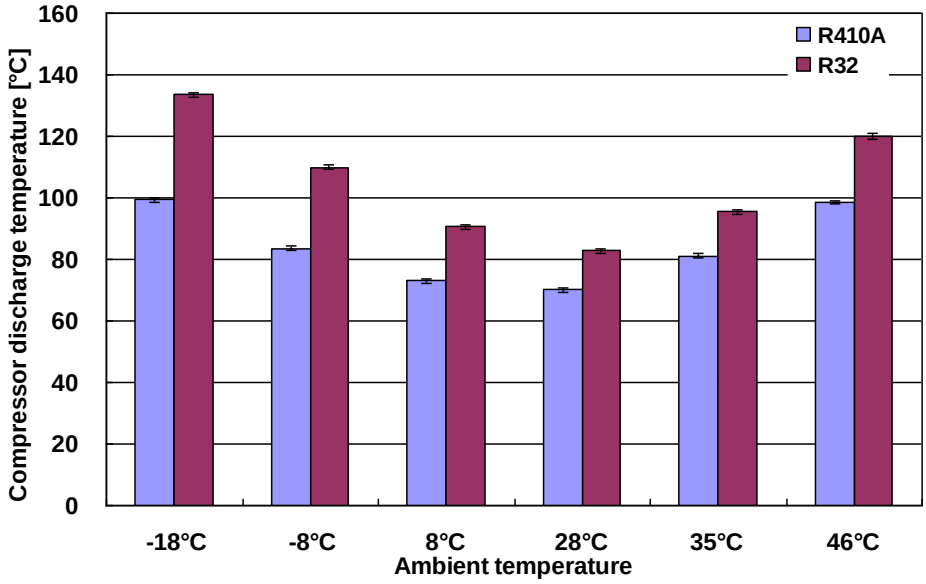

Figure 4-13: Comparison of compressor discharge temperature between R32 and R410A in a non-injection system

The compressor isentropic and volumetric efficiencies are calculated in Equation 4-1 and Equation 4-2, respectively. The compressor isentropic efficiency is defined as the enthalpy difference when the compression process is isentropic divided by the actual enthalpy difference. The compression process is shown in Figure 4-14. The compressor volumetric efficiency is defined as the actual refrigerant mass flow rate divided by the theoretical refrigerant mass flow rate.

$$\eta_{ise} = \frac{h_{2s} - h_1}{h_2 - h_1}$$ **Equation 4-1**

$$\eta_{vol} = \frac{MFR}{\rho_1 V \frac{RPM}{60}}$$ **Equation 4-2**

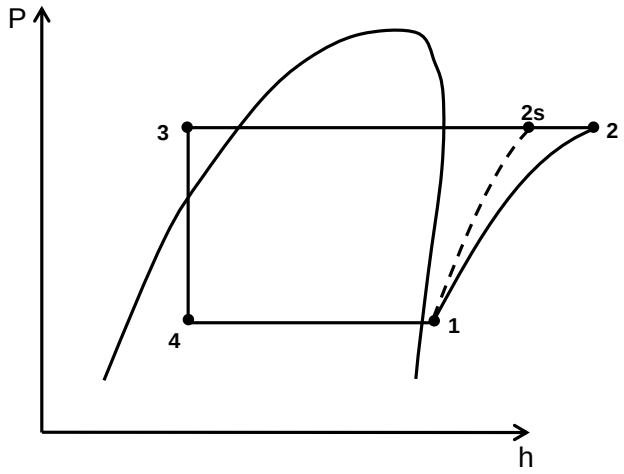

Figure 4-14: Single stage cycle in a P-h diagram

Figure 4-15 summarizes the isentropic and volumetric efficiencies comparison for R32 and R410A in a single stage cycle without vapor injection. It can be seen that the isentropic efficiency for R32 and R410A are almost the same for all ambient temperature conditions. The volumetric efficiency of R32 was slightly lower than that of R410A. This is mainly due to the fact that the compressor is designed for R410A, and therefore it cannot reach optimum performance when drop-in test is conducted using R32. It was calculated in the property comparison that the volumetric capacities of R410A and R32 are different depending on the evaporating temperature, which indicates that the current compressor tested in the system may be inappropriately sized for R32.

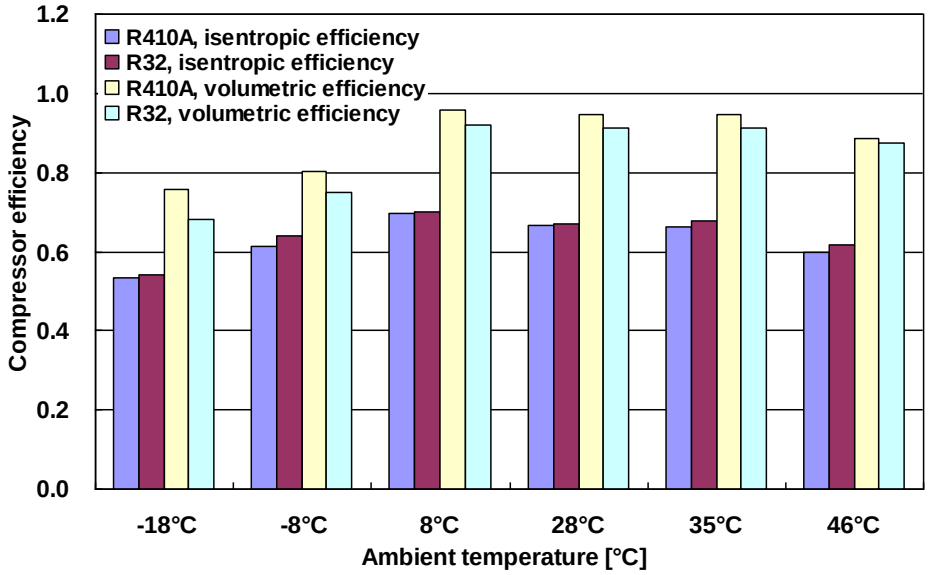

Figure 4-15: Isentropic and volumetric efficiencies comparison for R32 and R410A in a non-injection system

Figure 4-16 shows the cycle comparison of R32 and R410A at extreme cooling and heating conditions in a P-h diagram. It can be seen that the enthalpy difference between saturated liquid and vapor lines of R32 are much larger than that of R410A. As the ambient temperature decreases, the pressure difference between the high side and low side also becomes larger. This increases the power consumption, and decreases the system COP. It can also be seen that the condensing and evaporating temperatures of R32 and R410A at the same ambient temperature conditions are quite close to each other.

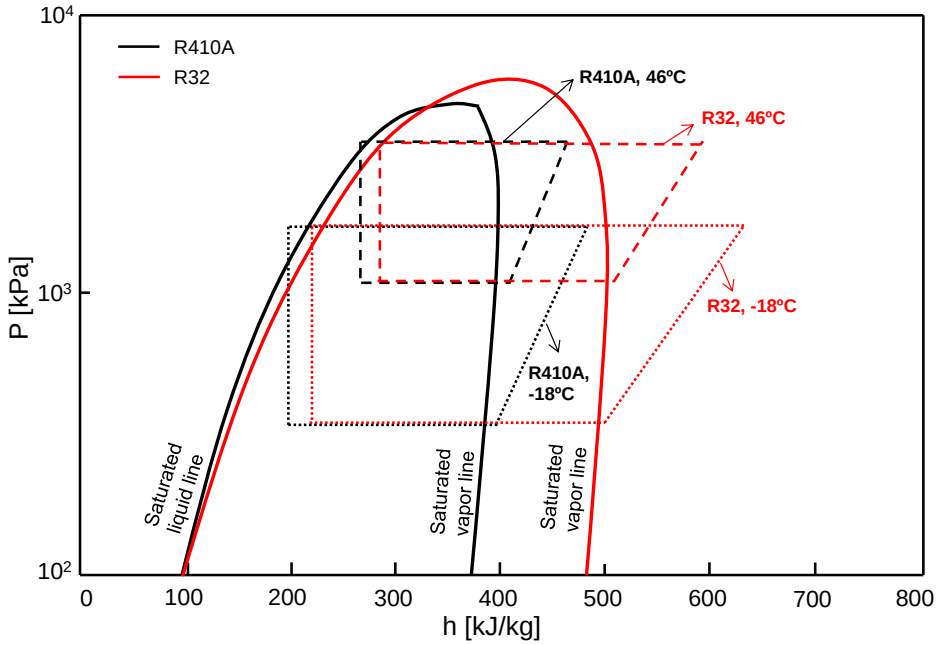

Figure 4-16: Single stage cycle comparison between R32 and R410A at two extreme ambient temperature conditions in a P-h diagram

4.4 Performance comparison between R32 and R410A with vapor injection

4.4.1 Performance comparison at different injection ratios

Experimental tests with vapor injection were also conducted. In this operation mode the heat pump system works as a two-stage cycle. During the experiments the upper-stage expansion valve was controlled to vary the injection pressure, which resulted in different injection ratios. The vapor injection system performance was compared with non-injection performance to investigate the system performance improvement at different injection ratios. In this case, the baseline performance is from a non-injected single stage cycle. Figure 4-17 and Figure 4-18 show the vapor injection capacity improvement for R32 and R410A in heating and cooling modes, respectively. In the

heating mode as shown in Figure 4-17, the capacity improvement is observed to be significant. The maximum capacity improvement is observed at the lowest ambient temperature of -18℃, and the corresponding capacity improvements for R410A and R32 are observed to be 33% and 25%, respectively. It should be noted that the maximum injection ratio is limited by the amount of vapor available in the flash tank, and also limited by the liquid level in the flash tank. Increasing the opening of the upper-stage expansion valve leads to a higher injection pressure, and therefore, increases the injection ratio. However, the liquid level in the flash tank is also increased as the upper-stage expansion valve's opening increases. From the same figure it can also be observed that the capacity improvement increases with the injection ratio. At the ambient temperature of -8℃, the performance increase is not as obvious as the other two ambient temperature conditions. This is mainly due to the fact that the frost accumulation on the outdoor coil is more severe at -8℃ ambient compared to other operating conditions. Figure 4-18 shows the capacity comparison between R32 and R410A for the cooling mode. The maximum capacity improvement for R410A is observed to be 18%, and the maximum improvement for R32 is only 4%. As the injection ratio increases, the improvement remains almost the same. The main reason is that vapor injection have larger impact on the condenser than on the evaporator, and therefore the benefits in heating mode is more than in cooling mode. Moreover, a compressor designed for R410A is not well suited for R32, and therefore it results in lower improvements for R32.

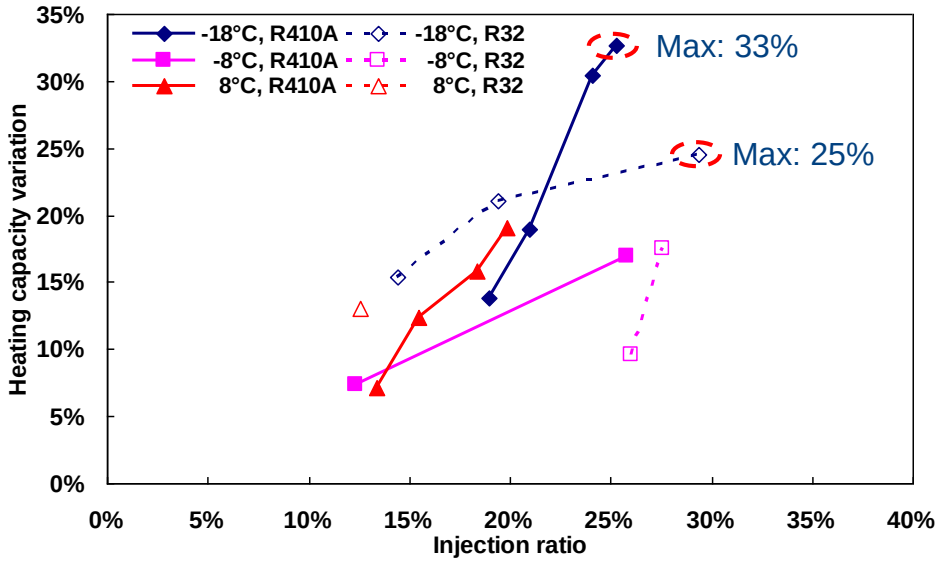

Figure 4-17: Vapor injection heating capacity improvement for R32 and R410A, compared to non-injection systems as the baseline

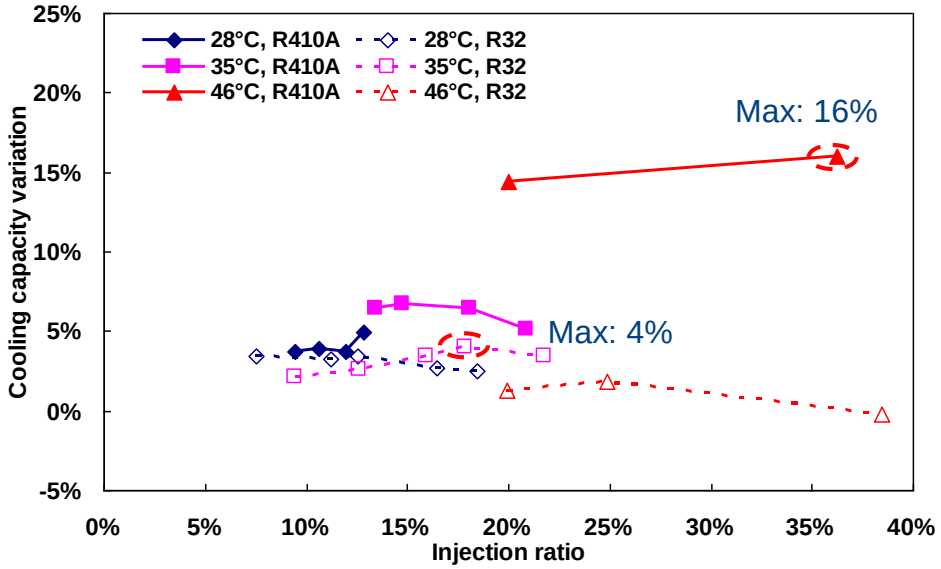

Figure 4-18: Vapor injection cooling capacity improvement for R32 and R410A, compared to non-injection systems as the baseline

Figure 4-19 and Figure 4-20 show the COP improvement for R32 and R410A in heating and cooling modes, respectively. In the heating mode as shown in Figure 4-19, the COP improvement increases as the injection ratio. The maximum COP improvement for R410A and R32 is observed to be 18% and 11%, respectively at the ambient temperature of -18℃. Figure 4-20 shows the cooling COP variations. As the injection ratio increases, the COP even decreases rapidly, and this is quite obvious for R32. Therefore, vapor injection is more beneficial for the heating application compared to the cooling application.

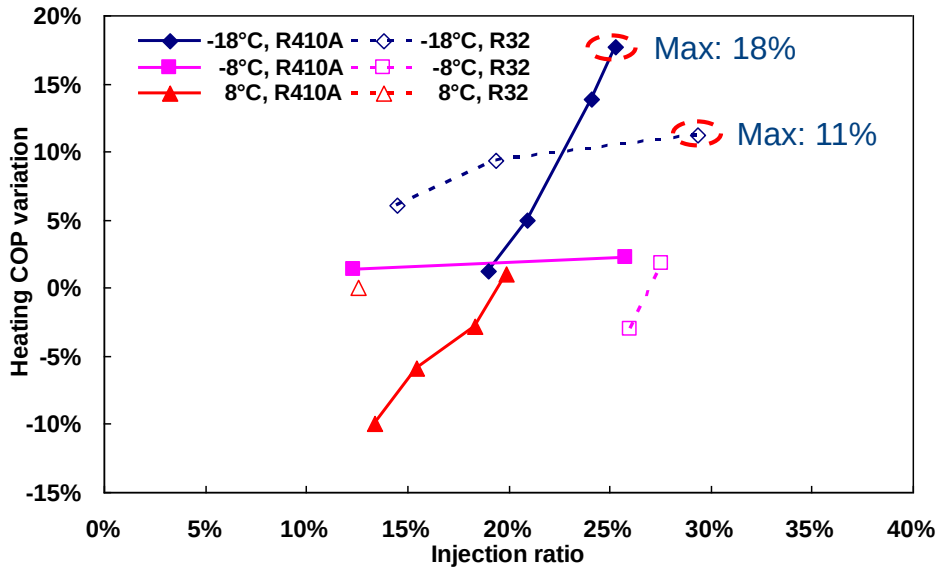

Figure 4-19: Vapor injection heating COP improvement for R32 and R410A, compared to non-injection systems as the baseline

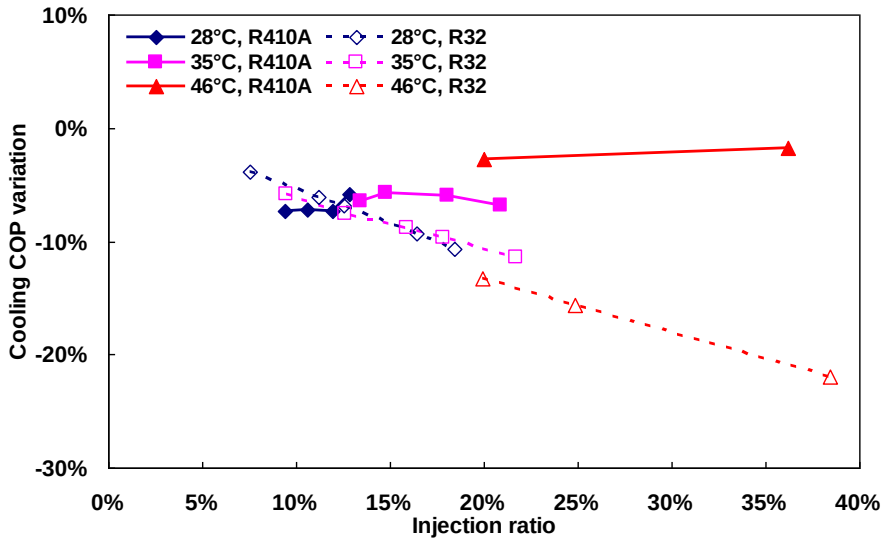

Figure 4-20: Vapor injection cooling COP improvement for R32 and R410A, compared to non-injection systems as the baseline

Figure 4-21 and Figure 4-22 show the total system power consumption variation comparison in heating and cooling modes, respectively. Typically the injection ratio increases the power consumption, because the increasing injection ratios means that the compressor needs to compress more refrigerant. However, it can be seen that the power consumption increase for R32 in the cooling mode shown in Figure 4-22 is much more remarkable than for the heating mode, as compared to the results of R410A. The main reason is that the compressor motor efficiency for the cooling mode is lower than for the heating mode, because the compressor loads at the cooling mode are much higher than those at the heating mode. The dramatic increase of compressor power consumption explains the reason of the quick COP degradation in Figure 4-20 as the injection ratio increases.

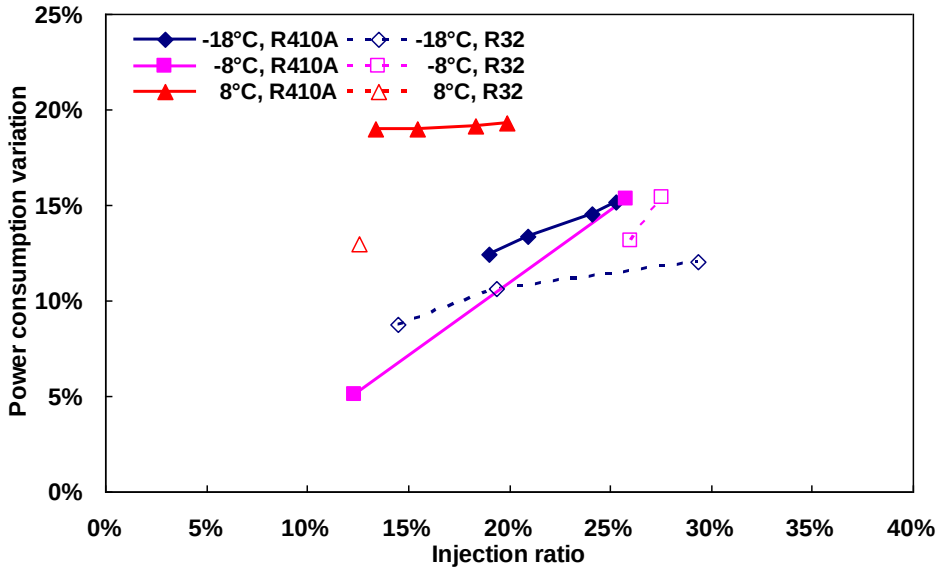

Figure 4-21: Vapor injection system power consumption in heating mode for R32 and R410A, compared to non-injection systems as the baseline

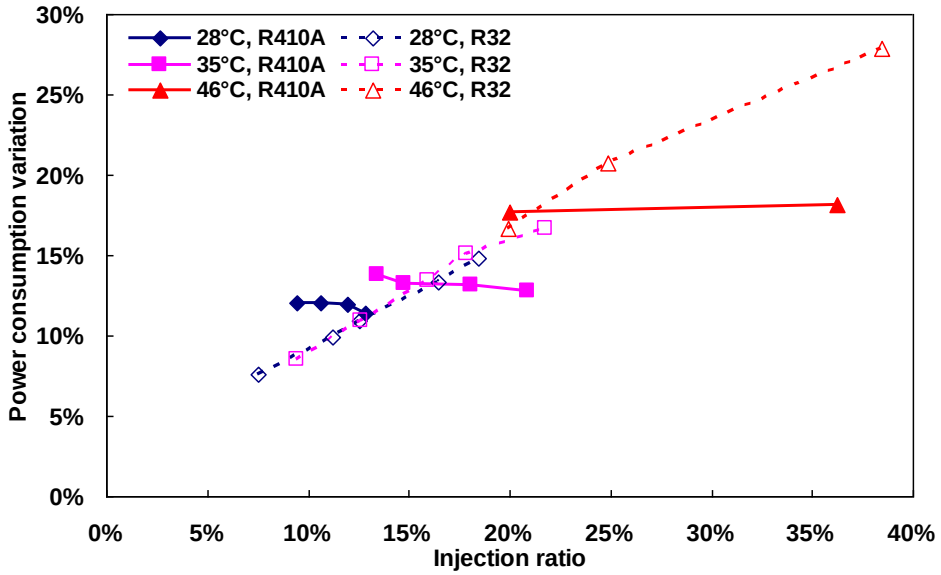

Figure 4-22: Vapor injection system power consumption in cooling mode for R32 and R410A, compared to non-injection systems as the baseline

Figure 4-23 and Figure 4-24 show the injection pressure comparison between R32 and R410A in heating and cooling modes, respectively. It should be noted that the Y-axis of these two figures is showing absolute values, and is not expressed in percentage compared to the baseline results of non-injection systems, as shown in the previous few figures. Typically the injection pressure increases with the increasing injection ratio. The injection pressure is directly affected by the upper-stage expansion valve. As the upper-stage expansion valve's opening increases, the injection pressure increases. Therefore, more vapor refrigerant is injected to the compressor, which increases the injection ratio.

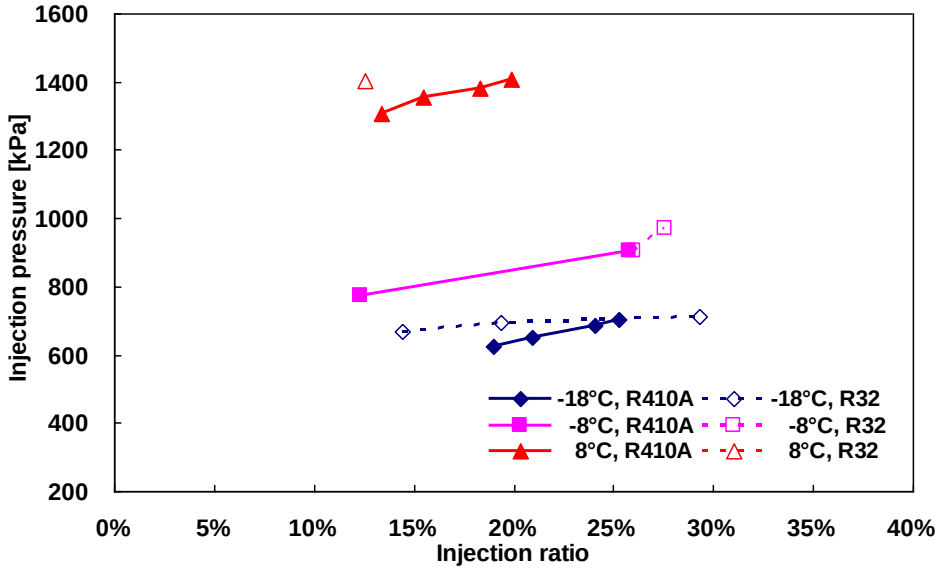

Figure 4-23: Injection pressure comparison between R32 and R410A in heating mode

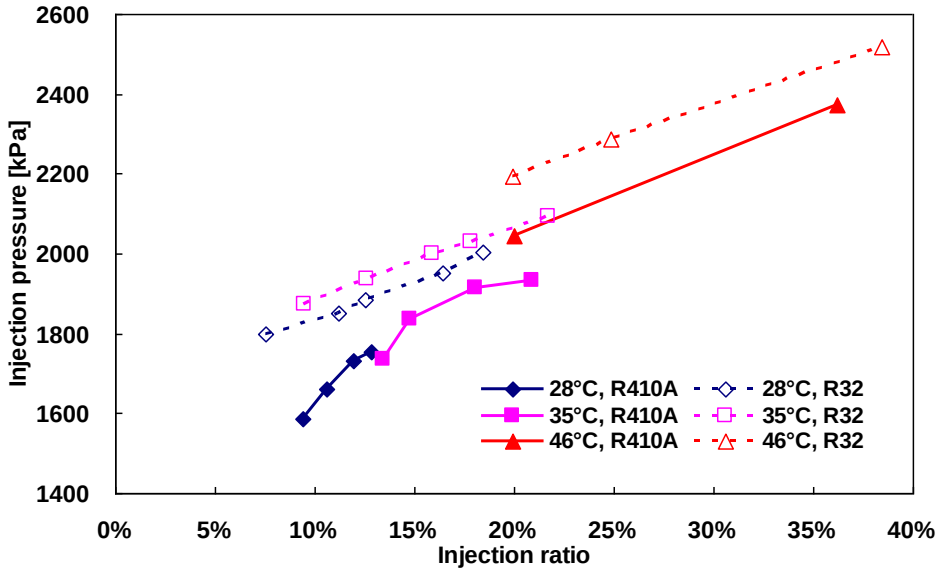

Figure 4-24: Injection pressure comparison between R32 and R410A in cooling mode

Figure 4-25 and Figure 4-26 show the compressor discharge temperature comparison between R32 and R410A in heating and cooling modes, respectively. It should also be noted that the Y-axis is showing absolute values, instead of showing the difference as compared to the baseline non-injection results. For both the heating and cooling modes, the compressor discharge temperatures of R32 are much higher than the results of R410A. The compressor discharge temperature also decreases with the increasing injection ratios. Increasing injection ratio means that more refrigerant is injected to the compressor to provide better compressor cooling, and therefore decreases the compressor discharge temperature.

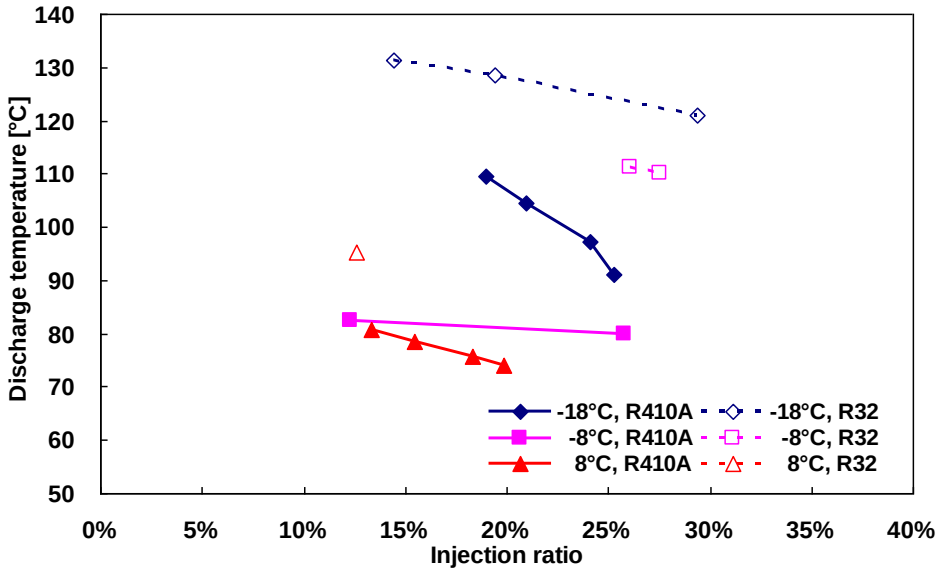

Figure 4-25: Vapor injection compressor discharge temperature comparison between R32 and R410A in heating mode

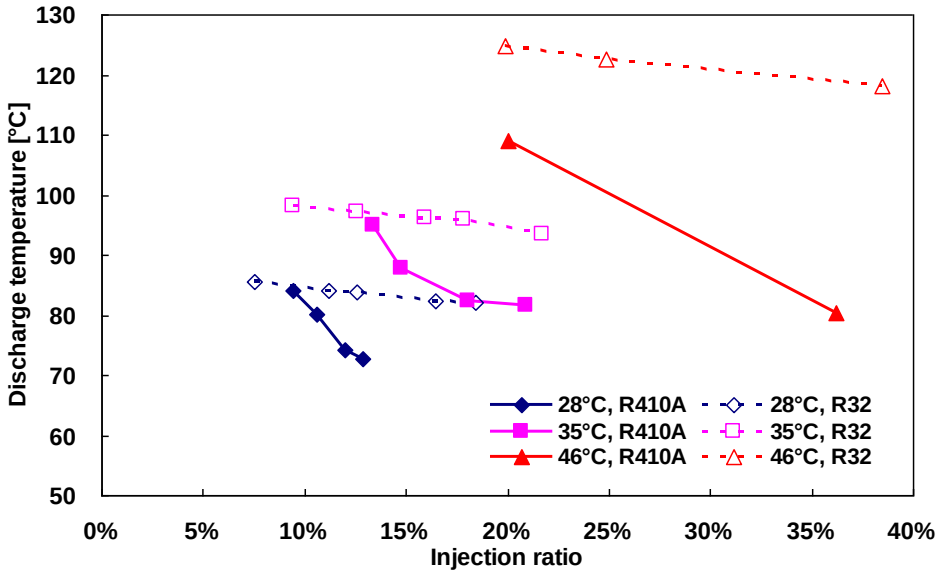

Figure 4-26: Vapor injection compressor discharge temperature comparison between R32 and R410A in cooling mode

4.4.2 Performance comparison at the same injection ratio

To better understand the vapor injection benefits for R32 and R410A, the system performance with the same injection ratio was compared. The injection ratio is selected from the experimental results that show closest match of the injection ratios of R32 and R410A. In such a case the R410A performance with vapor injection was used as the baseline. Figure 4-27 to Figure 4-29 show the performance comparison between R32 and R410A with vapor injection. As seen from Figure 4-27, the capacity improvement comparing R32 to R410A is observed to be 2% to 7%, and COP improvement is observed to be 1% to 6%. However, there is no improvement at the extreme heating condition of -18℃ and extreme cooling condition of 46℃. At the extreme heating condition, the capacity and COP degradation is observed to be 11% and 11%, respectively. At the extreme cooling condition, the capacity and COP degradation is observed to be 3% and 4%, respectively. The power consumption increase is observed to be 2% to 3%. Figure 4-28 shows the total refrigerant mass flow rate comparison. It can be seen that the refrigerant mass flow reduction at the extreme conditions is quite significant. -41% is observed at the extreme heating condition, and -37% is observed at the extreme cooling conditions. As seen from Figure 4-29, the compressor discharge temperatures using R32 are significantly higher than those of R410A. A maximum discharge temperature increase of 39 K is noticed at the extreme heating condition of -18℃.

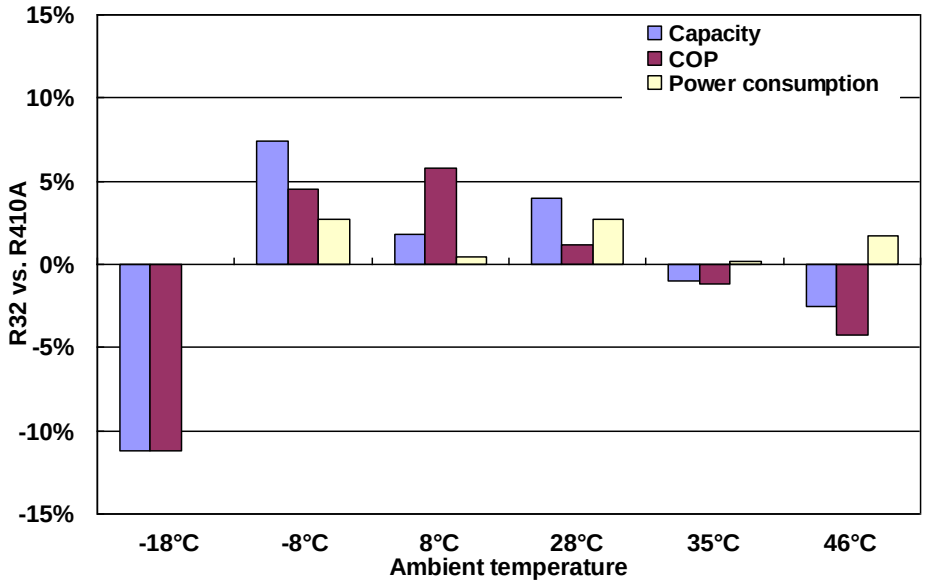

Figure 4-27: Comparison of capacity, COP and power consumption between R32 and R410A in a vapor injection system, baseline is R410A with vapor injection

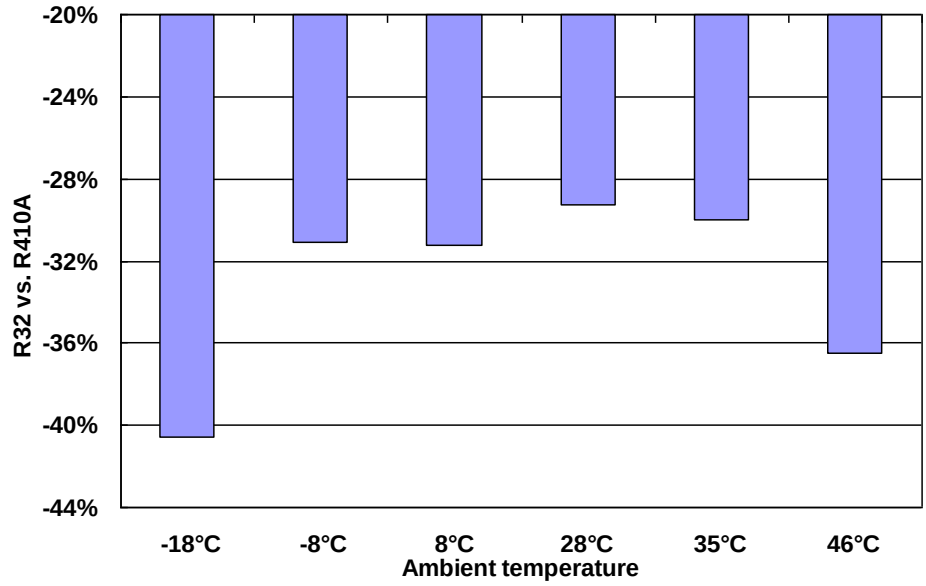

Figure 4-28: Comparison of total refrigerant mass flow rate between R32 and R410A in a vapor injection system, baseline is R410A with vapor injection

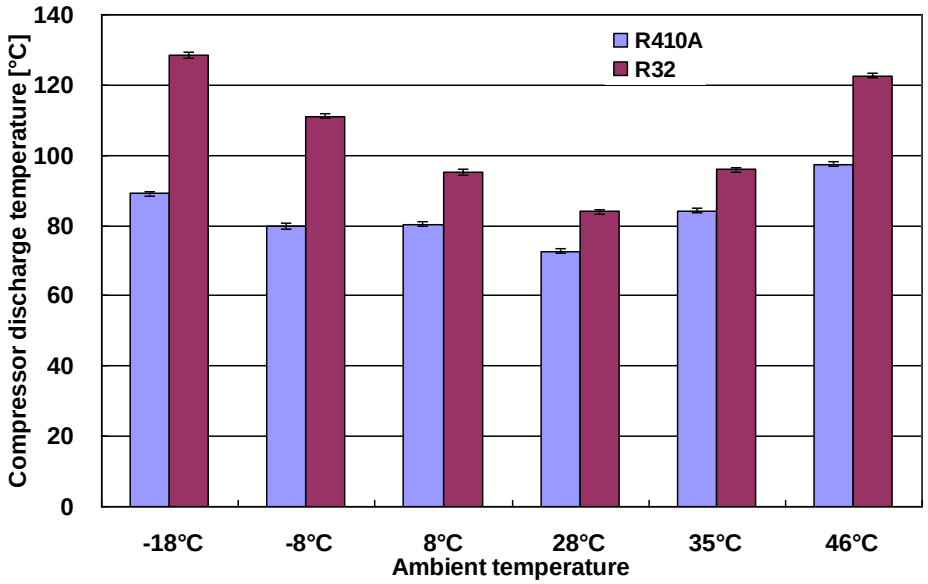

Figure 4-29: Comparison of compressor discharge temperature between R32 and R410A in a vapor injection system

The compressor isentropic and volumetric efficiencies are defined for the low and high stages in a similar manner as in a single stage cycle. Equation 4-3 to Equation 4-6 shows the definitions of these efficiencies. The schematic of the two-stage compression is shown in Figure 4-30.

$$\eta_{ise,low} = \frac{h_{3s} - h_1}{h_3 - h_1} \qquad \textbf{Equation 4-3}$$

$$\eta_{vol,low} = \frac{MFR_{suc}}{\rho_1 V \frac{RPM}{60}} \qquad \textbf{Equation 4-4}$$

$$\eta_{ise,high} = \frac{h_{2s} - h_5}{h_2 - h_5} \qquad \textbf{Equation 4-5}$$

$$\eta_{vol,high} = \frac{MFR_{total}}{\rho_5 V_2 \frac{RPM}{60}}$$ **Equation 4-6**

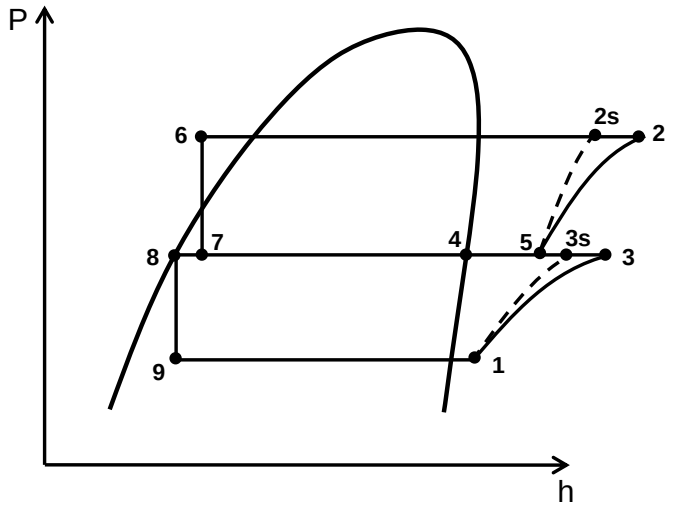

Figure 4-30: Two-stage compressor efficiencies defined in a P-h diagram

Essentially the main reason for the decrease of capacity and COP at extreme ambient conditions is due to the reduction of refrigerant mass flow rate. Through the thermophysical property comparison between R32 and R410A it's known that the density difference between R32 and R410A is around 28%, and therefore the ideal mass flow rate difference should be close to 28%. However, the refrigerant mass flow rate difference was much larger than 28% for extreme cooling and heating conditions. This indicates that the compressor underperformed when R32 was used in these conditions.

Figure 4-31 summarizes the comparison of low-stage and high-stage isentropic and volumetric efficiencies for R32 and R410A in a two-stage cycle with vapor injection. It can be seen that at the ambient temperature of 46℃ and -18℃, the isentropic

efficiencies remain almost the same, yet the volumetric efficiencies of R32 were significantly lower than those of R410A. This explains the significant refrigerant mass flow rate decrease in these conditions, as seen in Figure 4-28. The volumetric and isentropic efficiencies remain almost the same for other temperature conditions.

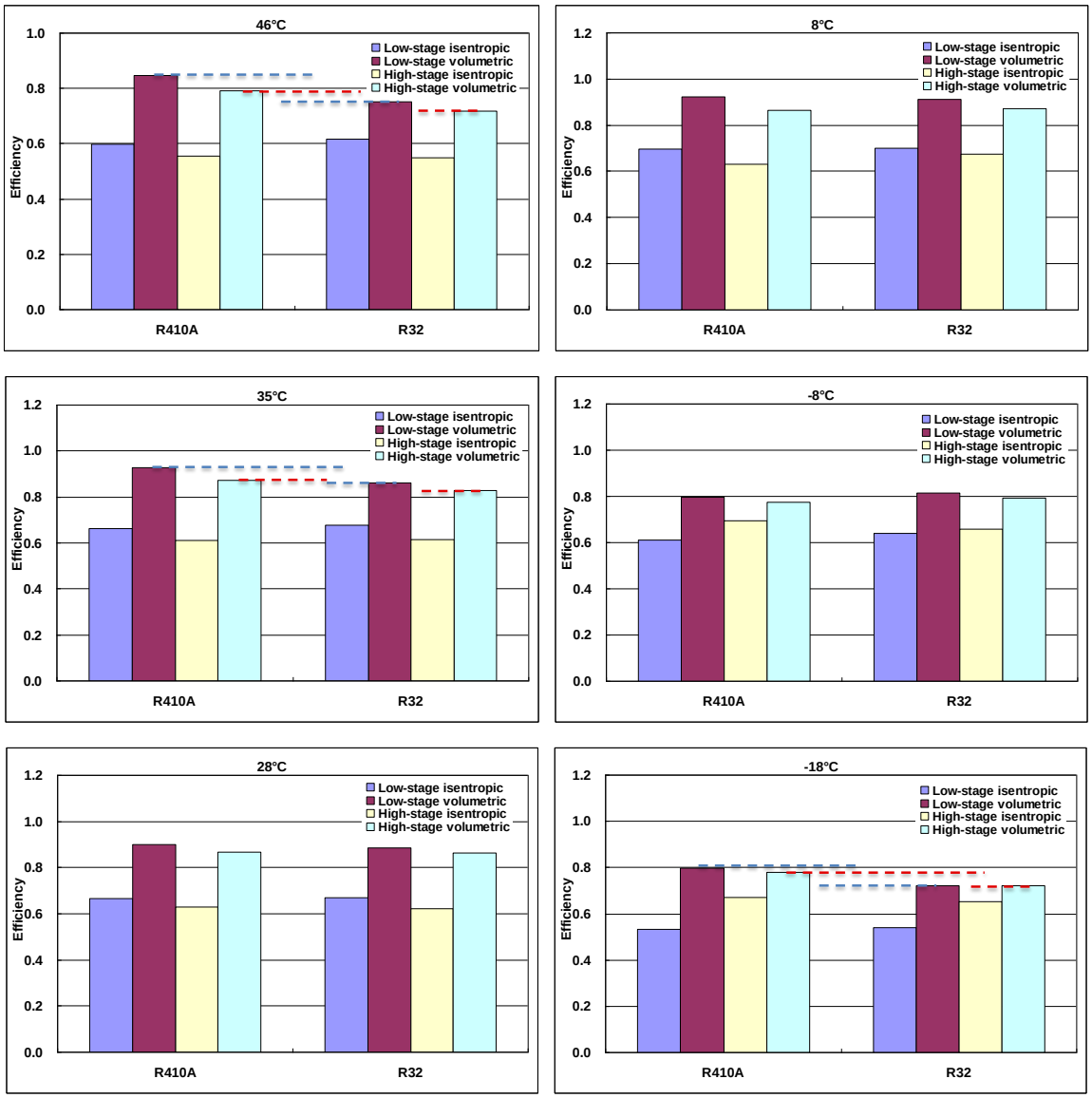

Figure 4-31: Low-stage and high-stage isentropic and volumetric efficiencies comparison for R32 and R410A in a two-stage cycle with vapor injection

4.5 More discussion on R410A and R32

From the experimental results it can be seen that R32 outperforms R410A overall, and it should also be noted that the experimental results performed was on a drop-in basis, and as such, a system with optimized components for R32 is expected to achieve even better performance. However, there are also other concerns in regards to using R32, such as the flammability and oil compatibility.

For flammability, R410A is classified as the A1 class which is non-flammable. R32 is classified as the A2L class, which is slightly flammable. As the global warming has increasingly become a critical issue, the HVAC industry has also started to consider adopting slightly flammable or even flammable refrigerants. There are currently global efforts to accelerate the development for A2L standards (Pham and Rajendran, 2012). Moreover, due to the property difference, the refrigerant charge amount of a R32 system can be significantly less than that of a R410A system. The results from this dissertation show a decrease of 29% reduction for total refrigerant charge amount. As the heat exchangers are designed to be more compact, further refrigerant charge amount reduction is expected.

Oil compatibility has also been studied by different research groups. Yan et al. (2012) has experimentally evaluated the performance and reliability of lubricating oil designed for R410A, and they concluded that the lubricant on sliding parts is behaving satisfactory for R32 compressors. It has also been predicted that current oil can function properly on a system point of view. In addition, there are also on-going efforts to develop refrigeration oil to best suit R32 in a vapor compression cycle (Okido et al., 2012).

Figure 4-32 shows the comparison of operating envelops of R32 and R410A. It can be seen that the operating envelop of R410A is larger than that of R32. This is essentially due to the property difference between these two refrigerants. As also seen from the experimental results, the compressor discharge temperature of R32 is much higher than that of R410A. This has limited the operating envelope of R32. Therefore, lowering the compressor suction superheating can be helpful to reduce the compressor discharge temperature for R32. Proper compressor cooling can also be beneficial for R32 to cover wider operating conditions. Detailed compressor cooling is discussed in Chapter 7.

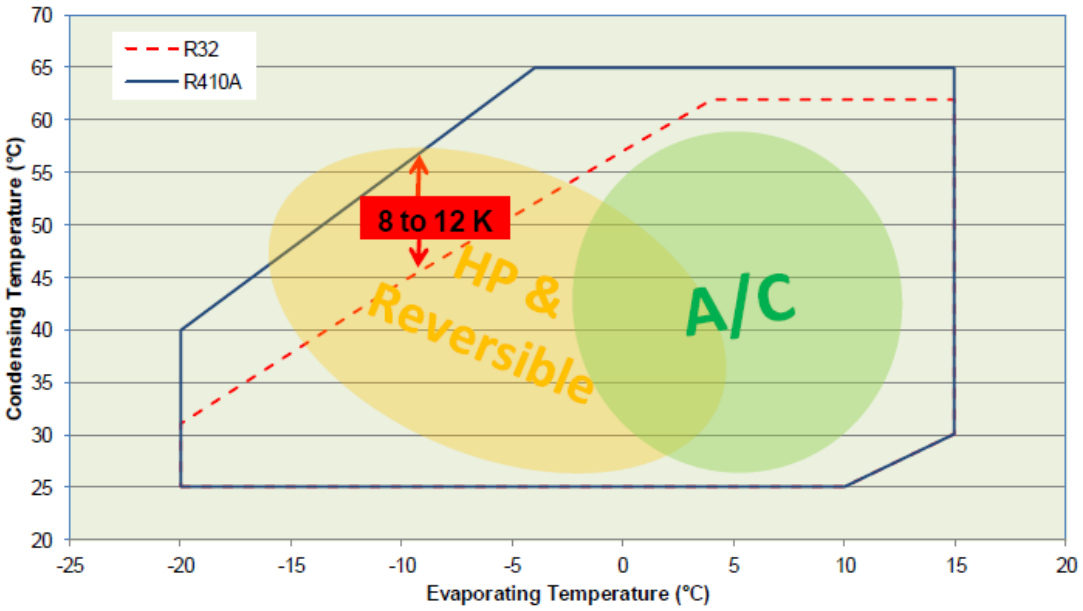

Figure 4-32: Comparison of operating envelopes of R32 and R410A

(Bella and Kaemmer, 2011)

4.6 Chapter summary and conclusions

This research work investigates the performance difference between R32 and R410A in a vapor-injected heat pump system with a flash tank. Drop-in test was performed with R32 in the heat pump system for both cooling and heating conditions. A single stage cycle without vapor injection and a two-stage cycle with vapor injection have been tested. Through experimentation, it was found that the capacity improvement of R32 over R410A was between 3% and 10%, and the COP improvement was between 2% and 9% for the single stage cycle without vapor injection. For the two-stage cycle with vapor injection, different injection ratios were investigated for R32 and R410A. The benefit of vapor injection was significant. Compared to a non-injection system, the maximum capacity improvement for R410A and R32 was observed to be 33% and 25%, respectively by utilizing vapor injection. The maximum COP improvement for R410A and R32 was observed to be 18% and 11%, respectively. The improvement was most pronounced at the extreme ambient heating condition of -18 ℃.

The system performance using R32 and R410A was also directly compared in vapor injection mode. Comparing R32 to R410A at the same injection ratio and using R410A as the baseline, the capacity improvement was found to be 2% to 7%, and COP improvement was found to be 1% to 6%. There was no improvement at extreme cooling and heating conditions. The inferior performance of R32 at the extreme conditions is mainly due to the refrigerant mass flow rate decrease caused by the compressor efficiency degradation.

There are differences in the compressor performance, comparing R32 and R410A with and without vapor injections. For a single stage cycle, compressor performance is almost the same for two refrigerants, and the difference observed is a slight decrease in the volumetric efficiency using R32. Refrigerant mass flow rate decrease associated with high compressor discharge temperature using R32 causes heat exchanger performance degradation at low ambient temperature conditions. For a two-stage cycle, there are compressor performance degradations using R32 at the extreme cooling and heating conditions.

Moreover, R32 shows higher compressor discharge temperature than R410A. This is partially due to the fact that the density of R32 is smaller than that of R410A, which results in a reduction in the refrigerant mass flow rate. The motor heat from the compressor would lead to higher temperature rise for R32 than for R410A. Moreover, it has been calculated that the volumetric capacities of R32 and R410A are different depending on the evaporating temperature. The current compressor is originally designed for R410A, and therefore, it may have been inappropriately sized for R32. High compressor discharge temperature reduces the reliability of system operation due to the possibility of lubricating oil performance degradation. Therefore, reducing the compressor discharge temperature would be critical in applying R32, especially at extreme cooling and heating conditions.

To design a vapor injection system that is optimized for R32, the compressor should be appropriately sized. The gas path inside of the compressor should be better designed to avoid unexpected heat gain from the motor to avoid high discharge

temperature. The compressor suction superheat setting can also be decreased to lower the compressor discharge temperature. Furthermore, introducing additional liquid injection to the compressor at extreme conditions can also be used to reduce compressor discharge temperature. With all these methods, the compressor efficiencies are expected to be increased. This in further improves the heat exchanger performance, and therefore, leads to an improvement in the overall system efficiency. More detailed analysis on the compressor cooling will be presented in Chapter 7.

5. Compressor and heat exchanger modeling

5.1 Two-stage compressor model

5.1.1 Model descriptions

As seen from the experimental results in the previous chapter, a main challenge for R32 is the high compressor discharge temperature, especially at extreme ambient temperature cooling and heating conditions. The objective of the compressor study is to investigate the technology that can address the high compressor discharge temperature when R32 is used in a vapor compression system. A two-stage vapor injection compressor model needs to be developed in order to simulate the compressor performance.

For a single stage compressor without vapor injection, a 10-coefficient model can be employed to predict the compressor performance (ANSI/AHRI Standard 540, 2004). Wang (2008) has improved the 10-coefficient model and simulated a two-stage vapor injection compressor by applying a map-based modeling approach. In this model, the low-stage isentropic and volumetric efficiencies were treated as a function of the evaporating and condensing temperatures, and the high-stage isentropic and volumetric efficiencies were treated as a function of the saturation injection and condensing temperatures. This approach gives reasonably accurate results. However, this model treats the compressor as a lumped model, which doesn't take into account of the heat transfer inside of the compressor, such as the heat transfer between the suction gas and the motor, and the compressor shell with the ambient environment. Therefore, to have a more accurate model, the heat transfer process needs to be taken into account. Winkler

(2009) has simulated the performance of a single stage scroll compressor. In this model, the heat transfer between the suction gas and the motor, and between the shell and the ambient environment were considered. However, this model was based on a single stage scroll compressor, and no vapor injection was considered in this case. Moreover, the heat transfer from the high-pressure cylinder to the low-pressure cylinders was not taken into account. This may further affect the accuracy of this model.

To obtain a more accurate two-stage compressor model with vapor injection, a physics-based model was developed and investigated. Figure 5-1 shows the two-stage vapor injection compressor model. This model improves the single stage model by Winker (2009), and has included the heat transfer between the high-pressure and low-pressure cylinder which was not considered by Winkler (2009). The scrolls in Figure 5-1 represent two-stage compression scrolls with an intermediate vapor injection port. The two-stage compression process is shown in Figure 5-2. State point "1a" represents the actual suction port of the scroll inside of the compressor, which is different from the suction port state "1" on the compressor shell. State point "3" stands for the low-stage compression discharge point, which is mixed with the injected refrigerant from state point "4", reaching state "5". State point "2a" indicates the scroll high-stage compression discharge point, which is different from the compressor shell discharge port described by state point "2", as shown in Figure 5-1.

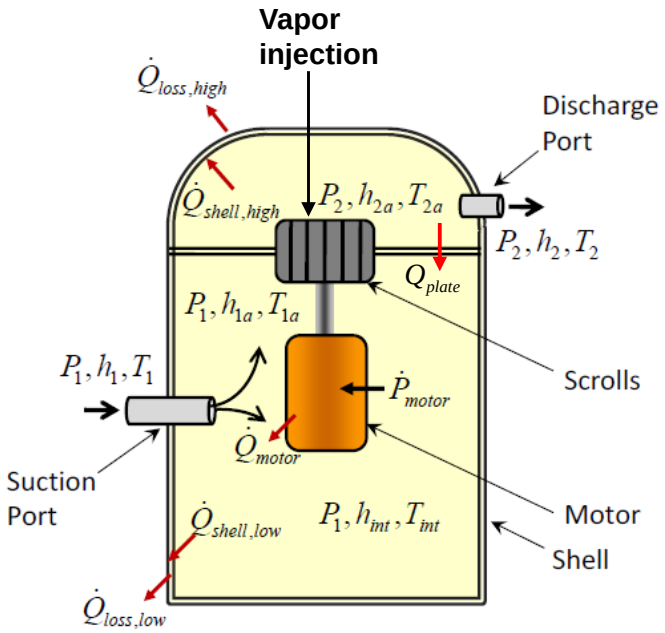

Figure 5-1: Two-stage vapor injection compressor model

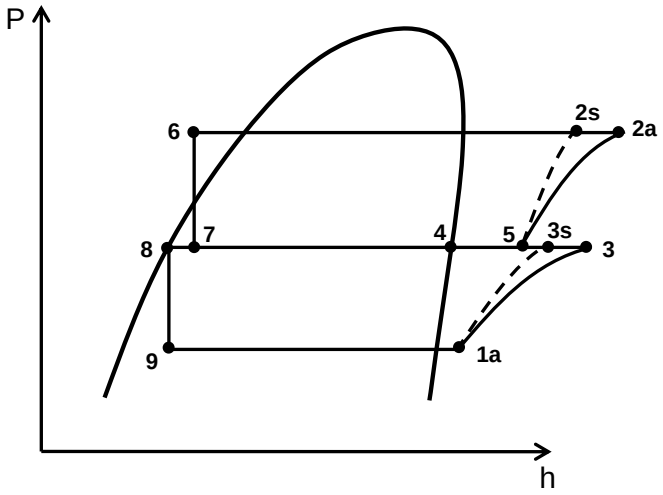

Figure 5-2: Two-stage compression process with vapor injection

5.1.2 Compressor efficiency evaluation

Compressor performance is closely related to the isentropic and volumetric efficiencies. Therefore, obtaining accurate compressor isentropic and volumetric

efficiencies are critical for simulating the compressor performance. In the model investigated by Wang (2008), the compressor was treated as a lumped model, and therefore the heat transfer between the suction gas and the motor, and between the compressor shell and the ambient environment was not considered. As a result, the definitions of the compressor isentropic and volumetric efficiencies are not quite accurate, because the efficiencies were calculated based on the suction and discharge ports on the compressor shell. In the modeling work described in this chapter, the compressor isentropic and volumetric efficiencies are defined using the actual scroll suction and discharge port parameters instead of using compressor shell suction and discharge port parameters. Therefore, the isentropic and volumetric efficiencies used in this chapter are expressed as $\eta_{ise,low,s}$, $\eta_{ise,high,s}$, $\eta_{vol,low,s}$, $\eta_{vol,high,s}$, and "s" indicates that the parameters are calculated based on the scrolls instead of the compressor shell.

For a single stage compressor, the AHRI 10-coefficient model can be described by Equation 5-1. In this equation, C_1 to C_{10} represents the coefficients for a specific compressor. X represents the isentropic and volumetric efficiencies. In a two-stage vapor-injected compressor, the compressor efficiency can be calculated using a similar approach. The low-stage compressor isentropic and volumetric efficiencies can be calculated using the same equation as for a single stage cycle shown in Equation 5-1. In this equation, the system parameters are expressed as a function of the evaporating temperature T_{evap} and condensing temperature T_{cond}. The high-stage compressor isentropic and volumetric efficiencies can be calculated using Equation 5-2. In this

equation, the system parameters are expressed as a function of the saturated injection temperature $T_{sat,inj}$ and the condensing temperature T_{cond}.

$$X=C_1+C_2T_{evap}+C_3T_{cond}+C_4T_{evap}^2+C_5T_{evap}T_{cond}+C_6T_{cond}^2+C_7T_{evap}^3+C_8T_{cond}T_{evap}^2+C_9T_{evap}T_{cond}^2+C_{10}T_{cond}^3 \quad \textbf{Equation 5-1}$$

$$X=C_1+C_2T_{sat,inj}+C_3T_{cond}+C_4T_{sat,inj}^2+C_5T_{sat,inj}T_{cond}+C_6T_{cond}^2+C_7T_{sat,inj}^3+C_8T_{cond}T_{sat,inj}^2+C_9T_{sat,inj}T_{cond}^2+C_{10}T_{cond}^3 \quad \textbf{Equation 5-2}$$

The coefficients C_1 to C_{10} can be obtained through curve fitting experimental results. The curve fit was performed in the software TableCurve3D (2012). The coefficients in the 10-coefficients model were obtained for R410A and R32, and are shown in Table 5-1 and Table 5-2, respectively.

Table 5-1: Summary of 10-coefficients for vapor-injected compressor for R410A

Coefficients	Low-stage isentropic efficiency	Low-stage volumetric efficiency	High-stage isentropic efficiency	High-stage volumetric efficiency
C_1	-2.38582511	0.780422123	54.43171224	-7.880082
C_2	0.020448763	0.259291924	-0.20867889	0.103940191
C_3	0.178349762	-0.04876955	-3.23656064	4.85E-01
C_4	0.00132692	0.006236341	-0.05509227	0.007339927
C_5	-0.00141736	-0.01313295	0.071267382	-0.01278533
C_6	-0.00331075	0.002523237	0.046506023	-6.16E-03
C_7	1.01E-05	2.67E-05	-0.00041231	6.29E-05
C_8	-3.98E-05	-1.61E-04	2.00E-03	-0.0002625
C_9	2.04E-05	1.67E-04	-0.00195808	0.000287801
C_{10}	1.93E-05	-3.01E-05	7.17E-05	-1.68E-05

Table 5-2: Summary of 10-coefficients for vapor-injected compressor for R32

Coefficients	Low-stage isentropic efficiency	Low-stage volumetric efficiency	High-stage isentropic efficiency	High-stage volumetric efficiency
C_1	40.22236926	-94.8563851	18.63014494	-32.6393154
C_2	-2.52441536	7.940007344	-0.07523598	-0.24185732
C_3	-1.96250381	4.208124317	-1.10039757	2.3232361
C_4	-0.07884349	0.247741848	-0.00874735	0.007173489
C_5	0.144973987	-0.44504544	0.014441261	5.18E-04
C_6	0.025104813	-0.03681357	0.019023125	-0.04946263
C_7	-0.00050285	0.001638157	-9.46E-05	7.71E-05
C_8	0.002049113	-0.00636699	0.000330685	-0.0003036
C_9	-0.00203726	0.006100873	-0.00034821	0.000203316
C_{10}	-1.84E-05	-2.14E-04	-6.42E-05	0.000297549

5.1.3 Governing equations

The two-stage compression process can be divided into the low-stage and high-stage compressions. Low-stage discharge state “3” can be calculated by Equation 5-3. The refrigerant mass flow rate through the low-stage suction port can be calculated by

Equation 5-4. ρ_{1a} stands for the low-stage refrigerant suction density, and V_1 represents the low-stage displacement volume of the compressor.

$$h_3 = h_{1a} + \frac{h_{3s} - h_{1a}}{\eta_{ise,low,s}} \quad \textbf{Equation 5-3}$$

$$\dot{m}_{suc} = \eta_{vol,low,s} \rho_{1a} V_1 \frac{RPM}{60} \quad \textbf{Equation 5-4}$$

Refrigerant discharged from the low-stage compression state "3" is mixed with the injected refrigerant state "4", reaching state "5". The mass and energy balances for this process are shown in Equation 5-5 and Equation 5-6, respectively.

$$\dot{m}_{total} = \dot{m}_{suc} + \dot{m}_{inj,vap} \quad \textbf{Equation 5-5}$$

$$\dot{m}_{suc} h_3 + \dot{m}_{inj,vap} h_4 = \dot{m}_{total} h_5 \quad \textbf{Equation 5-6}$$

The high-stage compression discharge state "2a" can be calculated by Equation 5-7. The total refrigerant mass flow rate can be calculated by Equation 5-8. ρ_5 stands for the high-stage suction port density, and V_2 represents the high-stage displacement volume. It should be noted that the vapor-injection scroll compressor was regarded as a two-stage compressor with a volume ratio of 0.76. The volume ratio is defined as the ratio of high-stage displacement volume to the low-stage displacement volume.

$$h_{2a} = h_5 + \frac{h_{2s} - h_5}{\eta_{ise,high,s}} \quad \textbf{Equation 5-7}$$

$$\dot{m}_{total} = \eta_{vol,high,s} \rho_5 V_2 \frac{RPM}{60} \quad \textbf{Equation 5-8}$$

Refrigerant enters the compressor from the compressor shell suction port at T_1, and then exchanges heat with the motor, the low pressure side compressor shell and the plate separating the high-pressure and low-pressure cylinders to reach state T_{int}. The heat transfer can be calculated by Equation 5-9. *r* represents the portion of refrigerant that flows directly into the scroll compression chamber. Therefore the refrigerant enthalpy at the actual suction port for the scroll can be calculated by Equation 5-10.

$$h_{\text{int}} = h_1 + \frac{(\dot{Q}_{motor} - \dot{Q}_{shell,low} + \dot{Q}_{plate})}{(1-r)\dot{m}_{suc}} \qquad \textbf{Equation 5-9}$$

$$h_{1a} = rh_1 + (1-r)h_{\text{int}} \qquad \textbf{Equation 5-10}$$

The heat transfer between the refrigerant and the compressor shell at the low-pressure cylinder can be calculated by Equation 5-11. $P_{A,low}$ represents the percent of compressor surface area for the low-pressure cylinder, and $U_{i,low}$ stands for the refrigerant heat transfer coefficient on low-pressure cylinder inside of the compressor shell. A_i is the heat transfer area inside of the compressor shell. Similarly, the heat transfer between the refrigerant and the compressor shell at the high-pressure cylinder can be calculated by Equation 5-12. $U_{i,high}$ represents the refrigerant heat transfer coefficient on high-pressure cylinder inside of the compressor shell. The total heat transfer through the shell is calculated by Equation 5-13.

$$\dot{Q}_{shell,low} = P_{A,low}U_{i,low}A_i(T_{\text{int}} - T_{shell,low}) \qquad \textbf{Equation 5-11}$$

$$\dot{Q}_{shell,high} = (1-P_{A,low})U_{i,high}A_i(T_{2a} - T_{shell,high}) \qquad \textbf{Equation 5-12}$$

$$\dot{Q}_{shell} = \dot{Q}_{shell,low} + \dot{Q}_{shell,high}$$ **Equation 5-13**

Heat transfer from the high-pressure to the low-pressure cylinders is through the middle plate, which can be calculated by Equation 5-14. The temperature of the middle plate is assumed to be averaging the high-pressure and low-pressure sides of the refrigerant temperatures, as shown in Equation 5-15.

$$\dot{Q}_{plate} = U_{plate} A_{plate} (T_{plate} - T_{\text{int}})$$ **Equation 5-14**

$$T_{plate} = \frac{1}{2}(T_{2a} + T_{\text{int}})$$ **Equation 5-15**

For the high-pressure cylinder, the refrigerant discharge temperature from the compressor shell is different from the scroll discharge port, which is calculated from Equation 5-16. h_{2a} represents the enthalpy at the scroll discharge port, and h_2 stands for the enthalpy at the compressor shell discharge port.

$$h_2 = h_{2a} + \frac{(\dot{Q}_{shell,high} - \dot{Q}_{plate})}{\dot{m}_{total}}$$ **Equation 5-16**

The heat generated by the compressor motor is calculated by Equation 5-17. η_{motor} stands for the motor efficiency, and $\dot{P}_{motor}$ is the total motor power. The motor power is calculated by adding the low-stage and high-stage power, as shown in Equation 5-18. The low-stage and high-stage compression power is calculated by Equation 5-19 and Equation 5-20, respectively.

$$\dot{Q}_{motor} = (1 - \eta_{motor})\dot{P}_{motor}$$ **Equation 5-17**

$$\dot{P}_{motor} = \dot{P}_{motor,low} + \dot{P}_{motor,high}$$ **Equation 5-18**

$$\dot{P}_{motor,low} = \frac{\dot{m}_{suc}(h_3 - h_1)}{\eta_{motor}}$$ **Equation 5-19**

$$\dot{P}_{motor,high} = \frac{\dot{m}_{total}(h_2 - h_5)}{\eta_{motor}}$$ **Equation 5-20**

Compressor shell temperature is typically different from the ambient air temperature, and therefore, the heat transfer between the compressor shell and the ambient air should be considered. The compressor shell is also divided into the low-pressure and high-pressure sides due to the temperature difference. The heat loss from the low-pressure and high-pressure side of the compressor shell to the ambient air is calculated by Equation 5-21 and Equation 5-22, respectively. The total loss is the summation of the low-pressure and high-pressure side loss, as shown in Equation 5-23. U_o stands for the heat transfer coefficient of the outer shell of the compressor, and A_o represents the outer surface area of the compressor shell.

$$\dot{Q}_{loss,low} = P_{A,low} U_o A_o (T_{shell,low} - T_{amb})$$ **Equation 5-21**

$$\dot{Q}_{loss,high} = (1 - P_{A,low}) U_o A_o (T_{shell,high} - T_{amb})$$ **Equation 5-22**

$$\dot{Q}_{loss} = \dot{Q}_{loss,low} + \dot{Q}_{loss,high}$$ **Equation 5-23**

For steady-state condition, the compressor shell heat loss should be equivalent to the heat transfer from the refrigerant inside of the compressor to the compressor interior surface. Therefore, Equation 5-24 and Equation 5-25 hold.

$$\dot{Q}_{loss,low} = \dot{Q}_{shell,low}$$ **Equation 5-24**

$$\dot{Q}_{loss,high} = \dot{Q}_{shell,high} \qquad \textbf{Equation 5-25}$$

Taking the compressor as a control volume, the input and output energy should be balanced. The overall energy balance equation is shown in Equation 5-26.

$$\dot{m}_{total} h_2 - \dot{m}_{suc} h_1 - \dot{m}_{inj,vap} h_4 = \dot{P}_{comp} - \dot{Q}_{loss} \qquad \textbf{Equation 5-26}$$

5.1.4 Compressor modeling flow diagram

The flow diagram of the compressor model is shown in Figure 5-3. The input parameters include the suction pressure P_1, injection pressure P_4, discharge pressure P_2, suction temperature T_1, ambient temperature T_{amb}, low-stage and high-stage displacement volumes V_1 and V_2, motor efficiency η_{motor} and compressor speed RPM. Through the 10-coefficient model, the compressor low-stage and high-stage volumetric and isentropic efficiencies can be calculated. By assuming a scroll suction temperature T_{1a}, the low-stage discharge temperature T_3 can be calculated. Then by using the energy balance in Equation 5-6 with an assumed injected vapor mass flow rate $\dot{m}_{inj,vap}$, the mixing state "5" can be calculated. With the high-stage compression efficiency known, the scroll discharge temperature T_{2a} can be calculated. Motor power can be calculated by Equation 5-18 to Equation 5-20. Motor heat can be calculated by Equation 5-17. The next step is to calculate the heat transfer from the refrigerant to the shell, and from the shell to the ambient air. This requires solving the equation sets from Equation 5-9 to Equation 5-16, and from Equation 5-21 to Equation 5-26. It should be noted that the scroll suction temperature T_{1a} needs to be updated for the previously assumed value for correct heat

transfer. The injected vapor mass flow rate $\dot{m}_{inj,vap}$ should also be updated to achieve an energy balance. The final outputs include the compressor shell discharge temperature T_2, the compressor power consumption $\dot{P}_{comp}$, the injected vapor refrigerant mass flow rate $\dot{m}_{inj,vap}$ and the total refrigerant mass flow rate $\dot{m}_{total}$. Details of the input parameters used in this modeling work are shown in Table 5-3.

The modeling work was performed in Engineering Equation Solver (EES, 2011). EES provides a number of built-in mathematical and thermophysical property functions useful for engineering calculations. Transport properties are also provided for most of current refrigerants. EES allows equations to be entered in any order with unknown variables placed anywhere in the equations, and it will automatically reorders the equations for obtaining solutions efficiently.

Table 5-3: Details of the input parameters for the compressor modeling

Input parameter	Description	Value used	Source
A_i	Heat transfer area inside of compressor shell	0.1581 m^2	Calculated from compressor specifications
A_o	Heat transfer area on exterior of compressor shell	0.186 m^2	Calculated from compressor specifications
A_{plate}	Compressor intersectional area	0.01539 m^2	Calculated from compressor specifications
$\eta_{ise,low,s}$	Low-stage isentropic efficiency	Calculated from compressor 10-coefficient model	
$\eta_{vol,low,s}$	Low-stage volumetric efficiency		
$\eta_{ise,high,s}$	High-stage isentropic efficiency		
$\eta_{vol,high,s}$	High-stage volumetric efficiency		
η_{motor}	Compressor motor efficiency	0.9	Realistic value to match experimental data
$P_{A,low}$	Percent of surface area for the low-pressure cylinder	0.8	Calculated from compressor specifications
r	Mass flow ratio directed to shell	0.33	Winkler (2009)
RPM	Compressor speed	3500	From compressor specifications
T_{amb}	Ambient temperature	From experimental data	
$U_{i,high}$	Refrigerant heat transfer coefficient on high-pressure cylinder inside of shell	150 $W/(m^2 K)$	Winkler (2009)
$U_{i,low}$	Refrigerant heat transfer coefficient on low-pressure cylinder inside of shell	100 $W/(m^2 K)$	Winkler (2009)
U_o	Air overall heat transfer coefficient on outside of shell	50 $W/(m^2 K)$	Winkler (2009)
U_{plate}	Heat transfer coefficient of the plate separating the high-pressure and low-pressure cylinders	125 $W/(m^2 K)$	Realistic value to match experimental data
V_1	Compressor displacement	29.5 cm^3	From compressor specifications
V_2	High-stage displacement volume	$V_2 = 0.76 * V$	Manufacturer data

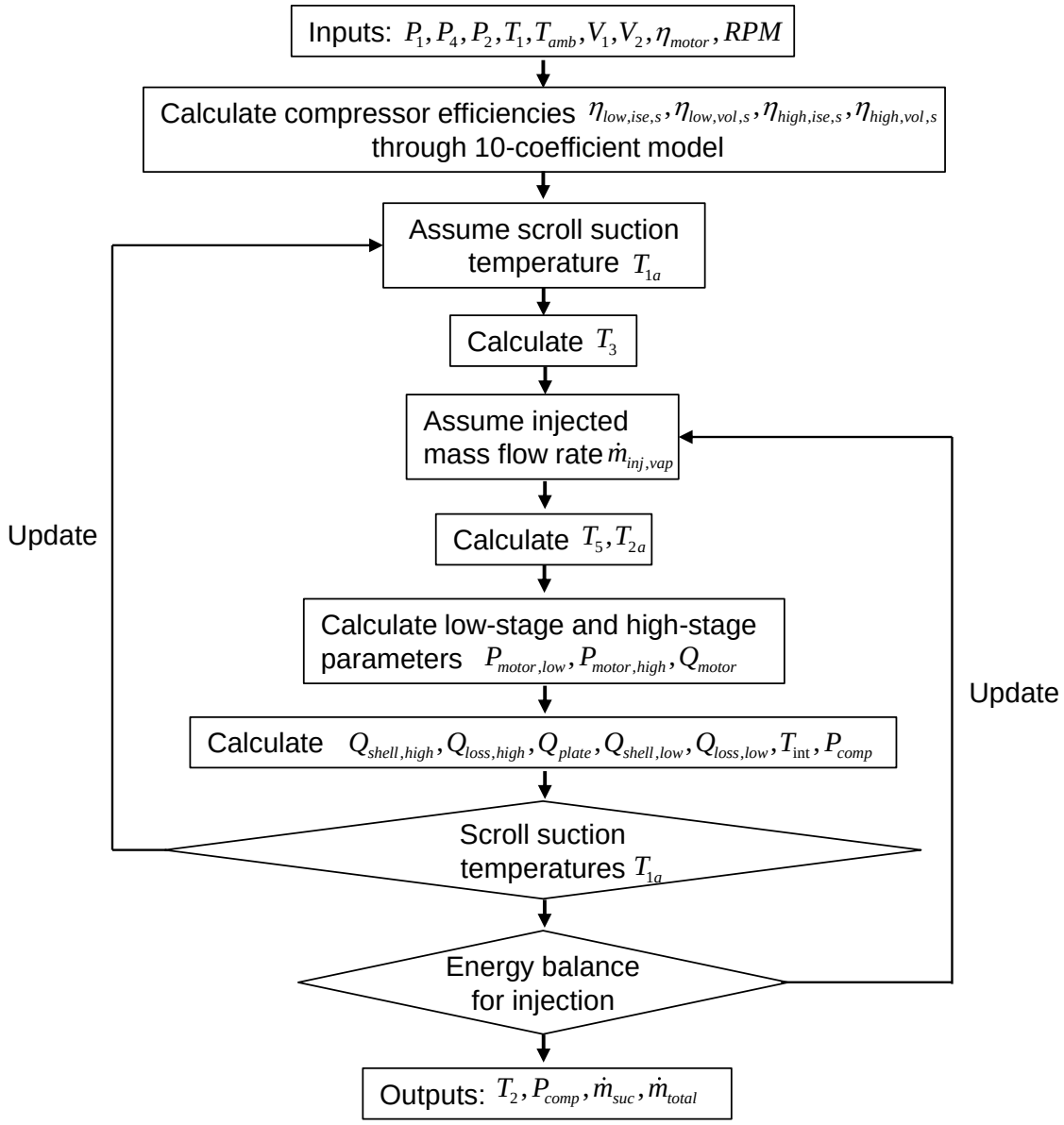

Figure 5-3: Two-stage compressor modeling flow diagram

5.1.5 Compressor model validation

The modeling results were validated by the experiment results. Figure 5-4 shows the comparison of modeling and experimental results for the compressor discharge temperature. 85% of the results fall into the range of ±3℃, and 93% of the results are

within ±5℃ variation. Figure 5-5 shows the comparison of modeling and experimental results for the system total power consumption. 95% of the results are within ±10% variation. Figure 5-6 shows the modeling and experimental results comparison for the refrigerant mass flow rate. All results show variation of within ±8%. Therefore, it can be concluded that the two-stage compressor model can predict the compressor performance in reasonable accuracy.

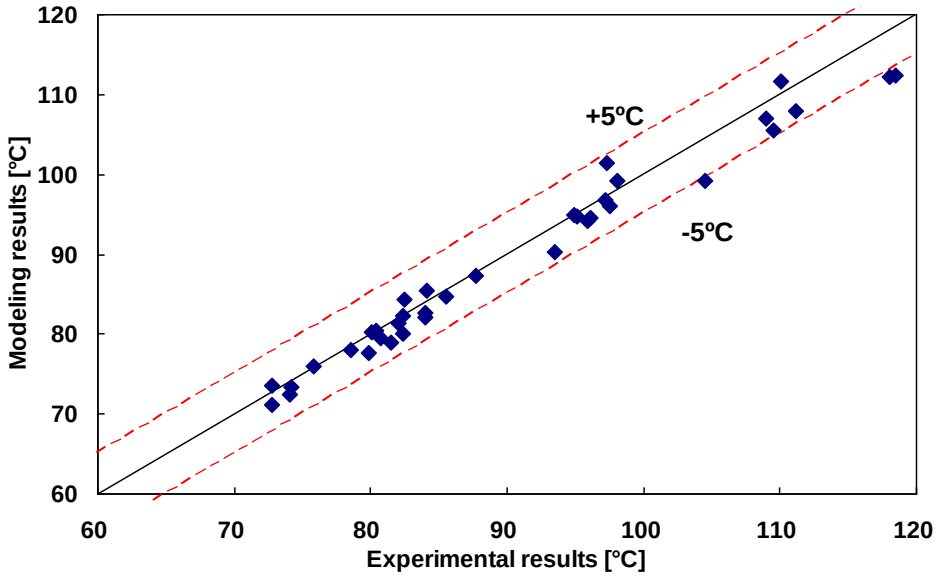

Figure 5-4: Modeling and experimental results comparison of the compressor discharge temperature

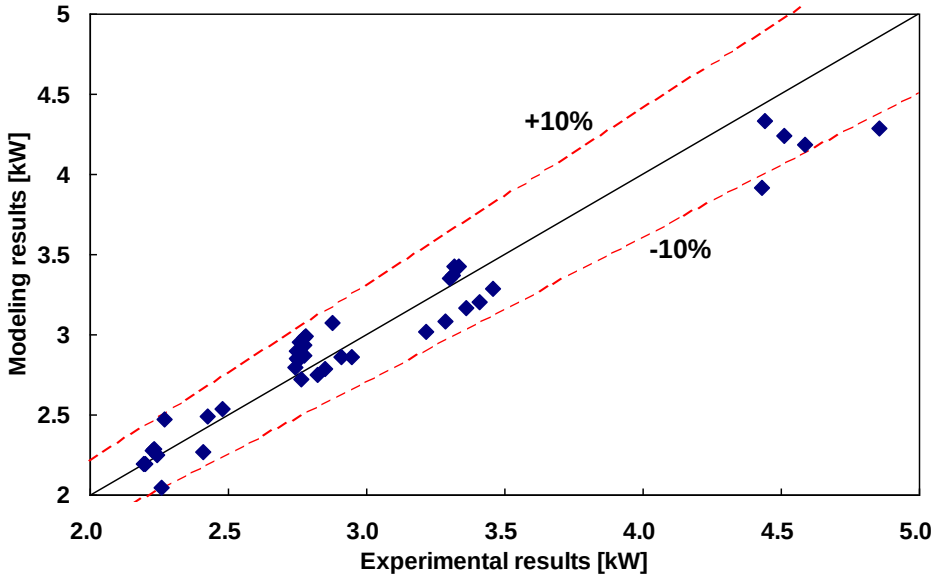

Figure 5-5: Modeling and experimental results comparison of the system power consumption

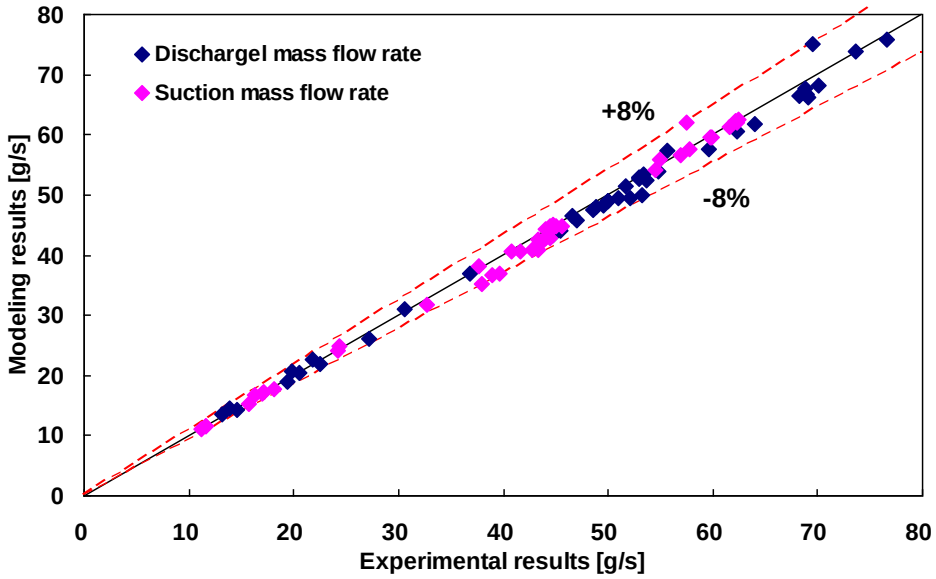

Figure 5-6: Modeling and experimental results comparison of the refrigerant mass flow rates

5.2 Heat exchanger modeling

5.2.1 Model descriptions

Both the indoor and outdoor heat exchangers were modeled in this dissertation. One objective is to better understand the heat transfer characteristic difference between R32 and R410A. A second objective is to have an experimentally validated heat exchanger model, and to perform heat exchanger design optimization study to better suit the new refrigerant R32. The in-house heat exchanger modeling software package CoilDesigner was used for this simulation work. This software package was developed by Jiang (2003). Basically the modeling approach is to divide the heat exchanger tubes into multiple segments, and each segment is treated as a single heat exchanger. Refrigerant-side and air-side heat transfer and pressure drop calculations are performed in each segment. This software provides the capability to model different types of heat exchangers, including tube-fin heat exchanger, micro-channel heat exchanger, tube-in-tube heat exchanger, etc. Different heat exchanger parameters can be defined through the user interface. To perform the heat exchanger modeling, inlet conditions of refrigerant- and air-sides are needed as the inputs, and outlet conditions could be calculated through the heat exchanger modeling. The output parameters include the refrigerant-side and air-side temperatures, pressures, capacities, etc. This software also has a number of heat transfer and pressure drop correlations to select from. In this modeling work, the heat transfer and pressure drop correlations used the ones that match the best for the experimental results. Table 5-4 summarizes the correlations used in this heat exchanger

modeling work. There is no correction factor applied for these correlations, and therefore the default value of 1.0 was used during this simulation work.

Table 5-4: Correlations used for the heat exchanger modeling

Parameter	Heat Exchanger	Mode	Refrigerant side			Air side
			Vapor-phase	Two-phase	Liquid-phase	
Heat transfer correlations	Indoor Coil	Cooling	Gnielinski[1]	Jung-Radermacher[2]	Gnielinski[1]	Kim-Yun-Webb[5, 9]
	Outdoor Coil			Shah[3]		
	Indoor Coil	Heating		Shah[4]		
	Outdoor Coil			Jung-Radermacher[2]		
Pressure drop correlations	Indoor Coil	Cooling	Blasius[6]	Jung-Radermacher[7]	Blasius[6]	Kim-Yun-Webb[5, 9]
	Outdoor Coil			Lockhart-Martinelli[8]		
	Indoor Coil	Heating		Lockhart-Martinelli[8]		
	Outdoor Coil			Jung-Radermacher[7]		

1: Gnielinski (1976)
2: Jung and Radermacher (1989a)
3: Shah (1979)
4: Shah (1982)
5: Kim et al. (1997)
6: Incropera and DeWitt (1996)
7: Jung and Radermacher (1989b)
8: Lockhart and Martinelli (1949)
9: Kim et al. (1999)

Both the indoor and outdoor heat exchangers are tube-fin type heat exchangers. The specifications of the two heat exchangers are shown in Table 2-1. The actual indoor heat exchanger is shown in Figure 2-2. Figure 5-7 shows the schematic of the indoor heat exchanger working as an evaporator. Each circle represents a refrigerant tube; solid and dotted lines represent the connecting tube at the front and back sides of the heat exchanger, respectively. The air flow direction is from the bottom to the top of the A-shaped coil. Since the indoor coil is symmetric, only one slab is selected for the

CoilDesigner modeling by assuming same air and refrigerant distributions. During the experimental tests, the total air flow rate through the entire heat exchanger was measured. In this modeling work, the air volume flow rate through each slab of the indoor coil is assumed to be equal. The overall capacity of the indoor heat exchanger is simply twice the capacity of each slab. From Figure 5-7 it can be seen that there are six refrigerant paths from the refrigerant distributor. The refrigerant mass flow rate through each path is assumed to be equal.

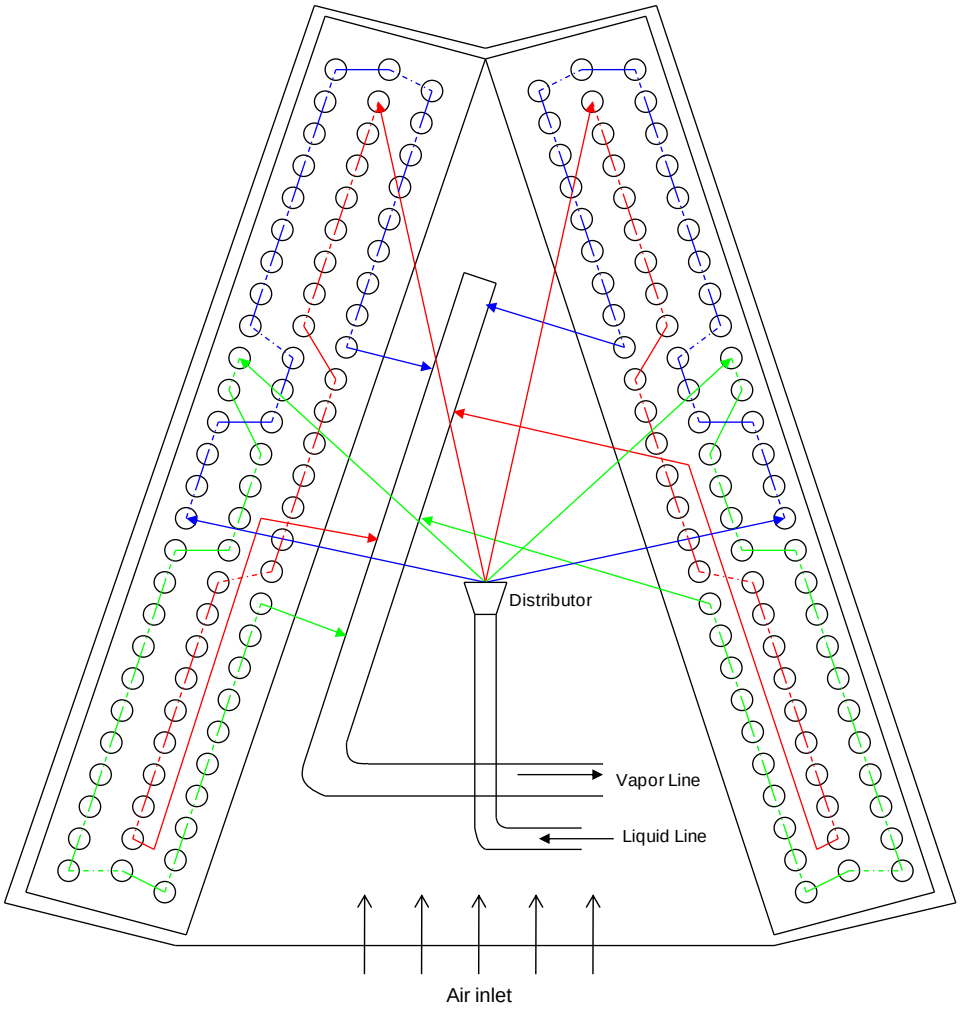

Figure 5-7: Schematic of the indoor heat exchanger as an evaporator

The air flow distribution is a critical factor for the indoor heat exchanger modeling. The air velocity through the heat exchanger was measured by an anemometer. The air velocity at different locations along the surface of the indoor coil was measured to generate the air velocity profile through each half of the indoor heat exchanger. Figure 5-8 shows the inlet air stream air velocity distribution across the indoor heat exchanger. The heat exchanger height was normalized from 0 to 1, which corresponds to the top and the bottom of the heat exchanger. A fourth order polynomial equation was obtained for the air velocity profile, as shown in Equation 5-27. The air velocity profile obtained here was used in CoilDesigner for the heat exchanger modeling.

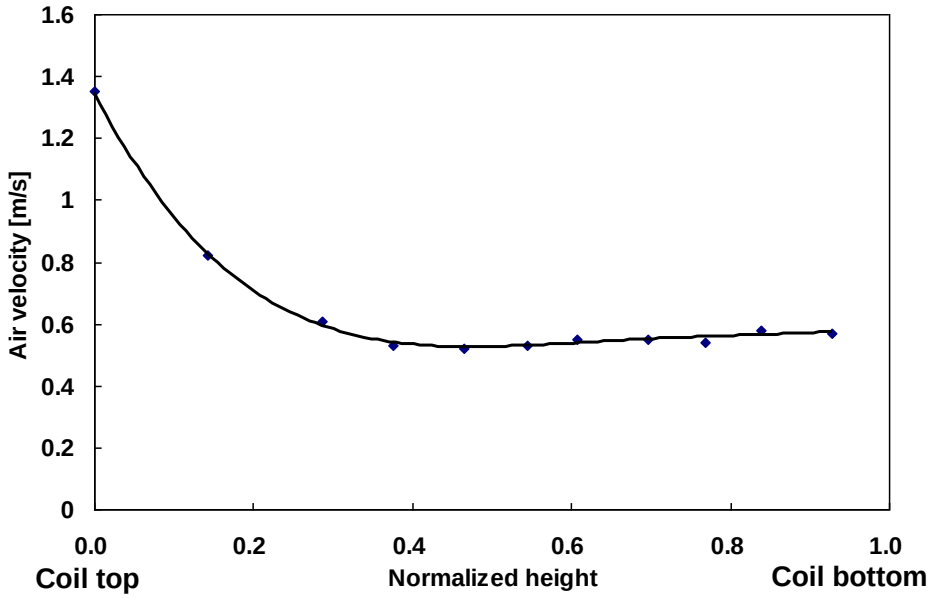

Figure 5-8: Air velocity distribution through the indoor heat exchanger

$$y = 3.5526x^4 - 10.352x^3 + 11.079x^2 - 5.0417x + 1.3488 \qquad \text{Equation 5-27}$$

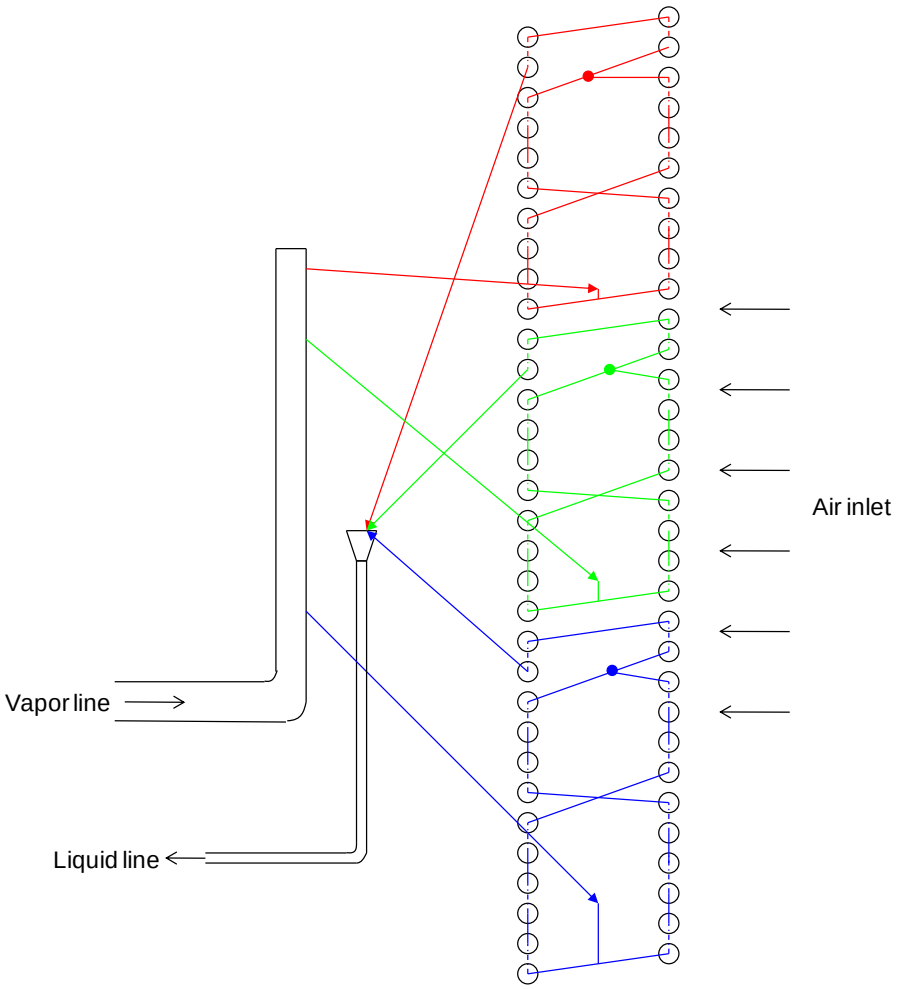

Figure 5-9: Schematic of the outdoor heat exchanger as a condenser

The actual outdoor unit is shown in Figure 2-3. It can be seen that it is a rectangular shape coil wrapped around the compressor in C-shape. Figure 5-9 shows the circuitry of the outdoor heat exchanger working as a condenser. Each circle represents a refrigerant tube, and the rectangular shape tubes are treated as straight tubes in this simulation work. The air flows from the right side to the left side of the heat exchanger. Ideally the air flow profile should be linear in the vertical direction, and with higher velocity at the top and lower velocity at the bottom of the heat exchanger. However, it

was measured that the air flow distribution through the outdoor heat exchanger was close to be uniform. The main reason is that the air velocity through the outdoor heat exchanger is low, and therefore, the reduced air-side pressure drop results in a close-to-uniform distribution. In the modeling work, uniform air flow distribution was used for the outdoor heat exchanger. The refrigerant flows in three major different paths; however, it should be noted that each path is then divided two different paths, and then merges before entering the last four tubes. Therefore, it's more accurate to claim that the outdoor heat exchanger has six circuitries in total. In this modeling work, it is assumed that the refrigerant mass flow rate in each circuitry is equal.

The input for the heat exchanger modeling includes both the refrigerant-side and air-side parameters. All the input parameters are from the experimental results. The refrigerant-side parameters include: refrigerant mass flow rate, temperature and pressure. The air-side parameters include: air mass flow rate and air velocity profile, pressure, air temperature and relative humidity.

5.2.2 Simulation results

Figure 5-10 shows the heat exchanger modeling and experimental results comparison. It can be seen that variations between modeling and experimental results are within ±6%. More detailed results for the condenser and the evaporator can be seen in Figure 5-11 and Figure 5-12, respectively. For the heat pumping mode, the system capacity increases with increasing ambient temperature. This is mainly due to the increase of refrigerant mass flow rate as ambient temperature increases. For the cooling mode, the system capacity decreases as ambient temperature increases. This is more

obvious for the evaporator than for the condenser. This is because that the system power consumption increases dramatically as the ambient temperature increases, and essentially the heat from the compression process needs to be dissipated to the ambient through the condenser. Moreover, the condensing pressure increases with ambient temperature so that the refrigerant mass flow rate decreases and the refrigerant enthalpy entering the evaporator increases. These two factors decrease the evaporator capacity.

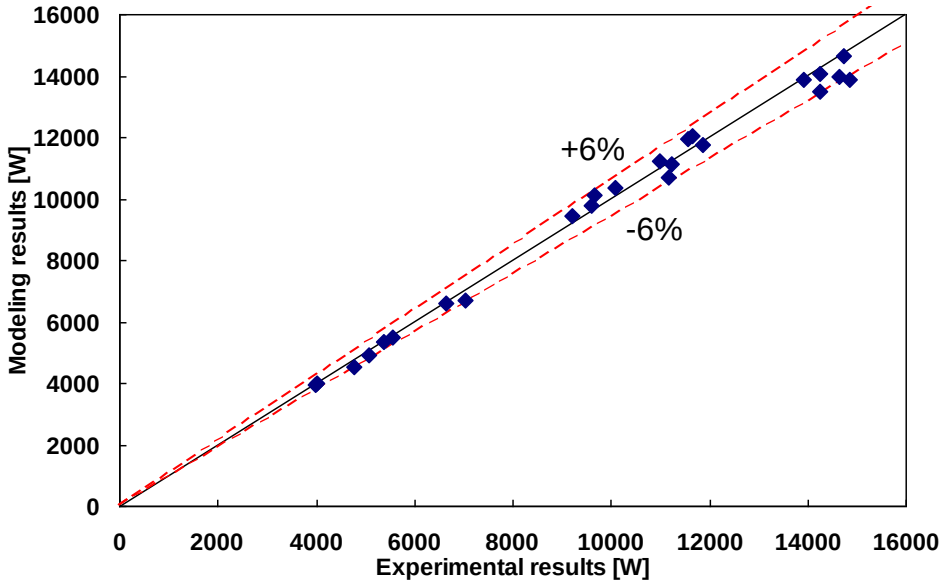

Figure 5-10: Modeling and experimental results comparison

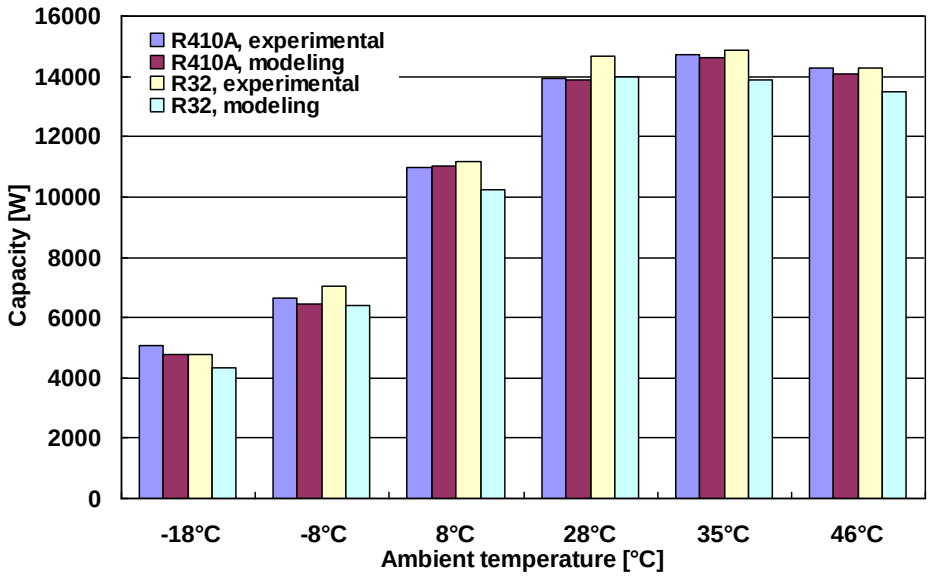

Figure 5-11: Heat exchanger modeling and experimental results with vapor injection: condenser capacity

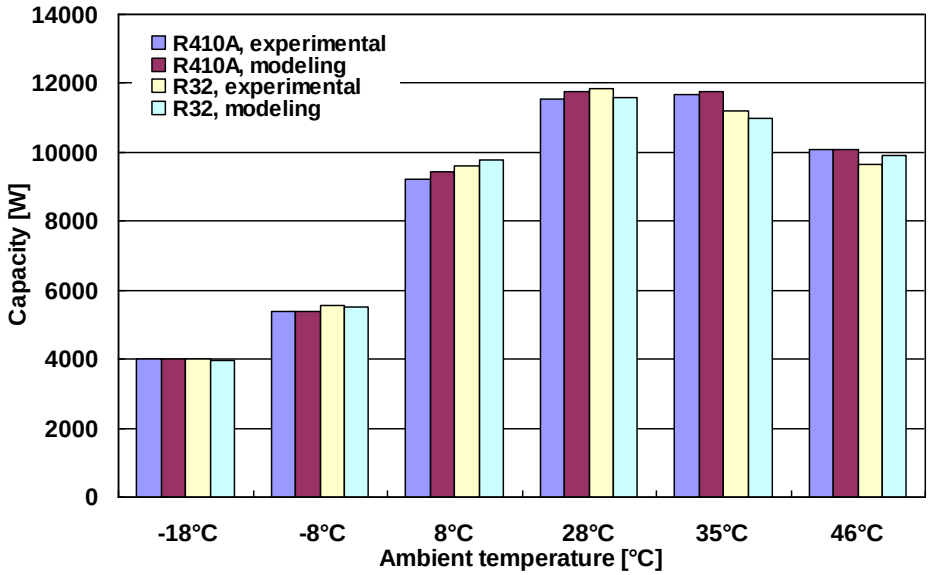

Figure 5-12: Heat exchanger modeling and experimental results with vapor injection: evaporator capacity

Figure 5-13 and Figure 5-14 show the refrigerant-side heat transfer coefficient of the condenser and evaporator, respectively. The general trend is that R32 has a higher heat transfer coefficient than R410A. However, for the conditions of 46℃ and -18℃, R32 has lower heat transfer coefficient than R410A. This is mainly due to the refrigerant mass flow rate decrease caused by compressor volumetric efficiency degradation. The reduced refrigerant mass flow rate leads to a decrease of the Reynolds number, and further decreases the Nusselt number, and therefore decreases the heat transfer coefficient.

Comparing the heat exchanger UA values in Figure 5-15 and Figure 5-16, it can be seen that the air-side UA is significantly lower than the refrigerant-side for the cooling condition; therefore, the dominating factor for heat transfer relies on the air side for the cooling mode. For the heating mode, it can be seen that the difference of refrigerant-side UA and air-side UA becomes smaller. For the condenser, the refrigerant-side UA is slightly higher than the air-side UA. However, for the evaporator, the refrigerant-side UA is even smaller than the air-side UA for the -8℃ and -18℃ conditions. This is because of the fact that the refrigerant-side mass flow rate becomes much smaller as the ambient temperature decreases. It also indicates that the refrigerant-side heat transfer needs to be enhanced if further system improvement is desired. Moreover, UA for cooling mode is significantly higher than that for heating mode for the condenser. This is because the outdoor heat exchanger is much larger than the indoor heat exchanger in physical size; the outdoor heat exchanger works as a condenser for the cooling mode, and the indoor heat exchanger works as a condenser for the heating mode. For the evaporator, the UA

for cooling mode is still larger than that for heating mode, but the difference becomes smaller as compared in the condenser.

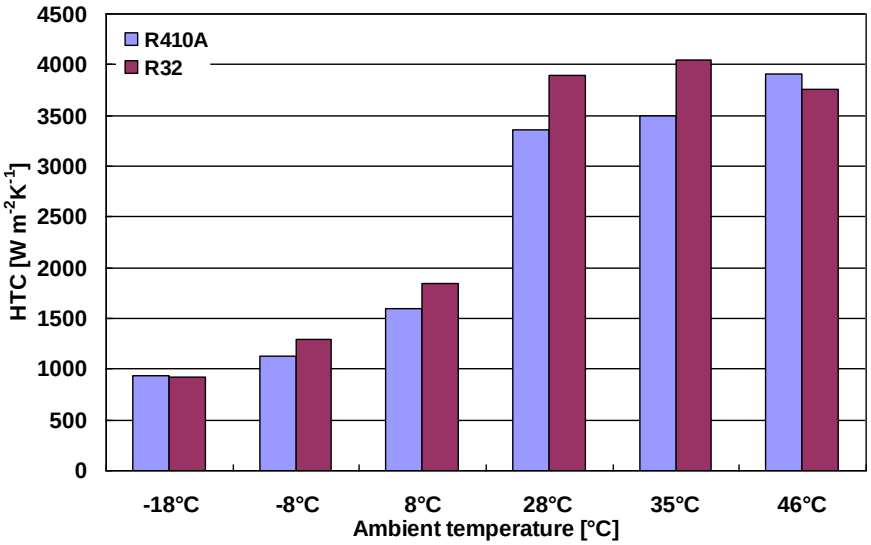

Figure 5-13: Heat exchanger modeling results with vapor injection: condenser refrigerant-side heat transfer coefficient

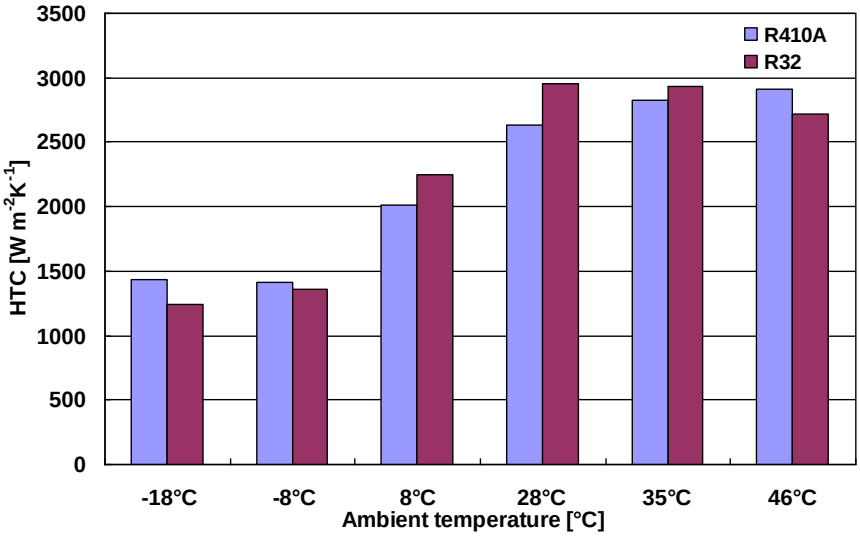

Figure 5-14: Heat exchanger modeling results with vapor injection: evaporator refrigerant-side heat transfer coefficient

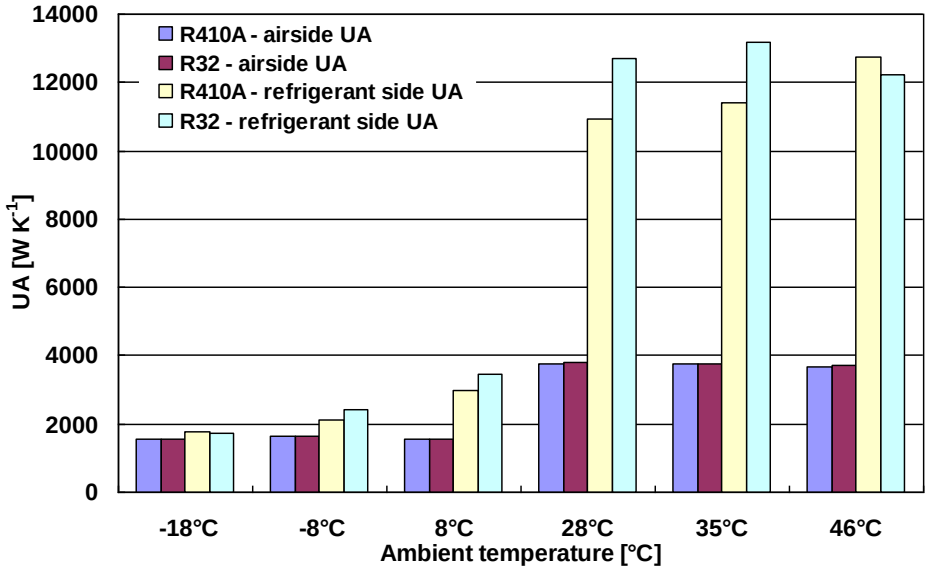

Figure 5-15: Heat exchanger modeling results with vapor injection: UA comparison in condenser

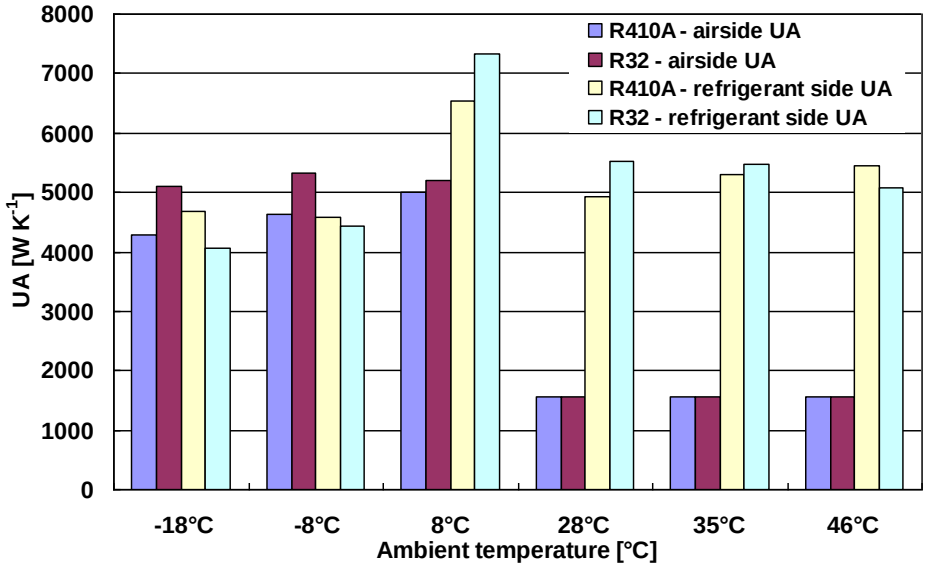

Figure 5-16: Heat exchanger modeling results with vapor injection: UA comparison in evaporator

Figure 5-17 shows the degrees of superheat comparison at the discharge point at different ambient temperature conditions. It can be seen that R32 has much higher degrees of superheat compared to R410A. The discrepancy becomes larger as the ambient temperature increases for the cooling mode and decreases for the heating mode. Figure 5-18 shows the de-superheating region comparison between R32 and R410A at different ambient temperature conditions. The general trend is that R32 has slightly higher de-superheating region than R410A, and the main reason is due to the fact that R32 has higher degrees of superheat than R410A. The only special case is at the condition at 46℃, where R410A shows higher de-superheating region than R32. This is due to the significant mass flow rate decrease at this condition, since the de-superheating region is associated with a few factors: the degree of superheat, the refrigerant mass flow rate, and the refrigerant specific heat. Figure 5-19 shows the vapor specific heat comparison between R32 and R410A. R32 has 1% to 6% higher specific heat than R410A at different ambient conditions.

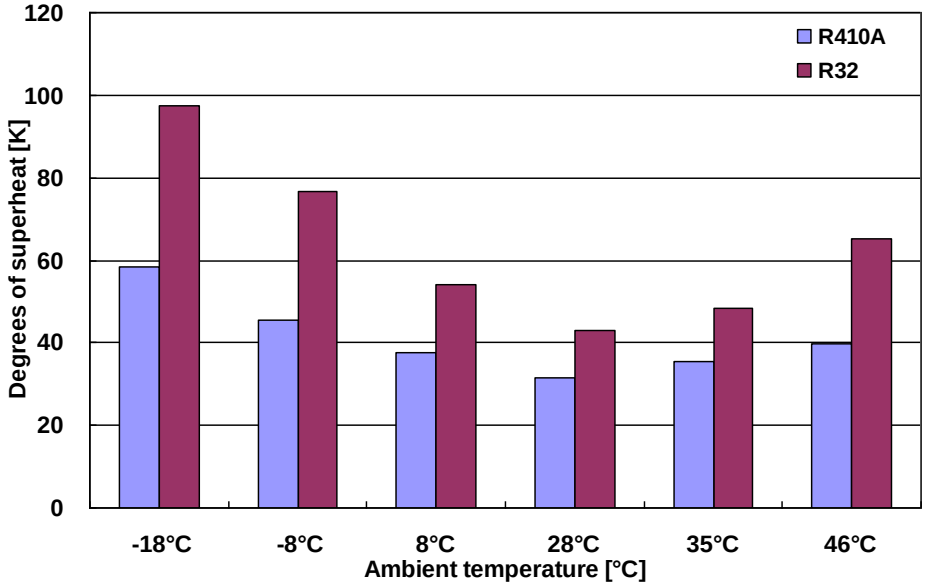

Figure 5-17: De-superheating region analysis on the condenser: degree of superheat variations

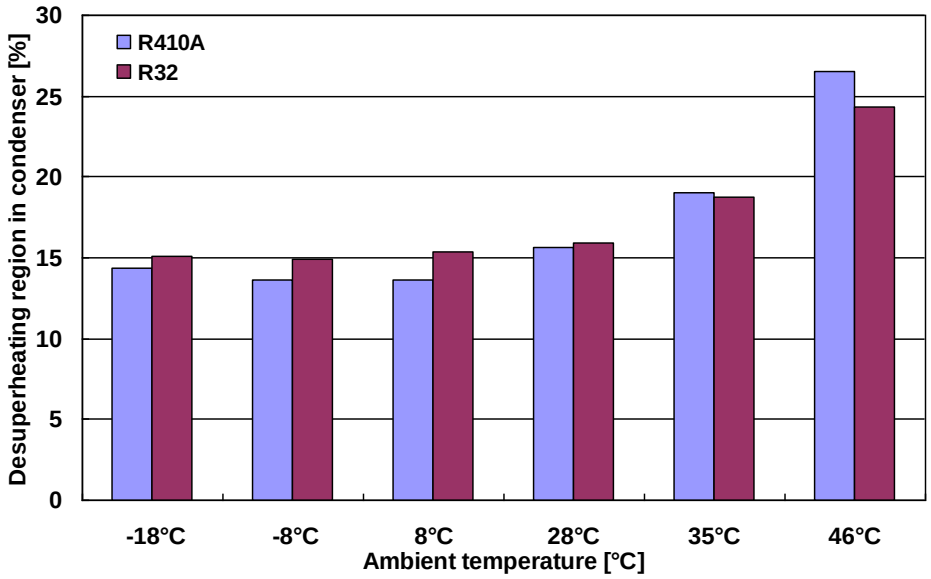

Figure 5-18: De-superheating region in the condenser

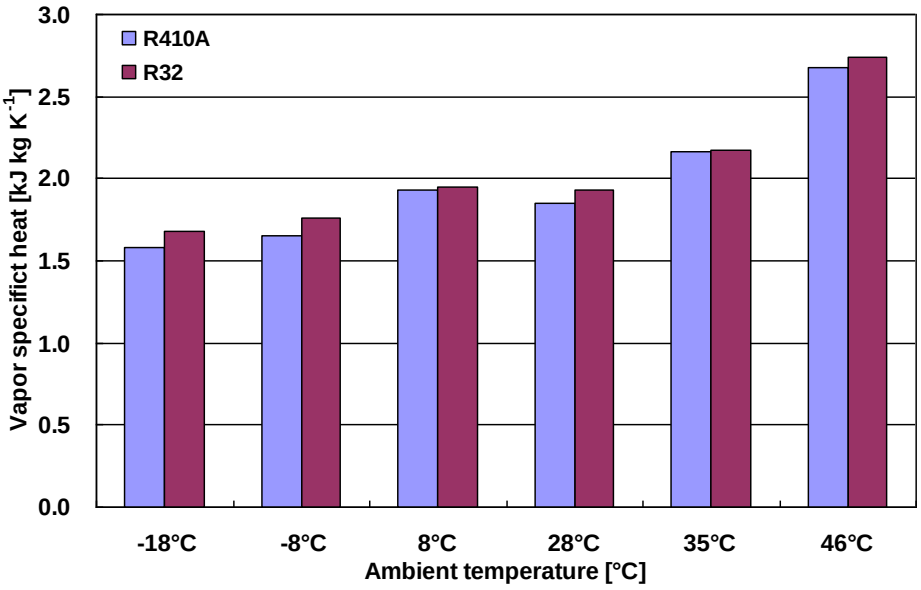

Figure 5-19: De-superheating region analysis on the condenser: vapor specific heat variations

5.3 Chapter summary and conclusions

Both the compressor and the heat exchangers have been modeled in this chapter. Modeling results were validated with experimental results. The two-stage vapor injection compressor model can accurately predict the compressor performance. The compressor discharge temperature from the model shows a deviation of ±3℃ with 85% accuracy compared to the experimental results, and 93% of the results are within ±5℃ variation. The total power consumption variation is within ±10% variation with 95% accuracy. The refrigerant mass flow rate from the model matched the experimental results all within ±8%.

Heat exchanger modeling using CoilDesigner matches the experimental results within ±6%. Heat exchanger modeling reveals that R32 has better heat transfer

characteristics than R410A in different operating conditions. Due to the high compressor discharge temperature, the condenser inlet degree of superheat for R32 is higher than that for R410A. The de-superheating region of R32 is also slightly higher than that of R410A. It was also found out that air-side heat transfer is the dominating factor in order to improvement the system performance for the cooling mode. For the heating mode, especially at the low ambient temperatures of -8℃ and -18℃, the refrigerant-side heat transfer also becomes a constraint for further system improvement. The verified compressor and heat exchanger models are used for the optimization study in Chapter 7.

6. Cycle modeling

6.1 Thermodynamic cycle modeling

In the experimental results, the performance using R410A and R32 was compared. In this chapter, the two refrigerants were compared in a thermodynamic cycle. The purpose of thermodynamic modeling is to investigate the theoretical system performance while excluding the performance loss in an actual system. The modeling work was also performed in Engineering Equation Solver (EES, 2011). For the thermodynamic model, the input parameters are listed as follows: evaporating pressure, condensing pressure, injection pressure, suction superheating, condenser outlet subcooling, compressor displacement, high stage/low stage volume ratio, compressor RPM, refrigerant type, compressor isentropic and volumetric efficiencies. The output parameters include: system capacity, COP, power consumption, refrigerant mass flow rate, discharge temperature, etc. Both single stage cycle without vapor injection and two-stage cycle with vapor injections have been modeled in this study.

6.1.1 Single stage thermodynamic cycle modeling

Table 6-1 shows the condensing and evaporating temperatures used for the single stage cycle modeling without vapor injection. These values were obtained from experimental results. Table 6-2 shows parameters defined in the single stage cycle modeling. Both subcooling and superheating were assumed to be 0 K for theoretical analysis purpose. The compressor used in the system has a constant speed of 3,500 rpm with a displacement of 29.5 cm^3 according to compressor specifications. Compressor

isentropic efficiency and volumetric efficiencies were assumed to be ideal of 1.0 to investigate the maximum system performance.

Table 6-1: Condensing and evaporating temperatures used for single stage cycle modeling without vapor injection

Parameter	Unit	Cooling			Heating		
T ambient	℃	46	35	28	8	-8	-18
T evaporating	℃	12	11	10	0	-14	-22
T condensing	℃	56	46	40	38	32	28

Table 6-2: Parameters used for single stage cycle modeling without vapor injection using ideal compressor efficiencies

Parameter	Unit	Value
Condenser outlet subcooling	K	0
Evaporator outlet superheating	K	0
Suction superheating	K	0
Compressor displacement	m^3	29.5e-6
Compressor speed	rpm	3,500
Isentropic efficiency	-	1.0
Volumetric efficiency	-	1.0

Figure 6-1 and Figure 6-2 shows the single stage thermodynamic cycle modeling comparison of R410A and R32 using ideal compressor efficiencies of 1.0. From Figure

6-1 it can be seen that capacity improvement is between 10% and 18% comparing R32 to R410A. For the heating mode, the improvement remains almost the same. For the cooling mode, as ambient temperature increases, the performance improvement becomes more pronounced. The main reason is that the condensing temperature remains almost the same for heating mode, since the air-side volume flow rate and temperature remains the same; yet the condensing temperature increases as ambient temperature increases for cooling mode. In a P-h diagram, the enthalpy difference between vapor and liquid for R32 and R410A becomes larger as the cycle schematic is shifted upward. The refrigerant mass flow rate difference between R32 and R410A remains the same at the same evaporating condition. Therefore, larger enthalpy difference results in a larger capacity across the evaporator. The COP improvements comparing R32 to R410A are found to be between 2% and 9%. Power consumption variation is relatively small. There is a slight decrease for the heating mode and a slight increase for the cooling mode as ambient temperature increases. The COP also shows an increasing trend as the ambient temperature increases. From Figure 6-2 it can be seen that the refrigerant mass flow rate decrease is 28% or so, which is due to the density difference at the compressor suction port.

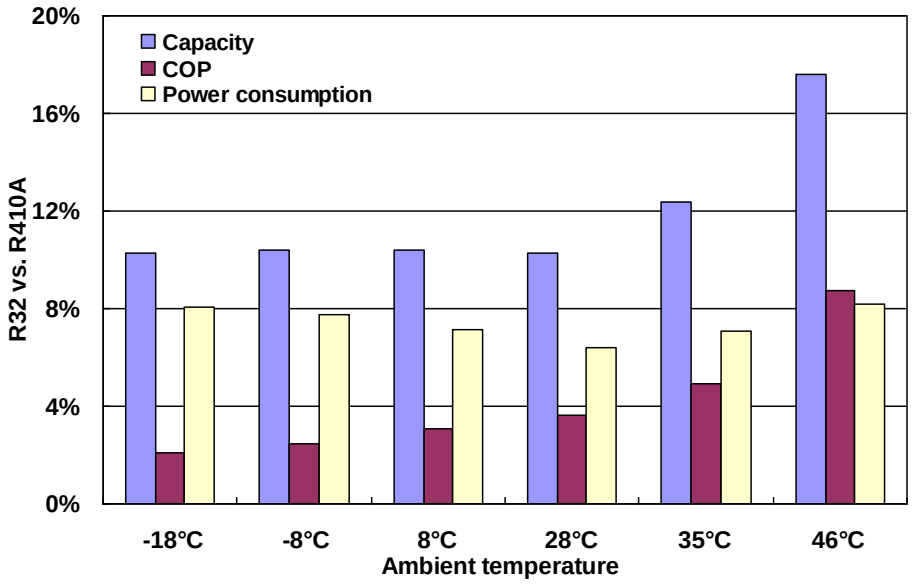

Figure 6-1: Single stage thermodynamic cycle modeling using ideal compressor efficiencies of 1.0: capacity, COP and power consumption comparisons

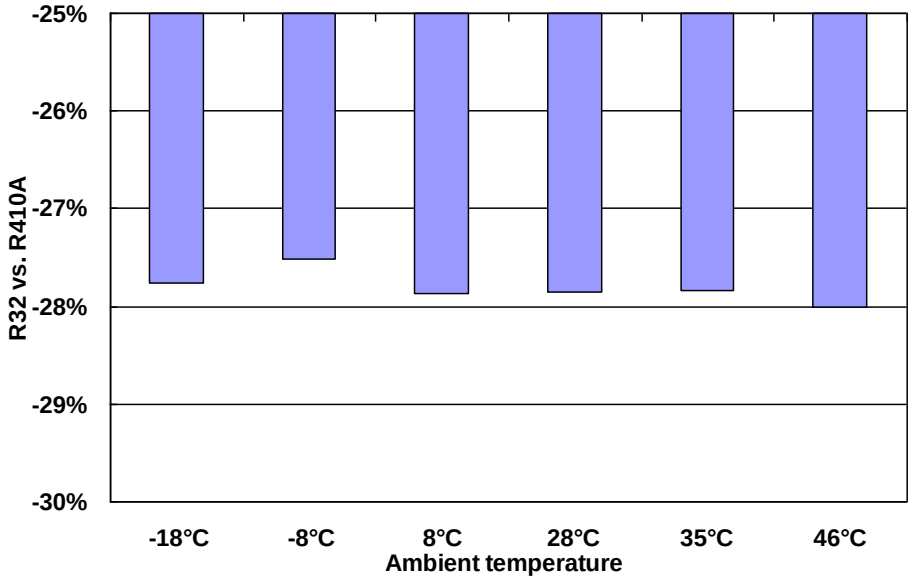

Figure 6-2: Single stage thermodynamic cycle modeling using ideal compressor efficiencies of 1.0: refrigerant mass flow rate comparison

Figure 6-3 and Figure 6-4 show the comparison of single stage thermodynamic cycle modeling of R32 and R410A using actual compressor efficiencies. The actual compressor efficiencies were calculated and already shown in Figure 4-15. From Figure 6-3 it can be seen that the highest improvement comparing R32 to R410A is still observed at the ambient temperature of 46 ℃, yet there is no improvement at the ambient temperature of -18 ℃. This is similar to the observations from experimental results. The main reason for performance degradation is also due to the low compressor efficiency at -18 ℃ condition. Comparing to the results using ideal compressor efficiencies, there are some differences when the actual compressor efficiencies were applied. The variation comes from the compressor performance difference in the actual system. R32 has lower volumetric efficiency compared to R410A, as seen in Figure 4-15. This also results in the refrigerant mass flow rate difference as shown in Figure 6-4.

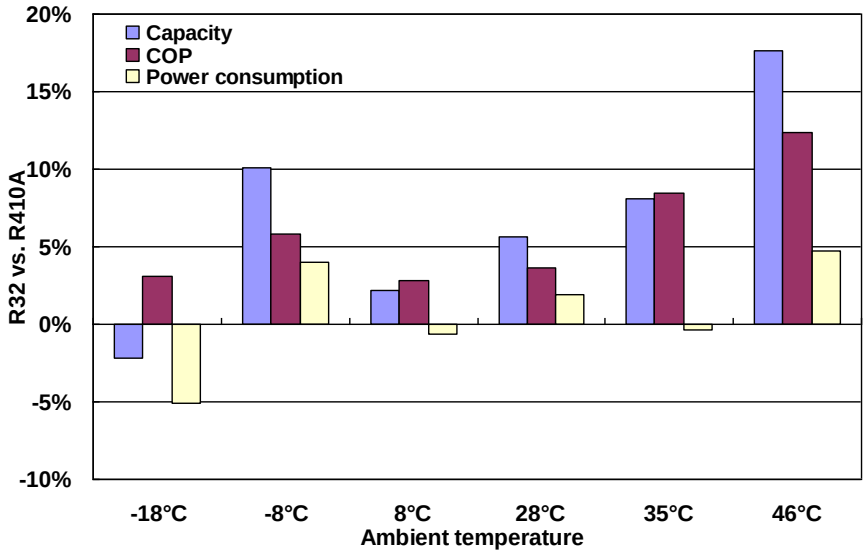

Figure 6-3: Single stage thermodynamic cycle modeling using actual compressor efficiencies: capacity, COP and power consumption comparisons

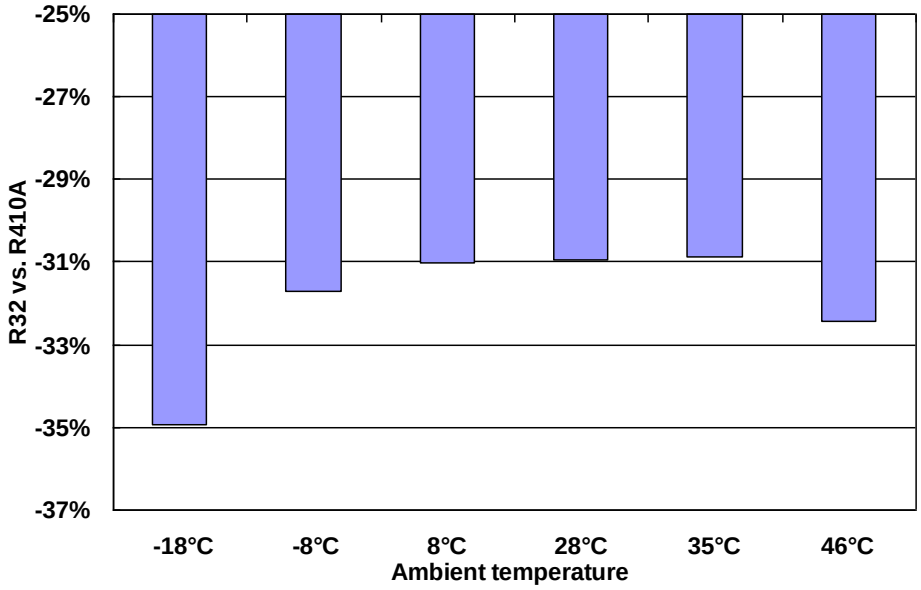

Figure 6-4: Single stage thermodynamic cycle modeling using actual compressor efficiencies: refrigerant mass flow rate comparison

6.1.2 Two-stage thermodynamic cycle modeling

When the vapor injection is initiated, the system operates as a two-stage system. The performance difference of R32 and R410A was also compared in a two-stage vapor injection system in a thermodynamic cycle. Table 6-3 shows the condensing and evaporating temperatures used for two-stage cycle modeling with vapor injection. These values were obtained from experimental results as well. Table 6-4 shows parameters defined in the two-stage cycle modeling. Both subcooling and superheating were assumed to be 0 K for ideal case comparison. Both low-stage and high-stage compressor's isentropic and volumetric efficiencies were assumed to be ideal of 1.0 to investigate the maximum system performance. The vapor injection ratio was set to be the same for R410A and R32 for a more fair comparison.

Table 6-3: Condensing and evaporating temperatures used for two-stage cycle modeling with vapor injection

Parameter	Unit	Cooling			Heating		
T ambient	℃	46	35	28	8	-8	-18
T evaporating	℃	12	11	10	0	-15	-22
T condensing	℃	58	48	41	42	34	31

Table 6-4: Parameters used for two-stage cycle modeling with vapor injection using ideal compressor efficiencies

Parameter	Unit	Value
Condenser outlet subcooling	K	0
Evaporator outlet superheating	K	0
Suction superheating	K	0
Compressor low-stage displacement	m^3	29.5e-6
Compressor high-stage displacement	m^3	22.4e-6
Compressor speed	rpm	3,500
Low-stage isentropic efficiency	-	1.0
Low-stage volumetric efficiency	-	1.0
High-stage isentropic efficiency	-	1.0
High-stage volumetric efficiency	-	1.0

Figure 6-5 and Figure 6-6 shows the two-stage thermodynamic cycle modeling comparison of R410A and R32 using ideal compressor efficiencies of 1.0. From Figure 6-5 it can be seen that capacity improvement is between 10% and 19% comparing R32 to R410A, and the maximum COP improvement is observed to be 5% at the ambient temperature of 46℃. There is no improvement at the heating conditions of -18℃ and -8℃. The main reason is due to the remarkable power consumption increase, which is observed to be between 8% and 13%. The power consumption increase for R32 is because that R32 has flatter isentropic lines, and therefore, the power increase at an identical pressure lift condition per unit mass refrigerant is more for R32 compared to that of R410A. From Figure 6-6 it can be seen that the total refrigerant mass flow rate decrease is 28% comparing R32 to R410A. The vapor injection ratio was set to be the same, and therefore, the suction mass flow comparison has the same trend as the total refrigerant mass flow rate.

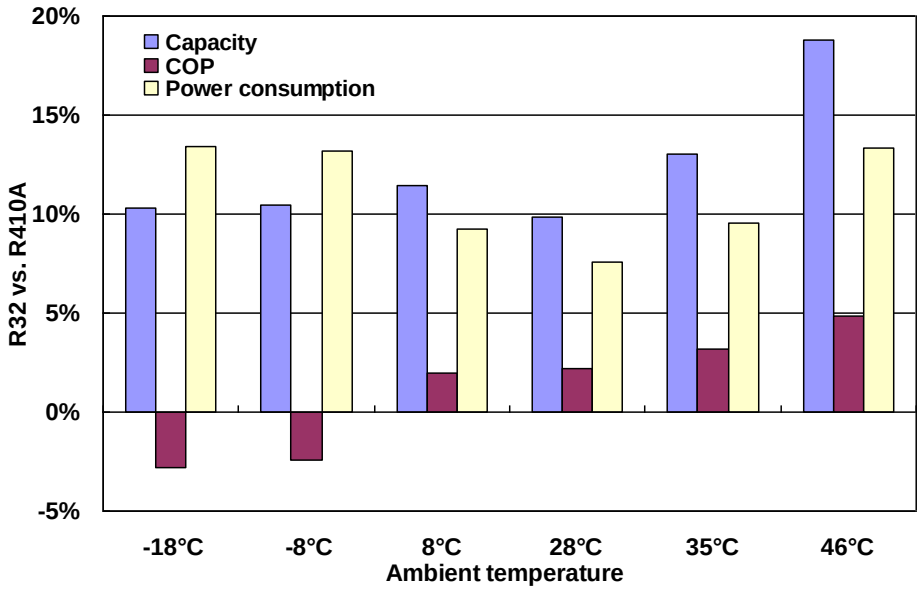

Figure 6-5: Two-stage thermodynamic cycle modeling using ideal compressor efficiencies of 1.0: capacity, COP and power consumption comparisons

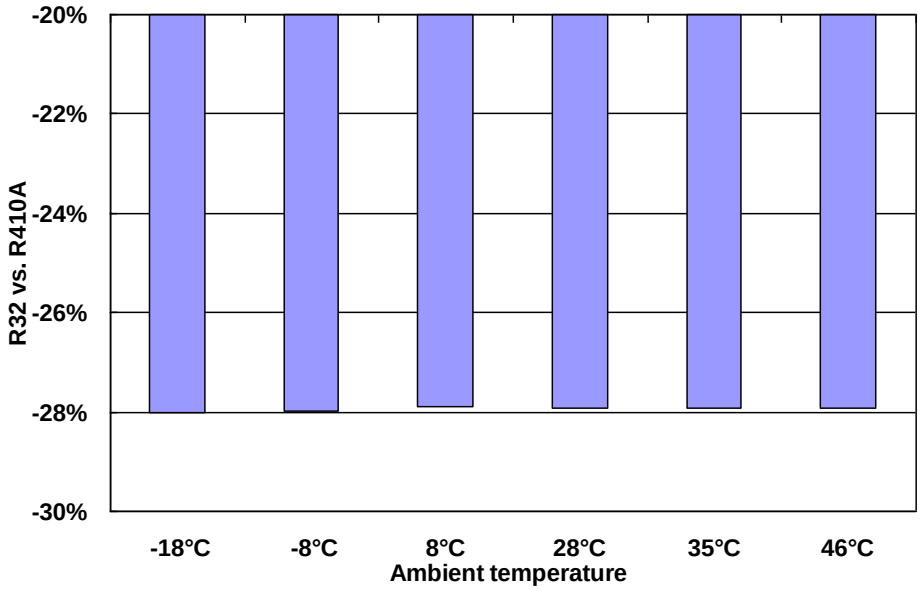

Figure 6-6: Two-stage thermodynamic cycle modeling using ideal compressor efficiencies of 1.0: total refrigerant mass flow rate comparison

Figure 6-7 and Figure 6-8 show the two-stage thermodynamic cycle modeling comparison of R32 and R410A using actual compressor efficiencies. Comparing to the results in Figure 6-5 and Figure 6-6, the biggest differences are for the conditions of 46℃ and -18℃. There is a significant degradation of capacity, COP and refrigerant mass flow rate. This is due to the compressor efficiency variation at this condition. From Figure 4-31 it can be seen that R32 has lower volumetric efficiencies than R410A for both low and high stages at the conditions of 46℃ and -18℃. This causes the decrease of refrigerant mass flow rate, and therefore, results in a capacity degradation. Moreover, the high-stage isentropic efficiency for R32 is also lower than that of R410A, and this is due to the high discharge temperature using R32. Decreased isentropic efficiency leads to higher compression work, and this also contributes to the degradation of COP.

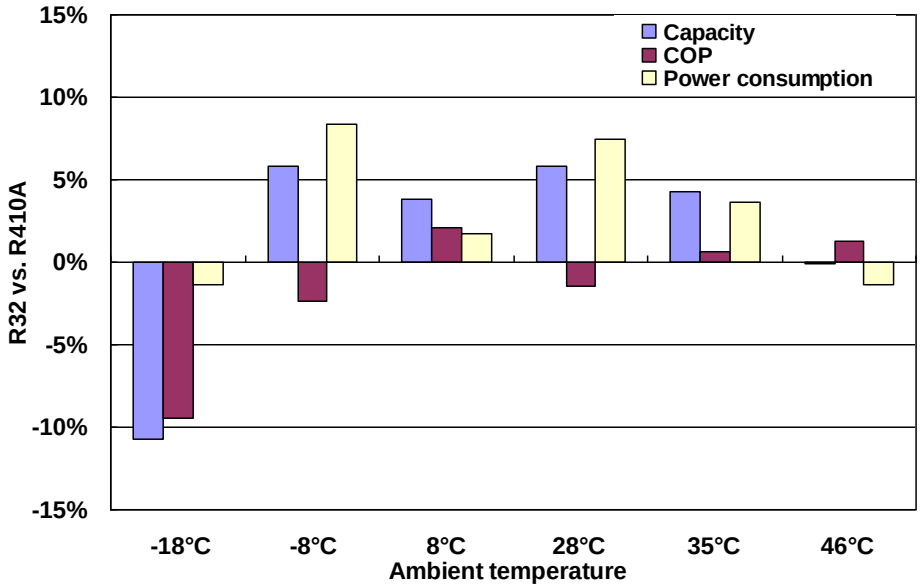

Figure 6-7: Two-stage thermodynamic cycle modeling using actual compressor efficiencies: capacity, COP and power consumption comparisons

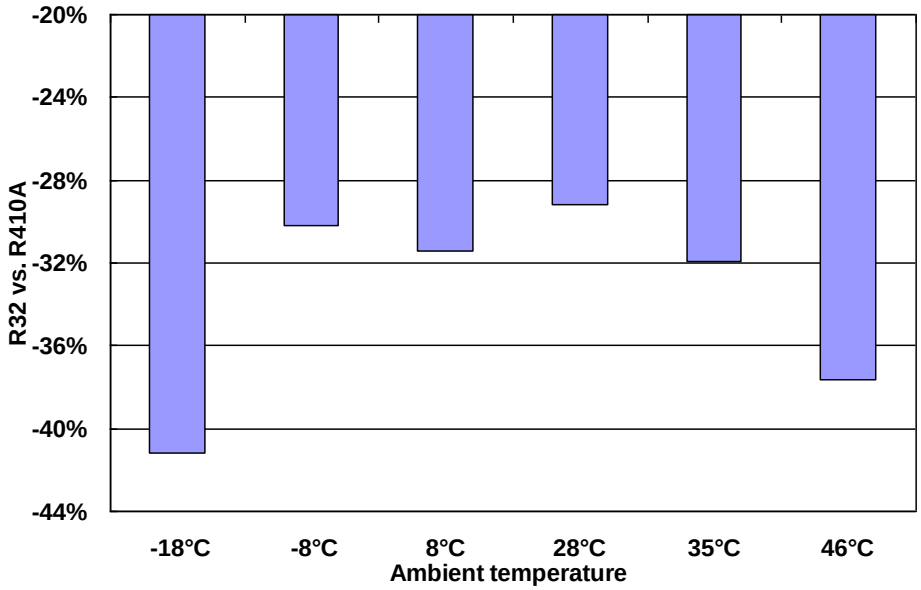

Figure 6-8: Two-stage thermodynamic cycle modeling using actual compressor efficiencies: total refrigerant mass flow rate comparison

6.2 Vapor injection cycle modeling

6.2.1 Model descriptions

Thermodynamic modeling provides theoretical insights of system performance, yet the actual heat exchanger performance effect was not taken into consideration. To model the actual system performance of a vapor injection cycle, a software package VapCyc developed by Richardson (2006) and Winkler (2009) was employed. The detailed description of VapCyc was elaborated by Winkler et al. (2008) and Winkler (2009), and therefore is not discussed here. VapCyc has proved to be effective and accurate in modeling a vapor compression cycle. Modeling results by Wang (2008) showed good agreement with corresponding experimental results. This software package has the capability to model vapor compression cycles with different system

configurations. Typical modeling capability includes modeling for a four-component single stage cycle, a single stage cycle with a suction line heat exchanger, and a two-stage flash tank cycle. In this modeling study, the flash tank cycle model was used. This cycle modeling tool integrates individual components, including the compressor, the condenser, the expansion valve, the flash tank, and the evaporator. Figure 6-9 shows a schematic of the flash tank cycle in VapCyc.

This two-stage compressor model is divided into the low-stage and high-stage sections. The input parameters are listed as follows: compressor displacement, RPM, volumetric efficiency, isentropic efficiency, and mechanical efficiency. The compressor RPM is 3,500, which follows the compressor specifications from the manufacturer. The mechanical efficiency was assumed to be between 0.9 and 1.0. At the extreme conditions of -18℃ and 46℃, the compressor motor operates at unfavorable conditions, and therefore, an efficiency of 0.9 was used. At the moderate ambient conditions of 28℃ and 8℃, an efficiency of 1.0 was used. An efficiency of 0.95 was assumed at the ambient conditions of 35℃ and -8℃. The volumetric efficiency and isentropic efficiency are critical parameters to the accuracy of the two-stage model. These two efficiencies vary with different operating conditions, and are directly from experimental data, as summarized in Figure 4-31. The indoor and outdoor heat exchangers were modeled using CoilDesigner, and they can be imported by VapCyc for the cycle modeling. Subcooling and superheating were also used as input parameters for the VapCyc modeling. The degrees of subcooling and superheating are both using experimental data.

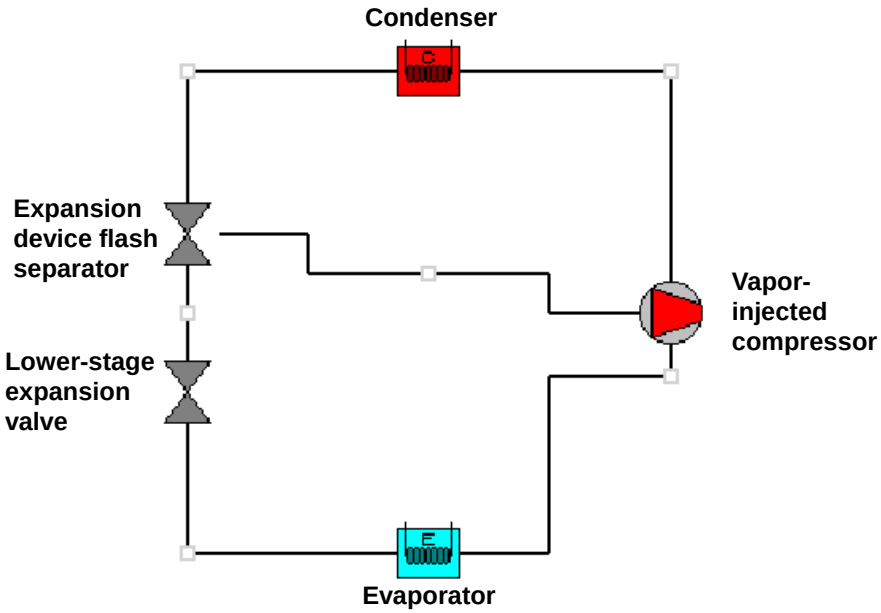

Figure 6-9: Schematic of the flash tank cycle in VapCyc

6.2.2 Simulation results

Figure 6-10 shows the system capacity comparison between experimental and modeling results. It can be seen that the variation is within 10%. Figure 6-11 shows the system power consumption comparison between the experimental and modeling results. It can be seen that the difference is also within 10%. This indicates that the model predicts the system capacity and power consumption accurately.

Figure 6-12 shows the system COP comparison. It can also be seen that the modeling results match well with the experimental data with ±10% accuracy. Figure 6-13 summaries the refrigerant mass flow rates comparison in the system. Both the suction and the total mass flow rates were modeled. The modeling results match well with the experimental data with ±10% accuracy. The overall modeling results show that VapCyc is quite effective in predicting the two-stage vapor injection system performance.

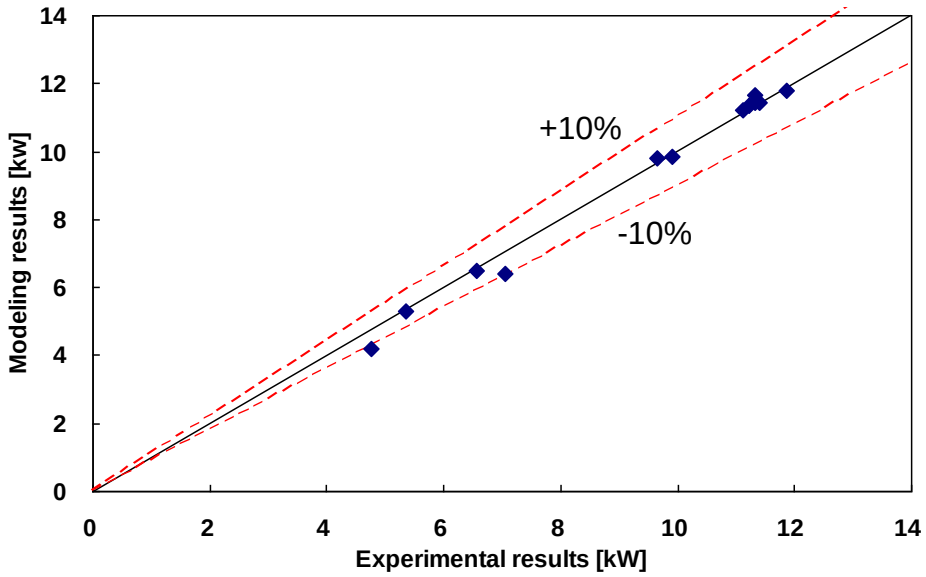

Figure 6-10: System capacity comparison

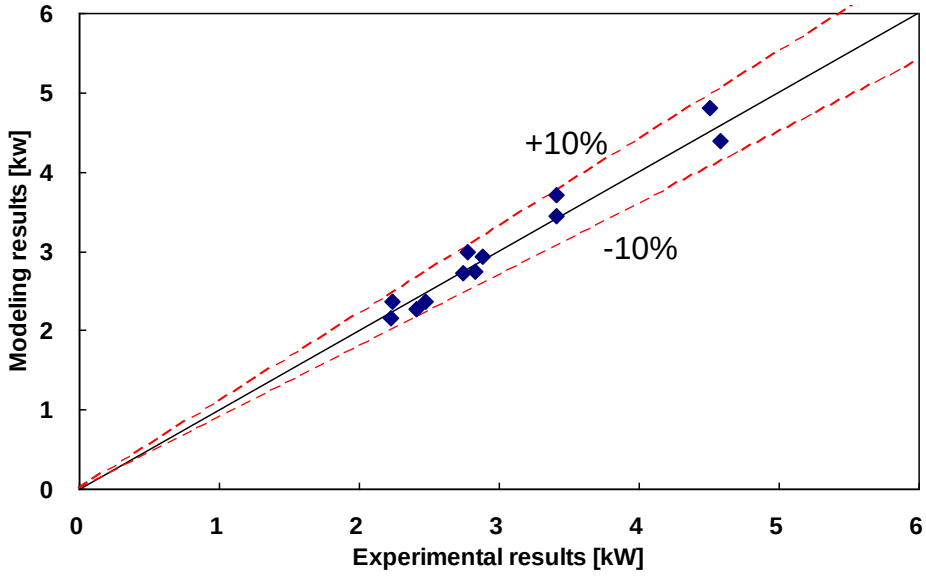

Figure 6-11: System power consumption comparison

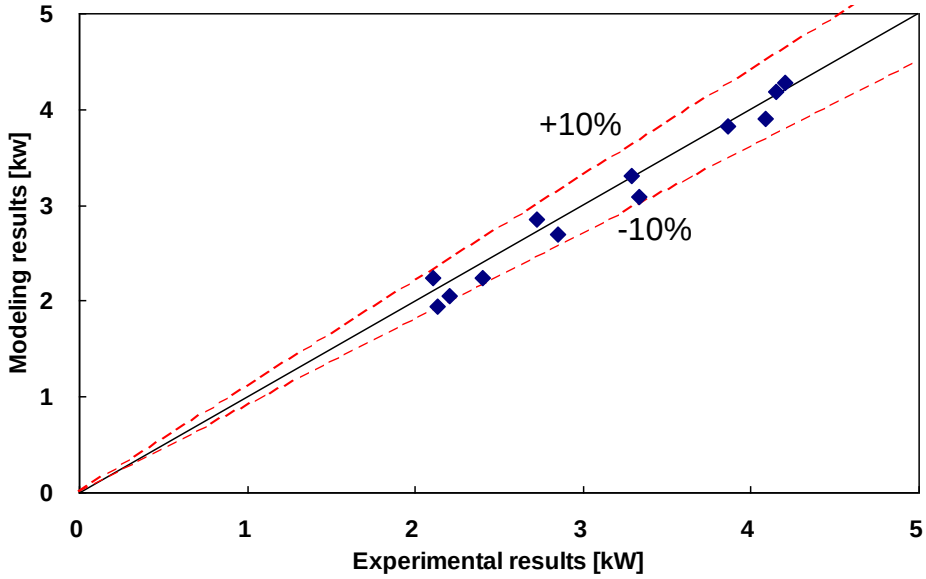

Figure 6-12: System COP comparison

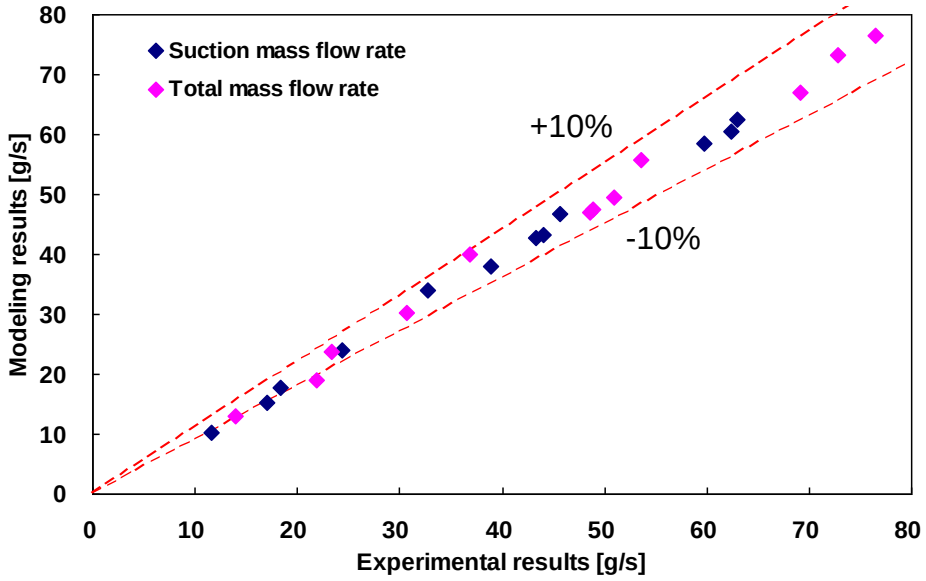

Figure 6-13: Compressor suction and total refrigerant mass flow rates comparison

6.3 Chapter summary and conclusions

This chapter summarizes the thermodynamic cycle modeling results as well as the actual cycle modeling results using VapCyc. Thermodynamic cycle modeling using ideal compressor efficiencies of 1.0 identifies the maximum performance that the system can reach. Difference between modeling results using ideal compressor efficiencies of 1.0 and actual compressor performances is from the actual compressor performance variations. Difference between experimental results and modeling results using actual compressor efficiencies is due to the actual heat exchanger performance. The comparison facilitates to pinpoint the reasons for the difference, and helps to better design the systems for R32.

Cycle modeling utilizing VapCyc integrates the two-stage compressor model as well as the heat exchanger models in CoilDesigner. The modeling results were validated against experimental results. Modeling results matched with experimental results within ±10% for the system capacity, COP, power consumption and refrigerant mass flow rates.

7. Optimization study for R32

From the drop-in test it was found that R32 outperformed R410A at most temperature conditions. However, R32 didn't show better performance than R410A at the extreme cooling and heating conditions in the vapor injection mode. Moreover, the current system is designed for R410A, and therefore, it is worthwhile to investigate the major components and perform an optimization study for a heat pump system utilizing R32. The following optimization study is based on the performance data for R32 from the experimental tests. Both the compressor and the heat exchangers have been investigated.

7.1 Compressor cooling study

7.1.1 Background and literature study

As seen from the experimental results, the compressor discharge temperature from using R32 was significant higher than that using R410A. High compressor discharge temperature can degrade the compressor oil and deteriorate the electrical coils of the compressor motor, and therefore, reduce the reliability of the compressor operation. Therefore, achieving proper compressor cooling is crucial for utilizing R32 in a vapor compressor cycle.

There are two types of compressor cooling: internal cooling and external cooling. Internal cooling typically refers to the cooling method by employing refrigerant or oil injection. External cooling can be achieved by circulating a certain fluid through the compressor to remove heat from the compressor. The fluid can be air, oil, water or even refrigerant. Wang et al. (2008b) investigated the benefits of compressor cooling theoretically. The systems utilizing different refrigerants R22, R410A, R134a and R744

were compared. They studied the method of cooling the compressor motor firstly. The greatest COP improvement of 5.4% was observed for R744 at AHRI low temperature refrigeration application (AHRI Standard 210/240, 2008). The capacity of the R744 system was improved by 5.5% for the same condition. However, cooling motor showed little effect in reducing the compressor power consumption. They also studied the benefits of removing heat from the compression chamber to approach an isothermal compression, as shown in Figure 7-1. As compared to the baseline case of ideal isentropic compression process, the compression work could be saved up to 14% at ASHRAE T condition (ANSI/AHRI Standard 540, 2004). ASHRAE T condition specifies the return gas and liquid temperatures to be 35 ℃ and 46 ℃, respectively. At an ambient temperature of 35 ℃, the evaporating and condensing temperatures are 7.2 ℃ and 54.4 ℃, respectively. However, the practicality of this approach is doubtable due to limited heat transfer area on the top of the compression chamber.

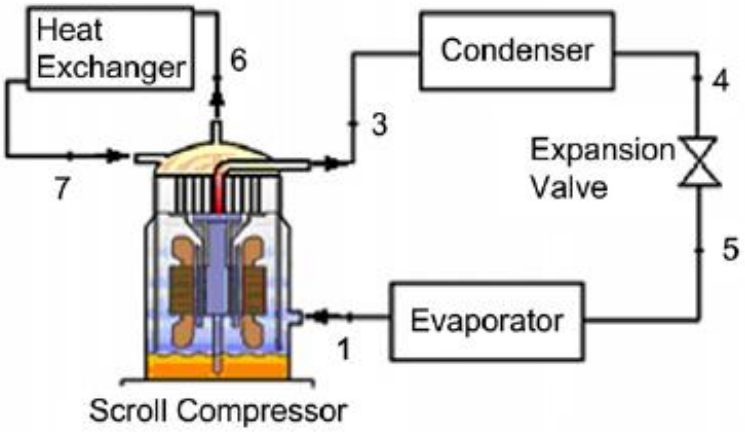

Figure 7-1: Schematic of compressor external cooling method (Wang et al., 2008b)

Sun et al. (2010) built a mathematical model to simulate the compression process of a scroll compressor with external cooling. The simulation results indicate that the isentropic efficiency is improved by 7.4% and the discharge temperature is reduced by 23℃ with water of 30℃ flowing through the cooling structure for the compression chamber. The improvement of compressor volumetric efficiency is limited. The water cooling effect on compressor performance remains almost the same with the variation of axial clearance, rotational speed and pressure ratio.

In addition to the approach of external cooling, there are different research groups conducting research on compressor internal cooling. Kang et al. (2008) investigated the effects of liquid refrigerant injection on the performance of a refrigeration system with an accumulator heat exchanger by varying the liquid injection rate at the conditions of constant expansion valve opening. In this study, the liquid was injected from the condenser outlet to the compressor suction port. It was found that the subcooling could be increased and the compressor suction temperature at high ambient temperatures could be decreased. They concluded that the liquid injection technique for the refrigeration system with an accumulator heat exchanger is an effective method for decreasing the compressor discharge temperature at high ambient temperatures. Liquid injection has also been applied for screw compressors to reduce compressor discharge temperature. Zlatanovic and Rudonja (2012) investigated a two-stage ammonia refrigeration system with screw compressors employing liquid injection. Refrigerant mass flow rate through the high-stage compressor was increased due to the low-stage compressor oil cooling process by

liquid injection. It was also mentioned that there is a possibility to increase specific isentropic work of the high-stage compressors.

As a result, internal cooling method was more effective in overall for reducing the compressor discharge temperature than the external cooling method. In this dissertation, the internal cooling was investigated to explore the benefits of compressor cooling in order to utilizing R32 in a two-stage vapor injection system. Figure 7-2 shows the schematic of a vapor injection system coupled with liquid injection. In additional to the stream of vapor injection, one more stream is added to introduce liquid refrigerant from the flash tank to be injected to the compressor. Figure 7-3 shows the P-h diagram of a vapor injection system coupled with liquid injection. By applying liquid injection, the mixing point of the low-stage discharge vapor and the injected vapor is shifted from state "5" to "5′". Therefore the compressor discharge temperature will also be shifted from state "2a" to "2a′". The energy balance equation for this process is shown in Equation 7-1. $\dot{m}_{inj,liq}$ indicates the injected liquid refrigerant mass flow rate, and h_{fg} represents the latent heat of the liquid refrigerant injected to the compressor.

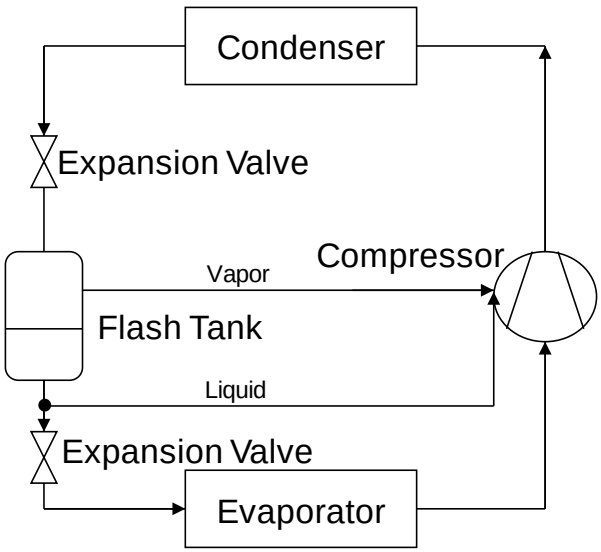

Figure 7-2: Schematic of a vapor injection system coupled with liquid injection

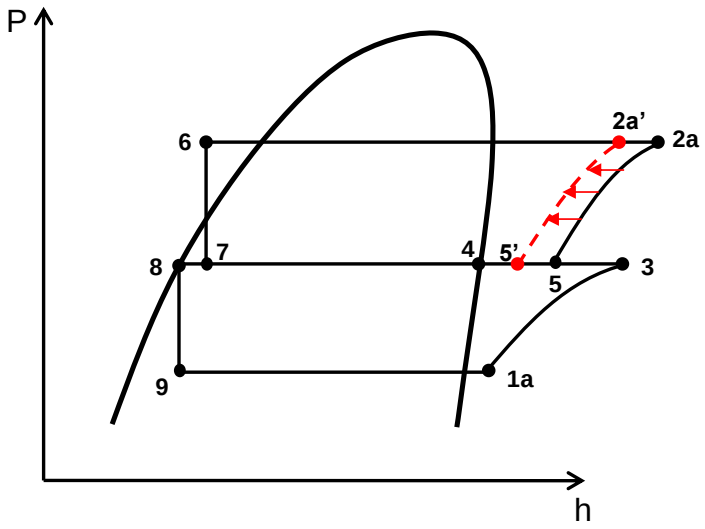

Figure 7-3: P-h diagram of a vapor injection system coupled with liquid injection

$$\dot{m}_{suc} h_3 + \dot{m}_{inj,vap} h_4 - \dot{m}_{inj,liq} h_{fg} = \dot{m}_{total} h_5 \qquad \textbf{Equation 7-1}$$

7.1.2 Liquid injection analysis

The liquid injection study was performed based on the experimentally verified compressor model described in Chapter 5. The liquid injection ratio is defined as the

injected liquid mass flow rate divided by the suction mass flow rate, as shown in Equation 7-2. $\dot{m}_{inj,liq}$ stands for the injected liquid mass flow rate, and β indicates the liquid injection ratio. The governing equations of the two-stage compressor model utilizing vapor coupled liquid injection remain mostly the same. The differences in equations are shown as follows. The total mass balance equation shown in Equation 5-5 is substituted by Equation 7-3, and the energy balance at the injection port described by Equation 5-6 is substituted by Equation 7-1. The overall energy balance is depicted by Equation 7-4 instead of Equation 5-26.

$$\beta = \frac{\dot{m}_{inj,liq}}{\dot{m}_{total}} \qquad \textbf{Equation 7-2}$$

$$\dot{m}_{total} = \dot{m}_{suc} + \dot{m}_{inj,vap} + \dot{m}_{inj,liq} \qquad \textbf{Equation 7-3}$$

$$\dot{m}_{total} h_2 - \dot{m}_{suc} h_1 - \dot{m}_{inj,vap} h_4 - \dot{m}_{inj,liq} h_{fg} = \dot{P}_{comp} - \dot{Q}_{loss} \qquad \textbf{Equation 7-4}$$

7.1.2.1 Cooling mode

By solving the governing equations, the performance of the system utilizing both vapor and liquid injection can be calculated. Figure 7-4 shows the capacity, COP and discharge temperature variations of an R32 system utilizing liquid injection at the ambient temperature of 46℃. It can be seen that with the increasing liquid injection ratio, the compressor discharge temperature could be decreased dramatically. With a liquid injection ratio of 4%, the compressor discharge could be decreased from 121℃ to 95℃. This can significantly increase the reliability of compressor operation during high ambient temperature of 46℃. It is also noticed that there is some degradation of the

cooling capacity and COP. The reason is that the refrigerant mass flow rate through the evaporator is decreased due to the fact that partial liquid refrigerant is extracted to cool the compressor. The decrease for cooling capacity and COP was found to be 4% and 2%, respectively, with a liquid injection ratio of 4%. This is acceptable considering the benefits of a more reliable operating compressor.

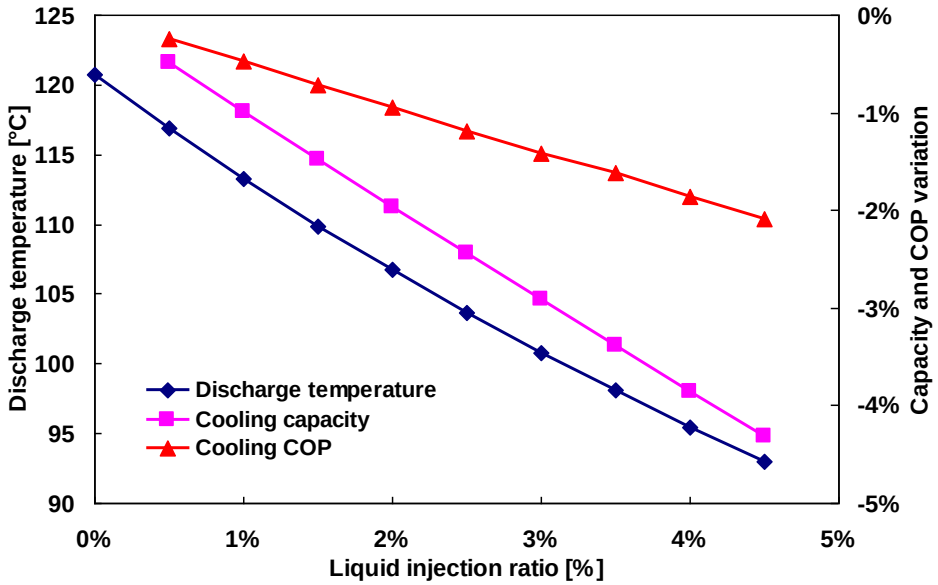

Figure 7-4: Capacity, COP and discharge temperature variations of an R32 system utilizing liquid injection at the ambient temperature of 46 ℃, baseline is a system without liquid injection

Figure 7-5 shows the high-stage suction temperature and density variations of an R32 system utilizing liquid injection at the ambient temperature of 46 ℃. With liquid injection, the high-stage suction temperature is decreased significantly. This results in the benefits of increasing the suction gas density, which can also be seen from the same figure. This indicates that more refrigerant flows through the high-stage compressor, and

the volumetric efficiency of the high-stage compressor is increased as well. Figure 7-6 shows the refrigerant mass flow rate variations. The suction mass flow rate decreases due to liquid injection, yet both the injected vapor and total mass flow rates increase due to the increased density at the high-stage. For the cooling mode, this is not beneficial for the capacity. However, this can be beneficial for the heating mode operation, which is shown in the next section of this chapter.

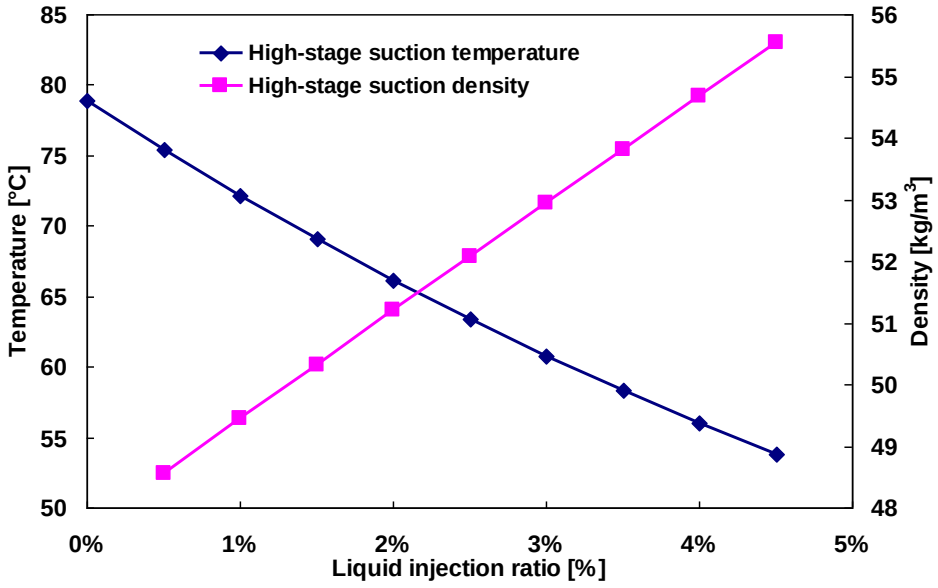

Figure 7-5: High-stage suction temperature and density variations of an R32 system utilizing liquid injection at the ambient temperature of 46 ℃

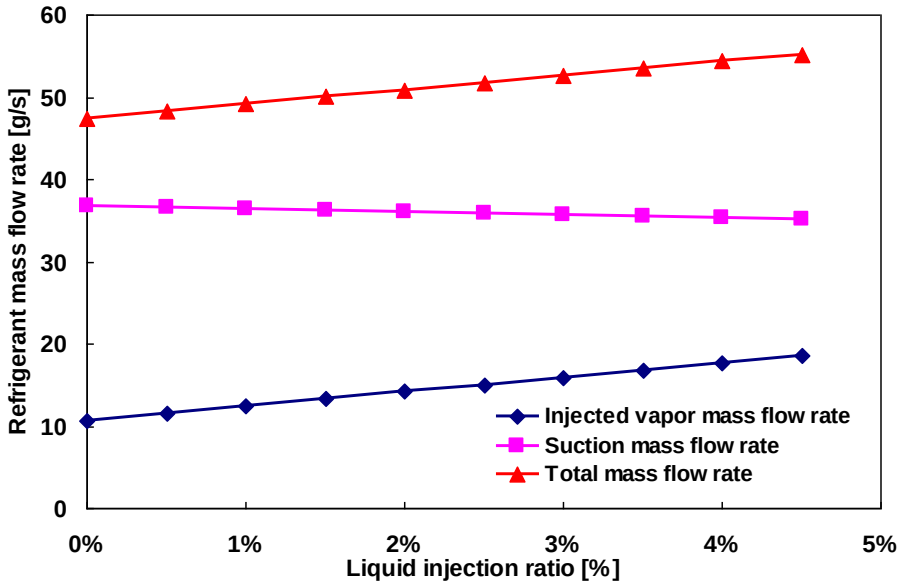

Figure 7-6: Refrigerant mass flow rate variations of an R32 system utilizing liquid injection at the ambient temperature of 46 ℃

7.1.2.2 Heating mode

Figure 7-7 shows the capacity, COP and discharge temperature variations of an R32 system utilizing liquid injection at the ambient temperature of -18 ℃. It can also be seen that the compressor discharge temperature is decreased significantly with increasing liquid injection ratio. With a liquid injection ratio of 4%, the compressor discharge temperature is decreased from 129 ℃ to 92 ℃. The liquid injection benefits become more pronounced for the heating mode than the cooling mode. It can also be seen that both the heating capacity and COP increases with the increasing liquid injection ratio. This is due to the increase of high-stage suction gas density, which leads to a higher refrigerant mass flow rate through the condenser. The high-stage suction gas density variation is shown in Figure 7-8. The refrigerant mass flow rate variations are shown in Figure 7-9. With the

increasing mass flow rate through the condenser, the heating capacity of the system increases. Although the refrigerant mass flow rate increases, the system power consumption remains almost the same. This is due to the fact that the compressor discharge temperature decreases, which compromise the power increase due to the mass flow rate increase. As a result, the heating COP increases as well.

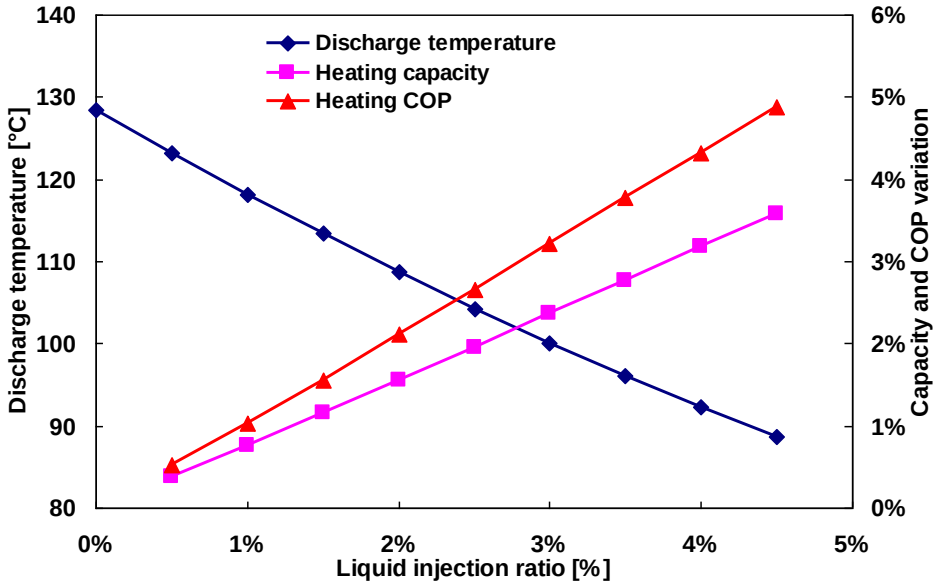

Figure 7-7: Capacity, COP and discharge temperature variations of an R32 system utilizing liquid injection at the ambient temperature of -18 ℃, baseline is a system without liquid injection

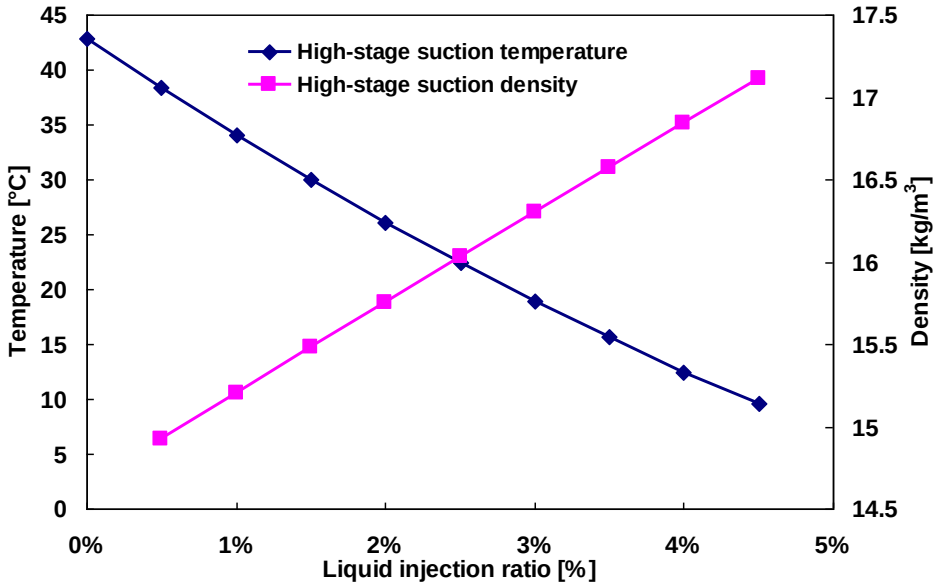

Figure 7-8: High-stage suction temperature and density variations of an R32 system utilizing liquid injection at the ambient temperature of -18 ℃

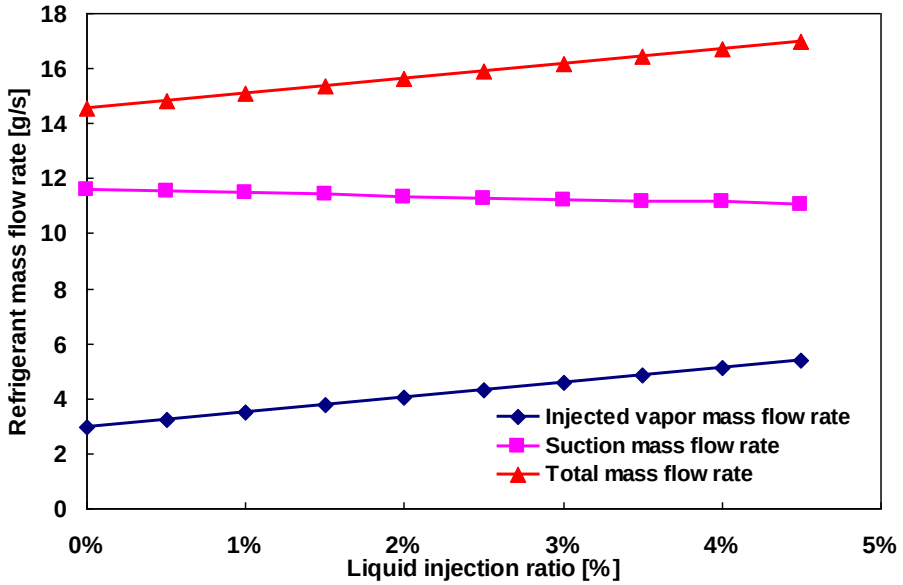

Figure 7-9: Refrigerant mass flow rate variations of an R32 system utilizing liquid injection at the ambient temperature of -18 ℃

7.1.3 Other compressor cooling approaches

In the current study, the compressor utilized in the system is a scroll compressor with a vapor injection port in an intermediate stage of the compressor. If the compressor selection is constrained, then other cooling approach could be employed as well. Figure 7-10 shows the schematic of compressor intercooling for a two-stage compression system. In this case, an internal heat exchanger could be employed to dissipate heat to the ambient, therefore, achieving compressor cooling to reduce the compressor discharge temperature. This system involves different compressor designs, which is beyond the scope of this dissertation, and therefore it's not discussed in detail here.

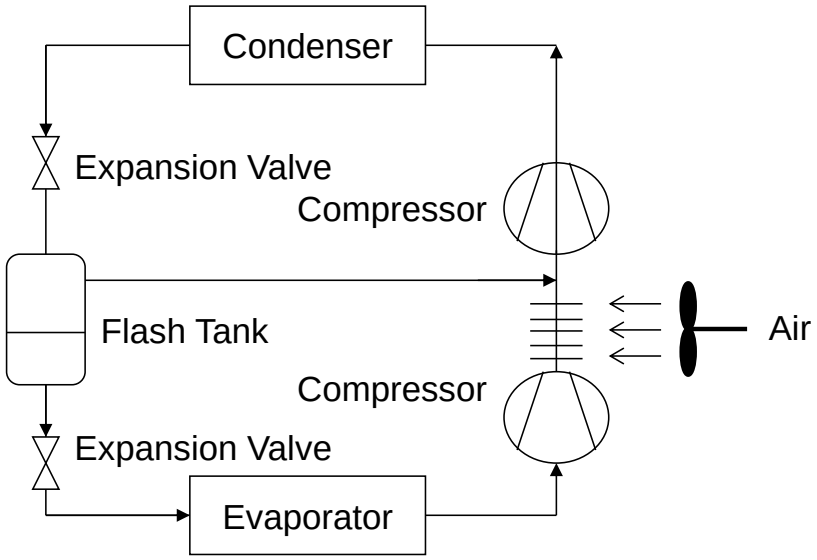

Figure 7-10: Compressor intercooling for a two-stage compression system using two separate compressors

7.2 Heat exchanger design optimization

Due to the thermophysical property differences between R32 and R410A, heat exchangers designed for R410A may not suit for R32 perfectly. Therefore, the heat

exchanger used in the current R410A system can be optimized for R32 use. The specifications of the baseline indoor and outdoor heat exchangers are shown in Table 2-1. A parametric study was conducted first to identify a proper range of different design variables for the new heat exchanger. Then a multi-objective optimization was performed utilizing Multi-Objective Genetic Algorithm (MOGA) to search for the optimum designs for the indoor and outdoor heat exchangers.

7.2.1 Parametric study

The key parameters of a heat exchanger are as follows: tube diameter, tube length, tube horizontal and vertical spacing, fin pitch (FPI), number of tubes per bank, number of banks, and number of circuitry. Different combinations of these parameters can lead to totally different heat exchanger designs, and therefore, various heat exchanger performances.

In the HVAC industry, as the material cost has been increasing over the years, heat exchanger manufacturers have been looking for designs that use smaller diameter tubes. 5 mm copper tube has been raising attention in recent years (Wu et al., 2012; Hipchen et al., 2012). The major benefit of using a smaller diameter tube is the low material cost and better performance. However, challenges arise with smaller diameter tubes because the refrigerant-side pressure drop becomes much higher as the tube diameter decreases. Therefore, the number of tubes needs to be increased, and the circuitry design is also different. In this research work, the copper tube outer diameter was fixed to be 5 mm. The wall thickness of the copper tube is 0.21 mm and is commercially available (Hipchen et al., 2012).

The design variables of this parametric study include: tube length, horizontal and vertical spacing, FPI, number of tubes per bank, number of tube banks, and circuitry number. The design matrix for the indoor heat exchanger is summarized in Table 7-1. The specified values of each design variable were selected with a reasonable range based on the current heat exchanger specifications. It should be noted that each column specifies the possible design options for that specific design variable. Therefore the total number of designs is by multiplying the number of designs for each design variable. The total number of designs for the indoor heat exchanger is 10,125. The indoor heat exchanger is a symmetric "A" shape coil, and therefore only one slab was used in the design optimization, as shown in Figure 7-11. It should be noted that all the optimization results of the indoor heat exchanger presented in this chapter only refer to one slab of the heat exchanger. Table 7-2 shows the design matrix for the outdoor heat exchanger. The outdoor heat exchanger is physically larger than the indoor heat exchanger, and therefore, the computation effort for the outdoor heat exchanger is more expensive than the indoor heat exchanger. As a result, the design matrix size was decreased to reduce the computation effort. The total number of designs of the outdoor heat exchanger is 2,187.

Table 7-1: Indoor heat exchanger design matrix for parametric study (One slab)

Tube length [mm]	Horizontal spacing [mm]	Vertical spacing [mm]	FPI	Tubes per bank	Tube banks	Circuitry number
386	7.5	7.5	8	40	4	7
435	12.0	12.0	12	50	5	8
483	16.5	16.5	16	60	6	9
531	20.9	20.9				
580	25.4	25.4				

Table 7-2: Outdoor heat exchanger design matrix for parametric study

Tube length [mm]	Horizontal spacing [mm]	Vertical spacing [mm]	FPI	Tubes per bank	Tube banks	Circuitry number
2052	7.5	7.5	18	40	3	8
2309	11.6	15.8	22	50	4	10
2565	15.7	24.1	26	60	5	12
2822						
3078						

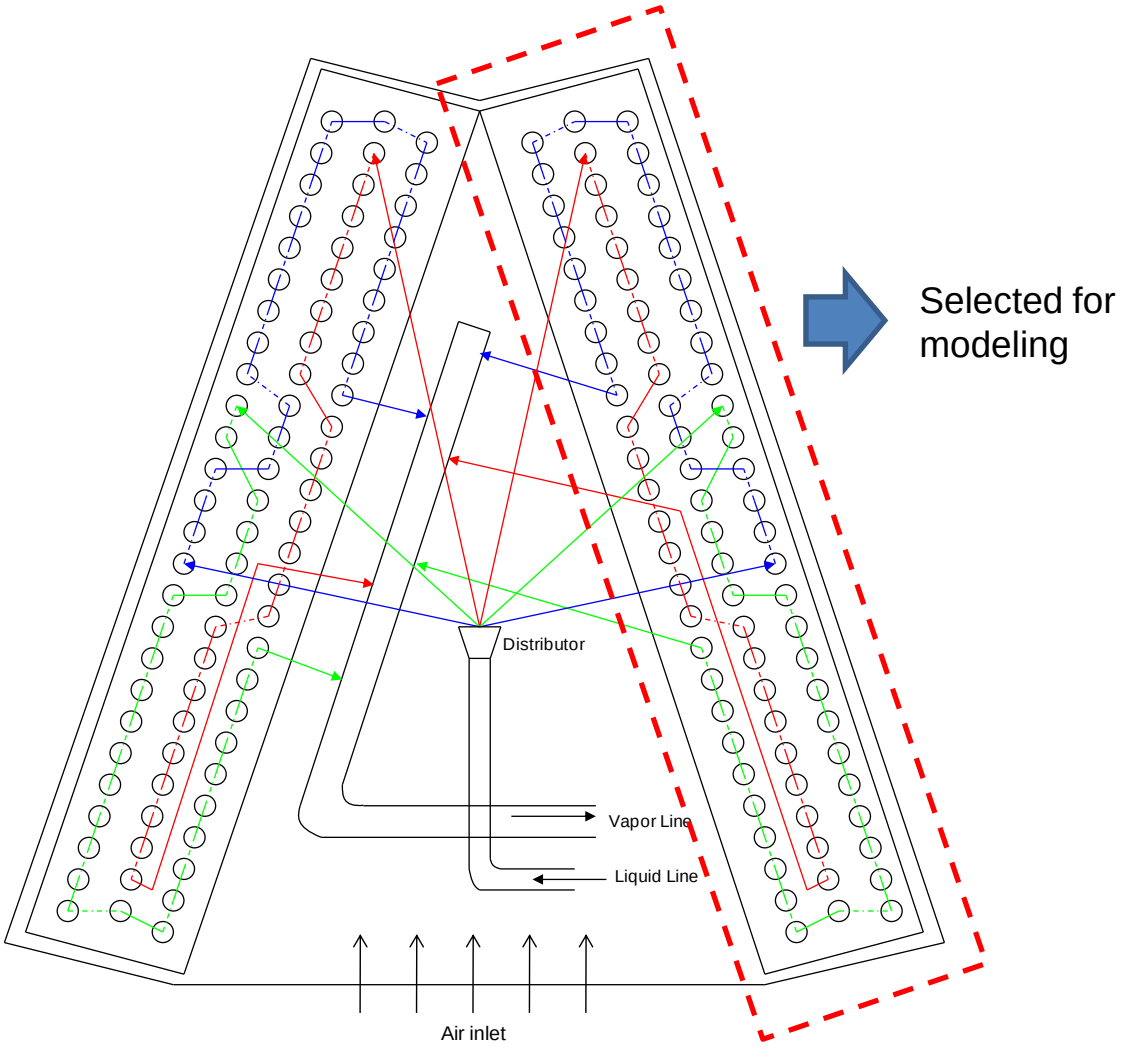

Figure 7-11: Schematic of the indoor heat exchanger selected for design optimization study

The parametric study was performed in CoilDesigner. Heat transfer and pressure drop correlations used the same as used in the heat exchanger modeling in Chapter 5, and are shown in Table 5-4. The heat exchanger's air-side and refrigerant-side inlet conditions used the experimental results at the ambient condition of 46 ℃, since the heat exchanger is expected to operate reliably at this extreme cooling load condition. If the

heat exchanger can satisfy the capacity requirement for this extreme condition, it would also satisfy the requirement at other conditions. The heat exchanger model in CoilDesigner has been validated against the experimental data to ensure the accuracy of the model, as discussed before in Chapter 5.

Proper heat exchanger design should satisfy certain criteria. For the air-side pressure drop, the new heat exchanger should have less or equivalent air-side pressure drop compared to the baseline. For the refrigerant-side pressure drop, it was found from the experimental tests that R32 has on average 25% less pressure drop than R410A at all test conditions due to the density difference. Therefore, the refrigerant-side pressure drop of the new heat exchanger allows 25% more pressure drop than the baseline case. Certain degrees of superheat and subcooling need to be maintained for the evaporator and condenser, respectively, to avoid two-phase outlet conditions for the heat exchangers. In the cooling mode, the indoor heat exchanger works as the evaporator, and therefore, the outlet should have a certain degree of superheat to avoid two-phase outlet condition. The outdoor heat exchanger functions as the condenser, and therefore, the outlet should achieve some degree of subcooling. In this study, the degree of superheat and subcooling requirement is greater than 1 K. Two design objectives investigated here are the maximizing the heat exchanger capacity and minimizing the material cost.

Figure 7-12 shows the parametric study results of the indoor heat exchanger. It can be seen that the feasible solutions only occupy a small region of the original design space. There is also a trade-off between cost and capacity. It can also be seen that there is

a sharp vertical edge on the right side of the solutions, which indicates the maximum capacity that can be achieved for the given inlet refrigerant-side and air-side conditions.

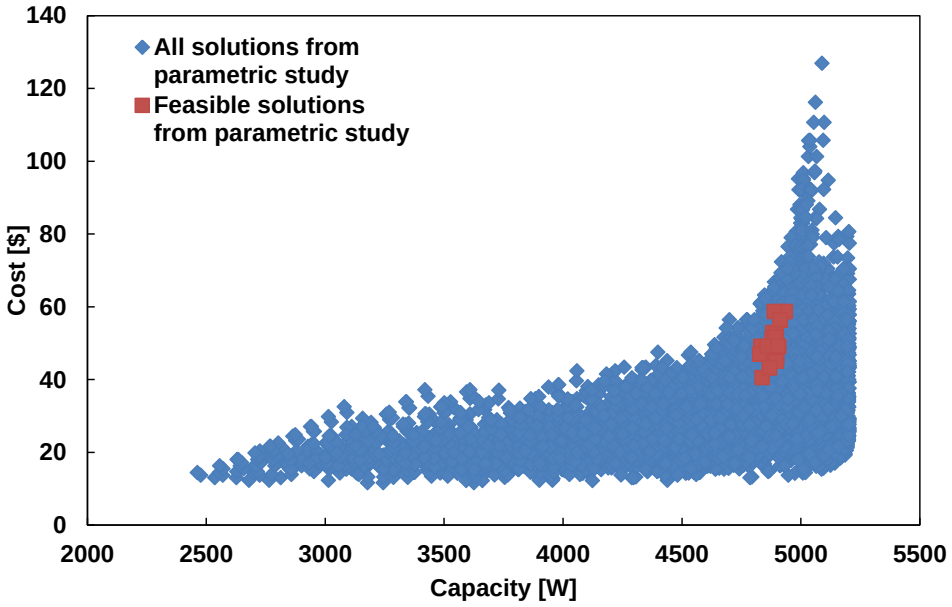

Figure 7-12: Parametric study results of the indoor heat exchanger (one slab)

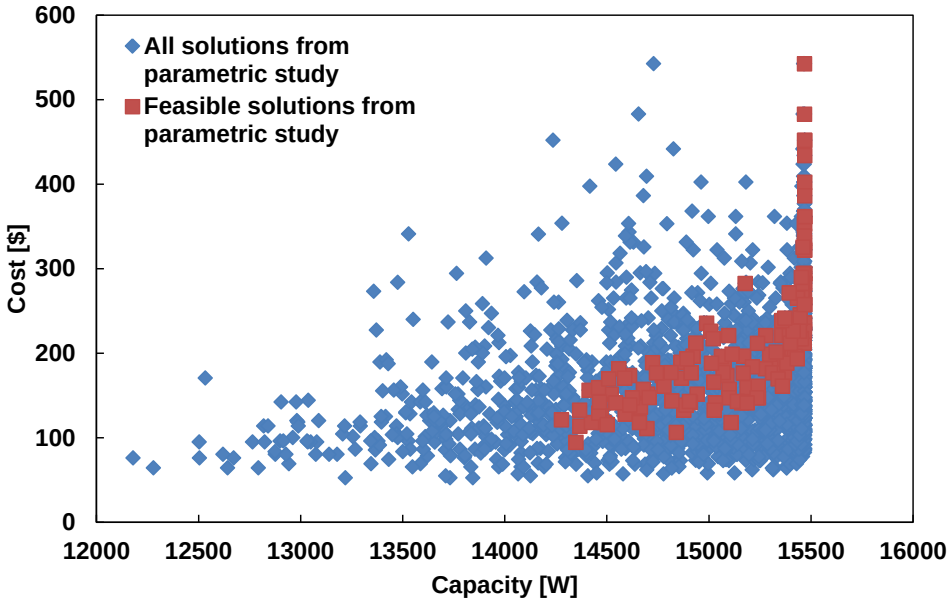

Figure 7-13: Parametric study results of the outdoor heat exchanger

Figure 7-13 shows the parametric study results of the outdoor heat exchanger. It can also be seen that there is a trade-off between capacity and cost. As the capacity is approaching 15,500 W, increasing the cost wouldn't lead to further capacity improvement. This is limited by the maximum heat transfer between the refrigerant and air sides.

7.2.2 Optimization utilizing Multi-Objective Genetic Algorithm

7.2.2.1 General description

The basic idea of genetic algorithm (GA) is to generate a new set of designs (population) from the current set such that the average fitness of the population is improved. The process is continued until a stopping criterion is satisfied or the number of iterations exceeds a specified limit (Arora, 2004). The GA methods are applicable to optimization problems in which the objective functions and/or constraint functions are highly nonlinear, non-differential, or discontinuous. In addition, the variables can be continuous, discrete, or a combination of the two. The GA method only requires the values of the objective functions and/or constraint functions and not their derivatives to reach the optimum. In addition, this method can converge to the global optimum (Magrab et al., 2000). Therefore, it's an effective approach to perform heat exchanger optimization to achieve the optimum design. GA can be applied to optimization problems that have multiple objectives. In this study, MOGA was employed to maximize the heat exchanger capacity and minimize the material cost for the two contradictory objectives.

This multi-objective optimization problem can be formulated as follows:

Objectives:

- Maximize capacity

- Minimize material cost

Design variables:

Continuous variables:

- Tube length
- Tube horizontal spacing
- Tube vertical spacing

Discrete variables:

- Number of tube circuitry
- Number of tube banks
- Number of tubes per bank
- FPI

Constraints:

- Refrigerant-side pressure drop
- Air-side pressure drop
- Degree of superheat (for evaporator)
- Degree of subcooling (for condenser)

The optimization problem formulation was written in C# programming language, and built to connect CoilDesigner and the MOGA optimizer developed in CEEE. Different design variables were defined in C# directly, and MOGA can select different combinations of design variables, and evaluate them in CoilDesigner. Through progressing evaluations of different generations, optimum solutions can be obtained.

Different circuitries can also be generated in CoilDesigner automatically given the specific design variables. The population in MOGA was set to be 100, coupled with a replacement number of 10, and the maximum number of iteration was set to be 100. The upper and lower bounds of each design variable are shown in Table 7-3. All the refrigerant-side and air-side input parameters for the heat exchangers used the same as in the parametric study.

Table 7-3: Upper and lower bounds of HX optimization using MOGA

Parameter	Indoor HX		Outdoor HX	
	Lower bound	Upper bound	Lower bound	Upper bound
Tube length [mm]	386	580	2052	3078
Horizontal spacing [mm]	7.5	25.4	7.5	15.7
Vertical spacing [mm]	7.5	25.4	7.5	24.1
FPI	8	20	10	30
Tubes per bank	20	60	20	60
Tube banks	1	8	1	8
Circuitry number	1	15	1	15

7.2.2.2 Indoor heat exchanger

Figure 7-14 shows the optimization results of the indoor heat exchanger. The green triangle symbols represent all successful evaluations from the optimization study. It can be seen that these points fall into the region of the parametric study results, but with a more scattered distribution. This indicates that the MOGA optimizer was able to find different designs, and push the optimum solutions towards the Pareto front that maximizes the capacity and minimizes the material cost. Among all the successful evaluations, only three feasible solutions were found after satisfying the three constraints: air-side and refrigerant-side pressure drops, and degree of superheat at the heat exchanger outlet. The air-side pressure drop should be less than that of the baseline heat exchanger. The refrigerant-side pressure drop should be less than 25% increase of the baseline pressure drop. The outlet superheat should be greater than 1 K. It should be noted that the heat exchanger volume was not used as a constraint in this particular case, because the optimization would return empty solution if the heat exchanger constraint was added as well. An over-constrained problem does not return feasible designs of the heat exchanger.

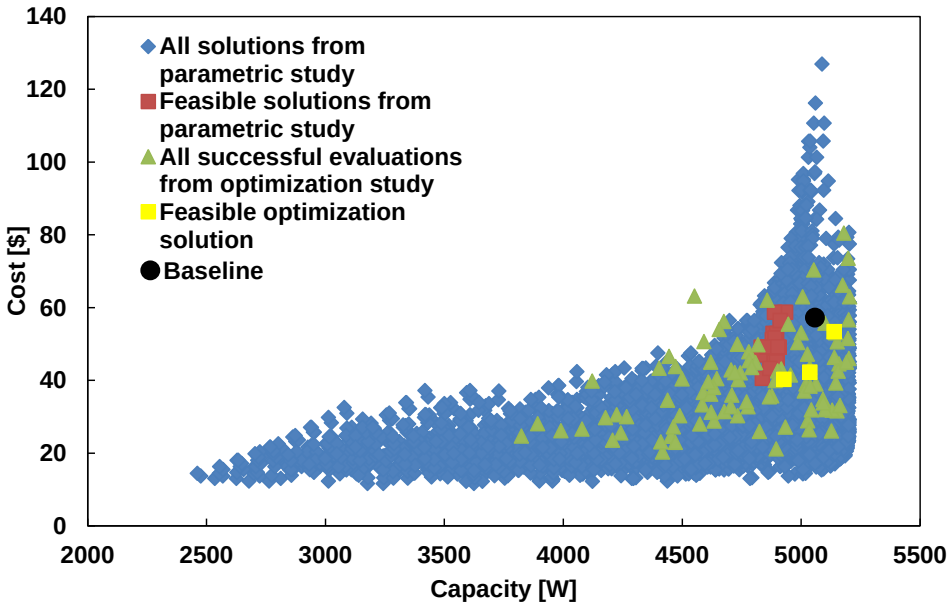

Figure 7-14: Optimization results of indoor heat exchanger (one slab), without a constraint on heat exchanger volume

Table 7-4 shows the comparison of the baseline design and optimum design of the indoor heat exchanger. It can be seen that the tube length is decreased, and the tube horizontal and vertical spacing is also decreased. The decreased tube diameter brings the benefits of a cost reduction of 26%, as seen from $57 to $42. The capacity is only 1% less than the baseline case. The reduced diameter heat exchanger requires more tubes, as can be seen from the increased number of tubes as well as tube banks and circuitries. It can also be seen that the heat exchanger volume increase is 70% with the given constraints. The internal volume increase is only 2%, which indicates almost the same refrigerant charge is needed as the baseline heat exchanger.

Table 7-4: Comparison of baseline design and optimum design of indoor heat exchanger (one slab), without a constraint on heat exchanger volume

Parameter	Baseline design	Optimum design
Tube length [mm]	483	455
Tube OD [mm]	9.5	5.0
Horizontal spacing [mm]	25.4	18.3
Vertical spacing [mm]	25.4	19.7
Tubes per bank	26	42
Tube banks	3	6
FPI	12	13
Circuitry	3	10
Capacity [W]	5064	5037
Cost [$]	57	42
HX volume [m^3]	0.02431	0.04134
Internal volume [m^3]	0.00185	0.00189

In this optimization study, it was noticed that the optimum design results are very sensitive to the refrigerant-side pressure drop constraint. This is because of the significant decrease of tube diameter. Therefore, the optimum solution shows a certain penalty in the overall heat exchanger volume by utilizing more number of tubes. However, if the refrigerant-side constraint can be relaxed, the goal of reducing heat exchanger volume can also be achieved. This is feasible in practice because the increased pressure drop in a

heat exchanger does not necessarily lead to a significant power increase on a system level. A second optimization study was performed with relaxing the refrigerant-side pressure drop constraint to be double that of the baseline pressure drop. In addition, a fourth constraint that the heat exchanger overall volume should be less than the baseline was added. The optimum results are shown in Figure 7-15. It can be seen that there are three feasible solutions.

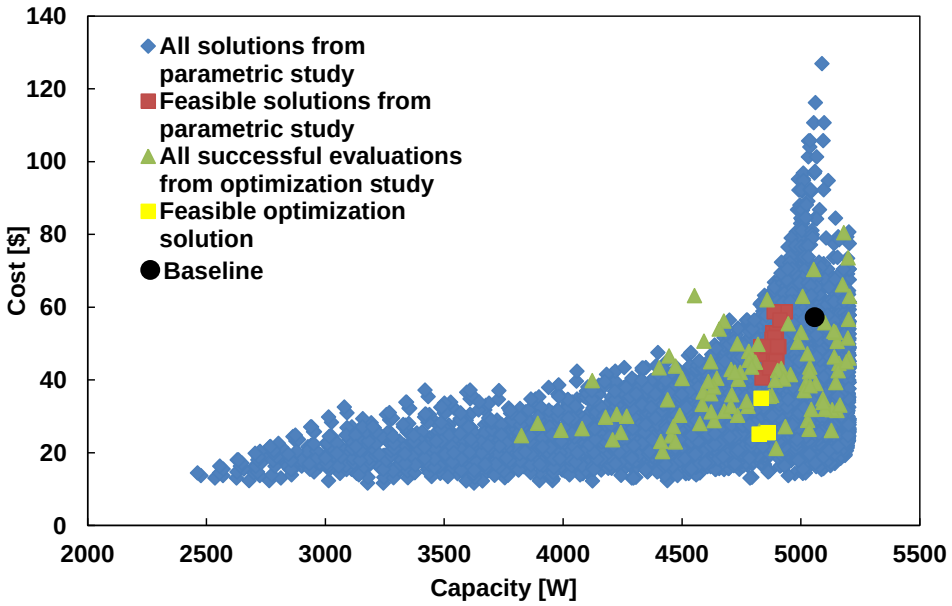

Figure 7-15: Optimization results of indoor heat exchanger (one slab), with a constraint on heat exchanger volume, relax refrigerant-side pressure drop

Table 7-5 shows the comparison of baseline and optimization results after applying the heat exchanger volume constraint while relaxing the refrigerant side pressure drop constraint. It can be seen that 56% cost reduction could be achieved. The optimized heat exchanger shows a reduction of 7% in volume, and 32% in internal volume. The baseline heat exchanger requires a refrigerant charge of 0.26 kg, and the

charge of the optimum heat exchanger could be reduced to 0.18 kg due to the internal volume decrease. There was a small degradation of 4% in capacity. As a result, there are always trade-offs among cost, volume, capacity and pressure drops.

Table 7-5: Comparison of baseline design and optimum design of indoor heat exchanger (one slab), with a constraint on heat exchanger volume, relax refrigerant side pressure drop

Parameter	Baseline design	Optimum design
Tube length [mm]	483	479
Tube OD [mm]	9.5	5.0
Horizontal spacing [mm]	25.4	14.8
Vertical spacing [mm]	25.4	20.0
Tubes per bank	26	40
Tube banks	3	4
FPI	12	13
Circuitry	3	8
Capacity [W]	5064	4862
Cost [$]	57	25
HX volume [m^3]	0.02431	0.02269
Internal volume [m^3]	0.00185	0.00126

7.2.2.3 Outdoor heat exchanger

The optimization of the outdoor heat exchanger was performed in a similar manner. Figure 7-16 shows the optimization results of the outdoor heat exchanger without applying the constraint on the heat exchanger volume. It can also be seen that the optimization results fall into the region of the parametric study, and four feasible solutions can be observed. A significant improvement can be achieved comparing the optimized solutions to the baseline design.

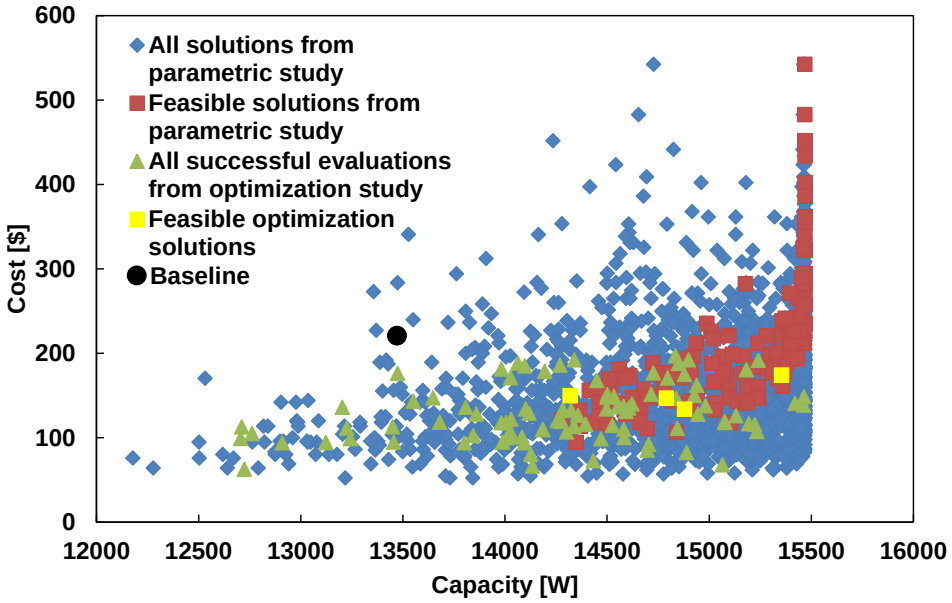

Figure 7-16: Optimization results of outdoor heat exchanger, without a constraint on heat exchanger volume

Table 7-6 shows the comparison of the baseline and optimum designs of the outdoor heat exchanger. It can be seen that with the decrease of the tube diameter, the tube horizontal and vertical spacing decrease correspondingly. To satisfy the pressure drop requirements, the number of tubes and circuitries increases. An improvement of

10% in capacity is observed, and a reduction of 33% in cost is also observed. However, the heat exchanger volume also increases compared to the baseline design. An increase of 42% in overall volume and 30% in tube internal volume are observed.

Table 7-6: Comparison of baseline design and optimum design of outdoor heat exchanger, without a constraint on heat exchanger volume

Parameter	Baseline design	Optimum design
Tube length [mm]	2565	2921
Tube OD [mm]	7.9	5.0
Horizontal spacing [mm]	15.7	10.8
Vertical spacing [mm]	24.1	20.2
Tubes per bank	32	46
Tube banks	2	3
FPI	22	21
Circuitry	6	11
Capacity [W]	13492	14791
Cost [$]	218	147
HX volume [m^3]	0.06211	0.08794
Internal volume [m^3]	0.00512	0.00664

In order to reduce the heat exchanger volume, the refrigerant-side pressure constraint has to be relaxed. It is also noticed that the air-side pressure drop constraint has to be relaxed since the baseline heat exchanger shows a small air-side pressure drop of

4.4 Pa due to low air velocity and large heat exchanger area. Therefore, the air-side pressure drop constraint was set to be less than 30 Pa to re-optimize the outdoor heat exchanger. Figure 7-17 shows the optimization results with a constraint on the heat exchanger volume, and relaxing the refrigerant-side pressure drop to be doubling the baseline, and increasing the air-side pressure drop limit to be 30 Pa. A further improvement can be achieved comparing the optimized solutions to the baseline design

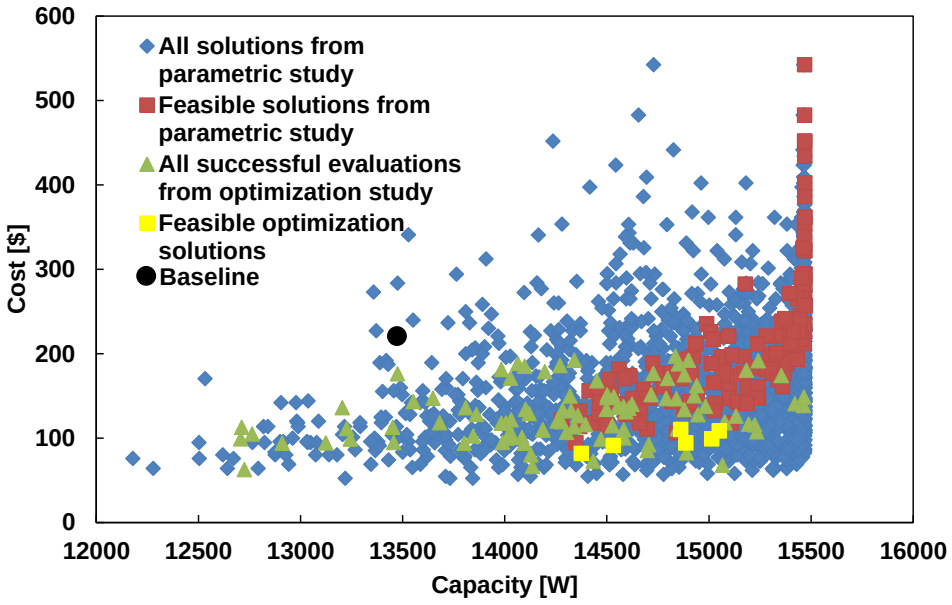

Figure 7-17: Optimization results of outdoor heat exchanger, with a constraint on heat exchanger volume, relax refrigerant-side and air-side pressure drops

Table 7-7 shows the optimum design of the heat exchanger when the volume constraint has been considered while relaxing the refrigerant-side and air-side pressure drops. It can be seen that a capacity improvement of 10% can be achieved, and cost reduction can reach up to 57%. Heat exchanger overall volume can be reduced by 3%, and the tube internal volume can be reduced by 8%. The baseline heat exchanger shows a

refrigerant charge amount of 1.21 kg, and the optimized heat exchanger only requires 1.11 kg refrigerant charge due to the internal volume decrease.

Table 7-7: Comparison of baseline design and optimum design of outdoor heat exchanger, with a constraint on heat exchanger volume, relax refrigerant-side and air-side pressure drops

Parameter	Baseline design	Optimum design
Tube length [mm]	2565	2064
Tube OD [mm]	7.9	5.0
Horizontal spacing [mm]	15.7	13.6
Vertical spacing [mm]	24.1	15.5
Tubes per bank	32	46
Tube banks	2	3
FPI	22	18
Circuitry	6	9
Capacity [W]	13492	14887
Cost [$]	218	94
HX volume [m^3]	0.06211	0.06004
Internal volume [m^3]	0.00512	0.00469

Overall the optimum designs of the outdoor heat exchanger show better results than the indoor heat exchanger. The main reason is that the outdoor heat exchanger is

much larger than the indoor heat exchanger. Therefore, the baseline design of the outdoor heat exchanger has more room for improvement than the indoor heat exchanger.

In this optimization study, the heat exchanger material cost and capacity were selected as the design objectives. Essentially the design objectives can also be heat exchanger volume or pressure drops, and it really depends on what the designers are mostly interested in. However, it should be noted that there are always trade-offs among cost, volume, capacity and pressure drops.

7.3 Chapter summary and conclusions

This chapter investigates compressor cooling and heat exchanger optimization for a R32 system. High compressor discharge temperature is a major challenging issue for R32, and by employing liquid injection, the compressor discharge temperature can be decreased dramatically. For the cooling mode, there is a slight decrease of cooling capacity and COP due to less refrigerant flowing through the evaporator. For the heating mode, liquid injection even increases the heating capacity and COP due to the increase of upper-stage volumetric efficiency, which leads to higher refrigerant mass flow rate through the condenser.

Heat exchangers designed for R410A may not be optimum for R32. This chapter investigates tube-fin type heat exchanger optimum designs for R32 using 5 mm diameter copper tubes. Smaller diameter tubes lead to lower heat exchanger cost, yet the refrigerant-side pressure becomes a major challenging issue. Therefore, the tube length, tube vertical and horizontal spacing, number of tubes per bank, tube banks and circuitries need to be changed correspondingly. It was found that given the same air-side pressure

drop and a 25% increase of the refrigerant-side pressure drop of the baseline, a cost reduction of 26% can be achieved, with 1% less in the capacity for the indoor heat exchanger. However, the heat exchanger volume increase is 70%. If the refrigerant-side pressure drop constraint is relaxed to be double that of the baseline, and a heat exchanger volume constraint is added, then the optimum design shows a cost reduction of 56%, and 7% reduction in heat exchanger volume. A small decrease of capacity is observed at 4%. For the outdoor heat exchanger, given the same air-side pressure drop and a 25% increase of the refrigerant-side pressure drop of the baseline, an improvement of 10% in capacity is observed, and a reduction of 33% in cost is observed. The overall volume increase is observed to be 42%. With relaxed constraints of doubling the refrigerant-side pressure drop and adding a 30 Pa air-side pressure drop constraint, plus the heat exchanger volume constraint, the optimum design shows a capacity improvement of 10%, and a cost reduction of 57%.

8. Conclusions

This dissertation investigates a residential heat pump system with a vapor-injected scroll compressor comprehensively. Both experimental and simulation work has been performed. The conclusions are summarized as follows:

8.1 Control strategy analysis

- The control of a two-stage cycle flash tank cycle is difficult because inappropriate control would lead to undesirable amount of liquid flooding the compressor. A new control strategy utilizing an EEV coupled with a PID controller for the upper-stage expansion and a TXV for the lower-stage expansion has been developed and experimentally investigated. A small electric heater is applied in the vapor injection line to introduce superheat to the injected vapor thus providing a control signal to the upper-stage EEV. The proposed control strategy functions effectively for both transient and steady-state operating conditions. The small electric heater can also be replaced by utilizing a small tube-in-tube heat exchanger to exchange heat from the compressor discharge line to the vapor injected line since the heat requirement is less than 100 W.
- The injected vapor superheat can be effectively used as the control signal of the upper-stage expansion valve. Injection pressure and liquid level increase as the target superheat decreases, and as the electric heater power input increases. Liquid level can be controlled properly with recommended heat power input and superheat settings. Considering the system performance and reliability of controlling the flash tank liquid level, 4 K to 6 K of superheating is a

recommended value. For the heating mode, 60 W heater power input is recommended; for the cooling mode, heater power input is preferred to be between 60 W and 90 W.

8.2 Experimental performance results comparison

- Drop-in test was performed with R32 in a heat pump system designed for R410A for both cooling and heating conditions. A refrigerant charge reduction of 29% was observed when switching from R410A to R32.
- In a single stage cycle without vapor injection, experimental results show that the capacity improvement of R32 over R410A is between 3% and 10%, and the COP improvement is between 2% and 9%.
- In a two-stage cycle with vapor injection, vapor injection shows great performance improvement. Comparing to a baseline system without vapor injection, the maximum capacity improvement for R410A and R32 is 33% and 25%, respectively. The maximum COP improvement for R410A and R32 is 18% and 11%, respectively. The improvement is most pronounced for heating mode at an ambient temperature condition of -18 ℃.
- Comparing R32 to R410A at the same injection ratio and using R410A as the baseline, the capacity improvement is between 2% and 7%, and COP improvement is between 1% and 6%. There is no improvement at extreme cooling and heating conditions. The inferior performance of R32 at the extreme conditions is mainly due to the refrigerant mass flow rate decrease caused by the compressor efficiency degradation.

- R32 shows higher compressor discharge temperature than R410A. High compressor discharge temperature reduces the reliability of system operation due to the possibility of lubricating oil degradation. Consequently, reducing the compressor discharge temperature is critical in applying R32, especially at extreme cooling and heating conditions.
- To design a vapor injection system that is optimized for R32, the gas path inside of the compressor should be better designed to minimize heat gain from the motor to avoid high discharge temperature. The compressor suction superheat setting can also be decreased to lower the compressor discharge temperature. Furthermore, introducing additional proper liquid injection to the compressor at extreme conditions can also be used to reduce compressor discharge temperature. With all these methods, the compressor efficiencies are expected to be increased. This in further improves the heat exchanger performance, and therefore leads to an improvement in the overall system efficiency.

8.3 Compressor and heat exchanger modeling

- The two-stage vapor injection compressor model can accurately predict the compressor performance. The compressor discharge temperature from the model shows a deviation of ±3℃ with 85% accuracy compared to experimental results, and 93% of the results are within ±5℃ variation. The total power consumption variation is within ±10% variation with 95% accuracy. The refrigerant mass flow rate from the model matches the experimental results all within ±8%. The

experimentally validated compressor model is used in the compressor cooling study.

- Heat exchanger modeling using CoilDesigner matches the experimental results within ±6%. Heat exchanger modeling reveals that R32 has better heat transfer characteristics than R410A in different operating conditions. The air-side heat transfer is the dominating factor in order to improve the system performance for the cooling mode. For the heating mode, especially at the low ambient temperatures of -8℃ and -18℃, the refrigerant-side heat transfer also becomes a constraint for further system improvement.

8.4 Cycle modeling

- Thermodynamic cycle modeling using ideal compressor efficiencies of 1.0 identifies the maximum performance that the system can reach. Difference between modeling results using ideal compressor efficiencies of 1.0 and actual compressor performances is from the actual compressor performance variations. Difference between experimental results and modeling results using actual compressor efficiencies is due to the actual heat exchanger performance.
- Cycle modeling utilizing VapCyc integrates the two-stage compressor model as well as the heat exchanger models in CoilDesigner. The modeling results were validated against experimental results. Modeling results match with experimental results within ±10% for the system capacity, COP, power consumption and refrigerant mass flow rates.

8.5 Optimization study for R32

- High compressor discharge temperature is a major challenging issue for R32, and by employing proper liquid injection, the compressor discharge temperature can be decreased dramatically. For the cooling mode, there is a slight decrease of cooling capacity and COP due to less refrigerant flowing through the evaporator. For the heating mode, liquid injection even increases the heating capacity and COP due to the increase of upper-stage volumetric efficiency, which leads to a higher refrigerant mass flow rate through the condenser.
- Heat exchangers designed for R410A may not be optimized for R32. An optimization was performed on the tube-fin type heat exchanger for R32 using 5 mm diameter copper tubes. Design parameters include tube length, tube vertical and horizontal spacing, number of tubes per bank, tube banks and heat exchanger circuitries. There are also trade-offs among cost, capacity, volume and pressure drops. For the indoor heat exchanger, the optimum design shows a cost reduction of 56% and 7% reduction in heat exchanger overall volume. A small decrease of capacity is observed at 4%. The air-side pressure drop is the same as the baseline, and the refrigerant-side pressure drop is double that of the baseline. For the outdoor heat exchanger, the optimum design shows a cost reduction of 57% and 3% reduction in overall volume. The capacity improvement is observed to be 10%. Air-side pressure drop is limited to be 30 Pa, and the refrigerant-side pressure drop is double that of the baseline.

- In conclusion, R32 is an excellent alternative to replace R410A. The optimization study reveals that some modifications are needed to design a system better to fit R32. Applying proper liquid injection for compressor cooling is an effective means in reducing the high discharge temperature of R32. A properly designed heat exchanger can achieve significant cost reduction while maintaining roughly the same or even higher capacity as a simple drop-in basis for R410A.

9. List of major contributions and future works

9.1 Major contributions

This work investigates a residential R410A flash tank vapor injection heat pump system experimentally and theoretically. Drop-in test utilizing a low-GWP refrigerant R32 was performed using the R410A heat pump system. The major contributions of this work are listed as follows:

1. A flash tank equipped with a flow visualization window was built and installed in a vapor injection heat pump system.
    a. The visualization window provided the convenience to monitor the liquid level in the flash tank during the experimental tests, and to develop effective control strategies.
    b. System has been tested under ASHRAE Standard and extended operation conditions to explore the potential benefits of vapor injection.
2. The control strategy for the flash tank cycle was developed.
    a. A novel control strategy employing an EEV coupled with a PID controller was investigated.
    b. System operated reliably in both steady-state and cyclic operating conditions.
3. As a potential candidate for R410A replacement, R32 was investigated in a flash tank vapor injection system. While conventional study only focused on R32 in a single stage cycle, this study investigated R32 not only in a single stage cycle, but also in a two-stage flash tank cycle.

4. Component and cycle models were validated against experimental results.
    a. Detailed modeling was performed on a two-stage vapor injection compressor, heat exchangers and two-stage vapor compression cycles.
    b. Good agreement between the experimental and modeling results was reached.
5. Optimization study was performed for R32.
    a. Compressor cooling technology was investigated to reduce compressor discharge temperature for using R32.
    b. Heat exchangers were optimized using 5 mm tubes to achieve significant cost reduction while maintaining identical capacity.

9.2 List of related publications

Peer-reviewed Journal papers:

1. **Xu, X.**, Hwang, Y., Radermacher, R., 2012, "Experimental evaluation and theoretical analysis of vapor injection cycles for R410A and R32" (Under review by International Journal of Refrigeration).
2. **Xu, X.**, Hwang, Y., Radermacher, R., 2011, "Transient and steady-state experimental investigation of flash tank vapor injection heat pump cycle control strategy", International Journal of Refrigeration, Vol. 34, pp. 1922-1933.
3. **Xu, X.**, Hwang, Y., Radermacher, R., 2011, "Refrigerant injection for heat pumping/air conditioning systems: literature review and challenges discussions", International Journal of Refrigeration, Vol. 34, pp.402-415.

4. **Xu, X.**, Hwang, Y., Radermacher, R., Pham, H.M., 2010, "Control strategy and refrigerant charging management of vapor injection system with a flash tank", Journal of Refrigeration and Air-Conditioning, Vol. 10, pp. 119-126.

Conference papers:

1. **Xu, X.**, Hwang, Y., Radermacher, R., Pham, H.M., 2012, "Performance measurement of R32 in vapor injection heat pump system", International Refrigeration and Air Conditioning Conference at Purdue.
2. **Xu, X.**, Hwang, Y., Radermacher, R., 2012, "Performance comparison of R410A and R32 in a vapor injection heat pump system with a flash tank", Asian Conference on Refrigeration and Air Conditioning at Xi'an, China.
3. Qiao, H., **Xu, X.**, Aute, V., Radermacher, R., 2012, "Modelica based transient modeling of a flash tank vapor injection system and experimental validation", International Refrigeration and Air Conditioning Conference at Purdue.
4. **Xu, X.**, Hwang, Y., Radermacher, R., Pham, H.M., 2011, "CFD modeling of two-phase fluid separation in a flash tank used in a vapor injection heat pump cycle," 10th IEA Heat Pump Conference, Tokyo, Japan.
5. **Xu, X.**, Hwang, Y., Radermacher, R., Pham, H.M., 2010, "Control strategy of vapor injection cycle," International Refrigeration and Air Conditioning Conference at Purdue.

Invention disclosure

1. Xu, X., Hwang, Y., Radermacher, R., 2011, "Novel design of a flash tank," University of Maryland College Par invention disclosure, PS 2011020.

9.3 Future work

Based on the work completed in this dissertation, the following listed tasks are worth further research efforts:

1. Develop a more precise compressor model including all the detailed physical parameters of the compressor, and investigate the heat transfer inside of the compression chamber as well as the compressor shell.
    a. This can be helpful to improve the gas path design inside of the compressor shell to minimize heat transfer of the motor to the refrigerant, and would be helpful to further reduce the compressor discharge temperature for R32.
    b. This can also be useful to understand if the high discharge temperature causes the scrolls to deform, which may lead to refrigerant leakage and result in low compressor efficiencies.
    c. This can be beneficial for optimizing the design of the scrolls to suit better R32.
2. Implement the compressor cooling technology and use optimized heat exchangers to perform experimental tests for R32.
    a. It would be interesting to investigate the performance of an optimized system experimentally.
    b. System integration may even show better performance than component optimization.
3. Investigate the control strategy of a variable speed vapor injection flash tank cycle.

a. Variable speed compressor can be more effective in terms of capacity control.
b. The system behavior and the control strategy may also be different from a constant speed compressor in the flash tank cycle.

4. Study the optimum injection location of the compressor.
    a. In the current study, the injection location of the compressor is fixed.
    b. Varying the injection location can potentially further increase the benefit of vapor injection.
5. Investigate the flash tank cycle using microchannel heat exchangers.
    a. The volume of a microchannel heat exchanger is much less than a tube-fin heat exchanger investigated in this study with identical capacity. Therefore, the refrigerant charge amount of a microchannel heat exchanger is also much less than a tube-fin heat exchanger.
    b. Implementing microchannel heat exchangers can potentially reduce the refrigerant charge amount significantly for a flash tank cycle.
6. Explore the vapor injection performance employing new low-GWP refrigerants or refrigerant mixtures.
    a. Currently there are also new potential refrigerant candidates being developed.
    b. Low-GWP refrigerant mixtures can also be potential candidates to replace R410A.

References

1. Abel, G.R., Wu, M.W., Lau, K.Y., Compressor with vapor injection system, U.S. Patent, No. 7275385B2, 2007.

2. AHRI Standard, Performance rating of unitary air-conditioning & air-source heat pump equipment, AHRI Standard 210/240, 2008.

3. ANSI/AHRI Standard 540, Standard for performance rating of positive displacement refrigerant compressors and compressor units, Air-Conditioning, Heating, and Refrigeration Institute, 2004.

4. ASHRAE Standard, Methods of testing for rating seasonal efficiency of unitary air conditioners and heat pumps, ANSI/ASHRAE Standard 116-2010, 2010.

5. Archon industries: http://archonind.com/

6. Arora, J, Introduction to optimum design, Second Edition, Elsevier Academic Press, 2004.

7. ASHRAE Handbook, Fundamentals, I-P Edition, ISBN: 1-883413-87-7, 2001.

8. ASHRAE Standard, Standard methods for laboratory air-flow measurement, ANSI/ASHRAE Standard 41.2, 1987.

9. Atsumi, A., Oguni, K., Kuroda S., Senshu T., Yoshioka K., Refrigerating apparatus having a gas injection path, U.S. Patent, No. 4517811, 1985.

10. Ayub, S., Bush, J. W., Haller, D. K., Liquid refrigerant injection in scroll compressors operating at high compression ratios, Proceedings of International Compressor Engineering Conference at Purdue, pp. 561-567, 1992.

11. Baek, C., Lee, E., Kang, H., Kim Y., Experimental study on the heating performance of a CO_2 heat pump with gas injection, Proceedings of International Refrigeration and Air Conditioning Conference at Purdue, 2008.

12. Beeton, W. L., Pham, H. M., Vapor-injected scroll compressor, ASHRAE Journal, Vol. 45, pp. 22-27, 2003.

13. Bella, B., Kaemmer, N., Analysis of R32 in A/C application. DKV-Tagung 2011, Aachen, AA IV.

14. Berezin, I.S., Effect of the method of a liquid coolant on the productivity and efficiency of a compressor, Khimicheskoe I neftyanoe Mashinostroenie, Vol. 5, pp. 18-19, 1987.

15. Bertsch, S.S., Groll, E.A., Two-stage air-source heat pump for residential heating and cooling applications in northern US climate, International Journal of Refrigeration, Vol. 31, pp. 1282-1292, 2008.

16. Bush, J.W., Daniels, M.A., Katra, T.S., Lifson, A., Lin, R.R., Marks, P.C., Rousseau, W.H., Wagner, T.C., Yannascoli D., Liquid injection for reduced discharge pressure pulsation in compressors, U.S. Patent, No. 6826926B2, 2004.

17. Cao, F., Wang, K., Wang, S., Xing, Z., Shu, P., Investigation of the heat pump water heater using economizer vapor injection system and mixture of R22/R600a, International Journal of Refrigeration, Vol. 32, pp. 509-514, 2009a.

18. Cao, F., Fei, J., Xing, Z., Li, L., Study on performance of a heat pump water heater using suction stream liquid injection, Applied Thermal Engineering, Vol. 29, pp. 2942-2948, 2009b.

19. Cavallini, A., Cecchinato, L., Corradi, M., Fornasieri, E., Zilio, C., Two-stage transcritical carbon dioxide cycle optimization: a theoretical and experimental analysis, International Journal of Refrigeration, Vol. 28, pp. 1274-1283, 2005.

20. Cawley, R.E., Replacement refrigerant for R410A. U.S. Patent, No. 0057396 A1, 2003.

21. Chen, W., A comparative study on the performance and environmental characteristics of R410A and R22 residential air conditioners, Applied Thermal Engineering, Vol. 28, pp. 1-7, 2008.

22. Chen, Y., Halm, N. P., Braun, J. E., Groll, E. A., Mathematical modeling of scroll compressors - part2: overall scroll compressor modeling, International Journal of Refrigeration, Vol. 25, pp. 751-764, 2002.

23. Cho, H., Kim, Y., Experimental study on an inverter-driven scroll compressor with an injection system, Proceedings of International Compressor Engineering Conference at Purdue University, pp.785-790, 2000.

24. Cho, H., Chung, J.T., Kim, Y., Influence of liquid refrigerant injection on the performance of an inverter-driven scroll compressor, International Journal of Refrigeration, Vol. 26, pp. 87-94, 2003.

25. Cho, Y.I., Bai, C., Refrigeration system with liquid refrigerant injection to the condenser, U.S. Patent, No. 0167792A1, 2003.

26. Cho, H., Baek, C., Park, C., Kim, Y., Performance evaluation of a two-stage CO_2 cycle with gas injection in the cooling mode operation, International Journal of Refrigeration, Vol. 32, pp. 40-46, 2009.

27. Climate change synthesis report, IPCC Fourth Assessment Report, 2007.

28. Copeland: http://www.emersonclimate.com/

29. Dutta, A., Yanagisawa, T., Fukuta, M., An investigation of the performance of a scroll compressor under liquid refrigerant injection, International Journal of Refrigeration, Vol. 24, pp. 577-587, 2001.

30. EES: http://www.mhhe.com/engcs/mech/ees/

31. Fan, S., Liu, Q., He, S., Scroll compressor development for air-source heat pump water heater applications, Proceedings of International Refrigeration and Air Conditioning Conference at Purdue, 2008.

32. Fujita, M., Amo, Y., Refrigerating apparatus, U.S. Patent, No. 0196449A1, 2003.

33. Gebbie, J., Jensen, M., Domanski, P., Experimental transient performance of a heat pump equipped with a distillation column, International Journal of Refrigeration, Vol. 30, pp. 499-505, 2007.

34. General Eastern: http://www.ge-mcs.com/en/moisture-and-humidity.html

35. Gnielinski, V., New equations for heat and mass transfer in turbulent pipe and channel flow, International Chemical Engineering, Vol. 16, pp. 359-368, 1976.

36. Haselden, G., Refrigerant screw compression with liquid refrigerant injection, U.S. Patent, No. 3931718, 1976.

37. He, S., Guo, W., Wu, M., Northern china heat pump application with the digital heating scroll compressor, Proceedings of International Compressor Engineering conference at Purdue, 2006.

38. Heo, J., Lee, Y., Lee, S., Kim, Y., Improvement of the heating performance in a variable speed heat pump by applying the gas injection technique into a twin rotary compressor, International Congress of Refrigeration, Beijing, 2007.

39. Hickman, C., Neal, W., Implications of cooling rotary sliding vane heat-pump compressors, International Journal of Ambient Energy, Vol. 5, pp. 207-212, 1984.

40. Hill, F.H., Crane, C.C., Buckley, M.L., Stabley, B.E., Flash tank economizer refrigeration systems, U.S. Patent, No. 6941769B1, 2005.

41. Hipchen, J., Weed, R., Zhang, M., Nasuta, D., Simulation-based comparison of optimized AC coils using smaller diameter copper and aluminum microchannel tubes, International Refrigeration and Ai Conditioning Conference at Purdue, 2012.

42. Hirano, T., Hagimoto, K., Matsuda, S., Study on scroll compressor behavior in case of liquid refrigerant injection, Transactions of Japanese Association of Refrigeration, Vol. 10, pp. 227-238, 1993.

43. Holtzapple, M., Reducing energy costs in vapor-compression refrigeration and air conditioning using liquid recycle - part 2: performance, ASHRAE Transactions No 3222, Vol. 95, pp.179-205, 1989.

44. Huang, M., Hewitt, N., Nugyen, M., Field testing of an economized vapor injection heat pump, Proceedings of International Congress of Refrigeration, Beijing, 2007.

45. Huang, Y., Yin, Q., Yu, J., Wang, J., Comparative experimental researches of air-to-water heat pump with R32 and R410A for household, International Congress of Refrigeration, 2011.

46. Hwang, Y., Celik, A., Radermacher, R., Performance of CO_2 cycles with a two-stage compressor, Proceedings of International Refrigeration and Air Conditioning Conference at Purdue, 2004.

47. Ignatiev, K., Caillat, J.L., Injection system and method for refrigeration system compressor, U.S. Patent, No. 0078192A1, 2008.

48. Incropera, F.P., DeWitt, D.P., Introduction to heat transfer. (3rd edition), John Wiley & Sons, New York, 1996.

49. Intempco Inc.: http://www.intempcousa.com/

50. Ishii, H., Matsuda, M., Sanuki, M., Compressor having refrigerant injection ports, U.S. Patent, No. 5722257, 1998.

51. Jang, Y., Lee, E., Chin, S., Ha, S., Effects of flash and vapor injection on the air-to-air heat pump system. International refrigeration and air conditioning conference at Purdue, 2010.

52. Jiang, H., Development of a simulation and optimization tool for heat exchanger Design, Ph.D. Dissertation, Department of Mechanical Engineering, University of Maryland, College Park, 2003.

53. Jung, D.S., Radermacher, R., A study of flow boiling heat transfer with refrigerant mixtures, International Journal of Heat and Mass Transfer, Vol. 32, pp. 1751-1764, 1989a.

54. Jung, D.S., Radermacher, R., Prediction of pressure drop during horizontal annular flow boiling of pure and mixed refrigerants, International Journal of Heat and Mass Transfer, Vol. 32, pp. 2435-2446, 1989b.

55. Joppolo, C.M., Molinaroli, L., Vecchi, G., Performance assessment of an air-to-water R407C heat pump with vapor injection scroll compressor, ASHRAE conference, 2010.

56. Kamimura, I., Sawada, N., Satou, K., Masuda, T., Mixed refrigerant injection method, U.S. Patent, No. 5970721, 1999.

57. Kang, H., Lee, S., Kim, Y., Effects of liquid refrigerant injection on the performance of a refrigeration system with an accumulator heat exchanger, International Journal of Refrigeration, Vol.31, pp. 883-891, 2008.

58. Kim, N.H., Yun, J.H., Webb, R.L., Heat Transfer and Friction Correlations for Wavy Plate Fin-and-Tube Heat Exchangers, Transactions of the ASME, Journal of Heat Transfer, Vol. 119, pp. 560-567, 1997.

59. Kim, N.H., Youn, B., Webb, R.L., Air-Side Heat Transfer and Friction Correlations for Plain Fin-and-Tube Heat Exchangers with Staggered Tube Arrangements, Transactions of the ASME, Journal of Heat Transfer, Vol. 121, pp. 662-667, 1999.

60. Koyama, S., Takata, N., Fukuda, S., Drop-in experiments on heat pump cycle using HFO-1234ze (E) and its mixtures with HFC-32, International Refrigeration and Air Conditioning Conference at Purdue, 2010.

61. Koyama, S., Takata, N., Fukuda, S., An experimental study on heat pump cycle using zeotropic binary refrigerant of HFO-1234ze (E) and HFC-32, IEA Heat Pump Conference, 2011.

62. Leimbach, J. G., Heffner, J. H., Injection valve for a refrigeration system, U.S. Patent, No. 5148684, 1992.

63. Lifson, A., Taras, M.F., Dobmeier, T.J., Flash tank for heat pump in heating and cooling modes of operation, U.S. Patent, No. 7137270B2, 2006.

64. Lifson, A., Taras, M., Economized refrigerant system with vapor injection at low pressure, U.S. Patent, No. 0256961A1, 2008.

65. Liu, F., Huang, H., Ma, Y., Zhuang, R., An experimental study on the heat pump water heater system with refrigerant injection, Proceedings of International Refrigeration and Air Conditioning Conference at Purdue, 2008.

66. Liu, Z., Soedel, W., An Investigation of compressor slugging problems, Proceedings of International Compressor Engineering Conference proceedings at Purdue, pp. 433-440, 1994.

67. Liu, Z., Soedel, W., A mathematical model for simulating liquid and vapor two-phase compression processes and investigating slugging problems in compressors, HVAC&R Research, Vol. 1, No. 2, pp. 99-109, 1995.

68. Lockhart, R.W., Martinelli, R.C., Proposed correlation of data for isothermal two-phase, two-component flow in pipes, Chemical Engineering Progress, Vol. 45, pp. 39-48, 1949.

69. Lord, R.G., Rabbia, M.R., Glover, K.J., Flash tank economizer, U.S. Patent, No. 5692389, 1997.

70. Ma, G., Chai, Q., Jiang, Y., Experimental investigation of air-source heat pump for cold regions, International Journal of Refrigeration, Vol. 26, pp. 12-18, 2003.

71. Ma, G.Y., Chai, Q.H., Characteristics of an improved heat-pump cycle for cold regions, Applied Energy, Vol. 77, pp. 235-247, 2004.

72. Ma, G.Y., Zhao, H.X., Experimental study of a heat pump system with flash tank coupled with scroll compressor, Energy and Buildings, Vol. 40, pp. 697-701, 2008.

73. Magrab, E., Azarm, S., Balachandran, B., Duncan, J., Herold, K., Walsh, G., An Engineer's Guide to Matlab, 1st edition, 2000.

74. Micro Motion: http://www2.emersonprocess.com/en-US/brands/micromotion

75. Monica, M.J., Rowland, F.S., Stratsperic sink for chlorofluoromethanes: chlorinme atom-catalysed distraction of ozone, Nature, Vol. 249, No. 5460, pp. 810-812, 1974.

76. Moriwaki, M., Sakitani, K., Inokuchi, Y., Sasaki, Y., Refrigeration apparatus, U.S. Patent, No. 0098758A1, 2008.

77. Moody, H.W., Hamilton, C.B., Liquid refrigerant injection system for hermetic electric motor driven helical screw compressor, U.S. Patent, No. 3913346, 1975.

78. Nakamura, K., High heating capacity packaged air conditioners with liquid injection cycle, Journal of Refrigeration, Vol. 82, No. 952, pp. 14-18, 2007 (In Japanese).

79. National Instrument: www.ni.com

80. Nguyen, Q. M., Neil, J. H., Philip, C. E., Improved vapor compression refrigeration cycles: literature review and their application to heat pumps, Proceedings of International Refrigeration and Air Conditioning Conference at Purdue, 2006.

81. Nguyen, M., Hewitt, N., Huang, M., Performance evaluation of an air source heat pump using economized vapor injection compressor and flash tank coupled with capillary tubes, Proceedings of International Congress of Refrigeration, Beijing, 2007.

82. Ohi Semitronics: https://www.ohiosemitronics.com/products.asp

83. Okido, T., Takigawa, K., Saito, M., Development of refrigeration oil for use with R32, International Refrigeration and Air Conditioning Conference at Purdue, paper 2221, 2012.

84. Omega: http://www.omega.com/

85. Pande, M., Hwang, Y., Judge, J., Radermacher, R., An experimental evaluation of flammable and non-flammable high pressure HFC replacements for R22, International Refrigeration and Air Conditioning Conference at Purdue, 1996.

86. Park, Y. C., Kim, Y., Cho, H., Thermodynamic analysis on the performance of a variable speed scroll compressor with refrigerant injection, International Journal of Refrigeration, Vol.25, pp. 1072-1082, 2002.

87. Pham, H.M., Caillat, J.L., Hoose, R.L., Flash tank design and control for heat pumps, U.S. Patent, No. 0251256A1, 2007.

88. Pham, H.M., Caillat, J.L., Hoose, R.L., Flash tank design and control for heat pumps, U.S. Patent, No. 0047284A1, 2008.

89. Pham, H.M., Caillat, J.L., Hoose, R.L., Flash tank design and control for heat pumps, U.S. Patent, No. 7484374B2, 2009.

90. Pham, H., Rajendran, R., R32 and HFOs as low-GWP refrigerants for air conditioning, International Refrigeration and Air Conditioning Conference at Purdue, paper 2262, 2012.

91. Qiao, H., Xu, X., Aute, V., Radermacher, R., Modelica based transient modeling of a flash tank vapor injection system and experimental validation, International Refrigeration and Air Conditioning Conference at Purdue, 2012.

92. Reynolds, T.W., Design of the flash tank, Heating and Ventilating, pp. 74-76, 1950.

93. Reynolds, T.W., Flash tank design, Heating and Ventilating, pp. 96-97, 1955.

94. Richardson, D. H., An object oriented simulation framework for steady-state analysis of vapor compression refrigeration systems and components, Ph.D. Dissertation, Department of Mechanical Engineering, University of Maryland, College Park, 2006.

95. Saito, M., Packaged air conditioners that improve the heating capacity by flash injection circuit, Journal of Refrigeration, Vol. 82, No. 952, pp. 19-22, 2007 (In Japanese).

96. Sami, S. M., Tulej, P. J., A new design for an air source heat pump using a ternary mixture for cold climates, Heat Recovery Systems & CHP, Vol.15, No.6, pp. 521-529, 2001.

97. Sami, S. M., Aucoin, S., Study of refrigerant mixtures with gas/liquid injection, Proceedings of the ASME Process Industries Division, Vol. 7, pp. 123-127, 2002.

98. Sami, S. M., Aucoin, S., Behavior of refrigerant mixtures with gas/liquid injection, International Journal of Energy Research, Vol. 27, pp. 1265-1277, 2003a.

99. Sami, S. M., Aucoin, S., Study of liquid injection impact on the performance of new refrigerant mixtures, International Journal of Energy Research, Vol. 27, pp. 121-130, 2003b.

100. Schein, C., Radermacher, R., Scroll compressor simulation model, Journal of Engineering for Gas Turbines and Power, Vol. 123, pp. 217-225, 2001.

101. Setra: http://www.setra.com/Product/Pressure.htm

102. Shah, M.M., A general correlation for heat transfer during film condensation inside pipes, International Journal of Heat and Mass Transfer, Vol. 22, pp. 547-556, 1979.

103. Shah, M.M., Chart correlation for saturated boiling heat transfer: equations and further study, ASHRAE Transactions, Vol. 88, pp.185-196, 1982.

104. Shcherba, V.E., Berezin, I.S., Danilenko, S.S., Efficient injection of cooling liquid into rotary compressor with a rolling rotor. Khimicheskoe I neftyanoe Mashinostroenie, Vol. 12, pp. 18-21, 1987.

105. Skinner, R.G., Scroll compressor with refrigerant injection system, U.S. Patent, No. 0184733A1, 2008.

106. Sporlan Thermostatic Expansion Valves, Bulletin 10-9, August 2005.

107. Sporlan Electric Expansion Valves, Bulletin 100-20, September 2008.

108. Sun, S., Zhao, Y., Li, L., Shu, P., Simulation research on scroll refrigeration compressor with external cooling, International Journal of Refrigeration, Vol. 33, pp. 897-906, 2010.

109. TableCurve3D: http://www.sigmaplot.com/products/tablecurve3d/tablecurve3d.php

110. Taira, S., Yamakawa, T., Nakai, A., Yajima, R., Examination regarding air-conditioners and heat pumps, using the next generation refrigerants, IEA Heat Pump Conference, 2011.

111. Tian, C.Q., Liang, N., Shi, W.X., Li, X.T., Development and experimental investigation on two-stage compression variable frequency air source heat pump, Proceedings of International Refrigeration and Air Conditioning Conference at Purdue, 2006.

112. Tian, C.Q., Liang, N., State of the art of air-source heat pump for cold regions, Renewable Energy Resources and a Greener Future, Vol. 8, 2006.

113. Tu, X., Liang, X., Zhuang, R., Study of R32 refrigerant for residential air-conditioning applications, International Congress of Refrigeration, 2011.

114. Ueno, F., Fukuhara, K., Refrigeration system, U.S. Patent, No. 4344297, 1982.

115. Umezu, K., Suma, S., Heat pump room air-conditioner using variable capacity compressor, ASHRAE transactions, Vol. 90, pp.335-349, 1984.

116. Vaisala: http://www.vaisala.com/en/products/humidity/Pages/default.aspx

117. Wang, B., Study on the scroll compressor with refrigerant injection and its application, Ph.D. Dissertation, Department of Civil Engineering, Tsinghua University, 2005.

118. Wang, B., Li, X., Shi, W., Yan, Q., Design of experimental bench and internal pressure measurement of scroll compressor with refrigerant injection, International Journal of Refrigeration, Vol. 30, pp. 179-186, 2007.

119. Wang, B., Shi, W., Li, X., Yan, Q., Numerical research on the scroll compressor with refrigeration injection, Applied Thermal Engineering, Vol. 28, pp. 440-449, 2008a.

120. Wang, B., Shi, W., Li, X., Numerical analysis on the effects of refrigerant injection on the scroll compressor, Applied Thermal Engineering. Vol. 29, pp. 37-46, 2009a.

121. Wang, B., Shi, W., Li, X., Optimization of refrigeration system with gas-injected scroll compressor, International Journal of Refrigeration, Vol. 32, pp. 1544-1554, 2009b.

122. Wang, X., Performance investigation of two-stage heat pump system with vapor injected scroll compressor, Ph.D. Dissertation, University of Maryland College Park, 2008.

123. Wang, X., Hwang, Y., Radermacher, R., Investigation of potential benefits of compressor cooling, Applied Thermal Engineering, Vol. 28, pp. 1791-1797, 2008b.

124. Wang, X., Hwang, Y., Radermacher R., Two-stage heat pump system with vapor-injected scroll compressor using R410A as a refrigerant, International Journal of Refrigeration, Vol. 32, pp. 1442-1451, 2009c.

125. WIKA Inc.: http://www.wika.us/

126. Winandy, E.L., Lebrun, J., Scroll compressors using gas and liquid injection: experimental analysis and modeling, International Journal of Refrigeration, Vol. 25, pp. 1143-1156, 2002.

127. Winkler, J., Aute, V., Radermacher, R., Comprehensive investigation of numerical methods in simulating a steady-state vapor compression system, International Journal of Refrigeration, Vol. 31, pp. 930-942, 2008.

128. Winkler, J., Development of a component based simulation tool for the steady state and transient analysis of vapor compression systems, Ph.D. Dissertation, University of Maryland College Park, 2009.

129. Wu, W., Ding, G., Zheng, Y., Gao, Y., Song, J., Principle of designing fin-and-tube heat exchanger with smaller diameter tubes for air conditioning, International Refrigeration and Air Conditioning Conference at Purdue, paper 2223, 2012.

130. Xu, X., Hwang, Y., Radermacher, R., Pham, H., Control strategy and refrigerant charging management of vapor injection system with a flash tank, Journal of Refrigeration and Air-Conditioning, Vol. 10, pp.119-126, 2010a. (In Chinese).

131. Xu, X., Hwang, Y., Radermacher, R., Pham, H., Control strategy of vapor injection cycle, International Refrigeration and Air Conditioning Conference at Purdue, paper 2249, 2010b.

132. Xu, X., Hwang, Y., Radermacher, R., Refrigerant injection for heat pumping/air conditioning systems: literature review and challenges discussions, International Journal of Refrigeration, Vol. 34, pp. 402-415, 2011a.

133. Xu, X., Hwang, Y., Radermacher, R., Transient and steady-state experimental investigation of flash tank vapor injection heat pump cycle control strategy, International Journal of Refrigeration, Vol. 34, pp. 1922-1933, 2011b.

134. Xu, X., Hwang, Y., Radermacher, R., Pham, H., CFD modeling of two-phase fluid separation in a flash tank used in a vapor injection heat pump cycle, 10th IEA Heat Pump Conference, Tokyo, Japan, 2011c.

135. Xu, X., Hwang, Y., Radermacher, R., Pham, H., Performance measurement of R32 in vapor injection heat pump system, International Refrigeration and Air Conditioning Conference at Purdue, paper 2328, 2012.

136. Yajima, R., Kita, K., Taira, S., Domyo, N., R32 as a solution for energy conservation and low emission, Eighth International Refrigeration Conference at Purdue, 2000.

137. Yan, C., Xu, H., Ginies, P., Watts, S., R32 scroll compressors technology, International Refrigeration and Air Conditioning Conference at Purdue, paper 1429, 2012.

138. Zlatanovic, I., Rudonja, N., Experimental evaluation of desuperheating and oil cooling process through liquid injection in two-staged ammonia refrigeration systems with screw compressors, Applied Thermal Engineering, Vol. 40, pp. 210-215, 2012.